Approche multi-échelle de la rupture des structures en béton : Influence des agrégats sur la longueur interne du matériau

Huu Phuoc Bui

UNIVERSITÉ DE GRENOBLE

THÈSE

Pour obtenir le grade de

DOCTEUR DE L'UNIVERSITÉ DE GRENOBLE

Spécialité : **Matériaux, Mécanique, Génie civil, Électrochimie**

Arrêté ministérial : 7 août 2006

Présentée par

Huu Phuoc BUI

Thèse dirigée par **Frédéric DUFOUR**
et codirigée par **François FAURE** et par **Vincent RICHEFEU**

préparée au sein du **Laboratoire Sols, Solides, Structures, Risques (3SR)**
dans **l'École doctorale Ingénierie – Matériaux, Mécanique, Énergétique, Environnement, Procédés, Production (I–MEP2)**

Multiscale approach of concrete structure failure: Influence of aggregates on material internal length

Thèse soutenue publiquement le **21 Novembre 2013**,
devant le jury composé de :

M. Jean-Yves DELENNE
Directeur de recherche CNRS, INRA, Président
M. Christian LA BORDERIE
Professeur des Universités, Université de Pau et des Pays de l'Adour, Rapporteur
M. Arnaud DELAPLACE
Chargé de recherche CNRS, Lafarge Centre de Recherche, Rapporteur
M. Yves BERTHAUD
Professeur des Universités, Université Pierre et Marie CURIE, Examinateur
M. Frédéric DUFOUR
Professeur des Universités, Grenoble INP, Directeur de thèse
M. François FAURE
Professeur des Universités, Université Joseph Fourier, Co-Directeur de thèse
M. Vincent RICHEFEU
Maître de Conférences, Université Joseph Fourier, Co-Encadrant de thèse

To my beloved mother and father,
To my lovely sister and brother,

Acknowledgments

"No guide, no realization" is a proverb that I have learned since my childhood. Without the guidances and visions of Frédéric Dufour, Vincent Richefeu and François Faure, this thesis would never reach completion. For these reasons, I would like to express my sincere gratitude to them, especially for their ideas, belief, enthusiasm, support, understanding and wisdom. Moreover, my honest thanks to Christian La Borderie, Arnaud Delaplace, Yves Berthaud, Jean-Yves Delenne who serve as my thesis committee, for their constructive remarks and observations.

My appreciation goes to Rémi Cailletaud and Jérôme Branon for their computer supports during the thesis. Thanks also to colleagues, friends at laboratory 3SR. I would like to thank my friends here in Grenoble, Jacques, Tieng, Dung, Nghia, Linh, Phuong, Thanh, Nguyet, Thi, Minh Bi, Hien, Son for the times we have spent together which have made my life here very enjoyable.

My special gratitude is directed to Chau Cam Hoang Tran, my fiancée. Her love, strength and wisdom have made me stronger to overcome difficult times of the thesis. I am greatly indebted to my parents, my sister and brother. Their love is the endless source of energy which has given me strong power to achieve every goals in my life.

Huu Phuoc Bui
Grenoble, November 2013

Summary

For durability analysis and economic design (less material) of structures made of concrete-like materials, modeling of cracking process and failure is essential. In the framework of continuum mechanics, an internal length is introduced in nonlocal models to remedy the problem related to mesh sensitivity which is a pathology of classical damage models, when dealing with softening materials. However, the assessment of the internal length from heterogeneities of the material is still a difficult question, which makes an obscure issue in using nonlocal models. Our work concerns developing of a numerical tool based on the Lattice Element Method (LEM) which is a discrete model for simulating and predicting fracture in concrete(-like) material. Using the lattice model at the mesoscopic scale, there is no need to introduce any internal length in the constitutive law, as done in nonlocal models, and we can enfranchise this parameter by explicitly introducing the material mesotructure via geometric description. Based on the developed numerical tool, we studied, by performing numerical uniaxial tensile tests, the geometric influence of the material mesotructure as well as the influence of the boundary conditions and specimen sizes (that result in different stress gradient and material rotation field) on the size of the FPZ (Fracture Process Zone) and on the characteristic length of the homogenized quasi-brittle material. These studies provide recommendations/warnings when extracting an internal length required for nonlocal damage models from the material microstructure. Moreover, the studies contribute a direct insight into the mesoscale origin of the FPZ size and the material characteristic length, and consequently into the origin and nature of the nonlinear behavior of the material.

Then, we implemented the lattice model into SOFA library developed by INRIA for realizing the coupling with the Finite Element Method (FEM) in order to deal with large-scale structures. We proposed a strong coupling algorithm between a macroscopic approach represented by FEM and a mesoscopic approach dealt by LEM within an adaptive manner. The coupling model is first used to validate the multiscale approach proposed on heuristic simulations. And in the long term, it provides a promising tool for simulations of large-scale structures made of quasi-brittle materials of real life.

Keywords: Quasi-brittle materials, material internal length, characteristic length, fracture, cracking, failure, multiscale modeling, LEM, FEM.

Résumé

Pour l'analyse de durabilité et la conception économique (moins de matériau) des structures en matériaux ressemblant à béton, la modélisation de la rupture est essentielle. Dans le cadre de la mécanique des milieux continus, une longueur interne est introduite dans les modèles non locaux pour remédier le problème lié à la sensibilité du maillage qui est une pathologie des modèles d'endommagement classiques, lorsqu'on fait face aux matériaux adoucissants. Toutefois, l'évaluation de la longueur interne à partir des hétérogénéités du matériau est toujours une question difficile, ce qui rend obscur en utilisant des modèles non locaux. Nos travaux portent sur le développement d'un outil numérique basé sur la méthode des éléments de lattice (LEM) qui est un modèle discret pour la simulation et la prévision de la rupture des structures en béton. En utilisant le modèle de lattice à l'échelle mésoscopique, il n'est pas nécessaire d'introduire une longueur interne dans la loi de comportement, comme cela se fait dans les modèles non locaux, et nous pouvons affranchir ce paramètre en introduisant explicitement la mesotructure du matériau via une description géométrique. Basé sur l'outil numérique développé, nous avons étudié, en effectuant des tests numériques de traction uni-axiale, l'influence géométrique de la mesotructure du matériau ainsi que l'influence des conditions aux limites et de tailles des échantillons (qui se traduisent par la différence du gradient de sollicitation et du champ de rotation matériel) sur la taille de la FPZ (fracture process zone) et sur la longueur caractéristique du matériau quasi-fragile homogénéisé. Ces études fournissent des recommandations/avertissements lors de l'extraction d'une longueur interne nécessaire pour les modèles non locaux à partir de la microstructure du matériau. Par ailleurs, les études contribuent un aperçu direct de l'origine mésoscopic de la taille de la FPZ et la longueur caractéristique du matériau, et par conséquent sur l'origine et la nature du comportement non linéaire du matériau.

Ensuite, nous avons implanté le modèle de lattice dans la bibliothèque de SOFA développé par l'INRIA pour réaliser le couplage avec la méthode des éléments finis (MEF) afin de faire face aux structures à grande échelle. Nous avons proposé un algorithme de couplage entre une approche macroscopique représentée par MEF et une approche mésoscopique représentée par LEM au sein d'une manière adaptative. Le modèle de couplage est d'abord utilisée pour valider l'approche multi-échelle proposée sur des simulations heuristiques. Et à long terme, il fournit un outil prometteur pour des simulations des grandes structures en matériaux quasi-fragiles de la vie réelle.

Mots-clés: Matériaux quasi-fragiles, la longueur interne, la longueur caractéristique, fracture, fissuration, rupture, approche multi-échelle, LEM, MEF.

Contents

List of Figures

List of Tables

Introduction

Background, context and objective

Concrete is widely used in our world today due to its simplicity in elaboration, low cost and high performance in heat resistance, compared to other materials such as metals, wood. Indeed, structures made of concrete have become ubiquitous, and it is really hard to imagine modern life without them. However in practice, structures made of concrete are actually more or less full of cracks due to extreme mechanical loadings, shrinkage or temperature changes. Furthermore, for any reinforced concrete structures, cracking is the entering point to aggressive contaminants (chloride and other ions from road salts, marine environments, and ground soils, etc.) that react either with hydrates or aggregates of concrete or with rebars. The increase of transfer properties will drastically reduce the service life duration of the structures. Therefore, knowledge about the fracture process in concrete is very useful for both conception and durability analysis of structures.

In engineering field, numerical modeling of failure of the material is very important because the description of structural behavior by experimentation might not be feasible due to too high cost, inaccessibility of input and output data because of too large dimensions of structures which are not compatible with human dimensions, etc. In addition, numerical modeling can provide fundamental understanding of the fracture process, which will be of great benefit in terms of design (less material), of service life and at the end for environment.

Nowadays, modeling of fracture of heterogeneous quasi-brittle materials including concrete, ceramics, rocks is evolving over the past twenty years, and becomes a key part of engineering and science development. It is well known that quasi-brittle materials are characterized initially by a quasi elastic stage, and before reaching the peak, microcracks begin to appear. Nearly from the peak, localization of damage occurs in a narrow band with finite size which is called the fracture process zone (FPZ). The macrocrack develops in the localization zone and gradually grows through the specimen, which causes the gradual drop in load carrying capacity, until fully separation. Because of this softening character, numerical simulations of quasi-brittle materials using continuum theory requires the use of models with a representative internal length accounted for the interactions of the material constituents at the microscale, e.g. nonlocal models (gradient or integral form), to remedy the problem of mesh sensitivity of the numerical solution with respect to the element size of the discretization. Physically, the internal length is related to the effective size of the FPZ. The internal length cannot be directly measured but can be indirectly inferred from experiment results. Based on experiments, the literature often reports a linear or affine relation between the internal length and the maximum size of aggregates, or between the internal length and the characteristic size of a structure in the size effect plot. But actually, varying the aggregate size or the specimen size in experiments may lead to a number of changes in the aggregate structure characterized by many other parameters such as the volume fraction of aggregate, their size dispersion, their fabric or connectivity, or in stress field, respectively. Accordingly, the proposed relations in the literature can hardly be considered as general rules. Since so far no explicitly reliable relation is proposed for the assessment of the internal length, it makes obscure in using the nonlocal models and one usually bases on a manual trial-and-error technique.

From that, the main motivation is to develop a numerical model that does not introduce any

internal length in the constitutive law and can enfranchise this parameter by explicitly introducing aggregates in the geometric description. Moreover, through this model, a study of the influence of the microstructure of the material on its behaviors at both prepeak and postpeak regimes can be regarded. Then, an internal length required for nonlocal models is tried to be extracted from the microstructure of the material or at least a better understanding of key features that may affect the internal length can be provided from such study.

We interest particularly in lattice models which have become pertinent tools for studying the fracture of heterogeneous materials. In fact, the lattice approach is very suitable for simulations of fracture process because firstly the discontinuous displacement field is well captured thanks to the intrinsic discrete feature of the models. Secondly, by using lattice approach with introduction of the material heterogeneity by generating the material constituents, the crack propagation and crack opening are explicitly produced, which are a direct tool in durability analyses of (concrete) structures instead of estimating them from a continuum-based approach. In addition, lattice approach provides a direct insight into the origin and nature of the nonlinear behavior of the material and can also reflect physical effects observed in experiments such as grain decohesion, microcracking and crack bridging observed in concrete. However, simulations with the lattice model at the mesoscale require fine resolutions of the discretized mesh. Together with dealing with large-scale structures, they thus lead to a vast number of degrees of freedom, in particular for three-dimensional analyses. Therefore, the analysis of realistic large structures only with lattice models at the mesoscale is not feasible. So, it seems that an appropriate combination of discrete approach at the mesoscale dealt by the lattice approach and continuous approach at the macroscale treated by the finite element method (FEM), which results in a multiscale approach, is essential

The objective of the research presented in this thesis is to develop a numerical tool based on lattice models that allows for simulating the fracture process of quasi-brittle heterogeneous materials. Based on this tool, a study of the mesoscale origin of the FPZ size and the material characteristic length is performed in order to find out a correlation between the material mesostructure and the internal length used in nonlocal models or simply to clarify the role of the mesotructure in the resulting FPZ size. Because of the localized nature of the fracture process in the softening branch, the specimen size and boundary conditions must have a significant effect on the fracture process. Their influence can be analyzed as well from this numerical tool. And in the long term, such numerical tool should be capable of modeling the failure of large structures made of quasi-brittle materials in civil engineering via a multiscale numerical approach.

An overview of the work done can be synthesized as follows:

- Developing a computational code based on the lattice models (normal-shear spring and beam elements).
- Studying the influence of the material mesostructure on the characteristic length and the fracture process zone size of the heterogeneous material using the lattice model at the mesoscale with an explicit description of material microstructure.
- Analyzing the effect of the specimen size and boundary conditions (or generally the stress gradient) on the characteristic length and the fracture process zone size.
- Implementing the lattice model into SOFA library developed by INRIA in order to perform the coupling with finite elements.
- Developing the coupling algorithm provided for parallel computations and implementing such coupling algorithm into SOFA architecture. However, the implementation of the *full* coupling algorithm has not been accomplished yet.

The model, which will be outlined in this thesis, adopts a perfectly elastic brittle fracture law at the mesoscale (aggregate particle scale) of the material and is capable of simulating crack face bridging in the softening regime quite realistically. It is well known that, using the lattice models

with the assumption of the brittleness of single lattice elements, the response of the material is too brittle, particularly in two-dimensional simulations, when neglecting small particles in the material microstructure. Nevertheless, in our studies, within the philosophy of keeping the simplicity of the model with a limited number of parameters and the complexity of macroscopic response coming from a rich geometric description of material microstructure, the brittleness assumption of lattice elements is kept holding. Another reason why lattice elements with brittle elastic parameters are used in the thesis is that, by performing the study on the influence of the material mesostructure, the specimen size, boundary conditions on the characteristic length and the fracture process zone size, we would like to analyze only the "physical" influence (coming from the aggregate structure, the specimen size, boundary conditions) and not that of model softening parameters. The study is first performed on elastic brittle model material by two-dimensional simulations. Then in the long term, the study should be performed by three-dimensional (3D) simulations which provide a 3D effect of cracking process as in structures of real life.

Scope and outline

The research presented in this thesis concerns the computational modeling of quasi-brittle materials with an emphasis on concrete, subjected to mechanical loadings. The study is restricted to mode-I failure problems occurring with small deformations under quasi-static loading conditions. The continuum mechanics is assumed to hold on the macroscopic scale if there are more than one length scale involved in the model. When there is only one scale involved in the model, the discrete lattice model is used at the mesoscopic scale to better capture failure mechanisms at the material scale, and the continuum mechanics is no longer assumed to hold. The term "multiscale" should be understood as multiple (more than one) length scales that are included in the same framework.

The manuscript is composed of four chapters. Chapter 1 briefly describes what is currently known about the behavior, particularly related to cracking of quasi-brittle materials with an emphasis on concrete. From this, an overview of the state-of-the-art of numerical models dealing with such materials is given. The pathologies of each model are pointed out, which lead to the goals of the research.

Chapter 2 presents the lattice model that is used to deal with failure of concrete-like materials. Formulation and implementation of the model will be outlined. The identification procedure of the model parameters is next discussed before validating the model by some tests.

In Chapter 3, the influence of the material microstructure on the characteristic length of the material and the FPZ size is analyzed by using the lattice model with an explicit geometric description of aggregate structure. The study of the influence of the specimen size and boundary conditions which result in different stress gradient on the FPZ size is pointed out as well. These studies provide recommendations/warnings when extracting an internal length required for nonlocal damage models from the material microstructure.

To deal with failure of large scale structures in civil engineering, Chapter 4 presents a coupling procedure between the beam lattice model and finite elements in a multiscale framework with parallel computations.

Finally, the thesis is ended by summarizing the key issues of the work presented in this report and posting recommendations and perspective for future research.

Chapter 1

Cracking of quasi-brittle materials: the state of the art

Contents

Nowadays, quasi-brittle materials such as ceramics, rocks or specially concrete are widely used in industry or civil engineering. Concrete, reinforced concrete and prestressed concrete structures have become ubiquitous, and in fact it is hard to imagine modern life without them. For designing structures made of concrete, it is essential to know the strength of the concrete material and the process of fracture growth in concrete under different loading conditions. Indeed reinforced concrete is a composite material designed such that the tensile stresses are mainly carried by reinforcements while the compressive stresses are assured by concrete. This is the main reason why, in contrary to other industrial materials, it is of a great importance to understand and model the cracking process of the concrete even beyond the maximum bearing capacity (peak load). The tensile strength of concrete is about 10% of the compressive strength. Because of this, the reinforcement (mostly by steel) is used to increase the bearing capacity of the material and to control the development of cracks when concrete is loaded in tension. Knowledge about the fracture process in concrete is also very useful for durability analysis of structures. Indeed, the life time of a reinforced concrete structure not only depends on strength of materials (steel, concrete) under mechanical loading but also on the corrosion of reinforcing steel coming from the ingress of chloride and other ions from road salts, marine environments, and ground soils. So, close attention has to be paid to the transport properties of concrete (diffusivity, permeability, absorptivity, etc.) which are mainly related to the cracking of concrete material. Therefore, cracking in concrete and its mechanism play an essential role in the behavior and durability of concrete structures. It should be noted that although shrinkage and temperature changes can lead to cracking, only cracks due to mechanical loadings are analyzed in this report.

Modeling is an indispensable design tool for concrete structures since it provides a prediction of the behavior of structures. However, the accuracy of the prediction mostly depends on the reliability of described material models. Therefore, material models have to be derived from a measurement of the behavior of the material in an experiment. The mechanical behavior of quasi-brittle materials with an emphasis on concrete is briefly presented in the next section before reviewing the latest numerical methods/models to deal with such materials. Furthermore, a short summary of the contents of this report will be given.

1.1 Mechanical behavior of heterogeneous quasi-brittle materials

Quasi-brittle materials, such as concrete, exhibit a complex fracture mechanism involving microcracks and macrocracks under extreme loading conditions. This complex fracture mechanism is clearly related to their disordered microstructure. Before reviewing the fracture of these materials, it is necessary to illustrate their heterogeneous microstructure, which might give a better understanding and an explanation for their failure mechanisms.

1.1.1 Heterogeneity: the complexity of concrete microstructure

Concrete has a heterogeneous material structure at a certain level of observation. Varying from millimeters to nanometers, its material structure contains different random constituents, in which each constituent can be considered as a new composite material when seen at lower length scale, refer to Figure 1.1.

At the length scale of millimeters, concrete (Figure 1.1a) can be considered as a mortar-large aggregate random composite, where large aggregates can range from 3mm to 30mm. Figure 1.1b shows an optical micrograph of the matrix phase from the previous image. The mortar now is itself seen as a cement paste-sand composite, where aggregate size varies from a millimeter or so down to a few tenth of a millimeter. Downing the scale on the order of micrometers, cement paste is also a composite material as shown in Figure 1.1c. It is made up of unreacted cement, capillary pores, and various other chemical phases that are a result of the hydration actions between water and cement (Taylor, 1997). The calcium silicate hydrate gel (C-S-H) produced via a hydration reaction

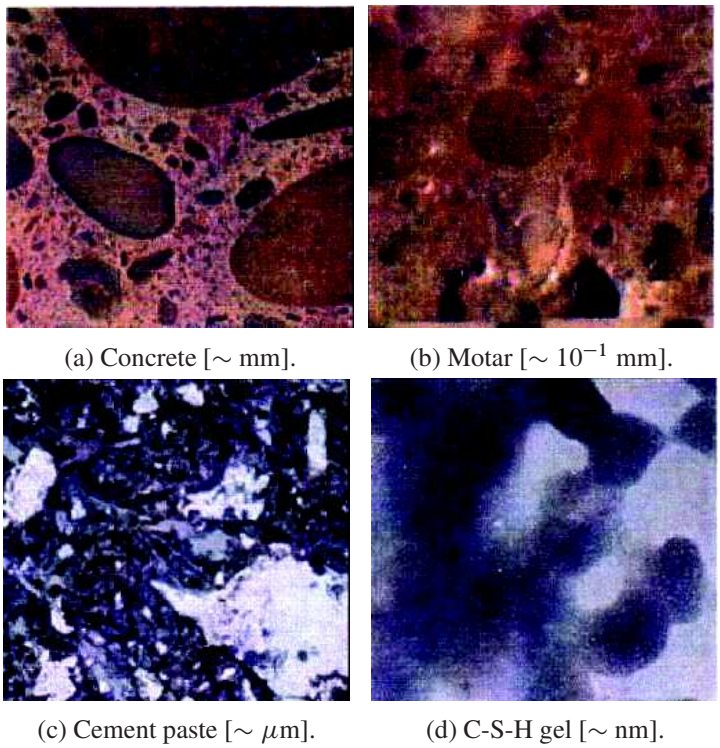

(a) Concrete [$\sim$ mm]. (b) Motar [$\sim 10^{-1}$ mm].

(c) Cement paste [$\sim \mu$m]. (d) C-S-H gel [$\sim$ nm].

Figure 1.1 – Material structure of concrete at different length scales. Based on (Garboczi and Bentz, 1995).

that holds the cement paste together is equally seen to be a complex material with a random porous nanostructure, see Figure 1.1d. The reader is referred to Garboczi and Bentz (1995) for details.

All of these point out that concrete is a non-homogeneous material with a wide range of degree of heterogeneity. It is evident that several parameters such as shape, size and distribution of the constituents and interfaces between them have strong influence on the mechanical behavior of concrete. However, despite the complex microstructure, concrete is usually considered to be a uniform material at the length scale of structures (10^{-1} m and above - the usual engineering length scale, or the macroscopic scale) with the bulk properties such as tensile strength, compressive strength, and other postpeak properties such as fracture energy, toughness, etc.Of course, these properties are directly influenced by its underlying microstructure. The size, shape, volume fraction, spatial distribution, and mechanical properties of each constituent making up of the microstructure all have a significant effect on the behavior of concrete observed at the macroscopic scale. Furthermore, the microstructure of concrete can be changed because of the external loading acting on the material at the macroscale, e.g., cracking appears in the mortar matrix or in the interfacial transition zone between mortar and aggregates in concrete.

For ordinary concrete, gravel, crushed stone and sand are primary aggregates used. It depends on each type of concrete but in general, aggregates account for 60-80% of the volume of concrete. They can be divided into two distinct categories, fine and coarse. The fine ones consist in most particles passing through a 4.75-mm sieve. The coarse ones occupy around 40-50% of the concrete volume. Gravels constitute the majority of coarse aggregate used in concrete while crushed stone makes up most of the remainder (Portland Cement Association, 2013). The shape of aggregate particles depends on the aggregate type. Generally, gravel aggregates have a rounded shape whereas crushed stone aggregates have an angular shape (Wang et al., 1999).

In practice, to study the influence of the constituents on the macroscopic properties and also to gain insight into the origin and nature of the nonlinear behavior, concrete is often seen at the so-called mesoscopic scale (millimeter scale) where three main components are separated: (i) coarse aggregates, (ii) homogeneous mortar matrix with fine aggregates dissolved in it, and (iii) the interfacial transition zone (ITZ) between them . Porosities within the matrix is usually disregarded at

this length scale. The ITZ is about 20-100 μm thickness (Liao et al., 2004). The experimental bond strength of the ITZ is about 33% to 67% of the tensile strength of the matrix (Hsu and Slate, 1963). The latter is in turn about 30% to 50% the tensile strength of aggregates (Alexander et al., 1968; Husem, 2003). Furthermore, for the normal-weight concrete, the aggregates are about twice to three times stiffer than the mortar matrix. These ratios were used for modeling concrete behaviors at the mesoscale, see, e.g., Schlangen and Garboczi (1997), Sagar and Prasad (2009), and Grassl et al. (2012).

Let us first present the macroscopic phenomena observed in experiments, which characterize the behavior of concrete related to mechanical failure. This will give an overview of characteristics of concrete and might provide a basic for finding the relation between macroscopic properties and microstructure or trying to reproduce these macroscopic phenomena by the numerical models.

1.1.2 Softening and localization of deformation

The mechanical behavior of concrete, under external mechanical loading, is characterized initially by a quasi elastic stage, which means that the material will return to its original configuration if unloaded. Then, upon the loading increase, the microcracks appear before the peak stress is reached. The microcracks evenly coalesce to form the macrocrack(s). This/these macrocrack(s) will grow and propagate up to complete failure. Along with the growth of cracks, concrete shows a gradual decrease of their load-carrying capacity when deformed beyond a certain limit, refer to Figure 1.2. Therefore, concrete is called "softening" material. The softening behavior of concrete is observed under both compressive and tensile loadings (Bažant, 1976; van Mier, 1984; Torrenti et al., 1993; Markeset and Hillerborg, 1995; Jansen and Shah, 1997).

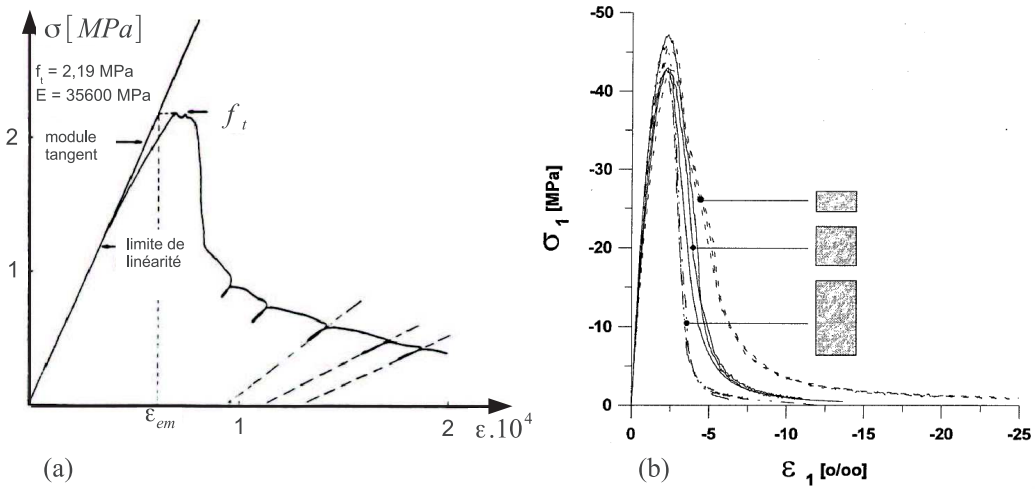

Figure 1.2 – Concrete behavior under axial loadings: traction (a) (Terrien, 1980) and compression (b) (Geel and Eindhoven, 1998).

Under either (uniaxial) tensile or compressive loadings, microcracking occurs before the peak stress (van Mier, 1986). In the first stage, microcracks arise at the interface between aggregate and mortar then at a higher load level, they also arise in the mortar. When the load reaches its maximum, microcracks start to interact and coalesce to form a macrocrack. The latter grows and traverses the sample. The difference between developments of microcracks in compression and in tension is the direction of microcracks. Under tension, microcracks develop to form the macrocrack perpendicular to the loading direction, whereas under compression, microcracks develop in a direction parallel to the (major) compressive direction due to the extension in the direction perpendicular to compressive loading, as schematically shown in Figure 1.3. Moreover, under uniaxial compression, the macrocracks can be found to be inclined to the loading direction when, e.g., the high friction exists between

the sample and the press, see Torrenti et al. (1993). This is because the boundary conditions that turn the principal direction of extension.

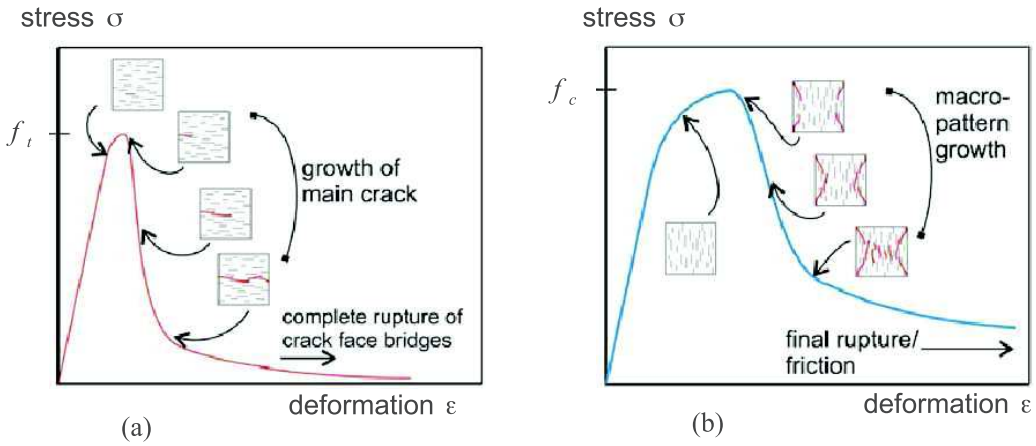

Figure 1.3 – Macroscopic failure modes under uniaxial tension (a) and uniaxial compression (b) (van Mier, 2008).

Specimen size and boundary conditions have strong effects on the softening behavior of concrete. Figure 1.2b shows that, for different size of specimens, before the peak, almost identical stress-strain behavior are obtained whereas in the softening regime, different-size specimens result in different shape of softening curve. More discussions about the size and boundary dependences can be found, e.g., in Hordijk (1991) and van Mier et al. (1996).

In uniaxial loading conditions, localization of deformation occurs from the peak. Under tension, strain localizes in a narrow band with finite size, which is called mode I localization. In multiaxial compression (with low confinement i.e. below the brittle-to-ductile transition), localization becomes manifest along shear bands, which is called mode II localization. Furthermore, in uniaxial compression, a shear band can be found when the specimen gets very short (van Mier, 1984; Desrues and Viggiani, 2004). Outside the localization zone, the material exhibits elastic unloading. The macrocrack develops in the localization zone and gradually grows through the specimen, which causes the gradual drop in load carrying capacity, until fully separation. Otherwise, the macrocrack does not develop continuously from one side to the other of the specimen, it might be formed from the bridging and branching mechanisms of microcracks, refer to the next section 1.1.3. Or conversely, the macrocrack can develop from one side and at a time, it bifurcates then might coalesce to attain the other side.

In summary, based on observations of fracture process in concrete, van Mier (2008) proposed four stages for behaviors of concrete in tension and in compression, see Figure 1.4:

(O) Elastic stage

(A) Microcracking stage

(B) Critical crack growth

(C) Crack bridging in tension and frictional restraint in compression, that cause some residual stress in the behavior.

It should be noted that, under multiaxial compressive loadings with high levels of confinement (i.e. above the brittle-to-ductile transition), microcracks are hard to nucleate and propagate, and failure occurs with the propagation of few macrocracks without any distributed microcracking. There is no softening behavior, instead the response exhibits a monotonically decreasing slope tending toward a *plateau* (Sfer et al., 2002). These observations for concrete are in good agreement with

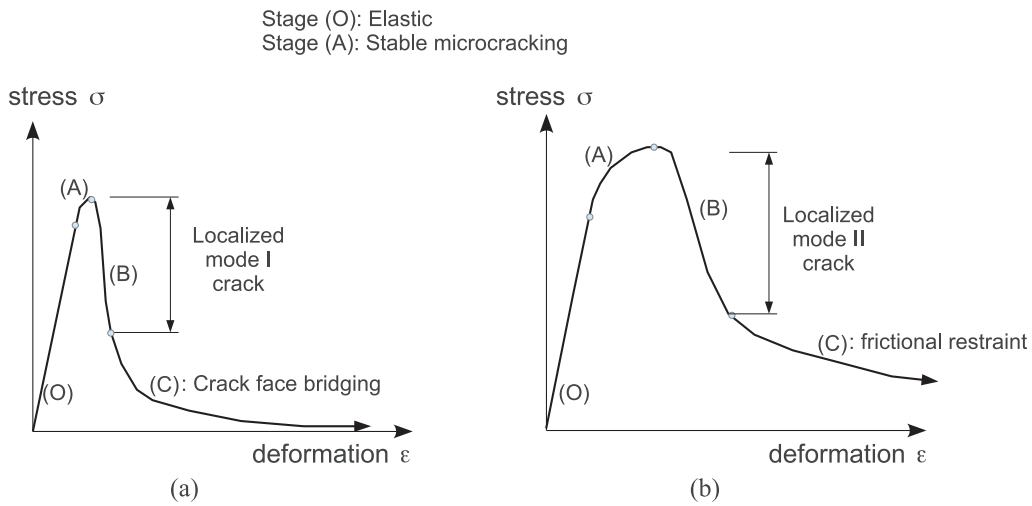

Figure 1.4 – Four-stage fracture process in concrete under uniaxial tension (a) and uniaxial compression (b). After van Mier (2008).

earlier similar observations in rocks by Bésuelle et al. (2000). Yet, the localization of deformation is always found and described in terms of shear band orientation and patterning.

Van Mier has pointed out that the onset of localization, i.e. microcracking process, appears to be an important point. It seems that the actual microcracking process determines the macroscopic strength of the material before the peak is reached. The macroscopic strength has no relation on localization and softening in post-peak regime which is nothing more than the global failure of the specimen. These observations can be found in Prado and van Mier (2003) and van Mier (2008) or recently in van Mier and Man (2009). Therefore, it is important that the microcracking process is considered in more details when analyzing the fracture behavior of quasi-brittle materials, particularly of concrete. This remark on the microcracking has to be taken into consideration for the modeling of failure of structures and materials.

Softening and localization behaviors are not only observed in concrete but also in other quasi-brittle materials as rock, ice or in cohesionless materials like sand (Desrues and Viggiani, 2004). For a more detailed description on softening behavior and strain localization, the reader is referred to van Mier (1984), Gopalaratnam and Shah (1985), van Mier (1991), and Sluys (1992) and references therein or recently van Mier and Man (2009).

The schematic representations of localization in tension and in compression are shown in Figure 1.5. Here, assuming that the total work, W_f, necessary for failure of the specimen, is equal to the work needed for failure of the localization zone (region D in Figure 1.5a) (Bažant and Planas, 1998), one defines the specific fracture energy, G_f, as

$$G_f = \frac{W_f}{A} = h_t \gamma_f \tag{1.1}$$

in which h_t is the characteristic length of the localization zone, γ_f stands for the area of the softening portion of the stress-strain curve.

It is noted that in compression, at the residual stress level, the specimen can still carry some load due to frictional restraint in localization zone. The specific fracture energy of concrete in compression is defined in the relation with the area under stress-strain curve in the softening regime with a cut-off at the ultimate strain ε_{cu} (Figure 1.5b). This energy which is often termed as the crushing energy (Petryna and Krätzig, 2005), denoted by G_f^c, is given by

$$G_f^c = \frac{W_f^c}{A} = h_c \gamma_f^c \tag{1.2}$$

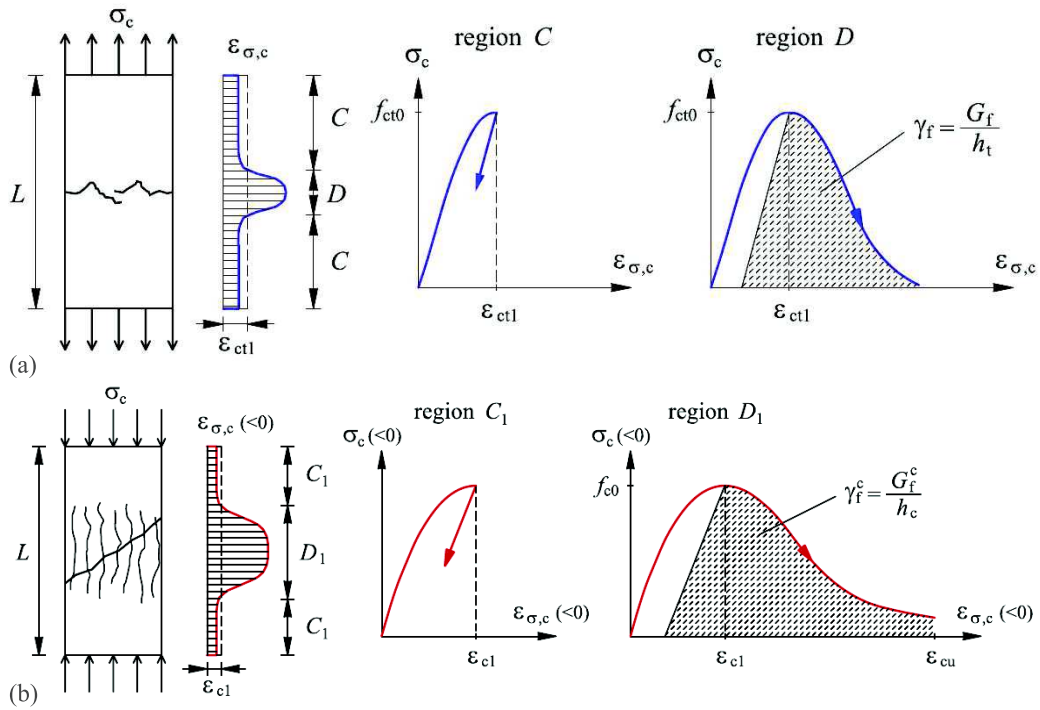

Figure 1.5 – Strain localization in concrete under traction (a) and compression (b) loadings (Markovič et al., 2012).

It has been recognized that the specific fracture energies of concrete, G_f and G_f^c, that are determined from experiments e.g. (RILEM, 1985), depend on various parameters such as material microstructure, water-cement ratio, specimen size and geometry, temperature or even on the boundary conditions of the experiment, see e.g., (Bažant and Kazemi, 1991; Guo and Gilbert, 2000). The specific fracture energy in compression is about 200-500 times larger than that in tension. The tensile specific fracture energy of normal concrete varies from 39 N/m (Maturana et al., 1990), 63.5 N/m (Bažant and Pijaudier-Cabot, 1989) to 144.2 N/m (Cifuentes et al., 2013) whereas the compressive specific fracture energy is about 20000 N/m (Jansen and Shah, 1997).

1.1.3 Fracture toughness and crack topology

As mentioned in the Section 1.1.2, macrocrack growth and localization of deformation occurs in the post-peak part of the softening curve. During softening in quasi-brittle materials, load-carrying capacity decreases gradually, however, it does not vanish totally. Some remaining stress can be observed under both tensile and compressive loading conditions. This can be explained by the mechanism called crack face bridging in tension and frictional restraint in compression. Crack face bridging is a mechanism observed in heterogeneous materials such as concrete, sandstone, and rock where two tips of neighboring cracks avoid each other rather than coalesce. Bridging mechanism that emanate simply because the growth of macrocracks from microcracks is not continuous but shows crack overlaps within a non-uniform process, as schematically shown in Figure 1.6.

The material structure, in all its details, has an influence on the microcrack process that leads to the macrocrack process with the bridging mechanism or not. Chiaia et al. (1998) analyzed the crack growth mechanisms in four different concretes that contained either river gravel with maximum aggregate size equal to 2 and 16 mm, phosphorous-slag aggregates, and Lytag aggregates, subjected to indirect tensile loading. They showed that aggregate structures have a strong effect on the microscopic cracking that in turn has a strong influence on strength, toughness, and ductility of concrete. Bridging mechanism was found in the sample with phosphorous-slag aggregates while a single crack was observed in the sample with river gravel aggregates ($d_{\max} = 2$ mm), see Figure 1.7.

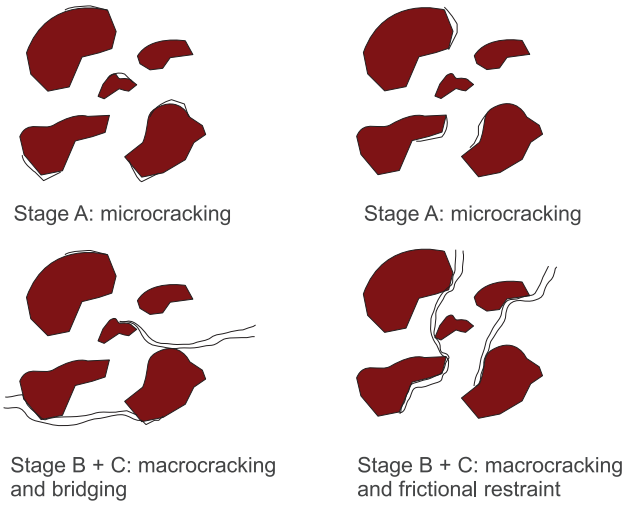

Figure 1.6 – Microcracking and crack face bridging in tension (a); Microcracking and frictional restraint in compression (b). Based on (van Mier and Man, 2009).

However, in both cases, cracks occur at the weakest link which is generally the ITZ between matrix and aggregates. This leads to the observation that cracks get around the aggregates. The macrocrack obtained is not straight but is tortuous, which leads to the roughness (or fractality) of the crack faces.

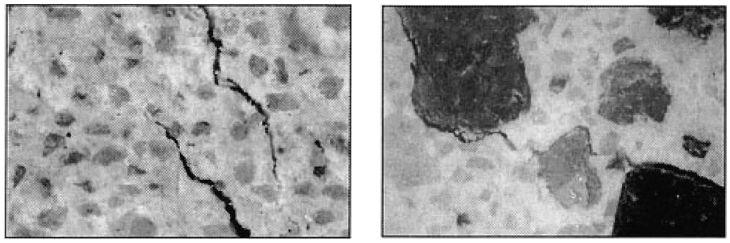

Figure 1.7 – Crack face bridging in the phosphorous-slag concrete (a) while a single crack was found in the river gravel concrete ($d_{\max} = 2$ mm) (b), after (Chiaia et al., 1998).

Crack growth within microcracking-to-macrocracking process can be detected using either a digital image correlation (DIC) technique, a high resolution optical microscope or a scanning electron microscope (SEM) technique. Using a DIC technique, Vasseur et al. (2009) measured the crack bridging of CFRP (carbon fiber reinforced polymer) strengthened concrete by means of both aggregate bridging and CFRP bridging, influencing the crack pattern, see Figure 1.8. Figure 1.9 shows cracks occurring in a concrete sample using a SEM technique. These figures are considered as the examples to confirm that the crack process in concrete is characterized by interfacial cracks growing through the matrix and joining into macrocracks. Microcracking, crack bridging and aggregate interlocking are the observed mechanisms that contribute to the tendency of the main crack to follow a discontinuous and tortuous path.

In compression, the roughness of crack faces plays a dominant role for the toughening during the softening process. In fact, the friction due to the roughness of crack faces causes the residual stress at the tail of the softening curve. The frictional stress between crack faces may be enhanced when the material is subjected to confinement. This explains why the stress in the tail part of the softening curve increases when increasing the confinement and the behavior may change from softening to hardening if the confinement is very important, see for example (Sfer et al., 2002).

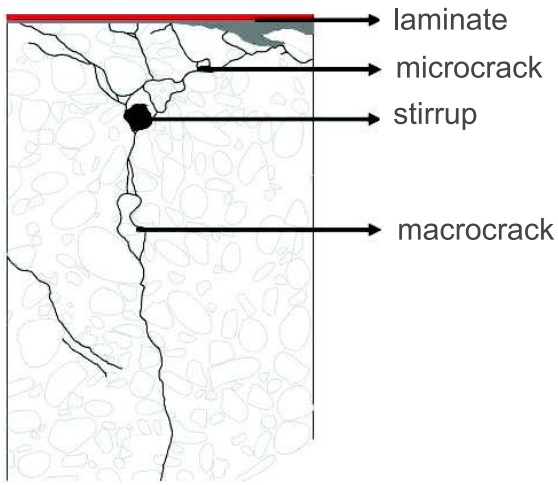

Figure 1.8 – Crack pattern obtained by a digital image correlation (DIC) technique (Vasseur et al., 2009).

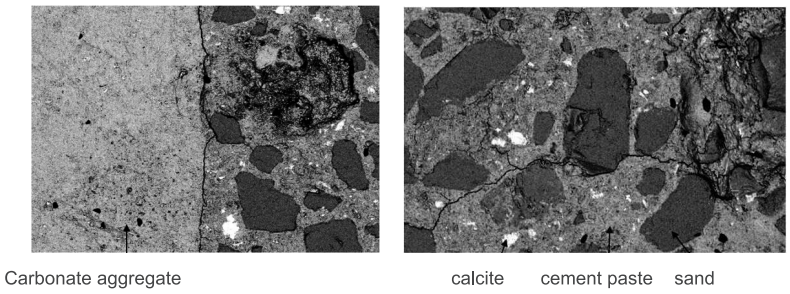

Figure 1.9 – Scanning electron microscope (SEM) images of fracture in concrete. Taken from (Musielak, 2012).

For many years, one of the challenges has been the question that whether there is any correlation between fracture properties and the roughness of crack faces. When analyzing the fracture surfaces of three different size wedge-splitting specimens with four different maximum aggregate sizes, Issa et al. (2003) found a clear correlation between roughness (fractal dimension) and fracture toughness: the tougher the material, the higher the fractal dimension. It was found that roughness increases with an increase in both specimen and maximum aggregate size, see Figure 1.10. The reader is referred

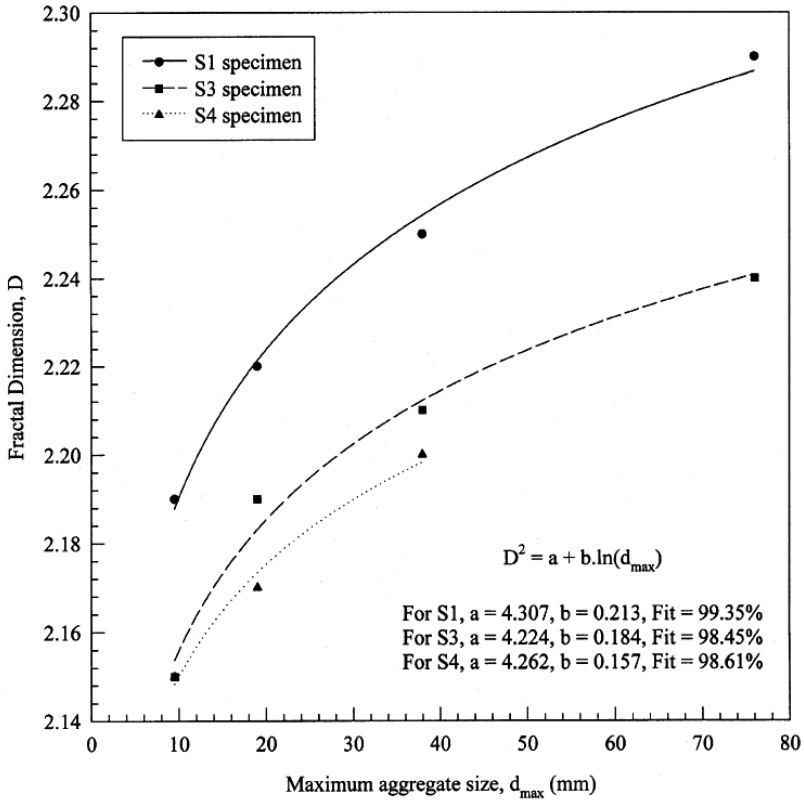

Figure 1.10 – Roughness (fraction dimension) dependency on specimen and aggregate size after (Issa et al., 2003).

to Issa et al. (2003) and references therein for more description about fractal dimension and the correlation with fracture toughness in concrete.

Thus, in summary, fracture process in concrete under both tensile and compressive loadings comprises of many mechanisms that absorb energy during crack growth. Under tensile loading, the growth of macrocracks is accompanied with branching and bridging mechanisms that make the material fail gradually under rather large deformations (compared with those of brittle materials). The size of the ligament between the two overlapping (bridging) cracks depends on the microstructure of the material. In compression, two mechanisms are active as well: the growth of a macrocrack and the frictional restraint due to the friction on the rough crack faces. The higher the friction, the higher the tail of the softening curve and the higher the toughness of the material. It is obvious that the friction between crack faces depends on the roughness of crack surfaces which is related to the material microstructure. Accordingly, from the modeling viewpoint, it seems to be important to employ/develop a model that can explicitly represent the microstructure of the material rather than phenomenological models to better capture these observed mechanisms during the fracture process of quasi-brittle materials.

1.1.4 Size effect

The rupture of structures made of quasi-brittle materials exhibits size effect, i.e. the nominal strength and nominal fracture energy of these structures strongly depends on their size. The size effect analysis is of interest because often the behavior of real size structures is estimated from tests of laboratory size structures. The effects of structure sizes on their nominal characteristics have been known for several centuries. In the 16th century, Leonardo da Vinci observed and mentioned an inversed proportionality of length of a cord and its strengths: the longer the cord the weaker the strength is. The questions of size effects in various materials and structures have been next studied by many authors for over 500 years (Mariotte, 1686; Young and Kelland, 1845; Griffith, 1921; Fisher and Tippett, 1928).

From the last century, attentions have been paid on the size effects in quasi-brittle materials and structures made of these materials. Numerous size effect experiments with different geometries, loading conditions, and size variations have been performed on concrete and other geomaterials. Different loading conditions were tested in either tension, compression, shear, bending or splitting tests. One of the difficulties in experiments comes from the test of the large scale samples. Therefore, the size effects were only observed in a limited size range. Furthermore, when performing a size effect experiment, the question of how to scale the sample sizes, in one, two or three dimensions should be answered. Ideally, specimens should be scaled in three dimensions. However, this makes a size effect experiments more massive. It is common in practice to scale specimens in two dimensions only and keep the third dimension, usually the thickness, constant. Regardless of these discussible features, the dependency of strengths of structures made of quasi-brittle materials on their sizes has been observed by many authors: tests of concrete by Şener (1997) and van Vliet and van Mier (2000), of sea ice by Dempsey et al. (1999a,b). Size effects are commonly represented by plotting data in a log (nominal strength) versus log (characteristic size) diagram. Van Vliet and van Mier (2000) tested concrete and sandstone under uniaxial tension with a size range of 1:32 and showed a size effect as depicted in Figure 1.11. One of the largest beams ever tested should be the 36 m long beam using for analysis of shear strength in reinforced concrete structure (Shioya et al., 1990). A set of sea-ice specimens from laboratory- to field-experiments with the largest size is 80 m and a

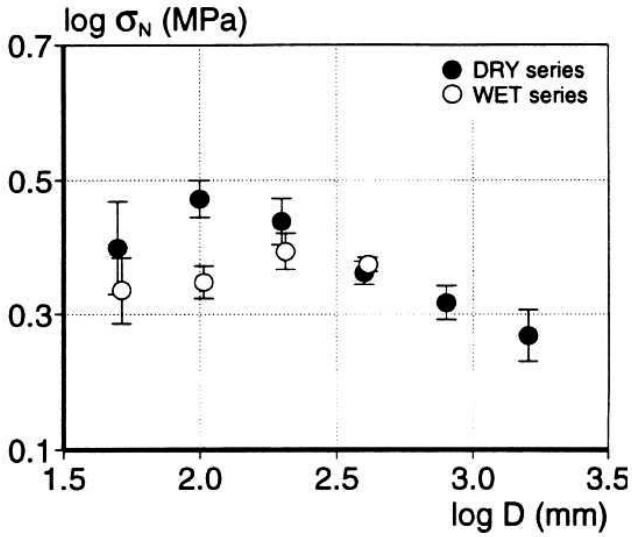

Figure 1.11 – Size effect from experimental tests of concrete under uniaxial tension after (van Vliet and van Mier, 2000).

size range of 1:800 was tested by Dempsey et al. (1999a,b) who showed a size effect on the normal tensile strength, see Figure 1.12.

However, the real structure size is much larger than those could be tested in laboratory. The two main questions should be considered are: (i) what is the physical reason for the size effect observed

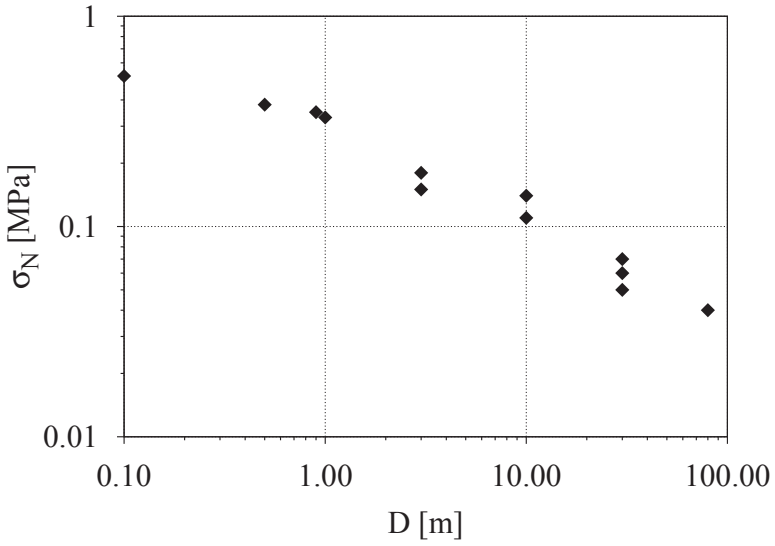

Figure 1.12 – Size effect of sea ice by Dempsey et al. (1999a).

in experiments?, and (ii) how to extrapolate to the strength of real full scale structures from those obtained from small size structure in laboratory?

When the first question is solved, i.e. the reason for the decrease of strength is known, extrapolation of results for larger structure sizes will be performed in a simple and straightforward manner.

To answer the first question, various theories have been developed and proposed. Weibull (1939) is the first, who tried to explain the effect of sizes on material strength based on the statistical theory. In fact, he suggested that the larger the structure the greater the probability to encounter in its volume a material element of a given critically small strength that may lead to complete failure. This approach, the so-called Weibull theory, is also known as the weakest link theory, in which the structure is assumed to be failed as soon as the first critical defect fails like in the series coupling. The relationship between nominal strength σ_N and characteristic size D based on Weibull theory reads (Bažant et al., 1991)

$$\sigma_N \propto D^{-\frac{n}{m}} \tag{1.3}$$

where m denotes Weibull modulus and n stands for number of dimensions, $n = 2$ for two-dimensional problems whereas $n = 3$ for three-dimensional ones. Based on the results of direct tensile tests of concrete (Zech and Wittmann, 1978), m is approximately equal to 12 for concrete. The Weibull theory is purely statistical and is expressed as random variations of strength within the structure and may ignore the fact that in quasi-brittle materials, there is a growth of stable large fracture (micro- and macro-cracks) prior to failure.

Taking into account the stress redistributions and energy release due to the growth of micro- and macro-cracks, Bažant (1984) proposed a size effect law (SEL), namely, deterministic energetic size effect law, that reads

$$\sigma_N = \frac{Bf_t}{\sqrt{1 + \dfrac{D}{D_0}}} \tag{1.4}$$

in which f_t is the tensile strength, D is the characteristic size of the structure, B is a geometrical factor that depends on the form of the structure, D_0 is an empirical constant, Bf_t and D_0 are determined by fitting test results from geometrically similar specimens. It should be noted that this size effect law is applicable to geometrically similar structures containing large cracks or notches because it is constructed from the energy balance condition where energy release rate is equal to

the energy dissipated per unit area of the crack surface to propagate a *preexisting* crack. Bažant (1997) extended (1.4) to deduce the size effect for crack initiation in the boundary layer from a smooth surface of structures i.e. without notches. The so-called universal size effect law (also called energetic-statistical size effect) for notched and unnotched structures expressing the relationship between nominal strength σ_N and characteristic size D, reads

$$\sigma_N = \sigma_0 \left[1 + \frac{D}{D_0}\right]^{-1/2} \left\{1 + \left[\left(\bar{\eta} + \frac{D}{D_b}\right)\left(1 + \frac{D}{D_0}\right)\right]^{-1}\right\} \tag{1.5}$$

where σ_0, D_0, D_b, $\bar{\eta}$ are the constants. We do not go further in detail here, the interested reader is refer to Bažant (1984) for more information.

Another explanation for the size effects based on the fractal geometry of the (final) fracture surfaces was proposed by Carpinteri and Ferro (1994) and Carpinteri et al. (1995). They assumed a multifractality for the damaged material microstructure and proposed the so-called multifractal scaling law (MFSL) as

$$\sigma_N = \sqrt{A + \frac{B}{D}} \tag{1.6}$$

in which D stands for the characteristic structural size, A is a constant with dimensions of the square of stress (Pa^2), and B is a constant with dimensions of the square of stress intensity factor ($Pa^2 \cdot m$). From a physical viewpoint, the MFSL emphasizes that the material microstructure disorder becomes less important on the mechanical behavior of progressively larger scale structures (for large D and $D \to \infty$) whereas it has a fundamental effect for smaller scales (for small D and $D \to 0$). Equation (1.6) can be rewritten in a more meaningful form which related to a limit nominal strength f_t and maximum aggregate size $d_{\max}$ as

$$\sigma_N = f_t \sqrt{1 + \frac{\alpha d_{\max}}{D}} \tag{1.7}$$

in which α and f_t are two constant parameters to be determined from the fit of experimental data.

Figure 1.13 shows previous three theories of size effects together with the range of the majority of experimental data (till now!). The experimental range is small compared to the real scale structures, e.g. spans of bridges are about several hundreds of meters. On other hand, these theories are all phenomenological. Either structural geometry, role of microcrack development or crack roughness may not be taken into consideration by these approaches. It has widely been recognized that size effect seems to depend not only on the material microstructure, e.g. the shape of aggregates or aggregate density, but also on boundary conditions i.e. the structural effects. Therefore, it seems that numerical modeling is of interest when dealing with large scale structures in both senses: (i) either directly model the large scale structures to get the nominal strength with constitutive laws accounting for size effect, or (ii) only model small scale structures but the numerical results should reproduce reliable size effects for extrapolating to large scale structures.

1.2 Modeling of macroscopic behaviors of quasi-brittle materials

1.2.1 Modeling scales

Quasi-brittle materials are usually heterogeneous. Concrete can be considered as a good example. It is obvious that the heterogeneous characteristic influences directly on the mechanical behavior of concrete. Therefore, it is important to take into consideration the heterogeneity when modeling the behavior of concrete. However, as mentioned before, concrete has a complex microstructure depending on the scale at which the material is observed. Wittmann (1983) proposed three scale levels for modeling concrete behavior as depicted in Figure 1.14.

At the microlevel, concrete is considered (modeled) as the structure of the hardened cement paste which is itself highly heterogeneous including unreacted cement particles, capillary pores and other

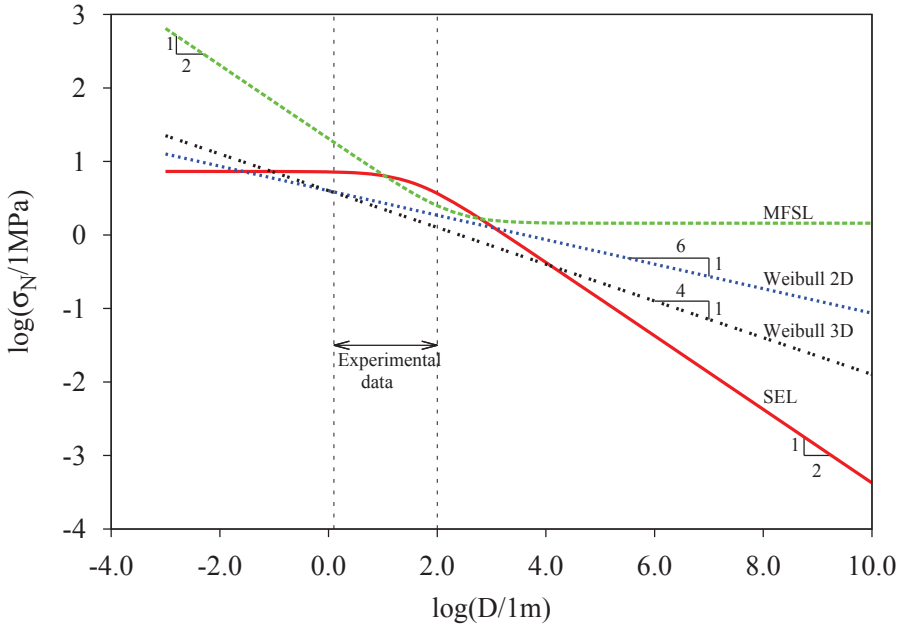

Figure 1.13 – Representation of size effect laws.

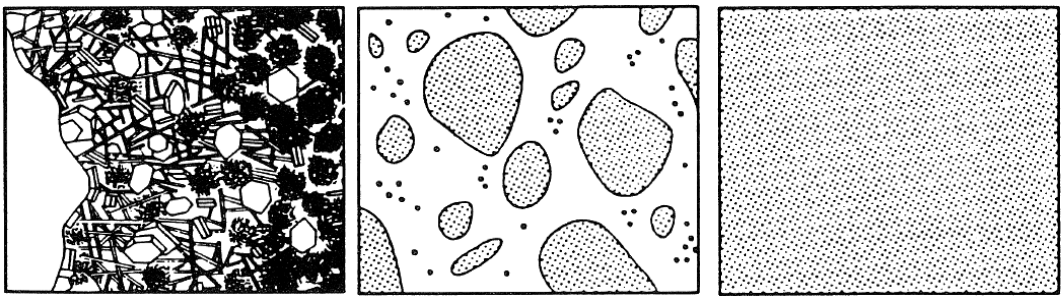

(a) Microlevel. (b) Mesolevel. (c) Macrolevel.

Figure 1.14 – Three level approaches after Wittmann (1983).

hydration products. At the mesolevel, concrete is modeled as the structure of aggregates embedded in mortar matrix with interfacial transition zones between them. Finally, concrete is treated as homogeneous material upon the macroscopic modeling viewpoint where its behavior is described by phenomenal constitutive laws.

From the numerical viewpoint, to deal with softening, strain localization during fracturing process and size effect problems in quasi-brittle materials, one has to base on a numerical technique accompanied with a numerical (constitutive) model. Finite element method (FEM) is the most successful numerical technique used in engineering and science research because it has great robustness and flexibility in the treatment of material heterogeneities, complex boundary conditions and nonlinear calculations. Because of its popular utilization and for the sake of completeness, the FEM is briefly described in the Section 1.2.3. Numerical models that may implemented in a FEM (or other method) code for dealing with softening, strain localization and reproducing size effects are next pointed out.

1.2.2 Formulation of a boundary value problem

Considering a solid Ω with its boundary Γ, as shown in Figure 1.15, that is subjected to a quasi-static mechanical excitation. Prescribed traction $\bar{t}$ is applied on $\Gamma_t \subset \Gamma$ and an imposed displacement $\bar{\mathbf{u}}$ is effected on $\Gamma_u \subset \Gamma$ where $\Gamma_t \cap \Gamma_u = 0$.

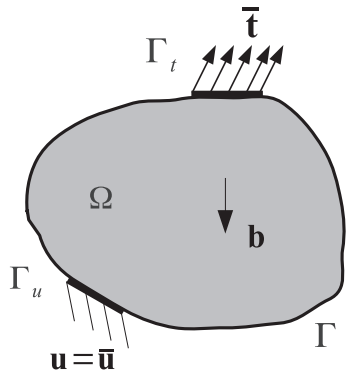

Figure 1.15 – A two-dimensional body Ω subjected to a traction $\bar{\mathbf{t}}$, a body force $\mathbf{b}$ and an imposed displacement $\bar{\mathbf{u}}$.

The posing problem is to seek an unknown displacement field $\mathbf{u}$ such that it satisfies, under the small perturbation assumption, the governing equation set

$$\operatorname{div}\boldsymbol{\sigma} + \mathbf{b} = \mathbf{0} \qquad \text{in } \Omega \tag{1.8a}$$

$$\boldsymbol{\varepsilon} = \frac{1}{2}\left(\operatorname{grad}\mathbf{u} + (\operatorname{grad}\mathbf{u})^T\right) \tag{1.8b}$$

$$\boldsymbol{\sigma} = f(\boldsymbol{\varepsilon}, \boldsymbol{\nu}) \tag{1.8c}$$

$$\boldsymbol{\sigma}\cdot\mathbf{n} = \bar{\mathbf{t}} \qquad \text{on } \Gamma_t \tag{1.8d}$$

$$\mathbf{u} = \bar{\mathbf{u}} \qquad \text{on } \Gamma_u \tag{1.8e}$$

where $\boldsymbol{\sigma}$ is the second order Cauchy stress tensor, $\mathbf{b}$ is the body force vector, $\boldsymbol{\varepsilon}$ is the strain tensor and $\mathbf{n}$ denotes outward unit normal vector on Γ_t. In the above, (1.8a) is the equilibrium equation, (1.8b) is the kinematic equation, (1.8c) is the constitutive equation that expresses the relation between stress and strain tensors with the so-called internal variables $\boldsymbol{\nu} = (\nu_1, \nu_2, \ldots, \nu_n)$, (1.8d) and (1.8e) are the Neumann and Dirichlet boundary conditions, respectively.

Multiplying (1.8a) by the so-called virtual displacement $\mathbf{v}^*$ such that

$$\mathbf{v}^*\colon \Omega \to \mathbb{R}^3,\ \mathbf{v}^* = \mathbf{0} \qquad \text{on } \Gamma_u, \tag{1.9}$$

yields

$$\mathbf{v}^{*T}\operatorname{div}\boldsymbol{\sigma} + \mathbf{v}^{*T}\mathbf{b} = 0 \qquad \text{in } \Omega \tag{1.10}$$

To develop the weak form of the equation (1.8a), (1.10) is integrated over the volume Ω as

$$\int_\Omega \mathbf{v}^{*T}\operatorname{div}\boldsymbol{\sigma}\,\mathrm{d}\Omega + \int_\Omega \mathbf{v}^{*T}\mathbf{b}\,\mathrm{d}\Omega = 0 \tag{1.11}$$

Applying integration by parts yields

$$\int_\Omega \operatorname{div}(\mathbf{v}^{*T}\boldsymbol{\sigma})\,\mathrm{d}\Omega - \int_\Omega \boldsymbol{\sigma}\operatorname{div}\mathbf{v}^{*T}\,\mathrm{d}\Omega + \int_\Omega \mathbf{v}^{*T}\mathbf{b}\,\mathrm{d}\Omega = 0 \tag{1.12}$$

By applying the Gauss divergence theorem for the first term of (1.12), one gets

$$\int_\Gamma \mathbf{v}^{*T}\boldsymbol{\sigma}\mathbf{n}\,\mathrm{d}\Gamma - \int_\Omega \boldsymbol{\sigma}\operatorname{div}\mathbf{v}^{*T}\,\mathrm{d}\Omega + \int_\Omega \mathbf{v}^{*T}\mathbf{b}\,\mathrm{d}\Omega = 0 \tag{1.13}$$

As $\mathbf{v}^* = \mathbf{0}$ on Γ_u by definition and noting that $\operatorname{div}\mathbf{v}^{*T} = \boldsymbol{\varepsilon}(\mathbf{v}^*)^T$, we substitute the Neumann boundary condition (1.8d) into Equation (1.13), the weak form of the equilibrium equation is obtained from (1.13) as

$$\int_\Omega \boldsymbol{\varepsilon}(\mathbf{v}^*)^T\boldsymbol{\sigma}\,\mathrm{d}\Omega = \int_\Omega \mathbf{v}^{*T}\mathbf{b}\,\mathrm{d}\Omega + \int_{\Gamma_t} \mathbf{v}^{*T}\bar{\mathbf{t}}\,\mathrm{d}\Gamma \tag{1.14}$$

The problem is now to find an unknown displacement field $\mathbf{u}$ such that it satisfies Equation (1.14).

1.2.3 The finite element method

The aim of this section is to present a short introduction to the FEM that is partially used in this thesis. This provides a basic knowledge about the FEM which is useful for developing a multi-scale numerical tool later. For a more detailed description of the method, the reader is referred to textbooks, e.g., see (Belytschko et al., 2000; Hughes, 2000) or (Zienkiewicz and Taylor, 2000; Zienkiewicz et al., 2005).

The domain Ω is discretized into N_e elements Ω_e, $e = 1, 2, \ldots, N_e$, by N_n nodes as depicted in Figure 1.16. The finite element process will seek the solution of $\mathbf{u}$ in the approximate form

$$\mathbf{u} \approx \hat{\mathbf{u}} = \sum_{i=1}^{N_n} \mathbf{N}_i\mathbf{a}_i = \mathbf{N}_i\mathbf{a}_i \tag{1.15}$$

where $\mathbf{N}_i$ is the *shape functions* or *interpolation functions* associated to node i; $\mathbf{a}_i$ is the vector of nodal displacements that are unknown. It is noted that the shape functions are defined locally for elements that satisfy

$$\sum_{e=1}^{n_e} N_e = 1 \tag{1.16}$$

in which n_e is the number of nodes of element e. Therefore, the displacement inside element Ω_e as well as the virtual displacements are also approximated by

$$\mathbf{u}(\mathbf{x}) = \mathbf{N}(\mathbf{x})\mathbf{a}_e \tag{1.17a}$$

$$\mathbf{v}^*(\mathbf{x}) = \mathbf{N}(\mathbf{x})\mathbf{a}_e^* \tag{1.17b}$$

in which $\mathbf{x} \in \Omega_e$, $\mathbf{a}_e$ is the vector of nodal displacement of element e and $\mathbf{a}_e^*$ denotes arbitrary virtual displacement parameters of element e.

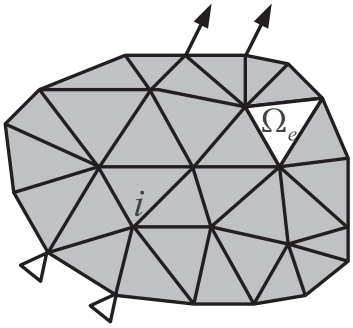

Figure 1.16 – Discretization of body Ω by FEM mesh.

Using Equation (1.8b), the strain inside the element Ω_e as well as the strain due to virtual displacements $\mathbf{v}^*$ are given by

$$\boldsymbol{\varepsilon}(\mathbf{u}) = \mathbf{B}_e \mathbf{a}_e \tag{1.18a}$$

$$\boldsymbol{\varepsilon}(\mathbf{v}^*) = \mathbf{B}_e \mathbf{a}_e^* \tag{1.18b}$$

where $\mathbf{B}_e$ is the strain-displacement matrix of element e defined as $\mathbf{B}_e = [\mathbf{B}_1, \mathbf{B}_2, \ldots, \mathbf{B}_{n_e}]$ with $\mathbf{B}_i$ being given by

$$\mathbf{B}_i = \begin{bmatrix} \mathbf{N}_{i,x} & 0 & 0 \\ 0 & \mathbf{N}_{i,y} & 0 \\ 0 & 0 & \mathbf{N}_{i,z} \\ \mathbf{N}_{i,y} & \mathbf{N}_{i,x} & 0 \\ 0 & \mathbf{N}_{i,z} & \mathbf{N}_{i,y} \\ \mathbf{N}_{i,z} & 0 & \mathbf{N}_{i,x} \end{bmatrix} \tag{1.19}$$

where a comma denotes differentiation with respect to the variable which follows.

The integral over Ω of the weak form (1.14), is computed as the sum of integrals over element domains Ω_e. Substituting Equations(1.17b) and (1.18b) into the weak form (1.14) gives

$$\sum_{e=1}^{N_e} \left(\int_{\Omega_e} \mathbf{a}_e^{*T} \mathbf{B}_e^T \boldsymbol{\sigma}_e \, \mathrm{d}\Omega \right) = \sum_{e=1}^{N_e} \left(\int_{\Omega_e} \mathbf{a}_e^{*T} \mathbf{N}_e^T \mathbf{b}_e \, \mathrm{d}\Omega \right) + \sum_{e=1}^{N_e} \left(\int_{\Gamma_{te}} \mathbf{a}_e^{*T} \mathbf{N}_e^T \bar{\mathbf{t}}_e \, \mathrm{d}\Gamma \right) \tag{1.20}$$

One defines the global nodal displacement vector $\mathbf{a}$ that contains the displacements of all nodes of the mesh. The elementary nodal displacement vectors $\mathbf{a}_e$ are related to $\mathbf{a}$ by

$$\mathbf{a}_e = \mathbf{L}_e \mathbf{a} \tag{1.21}$$

where $\mathbf{L}_e$ is the location matrix, which is a sparse, boolean matrix containing 1 at the location of element e, and 0 elsewhere. Similarly, the virtual nodal displacements of element e is expressed as $\mathbf{a}_e^* = \mathbf{L}_e \mathbf{a}^*$. With this, Equation (1.20) becomes

$$\sum_{e=1}^{N_e} \left(\int_{\Omega_e} \mathbf{a}^{*T} \mathbf{L}_e^T \mathbf{B}_e^T \boldsymbol{\sigma}_e \, \mathrm{d}\Omega \right) = \sum_{e=1}^{N_e} \left(\int_{\Omega_e} \mathbf{a}^{*T} \mathbf{L}_e^T \mathbf{N}_e^T \mathbf{b}_e \, \mathrm{d}\Omega \right) + \sum_{e=1}^{N_e} \left(\int_{\Gamma_{te}} \mathbf{a}^{*T} \mathbf{L}_e^T \mathbf{N}_e^T \bar{\mathbf{t}}_e \, \mathrm{d}\Gamma \right) \tag{1.22}$$

Since the above holds for any virtual displacement $\mathbf{a}^{*T}$, one obtains

$$\sum_{e=1}^{N_e} \left(\mathbf{L}_e^T \int_{\Omega_e} \mathbf{B}_e^T \boldsymbol{\sigma}_e \, \mathrm{d}\Omega \right) = \sum_{e=1}^{N_e} \left(\mathbf{L}_e^T \int_{\Omega_e} \mathbf{N}_e^T \mathbf{b}_e \, \mathrm{d}\Omega \right) + \sum_{e=1}^{N_e} \left(\mathbf{L}_e^T \int_{\Gamma_{te}} \mathbf{N}_e^T \bar{\mathbf{t}}_e \, \mathrm{d}\Gamma \right) \tag{1.23}$$

or equivalently

$$\mathbf{f}_{\text{int}}(\boldsymbol{\sigma}) = \mathbf{f}_{\text{ext}} \tag{1.24}$$

where

$$\mathbf{f}_{\text{int}}(\boldsymbol{\sigma}) = \sum_{e=1}^{N_e} \mathbf{L}_e^T \left(\int_{\Omega_e} \mathbf{B}_e^T \boldsymbol{\sigma}_e \, \mathrm{d}\Omega \right) \tag{1.25}$$

and

$$\mathbf{f}_{\text{ext}} = \sum_{e=1}^{N_e} \mathbf{L}_e^T \left(\int_{\Omega_e} \mathbf{N}_e^T \mathbf{b}_e \, \mathrm{d}\Omega + \int_{\Gamma_{te}} \mathbf{N}_e^T \bar{\mathbf{t}}_e \, \mathrm{d}\Gamma \right) \tag{1.26}$$

are internal and external nodal force vectors, respectively.

In the case of linear elasticity, the constitutive relation (1.8c) can be expressed directly as

$$\boldsymbol{\sigma} = \mathbf{D}\boldsymbol{\varepsilon} \tag{1.27}$$

where $\mathbf{D}$ is the material "tangent" matrix, a fourth order tensor, constructed from elastic moduli of the material. Substituting Equation (1.18a) into Equation (1.27) and then substituting the obtained equation into Equation (1.25), one obtains the internal nodal force vector

$$\mathbf{f}_{\text{int}} = \sum_{e=1}^{N_e} \mathbf{L}_e^T \left(\int_{\Omega_e} \mathbf{B}_e^T \mathbf{D} \mathbf{B}_e \mathbf{a}_e \, \mathrm{d}\Omega \right) = \sum_{e=1}^{N_e} \mathbf{L}_e^T \left(\int_{\Omega_e} \mathbf{B}_e^T \mathbf{D} \mathbf{B}_e \, \mathrm{d}\Omega \right) \mathbf{L}_e \mathbf{a} = \mathbf{K}\mathbf{a} \tag{1.28}$$

where Equation (1.21) has just been applied; $\mathbf{K}$ is the linear stiffness matrix given by

$$\mathbf{K} = \sum_{e=1}^{N_e} \mathbf{L}_e^T \left(\int_{\Omega_e} \mathbf{B}_e^T \mathbf{D} \mathbf{B}_e \, \mathrm{d}\Omega \right) \mathbf{L}_e \tag{1.29}$$

The problem to be solved is simply

$$\mathbf{K}\mathbf{a} = \mathbf{f}_{\text{ext}} \tag{1.30}$$

The solution of this equation is obtained by using a *linear solver* which can be a direct solver using direct method such as, e.g., Gaussian elimination or Cholesky decomposition method or can be an iterative solver using, e.g., the Preconditoned conjugate gradient method. Details can be found in Press et al. (2007).

However, in many situation, it is necessary to use nonlinear or time-dependent constitutive relations under the general form (1.8c), and the solution will be obtained by solving Equation (1.24). We can rewrite (1.24) by defining a residual vector $\mathbf{r}$ as

$$\mathbf{r} = \mathbf{f}_{\text{ext}} - \mathbf{f}_{\text{int}}(\mathbf{a}) = \mathbf{0} \tag{1.31}$$

since $\boldsymbol{\sigma}$ is also a function of nodal displacement vector $\mathbf{a}$. The problem is now to seek a nodal displacement vector $\mathbf{a}_{n+1}$ at current loading level or time step from the known previous one $\mathbf{a}_n$, that satisfies

$$\mathbf{r}_{n+1} = \mathbf{r}(\mathbf{a}_{n+1}) = \mathbf{f}_{\text{ext}|n+1} - \mathbf{f}_{\text{int}}(\mathbf{a}_{n+1}) = \mathbf{0} \tag{1.32}$$

and

$$\mathbf{a}_{n+1} = \mathbf{a}_n + \Delta\mathbf{a}_n \tag{1.33}$$

Because $\mathbf{a}_n$ is a solution, one always has

$$\mathbf{r}_n = \mathbf{0}, \ \mathbf{a} = \mathbf{a}_n, \ \mathbf{f}_{\text{ext}} = \mathbf{f}_{\text{ext}|n} \tag{1.34}$$

The solution of the problem posed by Equations (1.32, 1.33, 1.34) requires an iterative solver using an iterative method such as Newton-Raphson method which approximate Equation (1.32) as

$$\mathbf{r}(\mathbf{a}_{n+1}^{i+1}) \approx \mathbf{r}(\mathbf{a}_{n+1}^{i}) + \left(\frac{\partial \mathbf{r}}{\partial \mathbf{a}} \right)_{n+1}^{i} \delta\mathbf{a}_n^i. \tag{1.35}$$

The nodal displacement vector at level load $n+1$ and at iteration $i+1$, $\mathbf{a}_{n+1}^{i+1}$, is computed as

$$\mathbf{a}_{n+1}^{i+1} = \mathbf{a}_{n+1}^{i} + \delta\mathbf{a}_{n+1}^{i} = \mathbf{a}_n + \Delta\mathbf{a}_n^i \tag{1.36}$$

where

$$\Delta\mathbf{a}_n^i = \sum_{k=1}^{i} \delta\mathbf{a}_n^k \tag{1.37}$$

$$\delta\mathbf{a}_n^i = (\mathbf{K}_T^i)^{-1}\mathbf{r}_{n+1}^i \tag{1.38}$$

in which $\mathbf{K}_T^i$ is the stiffness matrix at iteration i is defined from Equation (1.35) as

$$\mathbf{K}_T^i = -\left(\frac{\partial\mathbf{r}}{\partial\mathbf{a}}\right)_{n+1}^{i} = \left(\frac{\partial\mathbf{f}_{\text{int}}}{\partial\mathbf{a}}\right)_{n+1}^{i} = \sum_{e=1}^{N_e}\mathbf{L}_e^T\left(\int_{\Omega_e}\mathbf{B}_e^T\mathbf{D}_T^i\mathbf{B}_e\,\mathrm{d}\Omega\right)\mathbf{L}_e \tag{1.39}$$

in which $\mathbf{D}_T^i$ is the tangent modulus tensor for stress-strain relation. It is noted that the above relation is similar but not identical to that of linear elasticity (1.29).

For softening materials, beyond the peak force, the behavior exhibits a crop of force with an increasing displacement. Thus, a displacement control or an arc-length control is needed to follow the path of this behavior. We refer to textbooks, e.g., Zienkiewicz et al. (2005) for details.

It is noted that the integral of elementary quantities $\int_{\Omega_e} q(\xi)\,\mathrm{d}\Omega$ is computed numerically using a quadrature rule, e.g. Gauss-Kronrod quadrature, where a suitable set of NIP points ξ_i and corresponding weights ω_i is chosen to approximate the integral as

$$\int_{\Omega_e} q(\xi)\,\mathrm{d}\Omega \approx \sum_{i=1}^{NIP}\omega_i q(\xi_i) \tag{1.40}$$

1.2.4 Continuum-based models for concrete behaviors

For studying fracture problems in quasi-brittle materials, the FEM is a tool which is generally used. The FEM describes the material as a continuum and the nonlineariry is implemented by using measured softening behaviors. Two main numerical approaches can be distinguished in the context of the FEM framework, namely, (i) discontinuous approach using discontinuous models and (ii) continuous approach using continuous models. The interested reader is referred to Appendix A for an overview of discontinuous models and of continuous models including smeared crack model, crack band model and anisotropic damage model.

1.2.4.1 Isotropic damage models

Under the assumption that the Poisson's ratio remains constant throughout the damage evolution, a softening material can be described by an isotropic damage model which specifies the stress-strain relation as (Lemaître, 1996)

$$\boldsymbol{\sigma} = (1-d)\mathbf{C} : \boldsymbol{\varepsilon} \tag{1.41}$$

with d the scalar damage variable and $\mathbf{C}$ the fourth order elastic stiffness tensor. The damage variable grows from 0 (intact material) to 1 (completely damaged material) according to a damage evolution law such that

$$d = d(\kappa) \tag{1.42}$$

in which κ is the history variable representing the largest strain ever reached during the loading history. The history variable κ is defined via the following loading function f

$$f(\tilde{\varepsilon},\kappa) = \tilde{\varepsilon} - \kappa \tag{1.43}$$

with $\tilde{\varepsilon}$ the scalar-valued function of the strain tensor $\boldsymbol{\varepsilon}$. The loading function f defines an elastic surface, i.e., the set of states for which damage does not evolve. The damage only increases when the current threshold of deformation (the current largest strain) κ is exceeded, i.e., the damage does not change during an unloading stage or an elastic loading stage. This is expressed mathematically by the Kuhn-Tucker condition

$$f \leq 0, \quad \dot{\kappa} \geq 0, \quad \dot{\kappa} f = 0 \tag{1.44}$$

Different damage models distinguish themselves by specifying different damage evolution laws (1.42) and different definition of the equivalent strain $\tilde{\varepsilon}$. It has been shown, experimentally, that concrete exhibits a highly asymmetric behavior under tensile and compressive loading conditions. Taking into account this characteristic, Mazars (1984) and Mazars and Pijaudier-Cabot (1989) proposed the definition

$$\tilde{\varepsilon} = \sqrt{\sum_{i=1}^{3} (\langle \varepsilon_i \rangle_+)^2} \tag{1.45}$$

with ε_i the principal strains and the McCauley's brackets $\langle x \rangle_+$ denote the positive part of a scalar x, which means $\langle x \rangle_+ = \max(x, 0)$. A contour plot for $\tilde{\varepsilon} = 1$ in the principal stress space is given in Figure 1.17a with Young's modulus $E = 30$ GPa and Poisson's ratio $\nu = 0.2$. Figure 1.17b shows the same plot but under the plane stress condition ($\sigma_3 = 0$).

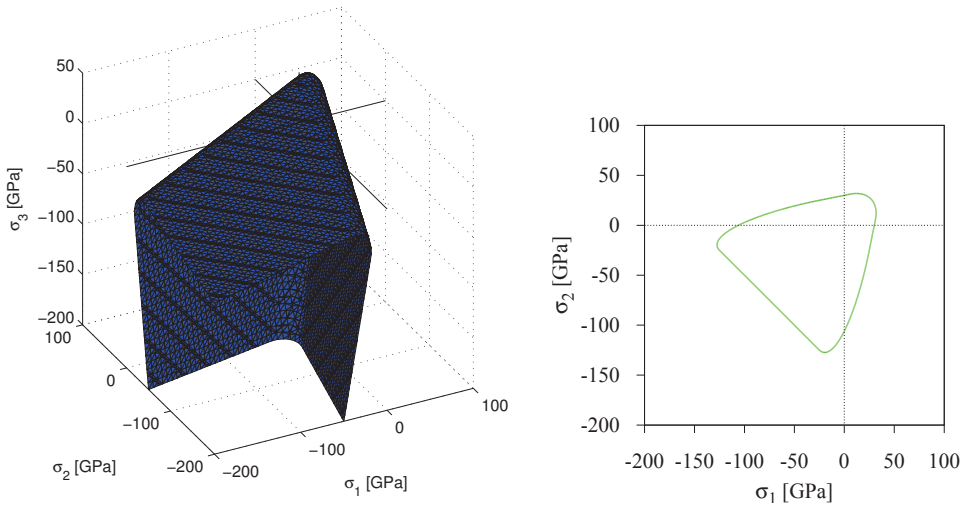

(a) (b)

Figure 1.17 – Contour plots for the equivalent strain of Mazars in principal stress space (a) and in the plane σ_1-σ_2 ($\sigma_3 = 0$) (b).

The equivalent strain (B.5) can produce a good approximation of the failure envelope of concrete under biaxial tension and under tension combined with compression. However, under biaxial compression, the shape of the failure envelope is not realistic. This can be improved by adjusting the multiplicative factor to the above definition of the equivalent strain as

$$\tilde{\varepsilon} = \gamma \sqrt{\sum_{i=1}^{3} (\langle \varepsilon_i \rangle_+)^2} \tag{1.46}$$

with

$$\gamma = \begin{cases} \dfrac{\sqrt{\sum_{i=1}^{3}(\langle\sigma_i\rangle_-)^2}}{\sum_{i=1}^{3}\langle\sigma_i\rangle_-} & \text{if } \sum_{i=1}^{3}\langle\sigma_i\rangle_- \neq 0 \\ 1 & \text{otherwise} \end{cases} \tag{1.47}$$

where $\langle x\rangle_-$ denotes the negative part of x, which means $\langle x\rangle_- = -\min(x, 0)$. The modified equivalent strain according to (1.46) is graphically represented in Figure 1.18.

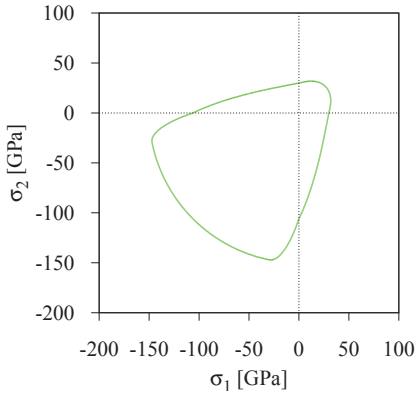

Figure 1.18 – Contour plots for the modified equivalent strain of Mazars in the plane σ_1-σ_2 ($\sigma_3 = 0$).

From the definitions of the equivalent strain and in order to capture the differences of material responses in tension and in compression, Mazars and Pijaudier-Cabot (1989) proposed a damage evolution law as

$$d = \alpha_t^\beta d_t + \alpha_c^\beta d_c \tag{1.48}$$

where d_t and d_c are the damage variables in tension and compression, respectively. The exponent $\beta > 1$ slows down the evolution of damage under shear loading (Pijaudier-Cabot et al., 1991), usually its value is fixed at 1.06. The coefficients α_t, α_c take into account the character of the stress state, which are given as

$$\alpha_t = \sum_{i=1}^{3} \frac{\varepsilon_{ti}\langle\varepsilon_i\rangle_+}{\tilde{\varepsilon}^2}, \quad \alpha_c = 1 - \alpha_t \tag{1.49}$$

where ε_{ti}, $i = 1, 2, 3$ are the principal strains due to positive stresses, i.e., the principal values of $\varepsilon_t = \mathbf{C}^{-1} : \langle\mathbf{C} : \varepsilon\rangle$. The damage variables in tension and compression, d_t and d_c, are given by

$$d_k = \begin{cases} 1 - (1 - A_k)\frac{\varepsilon_{d0}}{\kappa} - A_k \exp[-B_k(\kappa - \varepsilon_{d0})] & \text{if } \kappa \geq \varepsilon_{d0} \\ 0 & \text{if } \kappa < \varepsilon_{d0} \end{cases}, \quad k = t, c \tag{1.50}$$

where ε_{d0} is the equivalent strain at the onset of nonlinearity, and A_t, B_t, A_c, B_c are material parameters related to the shape of the uniaxial stress-strain diagrams. It should be noted that the damage evolution law (1.50) allows an independent control of the tensile and compressive stress-strain curves. However, it leads to a tension/compression dissymmetry of the elasticity limit usually not large enough.

Based on the von Mises equivalent strain, de Vree et al. (1995) proposed an equivalent strain adapted to concrete, which included the ratio k of the uniaxial compressive strength and the uniaxial

tensile strength. This proposition is given by

$$\tilde{\varepsilon} = \frac{k-1}{2k(1-\nu)} I_1 + \frac{1}{2k}\sqrt{\frac{(k-1)^2}{(1-2\nu)^2} I_1^2 + \frac{6k}{(1+\nu)^2} J_2} \tag{1.51}$$

in which $I_1 = \varepsilon_{kk}$ is the first invariant of the strain tensor and $J_2 = e_{ij}e_{ij}$ is the second invariant of the deviatoric strain tensor $e_{ij} = \varepsilon_{ij} - (1/3)\varepsilon_{kk}$. The graphical representation of this equivalent strain scaling to $\tilde{\varepsilon} = 1$ is given in Figure 1.19 with $k = 10$, $E = 30$ GPa and $\nu = 0.2$.

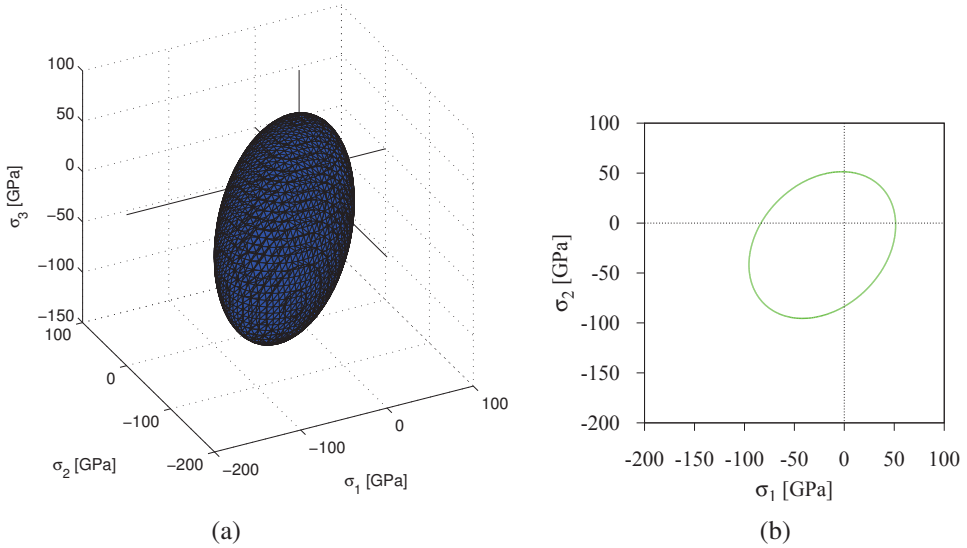

Figure 1.19 – Contour plots for the equivalent strain of de Vree in principal stress space (a) and in the plane σ_1-σ_2 ($\sigma_3 = 0$) (b).

From the definition of the equivalent strain (1.51), Peerlings et al. (1998) proposed an evolution law of damage variable as

$$d(\kappa) = 1 - \frac{\kappa_0}{\kappa}(1 - \alpha + \alpha \exp[-\beta(\kappa - \kappa_0)]) \tag{1.52}$$

with κ_0 the initial threshold at the onset of damage, α and β two other model parameters. These parameters were taken as $\kappa_0 = 2.1 \times 10^{-4}$, $\alpha = 0.96$ and $\beta = 350$ for concrete by Peerlings et al. (1998).

1.2.4.2 Nonlocal damage models

Nonlocal continuum theory abandons the classical assumption of locality and considers that a state variable (e.g., stress) at a certain point not only depends on the state of other variables (e.g., strain) at that point but also in general on the distribution of state variables of the neighboring points. Applying nonlocal continuum to damage models, there exist mainly two formulations, i.e., the *integral-type nonlocal* and *gradient-enhanced* damage models.

Integral-type nonlocal damage models To restore the well-posedness of the boundary value problem when softening occurs, Pijaudier-Cabot and Bažant (1987) proposed to compute damage variable from the nonlocal equivalent strain. This means that the local value $\tilde{\varepsilon}$ in the loading function (1.43) is replaced by its corresponding nonlocal definition as

$$\bar{\varepsilon}(\mathbf{x}) = \frac{1}{V_r(\mathbf{x})} \int_\Omega \psi(\mathbf{x}, \boldsymbol{\xi}) \tilde{\varepsilon}(\boldsymbol{\xi})\, \mathrm{d}\boldsymbol{\xi} \quad \text{with} \quad V_r(\mathbf{x}) = \int_\Omega \psi(\mathbf{x}, \boldsymbol{\xi})\, \mathrm{d}\boldsymbol{\xi} \tag{1.53}$$

where $\psi(\mathbf{x}, \boldsymbol{\xi})$ is a nonlocal weight function that depends on the distance between the "source" point $\boldsymbol{\xi}$ and the "receiver" point $\mathbf{x}$, $r = \|\mathbf{x} - \boldsymbol{\xi}\|$. The history variable κ is then the largest previously reached value of the nonlocal equivalent strain.

Several forms have been proposed for the weight function. It is often taken as the Gaussian distribution function

$$\psi(\mathbf{x}, \boldsymbol{\xi}) = \exp\left(-\frac{4r^2}{\ell_c^2}\right) \tag{1.54}$$

with ℓ_c an internal length of the model reflecting the nonlocality characteristic of the model. Another possible form for the weight function is the truncated polynomial function (Bažant and Ožbolt, 1990)

$$\psi(\mathbf{x}, \boldsymbol{\xi}) = \left\langle 1 - \frac{r^2}{R^2} \right\rangle^2 \tag{1.55}$$

where $\langle\cdot\rangle$ denotes always the positive part of a scalar, R is a parameter related to the internal length, which is called the interaction radius since it corresponds to the largest distance of point $\boldsymbol{\xi}$ affecting the nonlocal average at the point $\mathbf{x}$.

In the above formulations, the internal length ℓ_c or R is constant during the damage process. However, experimental observations from acoustic emission analyses provide that the FPZ expands from its initiation in the course of damage process (Haidar et al., 2005). Taking into account this behavior, a modified nonlocal damage model in which the internal length is evolved during the damage process depending on the local equivalent strain, was proposed by Pijaudier-Cabot et al. (2004). The weight function now reads

$$\psi(\mathbf{x}, \boldsymbol{\xi}, \tilde{\varepsilon}(\boldsymbol{\xi})) = \exp\left(-\frac{4r^2}{\ell_c^2(\tilde{\varepsilon}(\boldsymbol{\xi}))}\right) \tag{1.56}$$

and the internal length increases in a linear form

$$\ell_c(\tilde{\varepsilon}) = \alpha f_d(\tilde{\varepsilon}) + \ell_{c0} \tag{1.57}$$

where f_d is a function increase from 0 to 1 corresponding to the damage level, α is a material constant, ℓ_{c0} is related to initial defects in the material. This model introduces, however, in addition, one more material constant α if we assume that f_d is a linear function.

Based on the work of Pijaudier-Cabot and Dufour (2010) showing that the nonlocality corresponds to a stress redistribution due to the present of deffects, Giry et al. (2011) proposed a nonlocal damage model in which the nonlocal interaction, i.e. the internal length, evolves over time depending on the stress state of the neighboring material points. The weight function proposed by Giry et al. (2011) has the same form as (1.54) but the internal length ℓ_c was proposed as

$$\ell_c = \ell_{c0} \cdot \rho(\mathbf{x}, \boldsymbol{\sigma}_{prin}(\boldsymbol{\xi})) \tag{1.58}$$

where ℓ_{c0} is the intrinsic length that can be correlated with aggregate size of the material, ρ represents the evolution of the internal length during the damage process and depends on the principal stress state of the point located at $\boldsymbol{\xi}$.

Based on thermodynamic formulation, the nonlocal damage models have also been proposed, see e.g., Comi (2001) and references therein or a model with evolving nonlocal interactions (Nguyen, 2011).

It should be noted that the integral-type nonlocal formulations can be developed to regularize not only for isotropic damage models but also for other constitutive models with softening such as smeared crack models (Bažant and Lin, 1988), microplane models (Bažant and Ožbolt, 1990), anisotropic damage models (Desmorat et al., 2007). A good survey of process of nonlocal integral formulations can be found in Bažant and Jirásek (2002).

Gradient-enhanced damage models Gradient models incorporate the influences of gradients (of the first or higher order) of internal variables into constitutive relations. This concept was pioneered by Aifantis (1984). Gradient formulations was first applied into gradient-dependent plasticity model (de Borst and Mühlhaus, 1992). Applying this concept to damage models, there exist two formulations the *explicit* and *implicit* ones. Gradient-enhanced damage models have been proposed by Peerlings et al. (1996, 1998).

Explicit gradient formulation The damage evolution is assumed to be driven not only by the local equivalent strain $\tilde{\varepsilon}$ but also by its Laplacian $\nabla^2\tilde{\varepsilon}$. This means that in the loading function (1.43), the equivalent strain $\tilde{\varepsilon}$ is replaced by the corresponding nonlocal one defined as

$$\bar{\varepsilon} = \tilde{\varepsilon} + l^2\nabla^2\tilde{\varepsilon} \tag{1.59}$$

where l is a material parameter with dimension of length.

When the strain distribution remains uniform (as in uniaxial tensile test before the peak), the equivalent strain $\tilde{\varepsilon}$ is also uniform, and thus its Laplacian vanishes, leading to the same responses between local and nonlocal models. After the onset of localization, the strain distribution becomes nonuniform leading to the nonzero value of its Laplacian, and the internal length of the model l plays a role of localization limiter. However, as shown in Peerlings et al. (1996), using the explicit formulation (1.59) requires the $\mathcal{C}^1$-continuity for the displacement field, i.e. higher order FEs, when implemented in a FEM code. This disadvantage can be avoided by using the implicit gradient damage formulation.

Implicit gradient formulation By differentiating equation (1.59) twice and substituting the obtained expression back into (1.59), Peerlings et al. (1996) proposed an implicit definition of the nonlocal equivalent strain

$$\bar{\varepsilon} - l^2\nabla^2\bar{\varepsilon} = \tilde{\varepsilon} \tag{1.60}$$

The solution $\bar{\varepsilon}$ of the above equation is obtained from the boundary value problem posed by (1.60) and the Neumann boundary condition imposed on the boundary of the domain

$$\nabla\bar{\varepsilon}\cdot\mathbf{n} = 0 \tag{1.61}$$

with $\mathbf{n}$ the external normal unit vector of the boundary.

Peerlings et al. (2001) showed that the solution $\bar{\varepsilon}$ of (1.60) and (1.61) is of the form

$$\bar{\varepsilon}(\mathbf{x}) = \int_\Omega G(\|\mathbf{x}-\boldsymbol{\xi}\|)\tilde{\varepsilon}(\boldsymbol{\xi})\,\mathrm{d}\boldsymbol{\xi} \quad \text{with} \quad G(r) = \frac{1}{4\pi l r}\exp\left(-\frac{r}{\sqrt{l}}\right) \tag{1.62}$$

where G is the Green's function of (1.60). This means that the implicit enhancement is exactly the integral-type nonlocal damage model with the Green's function G as the weight function.

In summary, the common point of the nonlocal models is the introduction of an internal length. The question has to be posed is that how to determine the link between the characteristic length of the material (e.g., aggregate sizes) and the internal length of the nonlocal model. Critical discussions about this subject will be presented in Chapter 4, Section 4.1.

1.2.5 Internal length value

The common characteristic of the above nonlocal techniques (integral and gradient formulations) is the introduction of an internal length in the constitutive law, used as a localization limiter, to prevent the spurious localization of damage, to avoid the ill-posedness of the boundary value problem, and thus to avoid the mesh sensitivity. This internal length controls the spread of the nonlocal weight function. At this point, it is important to note that there is a difference between the notions of an internal length and of a characteristic length of the material. The former is a model parameter and

the latter is the length that characterizes the material and is an intrinsic length of the material e.g. aggregate sizes or, in general, heterogeneity of the material.

Physically, the internal length is related to the effective size of the FPZ whose evolution depends (at least) on details of material microstructure and on the specific failure mechanism that develops for a given type of loading (Jirásek et al., 2007; Giry et al., 2011).

The internal length cannot be directly measured but can be indirectly inferred from experimental results. For instance, the internal length can be determined by inverse analysis based on computations of size effect tests (Bellégo et al., 2003) or by comparing the energy dissipated in two kind of experimental tensile tests: (i) those leading to localized damage and (ii) those where the damage remains distributed (Bažant and Pijaudier-Cabot, 1989). However, the former procedure requires many computations and is still based on a manual trial-and-error technique and is held for a limited size range of specimens while the latter procedure exhibits the sensitivity to boundary conditions where the condition that the strain remains homogeneous throughout the specimen is difficult (even impossible) to assure. Furthermore, such calibration procedures are only based on one characteristic heterogeneity of the material and lead to observations that the internal length is proportional to the characteristic size D_0 in the size effect plot or to the maximum aggregate size $d_{\max}$. So, they can hardly be considered as a general rule.

An alternative technique to determine the internal length is that based on experiments with acoustic emission analysis (Maji and Shah, 1988). Acoustic emission is an experimental tool well suited for monitoring the fracture process (and its size, of course). Haidar et al. (2005) showed, with acoustic emission analyses, that the FPZ widens in the course of degradation processes. This led to the idea that the internal length not only depends on the geometric aspects of the material but also on the strain and/or stress state.

All of these explain the fact that calibration of the internal length of nonlocal models is still a difficult question since it seems to depend not only on the heterogeneity of the materials but also on the boundary conditions and of strain and stress fields in the FPZ.

Mathematically, the internal length is described by a function of at least two variables: one standing for the material microstructure m and other accounting for the form of the stress field s

$$\ell_{\mathrm{c}} = f(m, s) \tag{1.63}$$

The material microstructure variable m is again a function of the size and spacial distribution of the constituents (i.e. the characteristic length of the material) and of their corresponding strengths, which might be known. However, the function f is unknown. One possible suggestion is proposed by Giry et al. (2011), in which the internal length is described by the product of two functions: one is a function of the characteristic length of the material while other is a function of the stress field and strength of the material (refer to Equation (B.8) with $\boldsymbol{\sigma}_{prin}(\boldsymbol{\xi})$ is a function of the stress field and the material strength, proposed by Giry et al. (2011)). The influence of the stress field is easily accessible by the boundary conditions. The remaining question is to deal with the characteristic length of the material, i.e. determining the function to relate ℓ_{c0} (see Equation (B.8)) to the intrinsic length of the material (e.g. aggregate sizes). In what follows, for simplicity, ℓ_{c0} is also called the internal length.

As of today, no explicit relationship between the internal length and the characteristic length of the material has been devised for nonlocal models. This motivates to develop a numerical model that does not introduce any internal length and can enfranchise this parameter by explicitly introducing aggregates in the geometrical description. Moreover, through this model, a study of the influence of the microstructure of the material on its behaviors at both prepeak and postpeak regimes can be carried out. We then extract an internal length required for continuum nonlocal (integral or gradient type) damage models from the microstructure of the material. The talking model belongs to the class of discrete models which are next presented.

1.3 Discrete models

The above continuum-based models generally neglect the heterogeneity of the material and consider it as a homogeneous material with homogenized properties at the macroscale. These models disregard the randomness of material microstructure properties and consequently are unsuitable for characterizing entirely the complex fracture process from initiation, propagation and coalescence of microcracks to the formation of macrocracks. Moreover, the determination of homogenized properties of the material at the macroscale is not always feasible and these models do not always reflect all physical effects observed in experiments through their internal variables, e.g. grain decohesion, microcracking and crack bridging observed in concrete. Therefore, it is hardly to consider them as relevant models to provide a comprehensive understanding of the fracture process of heterogeneous materials.

Even though the mesoscopic approach using continuum-based models was proposed by, e.g., Vonk et al. (1991), Eckardt et al. (2004), Wriggers and Moftah (2006), and Nguyen et al. (2010), they cannot take into consideration the discrete nature of cracking and thus cannot reproduce exactly the crack opening which is an important parameter for durability analyses of structures. Discrete models used at the mesoscale seem to be the most useful approach for modeling the discrete character of cracking. Moreover, they can be considered as the useful approach for studying the influence of the concrete composition on the macroscopic properties and also to gain insight into the origin and nature of the nonlinear behavior of concrete.

Furthermore, when using continuum-based nonlocal models, an internal length has to be introduced as discussed above. Since the internal length results from microcracks and their interactions, thus, if a model could directly describe these phenomena, it would be consider as a better approach than the continuous ones. This is another key reason for using a discrete model.

For modeling of behaviors of quasi-brittle materials, there exist at least three types of discrete numerical methods/models that one can cite here: (i) the discrete element method, (ii) the molecular dynamics, and (iii) the lattice model.

1.3.1 Discrete element and molecular dynamics methods

The discrete element method (DEM) was initiated by Cundall and Strack (1979). The development of DEM has been growing fast for advanced applications in granular materials and geomaterials like soil, rock and concrete (Shiu et al., 2009; Nicot et al., 2011; Tran et al., 2011; Scholtès and Donzé, 2012a,b). The key concept of DEM is that the medium is divided into an assemblage of rigid or deformable geometric elements such as disks, ellipses, polygons (in two dimensions) or spheres, ellipsoids, polyhedra (in three dimensions), etc. Each element has a movement that is governed by the fundamental principles of dynamics, derived from Newton's second law and by the intergranular interaction laws.

Mainly due to the explicit representation of the discrete nature of the discontinuities when dealing with large scale problems of fractures, fragmentation or even flow of materials, DEM is widely used for applications in geomaterial mechanics and engineering (Scholtès et al., 2009). Nevertheless, there exist some shortcomings of DEM, e.g., extensive computational cost when dealing with large-scale problems, or when the equivalence with the continuum is required, homogenization is needed but is often a difficult task.

Having the same concept as DEM but the molecular dynamics (MD) method has atoms and molecules as the basic elements. MD can be used as a powerful tool to explain mechanical phenomena at atomic scale, e.g., studying the brittle to ductile transition in intrinsic fracture of crystals (Cheung and Yip, 1990), or studying the crack properties of crystalline metals (Farkas et al., 2002; Hasnaoui et al., 2003). Nevertheless, when using MD to deal with granular materials for solving problems in engineering, since the model consists of a vast number of degrees of freedom to include all atoms in a macroscopic system, the calculation time becomes unreasonable. Therefore, one could reduce the size of the system under consideration (usually to the representative volume

element), so that a MD simulation is possible. So, applications of MD for granular materials are limited to small-scale problems.

The methods of DEM and MD are relatively easy to understand because they are based on the numerical solution of Newton's second law. They have been widely applied with success. However, long MD and DEM simulations are mathematically ill-conditioned, generating the cumulative errors in numerical calculations. Based on the concept of "interaction" between particles, DEM and MD are most appropriate for non-cohesive granular materials like sand. They are out of the scope of this thesis since we only focus on concrete-like materials which are cohesive materials. The interested reader is referred to Donzé et al. (2009) for the latest DEM's developments in rock, soil and concrete mechanics, or to Radjaï and Dubois (2011) for a full description of discrete-element modeling of granular materials.

1.3.2 Lattice models

Lattice models for heterogeneous materials derive from the Lattice Element Method (LEM) which is based on lattice-type discretization of the medium (Radjai et al., 2010). The earliest lattice model was proposed by Hrennikoff (1941) for solving problems in linear elasticity by means of regular triangular lattice of truss elements. Later, lattice models have been broadly used to model the failure in brittle heterogeneous materials by physicists (Burt and Dougill, 1977; Herrmann et al., 1989). Nowadays, lattice models have become more popular in fracture modeling of heterogeneous materials due to the increase of computer performance. Just like DEM, for the problems in which the discontinuities are dominant, lattice models are considered as a suitable tool because they provide a discrete representation of material disorder and failure. However, lattice models, compared to DEM, are appropriate for fracture modeling of *cohesive* granular materials like concrete and have a major advantage in terms of numerical calculations.

There exist two different types of lattice models. In the first type of lattice models, called classical lattice models, the material is discretized as a network of two-node springs or beams (Schlangen and van Mier, 1992a, 1992b; Schlangen, 1993; van Mier and Vervuurt, 1995). The second type of lattice models, called particle lattice models, are classified as a discrete element method (Kikuchi et al., 1992) in which the material is discretized as an assemblage of rigid particles interconnected along their boundaries through normal and shear springs (Kawai, 1978). The models in this category also include the rigid-body-spring networks (Bolander Jr et al., 2000), bonded-particle model (Potyondy et al., 1996), random particle models (Bažant et al., 1990), beam-particle model (D'Addetta et al., 2002; Delaplace, 2005), confinement-shear lattice model (Cusatis et al., 2003). The main advantage of particle lattice models with respect to classical lattice models is that they account for the fact that crack surfaces may act on each other causing the repulsive force during the loading process. So the particle lattice models are more suitable for predicting the failure behavior in mode II or mode I under cyclic loadings whereas the classical ones are enough when the mode I failure prevails.

In both types of lattice models, fracture initiation and propagation are modeled by either removing brittlely, from the lattice, the elements in which the stress/strain exceeds the critical value (Schlangen and van Mier, 1992a; D'Addetta et al., 2002) or degrading their elastic properties via a softening response (Bolander Jr. and Saito, 1998; Arslan et al., 2002).

There exist at least two ways to describe the mesostructure of the material. In the first way, using by the particle lattice models, the particles are used to model the grains whereas in the second way, using by the classical lattice models, an aggregate structure is usually mapped onto the lattice and then different material properties are assigned to the elements representing the different material phases (grain, mortar matrix and the ITZ in the case of concrete). The first way is characterized by the computational efficiency with respect to the second one since a coarser resolution can be used. The second approach requires a finer resolution, however, it can produce more tortuous crack patterns.

Besides the attractiveness of lattice models such as simplicity or direct insight into the fracture process at the mesostructure level, they exhibit, however, mesh bias on crack propagation. Such limitation can be minimized by using a random mesh instead of a regular one and by introducing the material heterogeneities not only by incorporating the grain structure but also by assigning the random local material strength after a Weibull or Gaussian distribution.

The simplest lattice model is the central force model in which only the normal forces are considered as interaction forces. Nevertheless, this model exhibits a known restriction is that, when modeling the homogeneous materials (without inclusions), it produces a fixed value of Poisson's ratio, namely $\frac{1}{3}$ for two dimensional cases (Chang et al., 2002b) and $\frac{1}{4}$ for three dimensional problems (Ostoja-Starzewski, 2002). With such a restriction this model is not suitable for modeling many materials with different values of Poisson's ratio. It is overcome by introducing the shear interactions in the model. The normal-shear lattice models can reproduce a Poisson's ratio within the range -1 and $\frac{1}{3}$ (Schlangen and Garboczi, 1996). Therefore, they are more suitable for modeling many materials in civil engineering like concrete, soil, sandstone, etc.

In this thesis, we focus mostly on mode-I failure of the material submitted to monotonic mechanical loadings. Moreover, for studying the influence of the material microstructure on the fracture process zone which related to the characteristic length of the material, a detailed description of tortuous crack patterns is of importance. Therefore, a lattice model, based on the classical lattice models, in which the normal and shear springs are introduced, is fully developed in three dimensions for applications in both two and three dimensional problems. The model also includes a more realistic estimate of cross-section areas assigned to lattice springs for better reflecting the random mesostructure of the material. The lattice model is detailed in Chapter 2.

However, when more detail on the material microstructure is required, a fine mesh has to be used for incorporating small grains and/or when dealing with fracture of large-scale structures, especially in three dimensional problems, the lattice model exhibits limitation in computational time since it consists of a vast number of degrees of freedom. To deal with such problems within a reasonable computation time, improvements in numerical solver is proposed in Chapter 2 to speed up in finding the solution of the equilibrium equations, but on the other hand it seems necessary to couple the lattice model at the mesoscale level with the finite element method used to macroscopically model the material at regions that undergo elastic processes. This is the multiscale coupling, the so-called FEM–LEM coupling, proposed in Chapter 4. In the next section, an overview of multiscale techniques for modeling of heterogeneous materials is presented.

1.4 Multiscale approaches

Multiscale modeling has emerged as one of big challenges in material sciences and engineering due to its efficiency. We provide a comprehensive, though not exhaustive, overview of commonly multiscale techniques used to deal with heterogeneous materials. This overview is used in the thesis to classify and motivate the proposed multiscale approach. Traditionally, multiscale modeling of heterogeneous materials is performed either within the framework of "homogenization methods" or within the framework of "concurrent methods". In the former, the models include more than one length scales that are completely separated while in the latter, scales remain coupled.

1.4.1 Homogenization methods

Homogenization is a technique lied on complete scale separation to determine the *apparent* (or *overall*) properties of a heterogeneous material by considering it as an homogeneous material with the equivalent effective properties, see Figure 1.20. This means that the equivalent macroscopic properties are obtained from quantitative information at microlevel.

Depending on microstructure characteristics, the effective properties of heterogeneous materials can be determined by various approaches. In the case of materials with linear constitutive behavior,

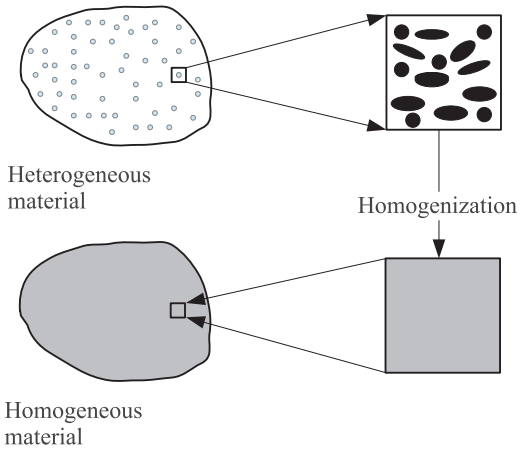

Figure 1.20 – Homogenization of a heterogeneous material. Based on Temizer and Zohdi (2007).

if the microstructure is sufficiently regular to be considered periodic, the effective properties may be determined by mathematical asymptotic homogenization techniques, documented in Bensoussan et al. (2011). Using the mathematical asymptotic homogenization techniques, the strain and stress fields are asymptotically expanded on the scale parameter, which is the ratio of a characteristic size of the heterogeneities and a measure of the macrostructure. These analytical techniques can be extended to applications of nonlinear materials (Christman et al., 1989; Yi et al., 1998; Fish et al., 1999; Miehe et al., 2002). If the microstructure is not regular, concrete for example, the effective properties cannot be determined exactly by analytical homogenization techniques. However, they can by estimated in terms of bounds, which depend on some parameters characterizing the microstructure such as volume fraction of inclusions in a matrix. For heterogeneous materials having linear constitutive behavior, Voigt assumes that strain field is uniform in each phase, arriving to estimate

$$\bar{\mathbf{L}} = \sum_{r=1}^{N} \mathbf{L}^{(r)} c^{(r)} \tag{1.64}$$

where $\mathbf{L}^{(r)}$ and $c^{(r)}$ are respectively the elastic tensors and the volume fraction of r phase of an N-phase material, $\bar{\mathbf{L}}$ is the homogenized elastic tensors of the material. A dual assumption of Voigt is made by Reuss who approximates the stress field is uniform in each phase, leading to

$$\bar{\mathbf{L}} = \left[\sum_{r=1}^{N} [\mathbf{L}^{(r)}]^{-1} \, c^{(r)} \right]^{-1} \tag{1.65}$$

Hill, 1952 and Paul, 1959 observed that Voigt estimate and Reuss estimate are respectively the upper and lower bounds of the effective properties. Bound estimates for materials with nonlinear behavior was also proposed, e.g.,the models of Talbot and Willis (1985) and Castañeda (1991) based on variational principles, the Hill's incremental model (Hill, 1965).

When dealing with nonlinear analysis of heterogeneous materials in which the information of the material microstructure is taken into account in the multiscale framework, there currently exist two main approaches based on homogenization methods: (i) Unit cell methods, and (ii) multiscale computational homogenization techniques.

Unit cell methods (Christman et al., 1989; Sluis et al., 2000) are classified as the explicit version of homogenization-based multiscale techniques in which the constitutive relations are explicitly constructed on the macrolevel with parameters subsequently identified by homogenization techniques and the knowledge of the material microstructure. These approaches have been used in a great number of different applications, e.g., the correlation between local and global damage effects of fiber-reinforced composites (Voyiadjis and Kattan, 1993), modeling of granular materials (Cambou

et al., 1995; Emeriault et al., 1996). However, when dealing with highly nonlinear materials that exhibit softening and strain localization resulted from geomaterial and physical changes of the microstructure, it is difficult to establish *a priori* the suitable form of constitutive relations. Hence this makes the unit cell methods less appropriate for materials with complex microstructure.

In multiscale computational homogenization techniques (Smit et al., 1998, 1999; Feyel, 2003), constitutive equations on the macrolevel are not defined explicitly but they are implicitly provided by the macro-meso-macro connection. Therefore, these techniques are classified as the implicit version of homogenization-based multiscale techniques. Two distinct stages, namely downscaling and upscaling, are typical for this kind of technique, see Figure 1.21. The procedure of computational homogenization technique shown in Figure 1.21, which is called the first-order homogenization, can be briefly described as follows. A solid Ω_M is modeled as homogeneous at macrolevel. At a material point, e.g., integration point in the FE method, instead of inserting the macroscopic strain $\boldsymbol{\varepsilon}_M$ into the phenomenological constitutive box to obtain macroscopic stress $\boldsymbol{\sigma}_M$, the macroscopic strain is imposed on the external boundary Γ_m of the micro/meso sample (RVE) Ω_m. The equilibrium of the micro/meso sample is obtained after solving the boundary value problem (BVP). The macroscopic stress is then defined as the volume average of the microscopic stress over the RVE and the macroscopic tangent moduli D_M can be directly obtained from the RVE stiffness matrix. They are then transferred to the macroscopic level at that material point. In case the FEM is used at both scales to solve the entire problem as a nested BVP, the method is known as FE^2 scheme (Feyel, 1999). Different kinds of boundary conditions (Miehe and Koch, 2002) can be chosen, such as linear displacements, constant tractions or periodic deformation and antiperiodic tractions on the boundaries, which highly influence the behavior at the boundaries of the RVE. Although the constitutive behavior is not need on the macrolevel, it must be included on the microlevel to produce the behavior of RVEs. If continuum-based approaches are used, the constitutive behavior of RVEs can be described by any model of those presented in Section 1.2.4 and in Appendix A of which parameters have to be identified prior to the simulation, but now applied for individual microstructural constituents and interfacial transition zones between them. However, identification of parameters for the interfacial transition zones is always a difficult question. Alternatively, constitutive models for each constituent and the interfacial transition zones at the microlevel can be defined using a homogenization technique by downing one more scale.

The main assumption of the homogenization techniques is the existence of the RVE. However, when dealing with strain localization and failure phenomena in softening materials, a RVE for softening regime cannot be found using the "standard" averaging technique over the microscopic sample volume since the material loses statistical homogeneity upon strain localization. On the other hand, the macroscopic discretization might suffer from mesh dependency and, at ultimate loading stages, the macroscopic BVP becomes ill-posed if there is no regularization technique adopted thereby. Furthermore, if a regularization technique is provided at the macrolevel, we turn back to the problem of identifying the internal length, see Section 1.2.5. Those drawbacks have been recently found by Gitman et al. (2008) and Bažant (2010). As a result, the numerical solution obtained is not objective and shows the dependence on both macrolevel mesh size and micro/meso level RVE size if the first-order multiscale scheme is used.

Several strategies have been proposed to overcome these sensibilities for decades. One of them is the use of gradient formulations (Kouznetsova et al., 2002; Kaczmarczyk et al., 2008) by incorporating a microscopic length scale, which is called the second-order homogenization. However, the method cannot properly resolve macroscopic localization bands beyond a quadrature nature of the displacements (Geers et al., 2010). In addition, the second-order scheme only overcomes dependence on the macrolevel discretization and does not solve the mesolevel RVE size dependence in case of softening response. These have been shown by Gitman et al. (2005, 2007). They proposed an alternative multiscale scheme which could resolve the macrolevel discretization sensitivity and the mesolevel RVE size dependency simultaneously, the coupled-volume approach (Gitman et al., 2008). An alternative approach is that called multiscale aggregating discontinuities (MAD), which

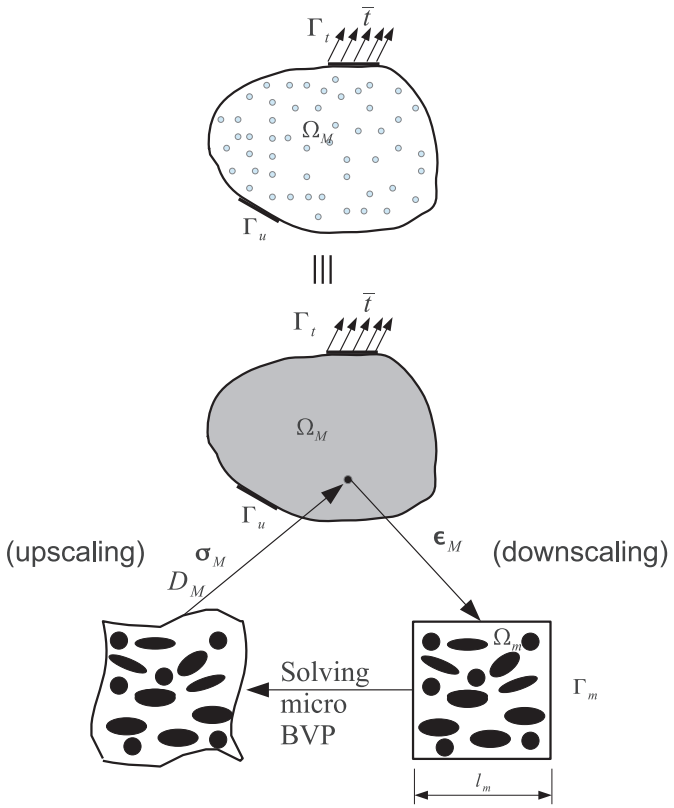

Figure 1.21 – Multiscale modeling of heterogeneous material with the computational homogenization.

has recently developed by Belytschko and Song (2010). The essential feature in the MAD approach is that, when material instabilities such as cracks or shear bands, occur in the micromodel, an equivalent discontinuity is computed and injected into the macromodel, which is treated by the extended finite element method (XFEM) (Belytschko and Black, 1999). Nguyen et al. (2011) proposed the failure zone averaging scheme for the multiscale computational technique in that only the active inelastic responses occurring in the microsample are extracted (rather than the whole responses in the microsample as in standard homogenization schemes) to determine the equivalent macroscopic ones. To better capture the discontinuities at the macro and micro levels in the limit case where the localization is intense, recent developments, can be found in Loehnert and Belytschko (2007) and Belytschko et al. (2008), are related to the continuous-discontinuous homogenization scheme in which the XFEM is used to take into account macrocracks as well as microcracks. However, the main drawback of all these techniques is that they provide a simplified representation of fracture i.e., cracks, strain localization, etc., at the macrolevel. Accordingly, they might fail to fully capture the more complex failure effects e.g., crack orientation, crack tortuosity, bridging, branching, etc., due to the heterogeneity of the micro/meso-structure. Moreover, the multiscale homogenization scheme, where the localization zone can steadily evolve in width (as experimentally observed for softening materials), is still open and raises challenges for researchers.

1.4.2 Concurrent methods

Concurrent multiscale techniques are characterized by the *simultaneous* resolution of the macrolevel and the mico/meso-level(s). This means that scales are coupled in the same framework and thus, global equilibrium and displacement compatibility need to be enforced on the whole structure. Concurrent methods have been developed in the context of continuum/continuum coupling, atomistic/continuum coupling i.e., MD-FEM coupling, and discrete/continuum coupling e.g., DEM-FEM coupling, where MD stands for molecular dynamic and DEM accounts for discrete element method.

For continuum/continuum coupling, we can refer to the works of Garikipati (2002), Larsson and Runesson (2008), and Mergheim (2009), which are based on the variational multiscale method (VMM) introduced by Hughes et al. (1998) or to the works of Schrader and Koenke (2011) and Lloberas-Valls et al. (2012a,b), which are based on domain decomposition techniques (Quarteroni and Valli, 1999). The basis of VMM is a decomposition of the field variables into a coarse-scale and a fine-scale contribution, the latter incorporating the local behavior whereas the domain decomposition techniques are based on a primal and dual spatial assembly (Tallec et al., 1991). The main drawback of continuum/continuum coupling is difficulties met when dealing with crack initiation and propagation. Indeed, different numerical methods have been proposed to model a propagating crack such as the strong discontinuity approach (Simo et al., 1993; Oliver et al., 2003), (widely used) XFEM approach (Babuška and Melenk, 1997; Belytschko and Black, 1999; Moës et al., 1999), discontinuous element with phantom-node method (Song et al., 2006). Even though these methods are appropriate in some particular cases e.g., a simple fracture mechanism without branching, bridging cracks, they are unsuitable to fully capture more complex failure mechanisms where the continuity of each crack path might be assured.

For multiscale approaches affected by MD-FEM coupling, we refer to an overview reported in Curtin and Miller (2003). Different methods have been proposed to handle the coupling. Xiao and Belytschko (2004) proposed a method to couple the continuum and molecular domains by bridging subdomains where the kinematic compatibility is strongly enforced by Lagrange multipliers, or Saether et al. (2009) suggested a method that replaces a direct linkage of individual MD atoms and FE nodes with a statistical averaging of atomistic displacements in local atomic volumes associated with each FE node in an interface region. Continuum and atomic scales are also coupled by MD and XFEM approaches in which a molecular dynamic approach describes fracture at the crack tip with an extended finite element method used for discretizing the remainder of the domain (Aubertin et al., 2010). MD and MD-FEM coupling are suitable for simulations at the material scale, however they are not appropriate for modeling at the scale of structures in civil engineering due to the important number of atomic degrees of freedom.

DEM-FEM coupling has been proposed for modeling of large structures in civil engineering. Localization due to impact on concrete structure was analyzed in the multiscale context by Frangin et al. (2006) and Rousseau et al. (2009), in which the coupling is handled by a transition bridging zone based on the method proposed by Xiao and Belytschko (2004) for MD-FEM coupling. Within the transition bridging zone, the total energy is defined as linear combination of discrete and continuous energies and compatibility is ensured through kinematic constraints by means of Lagrange multipliers in the strong form (strong coupling), refer to Figure 1.22a. Weak DEM-FEM coupling has alternatively been proposed that based on the Arlequin method (Dhia and Rateau, 2005). Alerquin method applied to DEM-FEM coupling is also based on a bridging domain with a weak formulation of the kinematic relations where displacements of the DEs at the transition zone are projected over shape functions of the FEs in assuming field continuity. This method is also used for multiscale simulations of cohesive granular materials (Rojek and Oñate, 2007) or of non-cohesive ones (Wellmann and Wriggers, 2012). The bridging zone has been proposed to reduce spurious wave reflections. It has been shown that, with increasing the width of the bridging domain, the spurious wave reflections reduce. Furthermore, if the Hamiltonian is defined with a nonlinear evolution of the weight parameter, it yields superior reflection reduction compared to a linear one. We refer to Rousseau et al. (2009) and Wellmann and Wriggers (2012) for more details. In static analysis, the coupling between DE and FE can also be performed without the transition zone, cf. Figure 1.22b, in which DEM particles are considered as directly slave of the FEM mesh (Azevedo and Lemos, 2006).

The previous DEM-FEM coupling strategies are classified as the "volume" couplings or the spatial couplings since the whole structures are split into subdomains, each of which is then adapted by DEM or FEM approach. The so-called "surface" couplings have been proposed as well by Nakashima and Oida (2004) and Onate and Rojek (2004) or recently, by Fakhimi (2009) and Villard et al. (2009) for dynamic analyses of geomaterials. The surface coupling techniques concern the

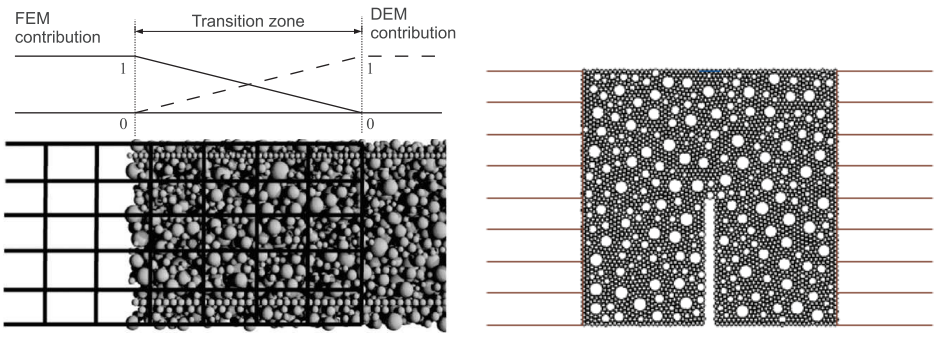

(a) Bridging domain coupling in dynamic analysis (Rousseau et al., 2009).

(b) Non-overlapping coupling in static analysis (Azevedo and Lemos, 2006).

Figure 1.22 – Two strategies applied to DEM–FEM coupling.

detection of contacts between finite elements and DEM particles. As an example of this coupling, the impact of the projectile against a thick rock plate is illustrated in Figure 1.23.

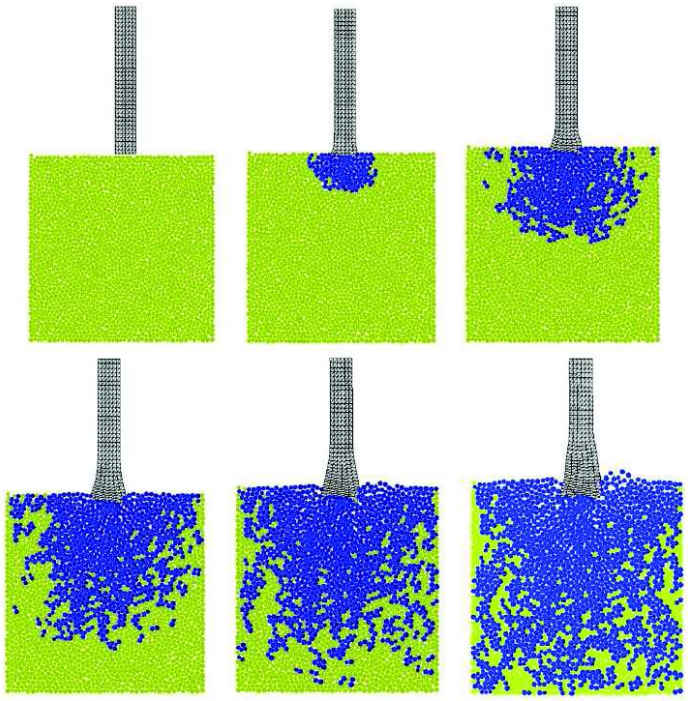

Figure 1.23 – Impact of projectile (Onate and Rojek, 2004).

Volume and surface couplings can be combined in some particular applications, e.g. the pile installation. The compacted soil under the pile tip is modeled by DEM, the pile itself modeled by FEM (here we have the surface coupling) and the rest of the soil domain simulated by FEM, see Figure 1.24.

The multiscale approach of the present work based on the LEM-FEM coupling falls in this group and shows similarities with the volume couplings. Different coupling algorithms will be pointed out in order to define a “dynamic” coupling at the crack tip where the strain localization is the most intense, see Chapter 4.

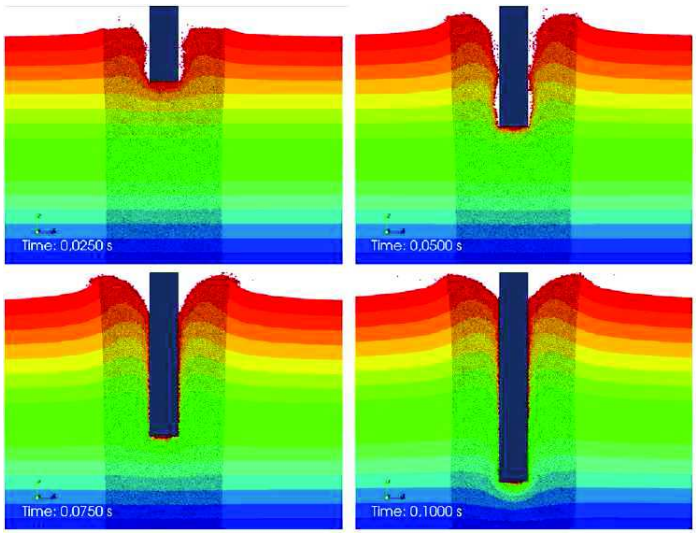

Figure 1.24 – Sample deformation during pile installation (Wellmann and Wriggers, 2012).

Chapter 2

Lattice model for concrete failure

Contents

This chapter deals with the concept of the numerical model for the simulations of crack propagation and failure of concrete-like materials in three dimensions (3D). However, when needed, the simulation can be performed in two dimensions (2D) as well. The procedure for crack propagation to simulate fracture is introduced. Moreover, the way in which the heterogeneity of the material structure is implemented is discussed. The identification of model parameters is presented before some applications of tensile tests with the post-processing treatment.

2.1 Introduction

Fracture process is a fundamental phenomenon related to cracking and failure of quasi-brittle materials (Bažant, 2003). As discussed in Chapter 1, for modeling the behavior of quasi-brittle materials at the aggregate scale, lattice models are considered as a better tool than continuum-based models. In fact, lattice models are suitable for problems in which discontinuities are dominant since they can describe a discrete nature of cracking when materials subjected to extreme loading conditions. Lattice models are simple but provide a direct insight into the fracture process and thus information of cracking such as crack opening can be extracted for durability analyses. Unlike the continuous approaches in which *many* internal parameters (sometimes with no physical meaning) have to be introduced to describe the material behaviors, lattice models can reproduce complex crack patterns and a global softening behavior within a limited number of parameters. Due to these advantages, lattice models have been widely used in fracture modeling of quasi-brittle materials (Schlangen and van Mier, 1992a, 1992b; Chiaia et al., 1997; van Mier and Vervuurt, 1997; Lilliu and van Mier, 2003).

However, lattice models exhibit mesh bias on crack propagation i.e. the direction and size of elements have an influence on the direction of the cracks. This drawback can be minimized by using a random mesh instead of a regular one and by introducing the material heterogeneities not only by incorporating the grain structure but also by assigning the random local material strength and stiffness. Moreover, the random mesostructure of the material can be better reflected by a procedure presented in Section 2.2.3.2 in which a more realistic estimate of cross-section areas is assigned to lattice elements. The second limitation of lattice models is that a big computation effort is needed when dealing with large structures. To reduce it, besides the improvements in numerical solver presented in Section 2.2.5, it seems that a coupling between the lattice model dealing with discontinuities and fracture process of the regions with nonlinear behavior and the continuum model representing the zones with elastic behavior is needed. This motivated multiscale coupling is proposed in Chapter 4 within a *dynamic* manner.

Another disadvantage of lattice models is that the response of the material is too brittle, particularly in 2D simulations, if the brittleness of single lattice elements is assumed. Nevertheless, in our studies, within the philosophy of keeping the simplicity of the model with a limited number of parameters and the complexity of macroscopic response coming from a rich geometric description of material microstructure, the brittleness assumption of lattice elements is kept holding and the ductility of global response is improved by 3D simulations and consideration of very small particles (Lilliu, 2007).

The adopted 3D lattice model is presented in details in the next section for a general purpose of three-dimensional calculations and coupling with continuum model (see Chapter 4) although most of simulations in the thesis performed on a 2D model due to a large amount of parametric studies.

2.2 The 3D lattice model

2.2.1 Concept

Lattice model is a numerical method based on a discretization of a continuum media by one-dimensional elements that can transfer loads. It depends on how many load components that an

element can carry, lattice is distinguished in different type models: normal spring, normal-shear spring, or beam model. The normal spring elements can transfer only the normal force (Meakin et al., 1989; Bažant et al., 1990; Bolander Jr. and Saito, 1998) while the normal-shear spring element can also support shear forces (Schlangen and Garboczi, 1997). The normal or normal-shear spring elements are generally called truss elements. In turn, the beam element can transfer in addition bending moment and torque. Lattice model using truss elements corresponds to a discrete Cauchy continuum whereas lattice model using beam element corresponds to a discrete Cosserat (micropolar) medium (Ieşan, 1969; Chang and Ma, 1990; Eringen, 1996; Chang et al., 2002b; Karihaloo et al., 2003) which accounts for a micro-rotation at the material scale.

The adopted lattice model used in this thesis is a beam model. However, for problems in which mode-I failure prevails, the normal-shear spring model can be used to gain in computational time since it is known that the rotational degrees of freedom and the corresponding moment transmitting in the medium do not play an important role in mode-I failure (Chang et al., 2002a).

2.2.2 Elastic formulation

The 3D beam element has two nodes, each nodes has six degrees of freedom including three translations and three rotations along three axes of local coordinate system *1-2-3* (Figure 2.1a). Each beam element can transmit axial force, shear forces, bending moments and torsional moment as shown in Figure 2.1b. Within the assumption of infinitesimal deformations, the vector of nodal displacements

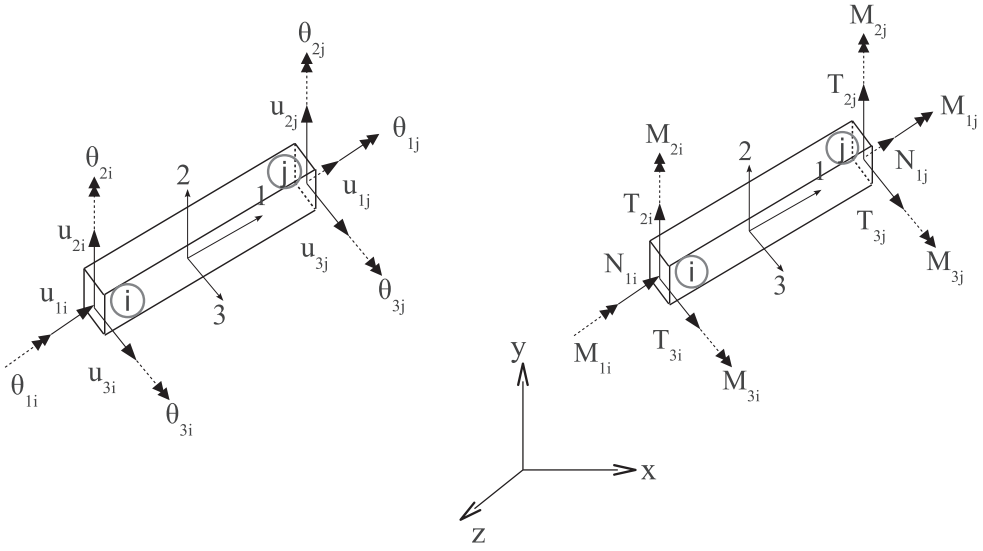

(a) (b)

Figure 2.1 – Nodal displacements (translations and rotations) (a) and nodal forces (b) on local coordinate system within a single element.

and rotations of an element are related to the vector of nodal forces and moments by the element stiffness matrix $\left[\mathbf{K}_e\right]$ as

$$\left\{\mathbf{F}_e\right\} = \left[\mathbf{K}_e\right]\left\{\mathbf{U}_e\right\} \tag{2.1}$$

The vector of nodal element forces and moments $\mathbf{F}_e$, the vector of nodal element displacements and rotations $\mathbf{U}_e$ and element stiffness matrix are then given as follows:

$$\{\mathbf{F}_e\} = \begin{Bmatrix} \mathbf{F}_i \\ \mathbf{F}_j \end{Bmatrix} \tag{2.2a}$$

$$\{\mathbf{U}_e\} = \begin{Bmatrix} \mathbf{U}_i \\ \mathbf{U}_j \end{Bmatrix} \tag{2.2b}$$

$$[\mathbf{K}_e] = \begin{bmatrix} [\mathbf{K}_{ii}] & [\mathbf{K}_{ij}] \\ [\mathbf{K}_{ji}] & [\mathbf{K}_{jj}] \end{bmatrix} \tag{2.2c}$$

so that

$$\begin{Bmatrix} \mathbf{F}_i \\ \mathbf{F}_j \end{Bmatrix} = \begin{bmatrix} [\mathbf{K}_{ii}] & [\mathbf{K}_{ij}] \\ [\mathbf{K}_{ji}] & [\mathbf{K}_{jj}] \end{bmatrix} \begin{Bmatrix} \mathbf{U}_i \\ \mathbf{U}_j \end{Bmatrix} \tag{2.3}$$

with

$$\{\mathbf{F}_i\} = \{N_{1i} \quad T_{2i} \quad T_{3i} \quad M_{1i} \quad M_{2i} \quad M_{3i}\}^T \tag{2.4}$$

$$\{\mathbf{U}_i\} = \{u_{1i} \quad u_{2i} \quad u_{3i} \quad \theta_{1i} \quad \theta_{2i} \quad \theta_{3i}\}^T \tag{2.5}$$

and identically for $\{\mathbf{F}_j\}$ and $\{\mathbf{U}_j\}$. T denotes the transpose of a matrix. The sub-matrices $[\mathbf{K}_{ii}]$, $[\mathbf{K}_{ij}]$, $[\mathbf{K}_{ji}]$ and $[\mathbf{K}_{jj}]$ are of the size 6×6. They are

$$[\mathbf{K}_{ii}] = \begin{bmatrix} \frac{EA}{l} & 0 & 0 & 0 & 0 & 0 \\ & \frac{12EI_3}{l^3} & 0 & 0 & 0 & \frac{6EI_3}{l^2} \\ & & \frac{12EI_2}{l^3} & 0 & -\frac{6EI_2}{l^2} & 0 \\ & & & \frac{GI_1}{l} & 0 & 0 \\ & \text{sym} & & & \frac{4EI_2}{l} & 0 \\ & & & & & \frac{4EI_3}{l} \end{bmatrix} \tag{2.6}$$

$$[\mathbf{K}_{ij}] = \begin{bmatrix} -\frac{EA}{l} & 0 & 0 & 0 & 0 & 0 \\ & -\frac{12EI_3}{l^3} & 0 & 0 & 0 & \frac{6EI_3}{l^2} \\ & & -\frac{12EI_2}{l^3} & 0 & -\frac{6EI_2}{l^2} & 0 \\ & & & -\frac{GI_1}{l} & 0 & 0 \\ & \text{sym} & & & \frac{2EI_2}{l} & 0 \\ & & & & & \frac{2EI_3}{l} \end{bmatrix} \tag{2.7}$$

$$[\mathbf{K}_{jj}] = \begin{bmatrix} \frac{EA}{l} & 0 & 0 & 0 & 0 & 0 \\ & \frac{12EI_3}{l^3} & 0 & 0 & 0 & -\frac{6EI_3}{l^2} \\ & & \frac{12EI_2}{l^3} & 0 & \frac{6EI_2}{l^2} & 0 \\ & & & \frac{GI_1}{l} & 0 & 0 \\ & \text{sym} & & & \frac{4EI_2}{l} & 0 \\ & & & & & \frac{4EI_3}{l} \end{bmatrix} \tag{2.8}$$

In Equations (2.6) to (2.8), E is the Young's modulus, G is the shear modulus, A is the cross-sectional area of the element, I_2, I_3 are the second moment of area about the 2-axis and 3-axis (in local coordinate system), respectively. I_1 is the polar second moment of area (with respect to the 1-axis) of the cross section of elements, l is the length of the element.

In the global coordinate system *x-y-z* (Figure 2.2), the vector of nodal displacements and rotations is related to the vector of nodal forces and moments as

$$\{\mathbf{F}_e^g\} = [\mathbf{K}_e^g]\{\mathbf{U}_e^g\} \tag{2.9}$$

where $\{\mathbf{F}_e^g\}$, $\{\mathbf{U}_e^g\}$ are the vectors of nodal forces and nodal displacements expressed in the global coordinate system *x-y-z*. $[\mathbf{K}_e^g]$ is the corresponding element stiffness matrix.

$$\{\mathbf{F}_e^g\} = [\mathbf{T}]\{\mathbf{F}_e\} \tag{2.10}$$

$$\{\mathbf{U}_e^g\} = [\mathbf{T}]\{\mathbf{U}_e\} \tag{2.11}$$

$$[\mathbf{K}_e^g] = [\mathbf{T}][\mathbf{K}_e][\mathbf{T}]^T \tag{2.12}$$

where $[\mathbf{T}]$ is the transformation matrix from the local to the global coordinate system.

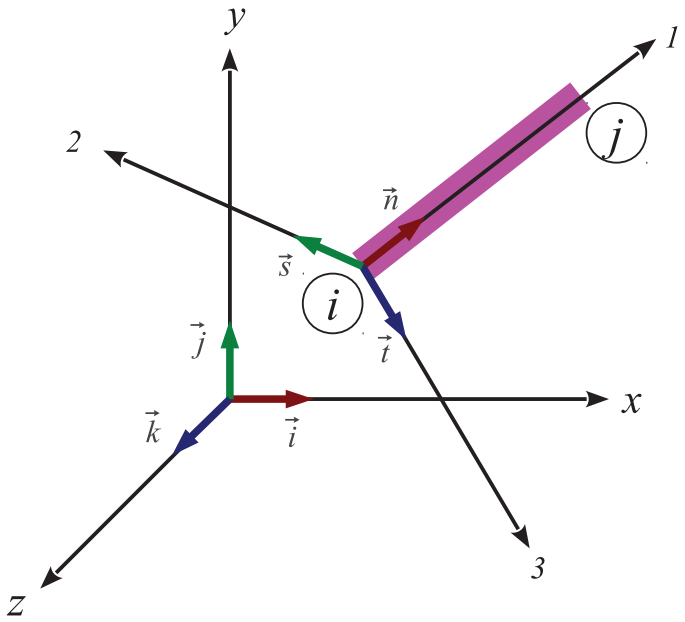

Figure 2.2 – Global and local coordinate systems.

The element ij which is attached to the local coordinate system *1-2-3* with the unit basic vectors $\vec{n}, \vec{s}, \vec{t}$ are shown in the global coordinate system in Figure 2.2. Note that the direction of $\vec{n}$ is chosen from i to j for the numerical implementation later. The choice of $\vec{s}$ and $\vec{t}$ is not unique. For the implementation, $\vec{s}$ and $\vec{t}$ are computed as follows

$$\begin{aligned} \vec{t} &= \begin{cases} \vec{i} & \text{if } \vec{n} \parallel \vec{j} \\ \vec{n} \times \vec{j} & \text{otherwise} \end{cases} \\ \vec{s} &= \vec{t} \times \vec{n} \end{aligned} \tag{2.13}$$

with $\vec{i}$ and $\vec{j}$ the unit vectors of x- and y-axis, respectively. The relationship between the two, global and local, coordinate systems is characterized by the transformation matrix $[\mathbf{T}]$ which is in the size of 12×12 and in the form of

$$[\mathbf{T}] = \begin{bmatrix} [\mathbf{t}] & & & \\ & [\mathbf{t}] & & \\ & & [\mathbf{t}] & \\ & & & [\mathbf{t}] \end{bmatrix} \tag{2.14}$$

in which the sub-matrix $[\mathbf{t}]$ having the size of 3×3 is given by

$$[\mathbf{t}] = \begin{bmatrix} \cos\alpha_n & \cos\alpha_s & \cos\alpha_t \\ \cos\beta_n & \cos\beta_s & \cos\beta_t \\ \cos\gamma_n & \cos\gamma_s & \cos\gamma_t \end{bmatrix} \tag{2.15}$$

where nine direction cosines are defined. These direction cosines are the cosines of the angles between the unit basic vectors $\vec{n}, \vec{s}, \vec{t}$ and the three unit basic vectors $\vec{i}, \vec{j}, \vec{k}$ of the global coordinate system.

In principle, a beam element can be schematically represented by three types of spring which are used to describe the stiffness between two particles, namely, a normal spring with normal stiffness K_n, a shear spring with shear stiffness K_s and a rotational spring with rotational stiffness K_w that includes the twisting stiffness K_t and the bending stiffness K_b (see Figure 2.3).

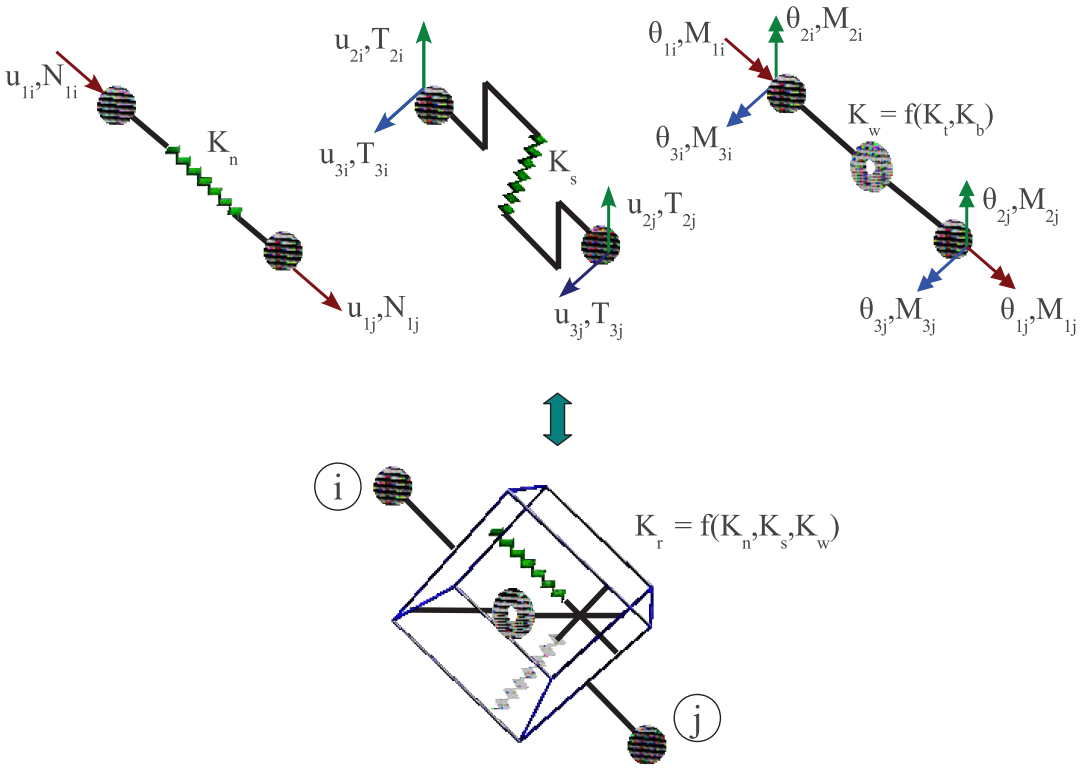

Figure 2.3 – Three types of spring: normal, shear and rotational spring. The bottom figure represents the three springs.

The relationship between the nodal kinematic and static vectors of the three springs is exactly the same as equation (2.3) in which the sub-matrices of stiffness $[\mathbf{K}_{ii}]$, $[\mathbf{K}_{ij}]$, $[\mathbf{K}_{jj}]$ are given by

$$[\mathbf{K}_{ii}] = \begin{bmatrix} K_n & 0 & 0 & 0 & 0 & 0 \\ & K_s & 0 & 0 & 0 & \frac{K_s l}{2} \\ & & K_s & 0 & -\frac{K_s l}{2} & 0 \\ & & & K_t & 0 & 0 \\ & \text{sym} & & & \frac{K_s l^2}{4} + K_b & 0 \\ & & & & & \frac{K_s l^2}{4} + K_b \end{bmatrix} \tag{2.16}$$

$$[\mathbf{K}_{ij}] = \begin{bmatrix} -K_n & 0 & 0 & 0 & 0 & 0 \\ & -K_s & 0 & 0 & 0 & \frac{K_s l}{2} \\ & & -K_s & 0 & -\frac{K_s l}{2} & 0 \\ & & & -K_t & 0 & 0 \\ & \text{sym} & & & \frac{K_s l^2}{4} - K_b & 0 \\ & & & & & \frac{K_s l^2}{4} - K_b \end{bmatrix} \tag{2.17}$$

$$[\mathbf{K}_{jj}] = \begin{bmatrix} K_n & 0 & 0 & 0 & 0 & 0 \\ & K_s & 0 & 0 & 0 & -\frac{K_s l}{2} \\ & & K_s & 0 & \frac{K_s l}{2} & 0 \\ & & & K_t & 0 & 0 \\ & \text{sym} & & & \frac{K_s l^2}{4} + K_b & 0 \\ & & & & & \frac{K_s l^2}{4} + K_b \end{bmatrix} \tag{2.18}$$

It is noticed that the Equations (2.6) to (2.8) and the Equations (2.16) to (2.18) are identical if the following relationships hold true:

$$\begin{aligned} K_n &= \frac{EA}{l} \\ K_s &= \frac{12EI}{l^3} \\ K_t &= \frac{GI_1}{l} \\ K_b &= \frac{EI}{l} \end{aligned} \tag{2.19}$$

in which $I = I_2 = I_3$ in the case of circular cross section. This means that by selecting appropriate spring stiffnesses, the behavior of a lattice network of beams can be identically represented by a network of springs with four types of stiffness K_n, K_s, K_t and K_b. This facilitates the comprehension in which the particle rotation and moment transmission is neglected and the medium is represented by a normal-shear spring network with only two stiffnesses K_n and K_s.

Since the units of nodal forces and of nodal moments are different, the global stiffness matrix of lattice network $\left[\mathbf{K}^g\right]$ may contain a big gap (in magnitude) between the largest of the $K_{ij}^g{}'s$ and the smallest of the $K_{ij}^g{}'s$, and possibly leading to the situation where the matrix could be *ill-conditioned*. To improve the accuracy of the resolution method which will be described in the following paragraph and speed up the solving process, all terms of the stiffness matrix $\left[\mathbf{K}^g\right]$ related to nodal moments and the corresponding nodal rotations should be normalized by a quantity $\langle l \rangle$ which is the arithmetic mean of length of the lattice elements of the analyzed domain. The vectors of nodal statics and kinematics at node i is now given by

$$\left\{\mathbf{F}_i\right\} = \left\{N_{1i} \quad T_{2i} \quad T_{3i} \quad \frac{M_{1i}}{\langle l \rangle} \quad \frac{M_{2i}}{\langle l \rangle} \quad \frac{M_{3i}}{\langle l \rangle}\right\}^T \tag{2.20}$$

$$\left\{\mathbf{U}_i\right\} = \left\{u_{1i} \quad u_{2i} \quad u_{3i} \quad \theta_{1i}\langle l \rangle \quad \theta_{2i}\langle l \rangle \quad \theta_{3i}\langle l \rangle\right\}^T \tag{2.21}$$

and the sub-matrices of stiffness become

$$[\mathbf{K}_{ii}] = \begin{bmatrix} K_n & 0 & 0 & 0 & 0 & 0 \\ & K_s & 0 & 0 & 0 & \frac{K_s l}{2\langle l \rangle} \\ & & K_s & 0 & -\frac{K_s l}{2\langle l \rangle} & 0 \\ & & & \frac{K_t}{\langle l \rangle^2} & 0 & 0 \\ & \text{sym} & & & \frac{K_s l^2}{4\langle l \rangle^2} + \frac{K_b}{\langle l \rangle^2} & 0 \\ & & & & & \frac{K_s l^2}{4\langle l \rangle^2} + \frac{K_b}{\langle l \rangle^2} \end{bmatrix} \tag{2.22}$$

$$[\mathbf{K}_{ij}] = \begin{bmatrix} -K_n & 0 & 0 & 0 & 0 & 0 \\ & -K_s & 0 & 0 & 0 & \frac{K_s l}{2\langle l\rangle} \\ & & -K_s & 0 & -\frac{K_s l}{2\langle l\rangle} & 0 \\ & & & -\frac{K_t}{\langle l\rangle^2} & 0 & 0 \\ & \text{sym} & & & \frac{K_s l^2}{4\langle l\rangle^2} - \frac{K_b}{\langle l\rangle^2} & 0 \\ & & & & & \frac{K_s l^2}{4\langle l\rangle^2} - \frac{K_b}{\langle l\rangle^2} \end{bmatrix} \tag{2.23}$$

$$[\mathbf{K}_{jj}] = \begin{bmatrix} K_n & 0 & 0 & 0 & 0 & 0 \\ & K_s & 0 & 0 & 0 & -\frac{K_s l}{2\langle l\rangle} \\ & & K_s & 0 & \frac{K_s l}{2\langle l\rangle} & 0 \\ & & & \frac{K_t}{\langle l\rangle^2} & 0 & 0 \\ & \text{sym} & & & \frac{K_s l^2}{4\langle l\rangle^2} + \frac{K_b}{\langle l\rangle^2} & 0 \\ & & & & & \frac{K_s l^2}{4\langle l\rangle^2} + \frac{K_b}{\langle l\rangle^2} \end{bmatrix} \tag{2.24}$$

The beam lattice model corresponds to the discrete representation of micro-polar continuum. However, it is desirable to use the non-polar (the normal-shear spring lattice) model because of some reasons:

- Many of damage/fracture models presented in the literature have been based on the classical continuum. So the non-polar provides a direct comparison to these models.
- Degrees of freedom of non-polar model are twice less than those of polar one. Therefore, using non-polar model in the appropriate cases can strongly save computational cost.
- It is also interesting to know how much difference there is between the polar and the non-polar models. It provides an understanding on the effect of moment transfer in the system.

By neglecting all variables associated with rotations (i.e., the components $\{M_{1k} \quad M_{2k} \quad M_{3k}\}$ of the nodal vector of statics and the corresponding components $\{\theta_{1k} \quad \theta_{2k} \quad \theta_{3k}\}$, $k = i, j$ of the nodal vector of kinematics) of the beam lattice model, the normal-shear spring lattice model can be defined by only two stiffness constants, normal stiffness K_n and shear stiffness K_s. If we define two parameters E_n and E_s the normal and shear moduli of each element, K_n and K_s can be expressed as

$$K_n = \frac{E_n A}{l}, \quad K_s = \frac{E_s A}{l} \tag{2.25}$$

where A and l can be generated from the mesh, two elastic parameters of the normal-shear spring lattice model are E_n and E_s.

2.2.3 Lattice geometry

2.2.3.1 Mesh generation

The random lattice network is used because it was found to better simulate the fracture process of concrete. In fact, the random lattice can reduce the influence of the mesh alignment on the crack patterns (Jirásek and Bazant, 1995; Schlangen and Garboczi, 1996). Moreover, the triangular lattice is found to better simulate the heterogeneous structure of the material than the rectangular one (Arslan et al., 2002). The lattice elements are obtained from the edges of the simplices of the Delaunay triangulation. In two dimensions the simplices of Delaunay triangulation are triangles, in three dimensions they are tetrahedra, see Figure 2.4.

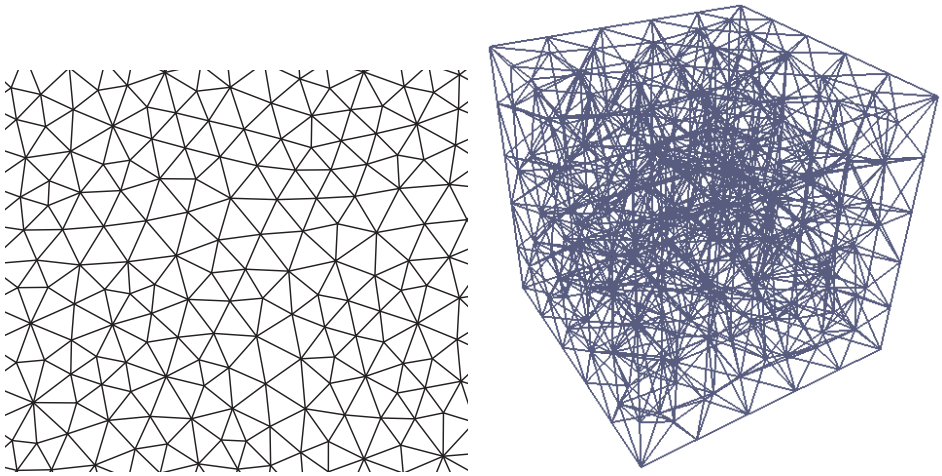

(a) (b)

Figure 2.4 – 2D random triangular lattice (a); and 3D random tetrahedron lattice (b).

Despite the fact that a random lattice obtained from Delaunay triangulation is employed, some privileged orientations can be found because of the specimen boundaries for which the elements are more or less orthogonal (see Figure 2.5). Figure 2.5b shows the orientation angles of the elements compared with the horizontal axis. It is seen that the horizontal and vertical elements dominate due to boundary effects and make the specimen less isotropic. Isotropy, in this sense, is characterized by a homogeneous distribution of a large enough number of lattice elements with respect to their orientation. To obtain a more isotropic mesh, one can define circles (or spheres in 3D case) whose

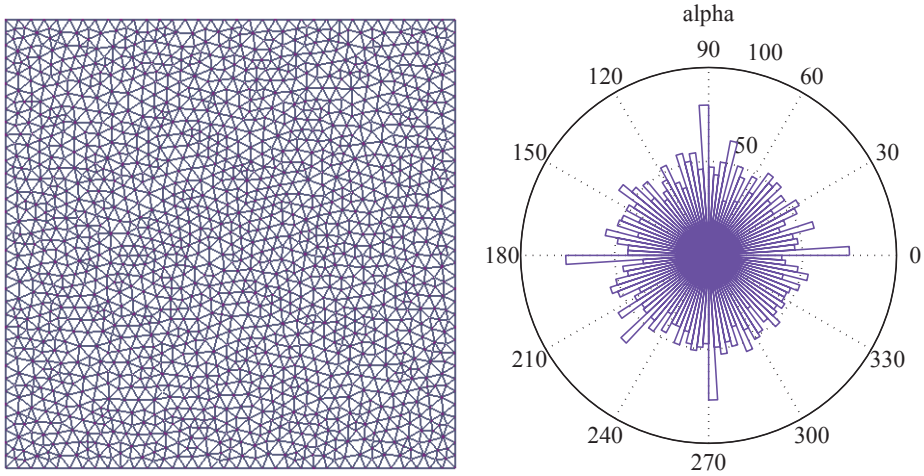

(a) (b)

Figure 2.5 – Delaunay triangulation mesh (a); and distribution of element orientations (b).

centers are the nodes themselves and whose diameters are $l_{\min}$ which is the minimum length of lattice elements. $l_{\min}$ is chosen to avoid overlapped circles/spheres. Each node can be now moved randomly (see Figure 2.6). Numerically, this can be done by adding to the position of the nodes a displacement vector $\Delta\mathbf{p}$ defined by

$$\Delta\mathbf{p} = (r \sin\theta \cos\phi, r \sin\theta \sin\phi, r \cos\theta) \tag{2.26}$$

in which r is an uniformly random number generated between 0 and $l_{\min}$, θ and ϕ are two uniformly random angles generated between 0 and 2π. In two dimensions, $\Delta\mathbf{p}$ reduces to

$$\Delta\mathbf{p} = (r \cos\phi, r \sin\phi) \tag{2.27}$$

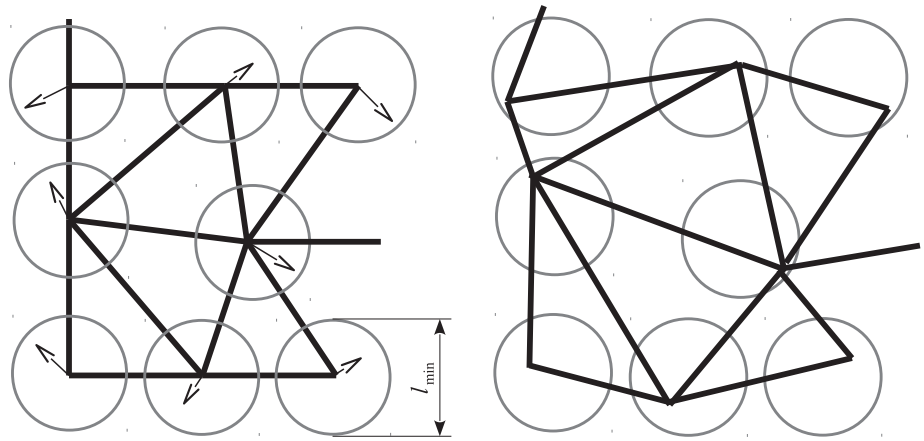

(a) (b)

Figure 2.6 – Random moving nodes (a); and more isotropic mesh obtained (b).

By applying this method, the more isotropic mesh comparing to the mesh in Figure 2.5 can be obtained (see Figure 2.7).

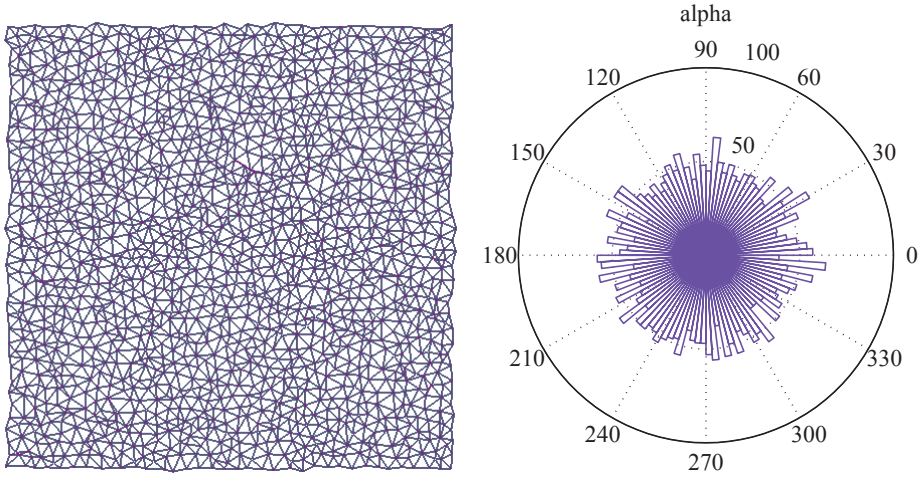

(a) (b)

Figure 2.7 – More isotropic mesh (a); and distribution of element orientations (b).

It should be noted that when applying this procedure on specimen boundaries, it reduces the mesh alignment on the boundaries and makes sense for problems of crack initiation in which the structural geometry is positive, i.e., without notches, even though one loses the straightness of the boundaries. One can also use this procedure to generate a random lattice from the regular one.

Figure 2.8 shows the distribution of the lattice element length of the mesh shown in Figure 2.7a. By fitting the distribution with the probability density function (pdf) of a Gaussian distribution, one gets the mean value and the standard deviation of the lattice element length which are 2.72 mm and 0.6 mm, respectively. It is seen that the random aspect of the mesh is assured, here the element length l, and thus the elastic parameters K_n, K_s, etc.

2.2.3.2 Mesh properties

A cross-sectional area needs to be assigned to each lattice element generated from a mesh (generated by the Delaunay triangulation). This can be done by using a dual graph of the Delaunay triangulation. A well known dual graph of the Delaunay triangulation is the Voronoi tessellation

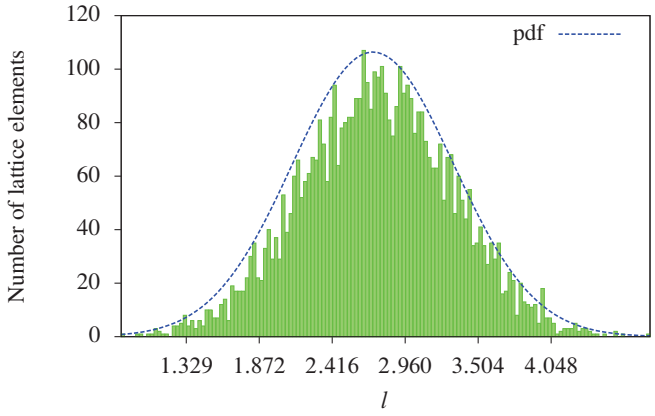

Figure 2.8 – Distribution of lattice element length.

(see Figure 2.9). However, a vertice of Voronoi tessellation which corresponds to a simplex of Delaunay triangulation (triangle in 2D and tetrahedron in 3D) can lie outside the latter itself, e.g., the vertices 2 and 4 in Figure 2.9. Thus, in order to better estimate the geometrical heterogeneity due to the random mesh, a new tessellation is adopted based on the one of Cusatis et al. (2006) except that the particle diameters are zero for our lattice model. It is exemplified in Figure 2.10a for two dimensions and in Figure 2.10b for three dimensions.

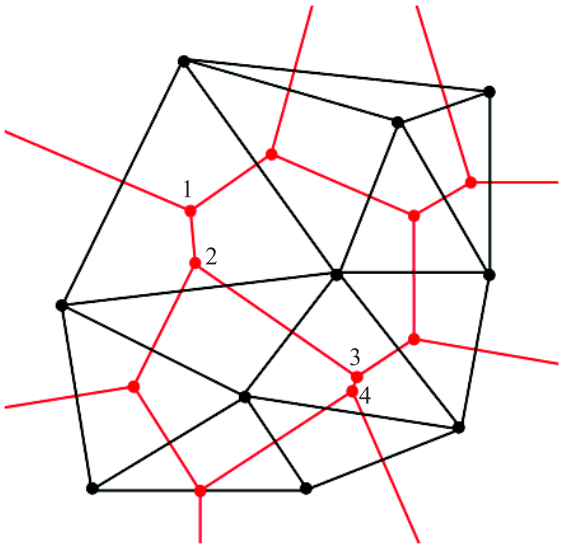

Figure 2.9 – Delaunay triangulation on top of Voronoi tessellation (in red lines).

Let us consider two-dimensional case first. Figure 2.10a shows the element P_1P_3 shared by two adjacent triangles $P_1P_2P_3$ and $P_1P_3P_4$ of the Delaunay triangulation. The definition of the sectional line (or, in 3D case, sectional area) of this element is obtained by connecting the points M_{13}, G_{123} and G_{134}. M_{13} is the midpoint of this element P_1P_3. Points G_{123} and G_{134} are the centroids of the triangles $P_1P_2P_3$ and $P_1P_3P_4$, respectively. Once having the sectional line, it is possible to define the cross-sectional area of the element by projecting this sectional line onto the line being perpendicular to the element. Finally, the cross-section of the element which is assumed to be rectangular, may be expressed as

$$A = b \times t \tag{2.28}$$

where $b = G_{123}M'_{13} + G_{134}M''_{13}$ is the height of the cross-section (bold solid lines in Figure 2.10) and t is the out-of-plane thickness (which can be assigned equal to unity or the specimen thickness).

We may note that the area associated with each lattice node can also be determined as follows:

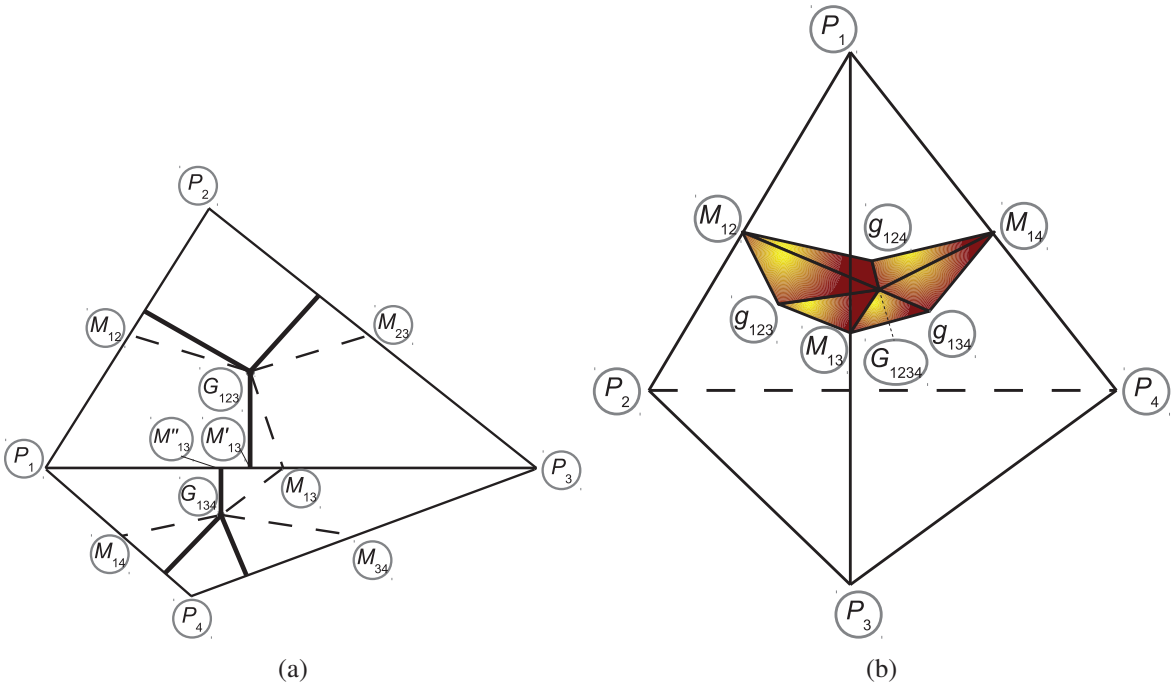

Figure 2.10 – Definition of characteristic points of the tessellation in 2D (a) and 3D (b).

- The area of each triangle is apportioned to its vertices using the centroid and three midpoints of three sides. For example, the area formed from the polygon $P_1M_{12}G_{123}M_{13}$ is associated to the lattice node P_1 (the dashed lines in Figure 2.10a).

- The total area associated to each lattice node is obtained by summing up the contributions of all the adjacent triangles.

This procedure is applied to any of triangles from Delaunay triangulation, so each lattice element is assigned a cross-sectional area, each lattice node is associated with one and only one cell, whose area is well known.

Extension to three dimensional case is quite straightforward. Figure 2.10b shows a tetrahedron $P_1P_2P_3P_4$ of the Delaunay triangulation in three dimensions. The sectional areas belonging to elements P_1P_2, P_1P_3, P_1P_4 (the ones belonging to elements P_2P_3, P_3P_4 and P_2P_4 can also be defined, but for the sake of clarity, they are not shown) are defined from the characteristic points G_{1234}, g_{123}, g_{124}, g_{134}, M_{12}, M_{13}, M_{14}. These points are defined in the same way as those defined in two-dimensional case, i.e., they are the midpoints and the centroids of corresponding objects. Point G_{1234} is the centroid of the tetrahedron. Points g_{ijk} $(i,j,k = 1,\ldots,4; i < j < k)$ are the centroids of triangular faces of the tetrahedron. Points M_{ij} $(i,j = 1,\ldots,4; i < j)$ are the midpoints of the edge P_iP_j of the tetrahedron. This procedure of tessellation is applied to any of tetrahedra from Delaunay triangulation so that each lattice element possesses a sectional area as shown in Figure 2.11a. In general, the sectional area S is not planar and not orthogonal to the lattice element. Therefore, the cross-sectional area of the element can be computed as follows. First, one projects S on the plane, which contains the midpoint M of the tessellation, orthogonal to the element (Figure 2.11b). Then the equivalent diameter D_s of the projected area S_p is defined (see Figure 2.11c), given by

$$D_s = 2\sqrt{\frac{S_p}{\pi}} \tag{2.29}$$

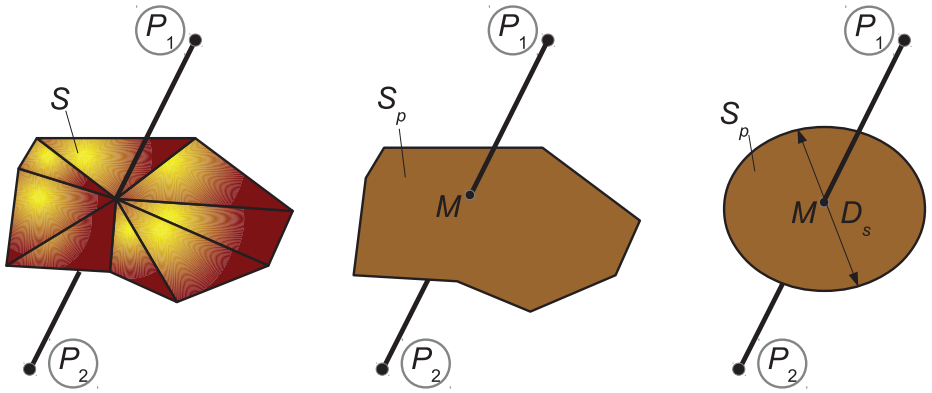

(a) (b) (c)

Figure 2.11 – Section area of lattice element (a); projected sectional area (b); and equivalent circular sectional area (c).

The cross-section of the lattice element in three dimensional case is considered as circular with the area is simply computed by

$$A = \frac{\pi D_s^2}{4} \tag{2.30}$$

2.2.3.3 Element size adaptation

The question raised here is that how to determine the lattice element size when using the lattice model. One can get the answer when responding two questions: (i) can the lattice model reproduce the isotropy of an homogenized material, if so is there the effect of the lattice element sizes on the isotropy of the modeled material?, and (ii) how detail of the aggregate structure that we want to introduce in the model? The element size can be deduced by the minimum of the sizes determined by answering these two questions.

Element size determined from isotropy requirement The lattice approach should be able to model the linear elastic behavior of a macroscopically isotropic homogenized material. If so, it should guarantee the isotropy of the material, i.e., the material behavior is not affected by the loading directions. One can choose the global elastic properties such as Young's modulus and Poisson's ratio computed under different loading directions to verify whether the lattice model can provide an isotropic response of the material. Furthermore, different discretizations (the different element sizes) of the lattice can also affect the global elastic properties of the material.

To verify whether the response of the lattice model is isotropic and to study the influence of the element sizes on that isotropy, the Young's modulus and Poisson's ratio are computed from the uniaxial tensile tests loaded in x and in y direction with different relative discretization size B/l_{m}, see Figure 2.12. B stands for the specimen size and l_{m} is the mean length of the lattice elements. The input parameters for the elastic analysis are taken from Table 2.1. Moreover, for each discretization with l_{m}, the nodes of the mesh are randomly moved by the procedure described in Section 2.2.3.1 (except the boundary nodes) to avoid some possible privileged orientations of the elements and then the average value $\bar{l}_{\mathrm{m}}$ of l_{m} is also computed. The average response of each discretization is then computed with the corresponding standard deviation. Young's modulus and Poisson's ratio in y

Table 2.1 – Input parameters.

$B = H$ [mm]	E_n [GPa]	E_s [GPa]
100	37.66	12.55

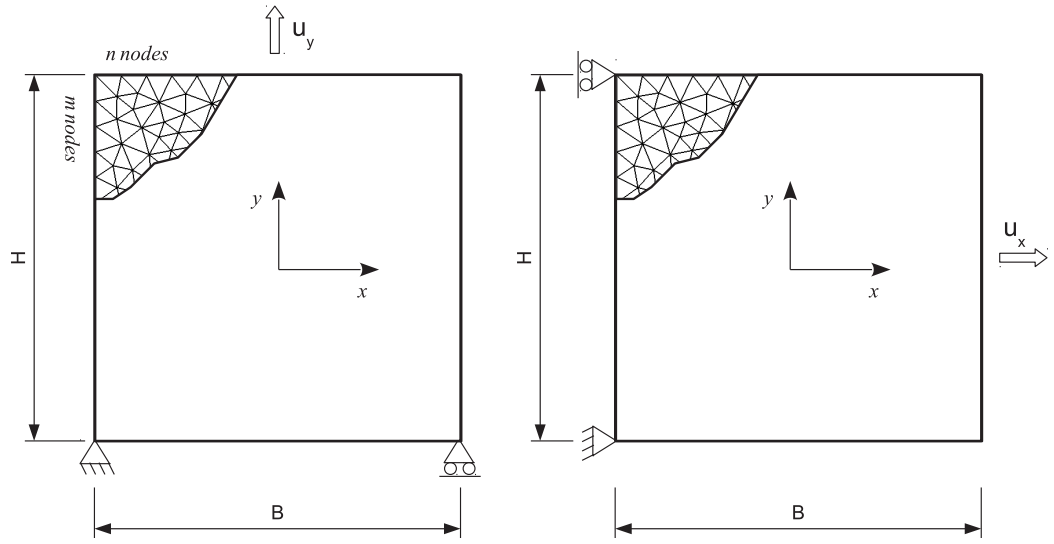

Figure 2.12 – Uniaxial tensile test loaded in y direction (a) and x direction (b).

and x directions are calculated as

$$E_y = \frac{\sigma_y}{\varepsilon_y} = \frac{\sum_{i=1}^{n} F_{i,y}}{Bt}\frac{H}{u_y}, \qquad \nu_x = -\frac{\varepsilon_x}{\varepsilon_y} = -\frac{\sum_{j=1}^{m} \delta u_{j,x}}{mB}\frac{H}{u_y} \tag{2.31a}$$

$$E_x = \frac{\sigma_x}{\varepsilon_x} = \frac{\sum_{j=1}^{m} F_{j,x}}{Ht}\frac{B}{u_x}, \qquad \nu_y = -\frac{\varepsilon_y}{\varepsilon_x} = -\frac{\sum_{i=1}^{n} \delta u_{i,y}}{nH}\frac{B}{u_x} \tag{2.31b}$$

in which $F_{i,y}$, $F_{j,x}$ are the reaction forces of nodes i and j in y and x direction of the boundaries, respectively; $\delta u_{j,x}$, $\delta u_{i,y}$ are the corresponding displacements; t is the thickness of the specimen.

The more the ratio E_x/E_y or ν_x/ν_y differs from 1 the more anisotropic the material will be. Thus these ratios are called the degree of anisotropy. Figure 2.13 shows the relation between the degree of anisotropy for the elastic properties and the relative discretization size $B/\bar{l}_{\mathrm{m}}$. The main observation is that with respect to Young's modulus the lattice can be considered quasi-isotropic. For the Poisson's ratio, directional differences are important when the relative size $B/\bar{l}_{\mathrm{m}}$ is small. When $B/\bar{l}_{\mathrm{m}} \geq 40$, the lattice can be considered again quasi-isotropic. In addition, when $B/\bar{l}_{\mathrm{m}} < 40$, the elastic properties are very sensitive for changes in element orientations obtained by randomly moving the nodes. The bigger the value of $B/\bar{l}_{\mathrm{m}}$ the smaller the value of the standard deviations. All of these observations can probably be explained by the boundary effects to lattices with finite dimensions. In fact, the larger the value of $B/\bar{l}_{\mathrm{m}}$ the greater the number of lattice elements will be and thus the effects of the boundaries are less important to the inner nodes. Moreover, the orientations of the elements become dominant when there are less elements in the lattices and this obviously makes the directional differences in the elastic properties.

The conclusion is that the isotropy of the lattice can be obtained if the discretization is fine enough. Giving the *characteristic* size B of a specimen to be modeled, the mean size of the lattice elements is determined as

$$l_{\mathrm{m}} \leq \frac{B}{40} \tag{2.32}$$

Element size determined from the minimum aggregate size It is worth mentioning that the relative ratio between the minimum particle size $d_{\min}$ and the average length l_{m} of lattice elements

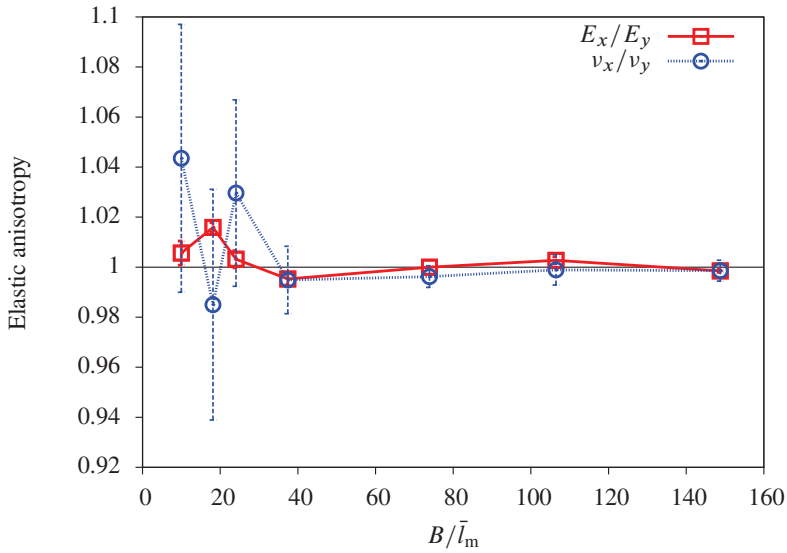

Figure 2.13 – Ratios E_x/E_y and ν_x/ν_y for different relative sizes $B/\bar{l}_m$ of the lattice discretization.

plays an important role in modeling the aggregate structure of the material. In Figure 2.14 a generated aggregate structure is projected on the lattice of different element lengths. Here only two material phases are distinguished, the aggregate and matrix phases. As shown the detail of the model is affected by the element length. The finest aggregates can only captured if the lattice element size is small enough. Thus the richer model is obtained (Figure 2.14c compared to Figure 2.14b) with the lower element size ($l_m = 0.6mm$ (Figure 2.14c) compared to $l_m = 4mm$ (Figure 2.14b)). However, the number of elements rapidly increases (the total number of elements $n_e = 78975$ (Figure 2.14c) compared to $n_e = 2134$ (Figure 2.14b)) which results in the tremendous computational time. Consequently, the balance between detail and computational time should be analyzed attentively.

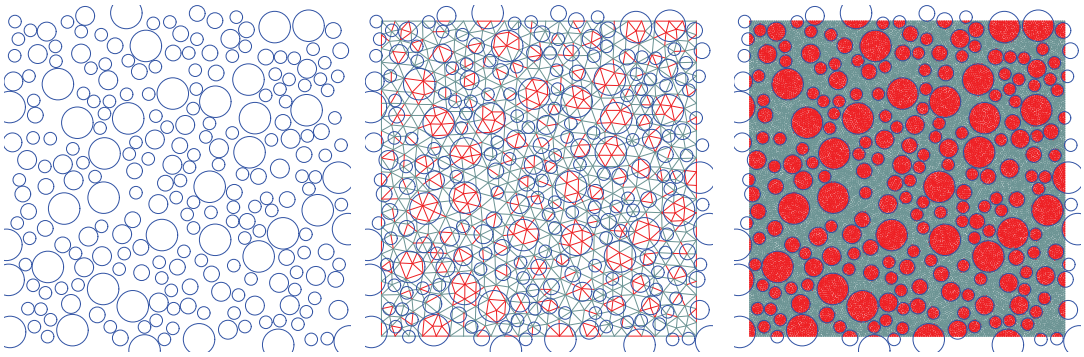

Figure 2.14 – (a) Generated grain structure of concrete with $4 \leq d \leq 10$ mm and grain density = 0.5; (b) a coarse ($l_m = 4$ mm); and (c) a fine ($l_m = 0.6$ mm) lattice overlay.

One question that one should answer when using the lattice model is that how small the size of the finest particles which are of interest to be directly introduced in the model. Once having the answer, an aggregate grading with the particle sizes from d_{min} to d_{max} could be known for generating the aggregate structure mapped into lattice discretizations. From that, the maximum mean length of the lattice elements can be determined by the empirical relation

$$l_m \leq \frac{d_{min}}{3} \tag{2.33}$$

so that there are always a large enough number of lattice elements within the finest aggregate d_{min}

but the total number of degrees of freedom is still limited.

2.2.4 Crack growth procedure

2.2.4.1 Fracture criteria and elimination algorithm

Fracture criteria A breaking rule has to be defined to simulate fracture. Many fracture criteria can be found in the literature (Herrmann et al., 1989; Pompe et al., 1991; Schlangen and Garboczi, 1997; Arslan et al., 2002; D'Addetta et al., 2002). The choice of fracture criterion depends on the type of lattice element in the model (e.g. axial spring elements, normal-shear spring elements or beam elements). The idea is that an element will be broken when some quantity of it, for example tensile stress, tensile strain or elastic energy is exceeded the predefined threshold in that element. In heterogeneous cohesive frictional materials such as concrete, the fracture process is caused by tensile failure (D'Addetta et al., 2002). Therefore, the fracture occurs solely in the case of elongation of the elements representing the meso-scale of that kind of material.

Several fracture laws have been implemented in the calculation code. It is worth first of all noting that the torque of lattice elements under mode-I failure is generally small and is not introduced in failure criteria. The classical failure criterion is the Mohr-Coulomb criterion describing the response of materials such as rock or concrete to shear stress as well as normal stress. Because concrete has a very low tensile strength as compared with their compressive strength and shear strength, the Mohr-Coulomb surface with tension cut-off (Bolander Jr. and Saito, 1998) is adopted. The criterion can be expressed by the following two inequations

$$P_{ij}(\sigma_n, \sigma_s) = \begin{cases} \frac{\sigma_n}{\sigma_{s0}/\tan\varphi} + \frac{|\sigma_s|}{\sigma_{s0}} \geq 1 \\ \frac{\sigma_n}{\sigma_{n0}} \geq 1 \end{cases} \tag{2.34}$$

where $\sigma_n = \frac{f_n}{A}$ and $\sigma_s = \frac{f_s}{A}$ are the normal and shear stresses, respectively; A is the cross-section area of elements. σ_n is related to the threshold value of the normal stress σ_{n0}, while σ_s is related to the threshold value of the shear stress σ_{s0}. φ is the friction angle. The element breakage is controlled by three parameters, σ_{n0}, σ_{s0} and φ as shown in Figure 2.15a. The axial force f_n and shear force f_s are given by

$$f_n = -N_{1i} = N_{1j} = K_n \delta_n \tag{2.35a}$$

$$f_s = \sqrt{T_{2i}^2 + T_{3i}^2} = \sqrt{T_{2j}^2 + T_{3j}^2} \tag{2.35b}$$

where, $\delta_n = u_{1j} - u_{1i}$ is the axial elongation; T_{2j}, T_{3j} (idem for T_{2i}, T_{3i}) are given by

$$T_{2j} = K_s(\delta_{s_2} - l\mu_{\omega_3}) \tag{2.36a}$$

$$T_{3j} = K_s(\delta_{s_3} + l\mu_{\omega_2}) \tag{2.36b}$$

where, $\delta_{s_2} = u_{2j} - u_{2i}$, $\delta_{s_3} = u_{3j} - u_{3i}$ are the relative shear displacements about 2-axis and 3-axis, respectively; $\mu_{\omega_2} = \frac{\theta_{2i}+\theta_{2j}}{2}$; $\mu_{\omega_3} = \frac{\theta_{3i}+\theta_{3j}}{2}$ are the averaged angular rotations about 2-axis and 3-axis, respectively.

Derived from Mohr-Coulomb criterion, one can also use the fracture criterion, namely, the general fracture law which is expressed in the form

$$P_{ij}(\sigma_n, \sigma_s) = \frac{\sigma_n}{\sigma_{n0}} + \left(\frac{|\sigma_s|}{\sigma_{s0}}\right)^n \geq 1 \tag{2.37}$$

in which the power parameter $n \geq 1$ representing how much the influence of shear stress is taken into account. The bigger the value of n the smaller the influence of shear stress. Depending on the value of n, the failure surface is varied from the linear form ($n = 1$) corresponding to the classical

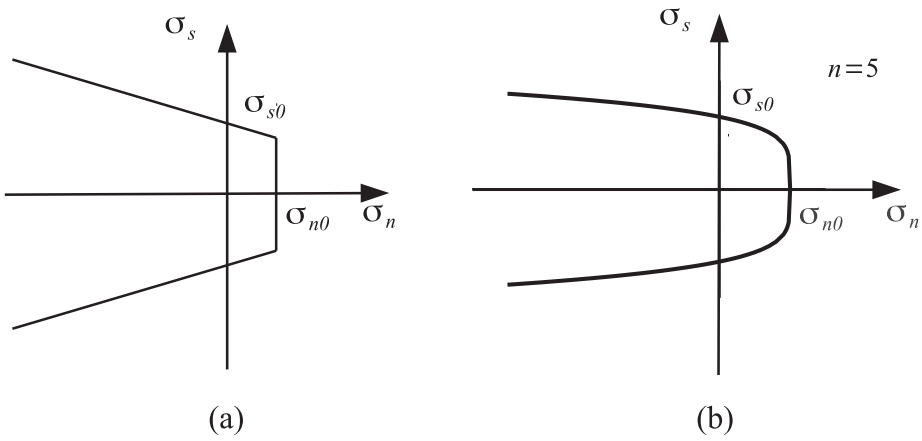

Figure 2.15 – Mohr-Coulomb strength surface with tension cut-off (a), general strength surface with $n = 5$ (b).

Mohr-Coulomb law to the nonlinear form ($n > 1$). Figure 2.15b shows the failure surface with $n = 5$.

The criterion that is used for the simulations later in the thesis will be mentioned after studying the influence of the fracture criteria on the failure of the material, detailed in Section 2.2.4.2.

Elimination algorithm At each time step, the elements that fulfill the condition $P_{ij} \geq 1$ are removed from the simulation. This means that the behavior of the elements is brittle elastic. It is possible to remove more than one element within each time step. However, if more than one element are removed during one time step, non-physical results can be obtained and the mechanical response depends on the loading magnitude (Delaplace, 2008). Therefore, in order to avoid those drawbacks, a solving procedure called elastic prediction algorithm (Delaplace and Desmorat, 2007) is preferred. Just one element is removed from the lattice network during one step. So, a unique response of the system can be obtained. The algorithm is described as follows. At each time step, an infinitesimal loading is applied. The meaning of infinitesimal loading is that no lattice element breaks under this loading. Afterward, a constant α is determined such that one would just break the element that has stress state being the closest to the strength surface. That means that the element ij is looked for, for which the coefficient α that satisfies the equality

$$P_{ij}(\alpha\sigma_n, \alpha\sigma_s) = 1 \tag{2.38}$$

is the smallest. If the Mohr-Coulomb law with tension cut-off is employed (Equation (2.34)), (2.38) implies

$$P_{ij}(\alpha\sigma_n, \alpha\sigma_s) = \alpha \cdot \max\left(\frac{\sigma_n}{\sigma_{s0}/\tan\varphi} + \frac{|\sigma_s|}{\sigma_{s0}}, \frac{\sigma_n}{\sigma_{n0}}\right) = 1 \tag{2.39}$$

or if the general fracture law is used (Equation (2.37)), Equation (2.38) implies

$$P_{ij}(\alpha\sigma_n, \alpha\sigma_s) = \frac{\sigma_n\alpha}{\sigma_{n0}} + \left(\frac{|\sigma_s|\alpha}{\sigma_{s0}}\right)^n = 1 \tag{2.40}$$

In other words, under the infinitesimal loading, we calculate for each lattice element ij the constant α

$$\alpha = \frac{1}{\max\left(\frac{\sigma_n}{\sigma_{s0}/\tan\varphi} + \frac{|\sigma_s|}{\sigma_{s0}}, \frac{\sigma_n}{\sigma_{n0}}\right)} \tag{2.41}$$

or α satisfying Equation (2.40) which is solved numerically by using a combination of Newton-Raphson and bisection algorithms (Press et al., 2007). The element that has the smallest value of

α (the so-called $\alpha_{\min}$) is removed from the lattice model. Before removing the element having $\alpha_{\min}$ from the lattice network, the displacement and force fields of all elements are recomputed due to the homothety with the factor $\alpha_{\min}$ as

$$\begin{array}{rcl} f_n & \mapsto & \alpha_{\min} f_n \\ f_s & \mapsto & \alpha_{\min} f_s \\ \delta_n & \mapsto & \alpha_{\min} \delta_n \\ \delta_{s_2} & \mapsto & \alpha_{\min} \delta_{s_2} \\ \delta_{s_3} & \mapsto & \alpha_{\min} \delta_{s_3} \end{array} \tag{2.42}$$

Those updated values are stored for the post-process analysis. After removing one element the system is relaxed again. The procedure is repeated in order to determine the next element that will break. The system stiffness gradually decreases after removing elements in a sequence at each time step. Parallel to this stiffness degradation, the micro and then macro cracks develop. When the last element connecting two parts of the system, separated by the macro crack, breaks, the system falls apart and the breaking procedure is stopped. The total number of elements that had to be broken to attain this state is called n_r. After this state all α would normally be infinite. Accordingly, the stopping of breaking procedure may be controlled by a predefined constant α_{cr}. The computation is hold off as long as the condition in equation (2.43) is fulfilled.

$$\alpha_{\min} > \alpha_{cr} \tag{2.43}$$

2.2.4.2 Influence of fracture criteria

It is noticed that different fracture criteria have been implemented in the calculation code for testing purposes. To analyze the influence of the fracture criteria on the material behaviors represented through, e.g., crack patterns and load-displacement curves, and thus decide which one is adopted for further studies, numerical simulations of double-edge-notched specimen loaded in uniaxial tension are carried out as shown in Figure 2.16. Note that this geometry (two notches) of the specimen is used here because it will reused for the simulations later. It is necessary to mention that the conclusions that will be drawn on the influence of the fracture criteria on the material behavior should be hold partially since only one type of geometry/loading is analyzed.

For the sake of simplicity, 2D non-polar (normal-shear spring) lattice model is used. Two types of fracture criteria, namely, the Mohr-Coulomb cut-off (2.34) and the fracture criterion (2.37) are used in which the influence of individual parameters φ and n is analyzed by varying their values, respectively, 10°, 20°, 40° for φ and 1, 2, 5 for n. The values of the input parameters are listed in Table 2.2.

Table 2.2 – Input parameters.

E_n [GPa]	E_s [GPa]	σ_{n0} [MPa]	σ_{s0} [MPa]
26	8.7	9	18

The crack patterns of the simulations are shown in Figure 2.17. It shows that the friction angle mostly has no influence on the crack patterns, see Figures 2.17a to 2.17c. That is because almost all elements break due to the tensile stress as shown in Figure 2.18. Furthermore, the Mohr-Coulomb cut-off criterion (2.34) results in the too brittle behaviors in terms of force-displacement curve (see Figure 2.19 for the different values of φ). When the influence of the shear stress is higher by using the fracture criterion (2.37), a curve crack is obtained with $n = 1$, see Figure 2.17d. That is because more elements break due to both tensile and shear stresses as shown in Figure 2.18. Decreasing the influence of the shear stress by increasing the value of n, straighter cracks are obtained, see Figures 2.17e and 2.17f. Indeed, the straight cracks are expected in the uniaxial tensile test because the homogeneous material with weak resistance in tension and higher resistance in shear is used.

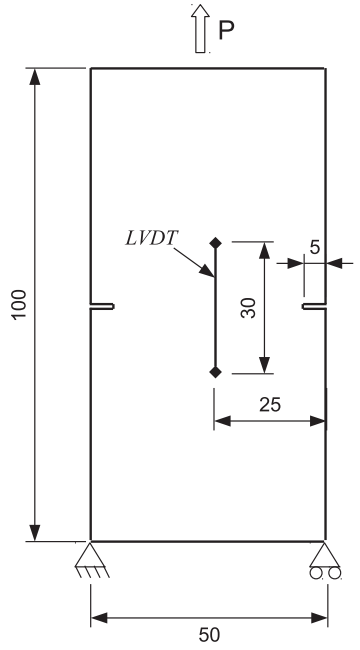

Figure 2.16 – Uniaxial tensile test.

Nevertheless, the more ductile behavior in term of force-displacement curve is obtained in the case of $n = 5$, see Figure 2.19. Thus, the general fracture law (2.37) with $n = 5$ is adopted for the following simulations.

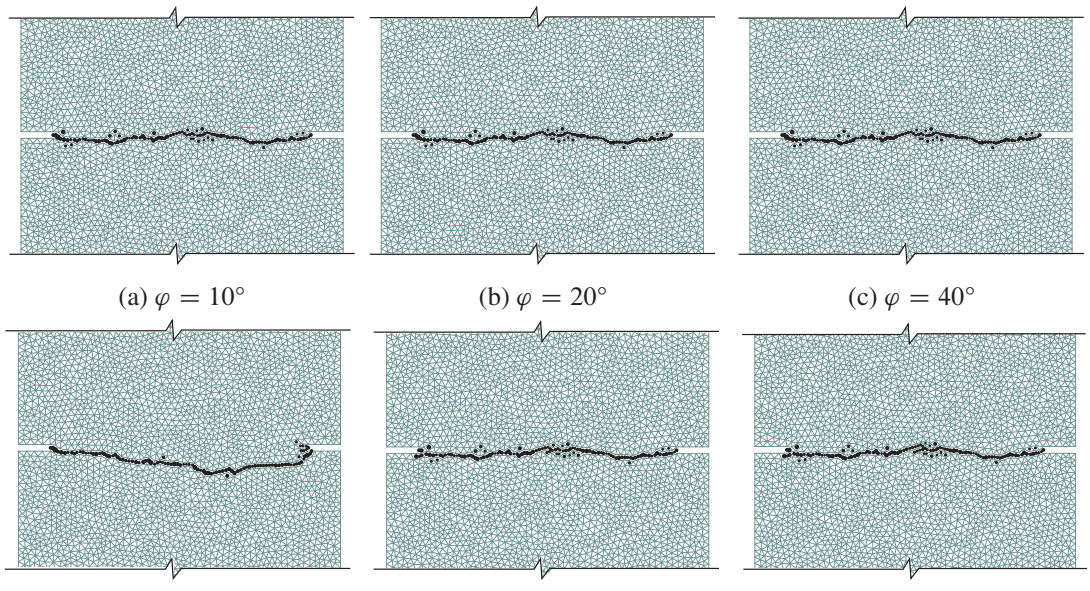

(a) $\varphi = 10°$ (b) $\varphi = 20°$ (c) $\varphi = 40°$

(d) $n = 1$ (e) $n = 2$ (f) $n = 5$

Figure 2.17 – Crack patterns obtained when using the Mohr-Coulomb cut-off criterion with different values of friction angle φ (a, b, c), and those obtained when using the fracture criterion (2.37) with different values of n (d, e, f).

It should be noted that the force-displacement curves shown in Figure 2.19 are smoothened by the procedure described in Section 2.4.3.

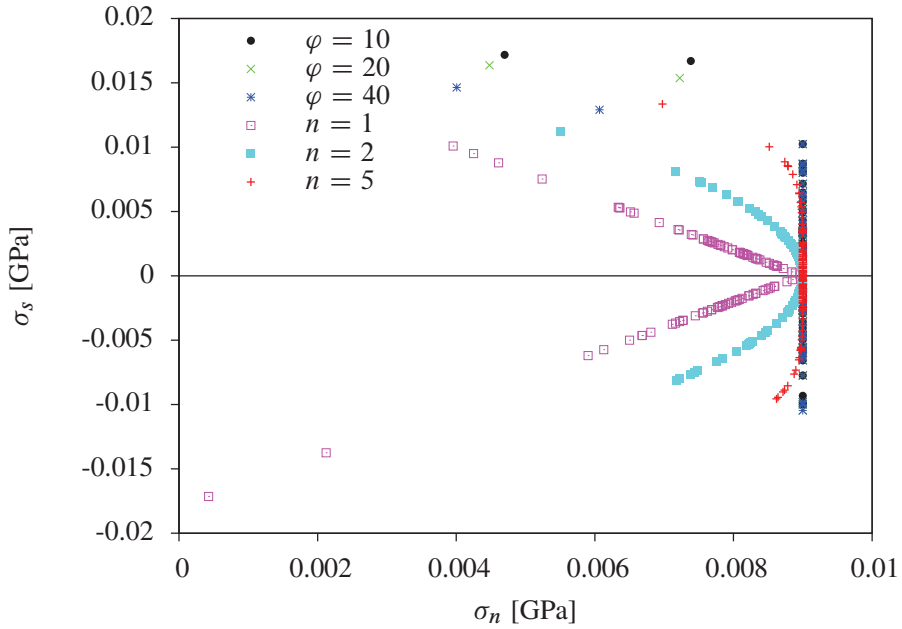

Figure 2.18 – Fracture surfaces for the corresponding fracture criteria.

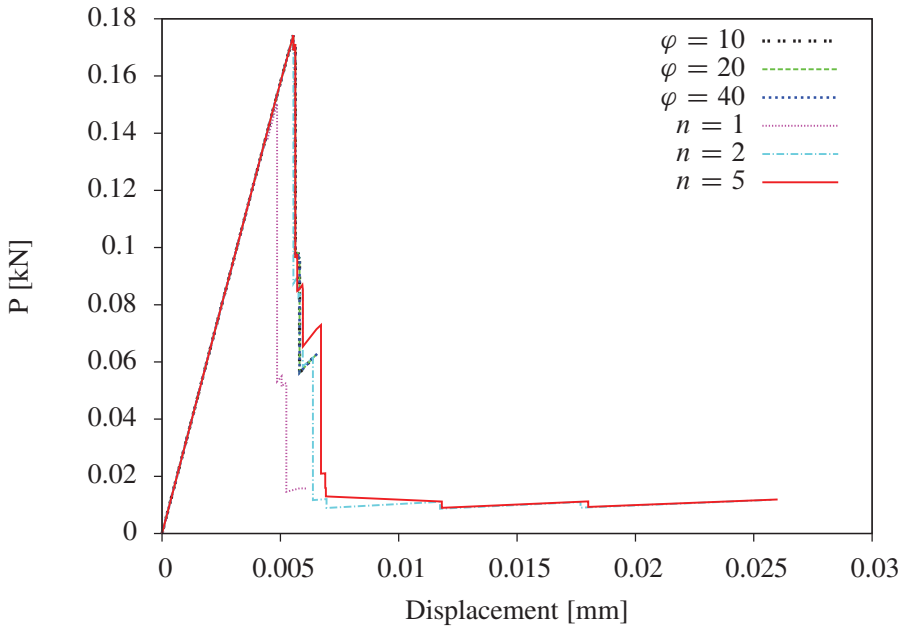

Figure 2.19 – Force-displacement curves for different fracture criteria.

2.2.5 Solvers

At each time step, after applying the boundary conditions, specimen will be loaded and one should find its new equilibrium configuration $\mathbf{p}$. From the initial configuration $\mathbf{p_0}$ which is considered as the reference state, the nodal displacement vector $\mathbf{u}$ can be deduced by

$$\mathbf{u} = \mathbf{p} - \mathbf{p_0} \tag{2.44}$$

It should be noted that the hypothesis of infinitesimal deformations is assumed. There are several ways to determine the equilibrium position of lattice network. In our calculation codes, two methods are implemented. The first one concerns the balance of nodal forces and the second one concerns the minimization of the potential energy of the system.

For the first one, a global vector of nodal forces $\mathbf{F}$ is constructed. The jth components of $\mathbf{F}$ is the vector force at node j which is the sum of nodal forces of n_v elements belonging to this node (bold lines in Figure 2.20),

$$F_j = \sum_{i=1}^{n_v} \left[T\right]_k F_i^e \tag{2.45}$$

where $\left[T\right]_k$ is the transformation matrix from the local coordinate system to the global one of the element k. The equilibrium position of the system is obtained by setting the balance of all nodal

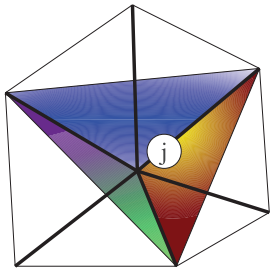

Figure 2.20 – Elements belonging to node j.

forces which means finding the solution such that

$$\mathbf{F} \to \mathbf{0} \tag{2.46}$$

where, $\mathbf{0}$ denotes the null vector. It returns to solve a set of linear algebraic equations

$$\mathbf{A} \cdot \mathbf{u} = \mathbf{b} \tag{2.47}$$

where, $\mathbf{A}$ is the global stiffness matrix, $\mathbf{u}$ is the displacement vector, $\mathbf{b}$ is the global vector of external forces.

The second method looking for the equilibrium position is based on the idea of minimizing the potential energy of the system. The equilibrium of the system is set at a position when its potential energy function at this position is minimum. For the lattice of beam elements, the potential energy of one element k are defined as

$$U_p^k = \frac{1}{2}\int_0^{l^k} \left(\frac{N^2}{EA} + \nu_Q \frac{T_2^2}{GA} + \nu_Q \frac{T_3^2}{GA} + \frac{M_1^2}{GI_1} + \frac{M_2^2}{EI_2} + \frac{M_3^2}{EI_3}\right)_k \mathrm{d}l \tag{2.48}$$

in which, ν_Q is the form factor which is dependent on the shape of the cross section, $\nu_Q = 1.18$ for the circular section; internal forces of element k are given by

$$N = K_n \delta_n \tag{2.49}$$

$$T_2 = K_s(\delta_{s_2} - l\mu_{\omega_3}) \tag{2.50}$$

$$T_3 = K_s(\delta_{s_3} + l\mu_{\omega_2}) \tag{2.51}$$

$$M_1 = K_t\delta_{\omega_1} \tag{2.52}$$

$$M_2 = -K_s\frac{l}{2}\delta_{s_3} + K_s\frac{l^2}{2}\mu_{\omega_2} - K_b\delta_{\omega_2} \tag{2.53}$$

$$M_3 = K_s\frac{l}{2}\delta_{s_2} + K_s\frac{l^2}{2}\mu_{\omega_3} - K_b\delta_{\omega_3} \tag{2.54}$$

In these equations, $\delta_n = u_{1j} - u_{1i}$ is the axial elongation; $\delta_{s_2} = u_{2j} - u_{2i}$, $\delta_{s_3} = u_{3j} - u_{3i}$ are the relative shear displacements about 2-axis and 3-axis, respectively; $\delta_{\omega_1} = \theta_{1j} - \theta_{1i}$, $\delta_{\omega_2} = \theta_{2j} - \theta_{2i}$, $\delta_{\omega_3} = \theta_{3j} - \theta_{3i}$ are the difference of angular rotations at two ends of the lattice element about 1-axis, 2-axis, 3-axis, respectively; $\mu_{\omega_2} = \frac{\theta_{2i}+\theta_{2j}}{2}$; $\mu_{\omega_3} = \frac{\theta_{3i}+\theta_{3j}}{2}$ are the averaged angular rotations about 2-axis and 3-axis, respectively. For each element k, the internal forces are constant along the axial direction of the element, so its potential energy is

$$U_p^k = \frac{l^k}{2}\left(\frac{N^2}{EA} + \nu_Q\frac{T_2^2}{GA} + \nu_Q\frac{T_3^2}{GA} + \frac{M_1^2}{GI_1} + \frac{M_2^2}{EI_2} + \frac{M_3^2}{EI_3}\right) \tag{2.55}$$

The total potential energy of the system is the sum of the potential energy of all elements in the system, is given by

$$U_p = f(\mathbf{u}) = \sum_{k=1}^{N_c} U_p^k \tag{2.56}$$

where, N_c is actual total contact number (the number of unbroken elements). This function is a quadratic form and is a function of displacement vector $\mathbf{u}$.

The conjugate gradient method (Press et al., 2007) is used to solve the set of linear equations (2.47) or to minimize the global potential energy function (2.56). Furthermore, solving equation (2.47) is equivalent to minimize the quadratic function

$$f(\mathbf{u}) = \frac{1}{2}\mathbf{u}\cdot\mathbf{A}\cdot\mathbf{u} - \mathbf{b}\cdot\mathbf{u} \tag{2.57}$$

since this function is minimized when its gradient

$$\nabla f = \mathbf{A}\cdot\mathbf{u} - \mathbf{b} \tag{2.58}$$

is zero, which is equivalent to Equation (2.47). One disadvantage of the method based on solving Equation (2.47) is that the global stiffness matrix has to be constructed explicitly. This does require a large amount of computer memory when dealing with a large system. Therefore, the method based on minimizing the potential energy of the system is used for the simulations in the thesis.

The vector displacement $\mathbf{u}$ is solved iteratively by minimizing Equation (2.56) until the precision threshold tol is attained. When the equilibrium of system is found at each time step, the breaking procedure is proceeded to remove an element as discussed in Section 2.2.4. After removing one element, in the next time step this element will not be taken into account in the summation of the Equation (2.56).

It is noted that removing an element from the system has a local effect. This means that removing an element from the system only implies small changes in the displacement vector and in the total potential energy of the system. Therefore, at any time step, if the initial guess $\mathbf{u_0}$ of the displacement vector is taken from the converged displacement vector of the previous step, the conjugate gradient method for finding the equilibrium position only needs a few iterations to converge. This was presented in Schlangen and Garboczi (1996) and is confirmed by our simulation in which only about 30 minutes are needed to totally break a specimen under tensile loading whereas 10 hours are required for the same simulation if the initial guess $\mathbf{u_0}$ is always taken as a null vector.

2.3 Numerical implementation

2.3.1 Accounting for material heterogeneities

At the mesoscale, concrete is substantially random and inhomogeneous and is consider as a three phase material including coarse aggregates, mortar matrix and an interfacial transition zone ITZ between them, see Section 1.1.1. The fracture is strongly influenced by the material structure. Thus, the heterogeneity has to be implemented in the model to better capture the fracture process of concrete.

For the sake of simplicity, in our studies, the aggregates introduced in the model are assumed as circular (in two dimensions) or spherical (in three dimensions) inclusions. However, it should be noted that other forms of the inclusions can also be modeled, such as ellipsoidal inclusions or angular ones, see Wang et al. (1999) and Häfner et al. (2006) but the geometrical description of these forms is more complex than the spherical ones. Moreover, an aggregate structure with realistic aggregate shapes obtained from the computed tomography (CT-scan) can be implemented in the lattice model (Man and van Mier, 2008).

In our model, the heterogeneities are introduced at two levels representing coarse aggregates explicitly and fine aggregates implicitly. From a given discretization, the average element size is known, a minimum threshold $d_{\min}$ can be determined such that an inclusion with diameter $d_{\min}$ can contain a large enough number of lattice elements to describe aggregates. In our simulations, this is approximated by choosing $d_{\min}$ greater than or equal to three times the average element size. As an example shown in Figure 2.21 in which the values of $d_{\min}$ are taken equal to three times the average element size for two different discretizations. The aggregates having diameters greater than $d_{\min}$ are considered as the coarse inclusions which are modeled directly by assigning different material properties to lattice elements corresponding to the material phases. Whereas the aggregates having diameters less than $d_{\min}$ are considered to be dissolved in the mortar matrix and the ITZs and they are modeled by assigning random strength values following the Gauss or Weibull distribution to the mortar matrix and the interface phases. The identification of the distribution parameters (e.g., the mean and standard deviation of the Gaussian distribution) of the strengths of the lattice elements is discussed in Section 2.5.2. The fine aggregates are modeled by the random fields since they do not contain a large enough number of lattice elements to be directly modeled as the coarse aggregates.

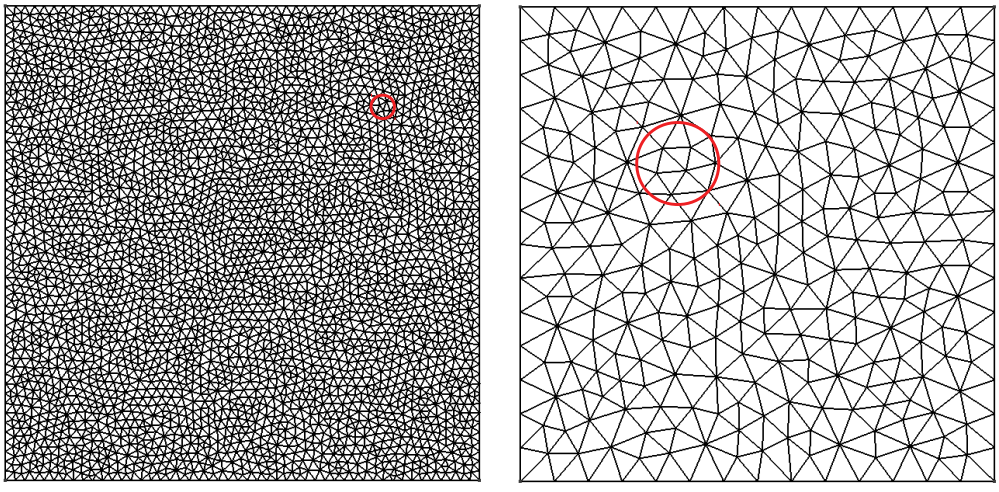

(a) (b)

Figure 2.21 – The values of $d_{\min}$ is of 6 mm and 14 mm which are determined from a given discretization with the average element size is of 2 mm (a) and 7 mm (b), respectively.

Note that to directly include the finest aggregates in the model, the finer discretization has to be used. This results in, however, an increase in the number of degrees of freedom of the system

and thus leading to an augmentation of the computational cost. We return to this problem in Section 2.2.3.3.

2.3.1.1 Coarse aggregate modeling

Aggregate size distribution Modeling of coarse aggregates requires the information of the gradation of the aggregates. The gradation can be taken from an aggregate grading curve of a real material obtained from sieve analysis in which a relation between the sizes of a set of standard sieves and the corresponding total amount of aggregates passing through that sieves, is defined. However, if one lacks data from experiments, aggregate grading can also be described by means of "ideal" grading curves which provide good aggregate packing. An aggregate gradation provided from "ideal" grading curve is well-graded which means that there are many different grain sizes, so that small grains fit into the voids between larger grains. There are different types of "ideal" curves worked out on the basis of practical experiments and theoretical calculation such as Bolomey's, Fuller's, Faury's curves (Fuller and Thompson, 1906; Dewar, 1999). The most known of them is the "ideal" Fuller's curve which is described by

$$p(d) = 100\% \times \sqrt{\frac{d}{d_{\max}}} \tag{2.59}$$

where p denotes the percentage of the aggregates that are finer than d, $d_{\max}$ is the maximum aggregate size.

Taking an example to demonstrate that the Fuller's curve can provide an aggregate packing from a real concrete. Table 2.3 shows the aggregate gradation of high performance concrete $M75C$ (compressive strength $f_c = 75$ MPa) used in Gaweska Hager (2004). The corresponding grading curve is shown in Figure 2.22. Based on the sizes of used aggregates (maximum aggregate size is 25 mm), a Fuller's curve is also plotted in that figure. Since the plot of aggregate gradation of concrete $M75C$ is close to the Fuller's curve, the aggregate of $M75C$ is well-graded. Or inversely, the Fuller's curve can approximate a well gradation of a real concrete.

Table 2.3 – Grain sizes and cumulative sieve passing of an aggregate grading.

Class N°	Aggregate size [mm]	Sieve passing [%]
12	0–1.25	22
11	1.25–2.5	35
10	2.5 –3.15	40
9	3.15–4	43
8	4–5	47
7	5–6.3	49
6	6.3–8	54
5	8–10	62
4	10–12.5	73
3	12.5–16	86
2	16–20	97
1	20–25	100

As mentioned above, only aggregates having diameters greater than $d_{\min}$ are directly modeled as inclusions in the lattice model. Therefore, if the gradation of a real grading curve is based on, only those of aggregates passing the sieve size being greater than $d_{\min}$ are used to generate the spherical aggregate structure. In the case of the gradation of the Fuller's curve is based on, we can define a gradation of the aggregates having sizes from $d_{\min}$ to $d_{\max}$ as

$$p(d) = 100\% \times \sqrt{\frac{d - d_{\min}}{d_{\max} - d_{\min}}} \tag{2.60}$$

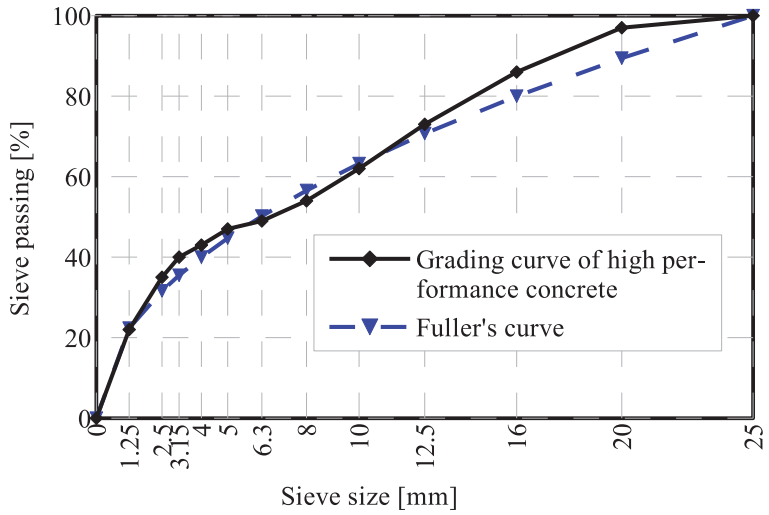

Figure 2.22 – Grading curve of concrete $M75C$.

From the grading curve, the relative amount of aggregates within the grading segment $[d_s, d_{s+1}]$ can be obtained as

$$V_{\text{Agg}}[d_s, d_{s+1}] = p(d_{s+1}) - p(d_s) \tag{2.61}$$

To generate the material structure, an aggregate volume fraction P_{a} has to be defined. Depending on each type of concrete, aggregates take up to 50%–90% of the total volume of concrete. The absolute volume fraction of aggregates within the grading segment $[d_s, d_{s+1}]$ is given by

$$V^{\text{abs}}_{\text{Agg}}[d_s, d_{s+1}] = P_{\text{a}} \times V_{\text{Agg}}[d_s, d_{s+1}] \tag{2.62}$$

As an example, Table 2.4 shows the volume fraction and absolute volume fraction (with $P_{\text{a}} = 75\ \%$) of each aggregate grading segment generated using Fuller's grading with $d_{\min} = 2.5$ mm and $d_{\max} = 16$ mm. The corresponding Fuller's curve is shown in Figure 2.23.

Table 2.4 – Volume fraction of each aggregate class.

Aggregate class [mm]	Sieve size [mm]	Sieve passing [%]	Volume fraction of each class [%]	Volume fraction of each aggregate class with $P_{\text{a}} = 75\%$ [%]
–	2.5	0		
2.5 - 3.15	3.15	21.94	21.94	16.46
3.15 - 4	4	33.33	11.39	8.54
4 - 5	5	43.03	9.70	7.27
5 - 6.3	6.3	53.05	10.02	7.52
6.3 - 8	8	63.83	10.77	8.08
8 - 10	10	74.54	10.71	8.03
10 - 12.5	12.5	86.07	11.53	8.65
12.5 - 16	16	100	13.93	10.45

Taking and placing processes After dividing the gradation of aggregates into segments, a spherical aggregate structure has to be generated to assure the volume fraction of each grading segment

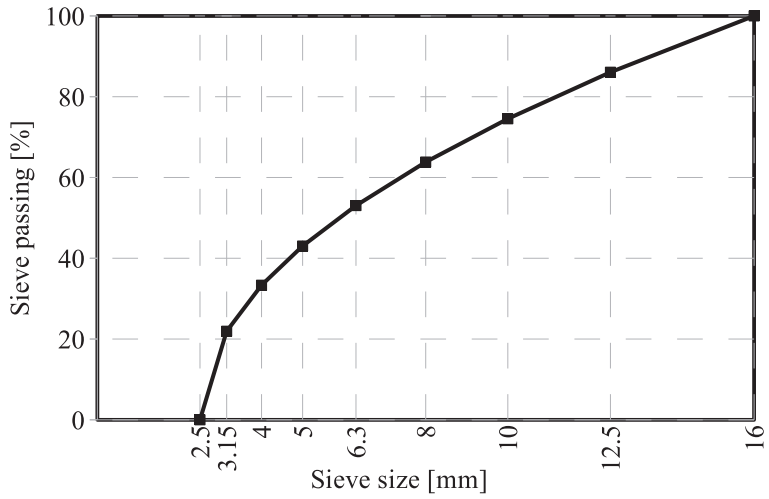

Figure 2.23 – Grading curve with $d_{\min} = 2.5$ mm and $d_{\max} = 16$ mm.

of aggregates as well as the total volume fraction of the aggregates. Depending on the type of creation of the specimen that one would like to simulate, i.e., the specimen created when sawing from the bigger sample or when directly casting in a mold, overlap between the aggregates with specimen boundaries is allowed or not when mapping the aggregates on the lattice mesh. In the case of allowing that overlap, only the parts of aggregates belonging to specimen are taken into account (hatched fields of Figure 2.24). In this section, the procedure to generate an aggregate structure with overlapping between aggregates and specimen boundaries is presented.

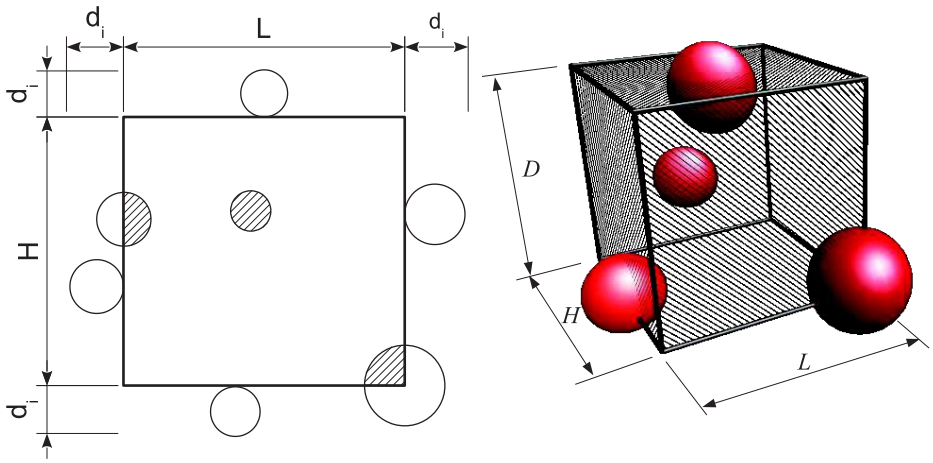

Figure 2.24 – Limiting of grain positions and effective parts of aggregates (hatched fields) in 2D (a) and 3D (b).

The taking and placing processes start with the grading segment containing the largest size particles and repeat for the next smaller size grading segment and then again for successively smaller size grading segment until the last one has been generated. For each grading segment $[d_s, d_{s+1}]$, the aggregates are generated by the following steps:

Step 1. Calculate the aggregate volume to be generated V^r_{Agg} in the grading segment.

Step 2. Generate a random number d_i defines the particle size and a random vector $\mathbf{x}_i$ defines the

position of the centroid of the particle. Assuming that the aggregate size d_i has a uniform distribution between d_s and d_{s+1}, and the particle has also a uniform distribution throughout the specimen, they are expressed as

$$d_i = \zeta(d_{s+1} - d_s) + d_s \tag{2.63}$$

where ζ is a random number uniformly distributed between 0 and 1, and

$$\mathbf{x}_i = \boldsymbol{\eta}(\mathbf{x}_{\max} - \mathbf{x}_{\min} + \mathbf{d}_i) + \mathbf{x}_{\min} - \frac{\mathbf{d}_i}{2} \tag{2.64}$$

in which $\mathbf{x}_{\min}$, $\mathbf{x}_{\max}$ are the minimum and maximum coordinates of the specimen, $\mathbf{x}_{\max} - \mathbf{x}_{\min}$ defines the specimen sizes L, H and D as shown in Figure 2.24; vector $\mathbf{d}_i = (d_i, d_i, d_i)$; $\boldsymbol{\eta}$ are the three independent random numbers uniformly distributed between 0 and 1.

Step 3. Check if the particle does not overlap any previously placed particles. Moreover, the distance between any two centroids of particles i and j has to be equal or larger than d_0 expressed as

$$d_0 = 1.1(\frac{d_i}{2} + \frac{d_j}{2}) \tag{2.65}$$

so that a minimum mortar thickness between two aggregates is always assured. If the conditions of this step is not satisfied, repeat the step 2.

Step 4. Calculate the volume fraction of the generated aggregate particle and add it to the total generated volume fraction of the current grading segment V^g_{Agg}. Note that only the part of the aggregate belonging to the specimen is taken into account.

Step 5. Repeat steps 2, 3, 4 until relative error between the total generated volume fraction of the grading segment and the required volume fraction to be generated of the grading segment is smaller than some predefined threshold tol, e.g. 0.1%. This is expressed as

$$err = 1 - \frac{V^g_{\text{Agg}}}{V^r_{\text{Agg}}} < tol. \tag{2.66}$$

The remaining aggregate volume to be generated $V^r_{\text{Agg}} - V^g_{\text{Agg}}$ is then transferred to the next grading segment.

As an example, Figure 2.25 shows the aggregate structures generated with 2.5 mm $\leq d \leq$ 16 mm and aggregate volume fraction $P_{\text{a}} = 75\%$ in two and three dimensional cases.

Note that if overlapping between aggregates and specimen boundaries is not allowed, the taking and placing processes should be performed separately since there is no overlapping between aggregates and specimen boundaries and thus the volume fraction of the generated grain can be calculated disregarding its position generated by the placing process, see e.g., Wang et al. (1999). The advantage of separately performing the taking and placing processes is that one can place the generated aggregate particles from the taking process, largest size first and smallest size last. Whereas in the above procedure, the particles are placed from the largest size grading segment to the smallest one but within one grading segment the particles are not placed as largest size first and smallest size last because of random generation of particle sizes. However, this difficulty can be reduced when reducing the gap in magnitude between d_s and d_{s+1} of the grading segment.

Material phase definition and property assignment After generating the aggregate structure, different material phases can be defined and different local mechanical properties are assigned to the elements falling in each phase. At the mesoscale, three phases can be distinguished: aggregate, matrix and interfacial transition zone (ITZ), see Figure 2.26a. If both ends of an element are located

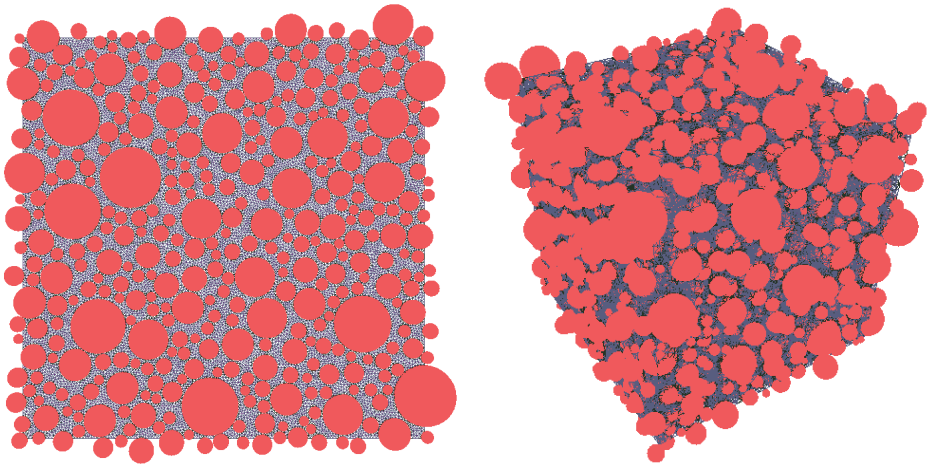

(a) (b)

Figure 2.25 – Generated aggregate structure with $d_{min} = 2.5$ mm, $d_{max} = 16$ mm and $P_a = 75\%$ in two dimensions (a) and three dimensions (b).

in the same phase, then this element is assigned the same mechanical properties of the corresponding phase (aggregate or matrix), otherwise it is considered as interface or aggregate element depending on the location of its midpoint, see Figure 2.26b. If its midpoint is located within the particle, the element is classified as aggregate element, or else it will be ranked as ITZ element. The reason for this definition of ITZ element is that the resulting density of aggregates (the ratio between the number of aggregate elements and the total number of elements) is closer to desired density of aggregates in material than those developed by other authors (Schlangen and van Mier, 1992a; Lilliu and van Mier, 2003; Sagar and Prasad, 2009). In their models, all elements that connect two different zones of particle structures are considered as ITZ elements.

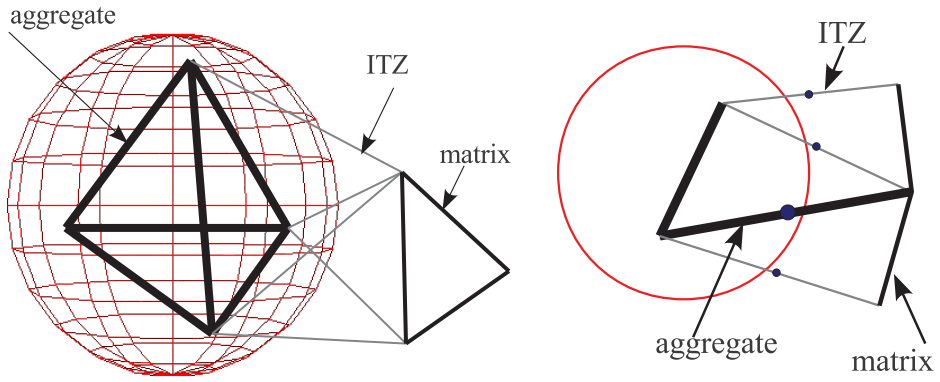

(a) (b)

Figure 2.26 – Distinction between aggregate, matrix and ITZ phase according to the location of a lattice element in the particle structure (a); Definition of aggregate element or ITZ element from the element that connect two zones of particle structure (b).

As presented in Chapter 1, for concrete, the aggregates are about twice to three times stiffer than the mortar matrix. The strengths of the aggregates are about 2 to 3.33 times greater than those of the mortar matrix. For the interface zones, it is found that their strength is about 33% to 67% of the tensile strength of the matrix. These relative differences of stiffnesses and strengths can be assigned to the corresponding lattice elements to simulate the mesostructure of concrete. However, in the lattice models, the length of the lattice elements is significantly greater than the width of the interfacial transition zone (about 20-100 μm). Therefore, the Young's modulus of the interface

elements can be taken as the Harmonic mean of that of aggregate and matrix elements (Grassl and Jirásek, 2010)

$$\frac{2}{E_I} = \frac{1}{E_M} + \frac{1}{E_A} \tag{2.67}$$

in which the subscripts I, M and A refer to the interface, matrix and aggregate elements, respectively.

2.3.1.2 Statistical distribution of local failure properties

It is recalled that the coarse aggregates that have diameters greater than $d_{\min}$ are directly modeled by generating the particle structure and then assigning different material properties corresponding to the material phases, see Section 2.3.1.1. If we assume that the macroscopic behavior of the material is primarily driven by the coarse aggregates, since at the softening regime, because of the localization of damage, the representative volume element is no longer existed, then we can disregard the influence of the fine aggregates. However, if we would like to take into account the contribution of the fine aggregates into the material behavior, the heterogeneities represented by the fine aggregates can be modeled by assigning random fields of local tensile and shear strengths, σ_{n0} and σ_{s0} to the matrix and ITZ phases. The Gauss and Weibull distributions are usually used, see e.g., van Mier et al. (2002).

A random variable x with the Gaussian distribution has the probability distribution function expressed as

$$f(x) = \frac{1}{\sigma_x\sqrt{2\pi}} e^{-\frac{1}{2}\left(\frac{x-\bar{x}}{\sigma_x}\right)^2} \tag{2.68}$$

in which $\bar{x}$ and σ_x are the mean and the standard deviation of x, respectively. If x has the Weibull distribution, its probability distribution function is given by

$$f(x) = \begin{cases} \frac{k}{\lambda} \cdot \left(\frac{x}{\lambda}\right)^{k-1} \cdot e^{-\left(\frac{x}{\lambda}\right)^k} & \text{if } x \geq 0 \\ 0 & \text{if } x < 0 \end{cases} \tag{2.69}$$

where $k > 0$ is the shape parameter and $\lambda > 0$ is the scale parameter of the distribution.

When the tensile strength σ_{n0} and the shear strength σ_{s0} are generated by Equation (2.68) or Equation (2.69) a minimum threshold value $\sigma_{0,\min}$ has to be defined (in our simulations, the value $\sigma_{0,\min} = 1 \times 10^{-6}$ MPa is used) to avoid null or negative generated strength values which cause unstable responses. When the generated strength value is smaller than $\sigma_{0,\min}$, a new value will be regenerated. As an example, Figure 2.27 shows the generated distributions after Gauss and Weibull distributions of the local shear strength σ_{s0} of 22812 mortar elements of the specimen presented in Figure 2.25a.

2.3.2 Numerical procedure

During the thesis, the lattice model is firstly implemented in our self-writing C++ code. The code consists of three modules presented in Figure 2.28. The input meshes for the pre-processing stage are generated by the finite element grid generator Gmsh (Geuzaine and Remacle, 2009). Image processing and visualization in the post-processing stage are done with the aids of the open-source software Paraview (Ahrens et al., 2005; Squillacote, 2007).

The lattice model is next implemented in the existing open-source code SOFA (Allard et al., 2007; Faure et al., 2007) to avail some efficient calculation algorithms such as parallel computation and to couple the lattice model with the finite elements for dealing with large scale structures.

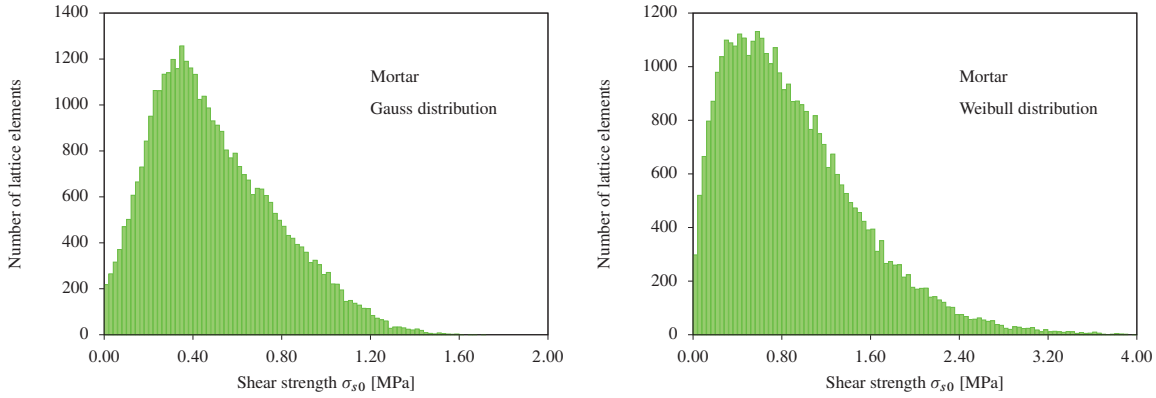

(a) (b)

Figure 2.27 – Generated distribution of local shear strength σ_{s0} of 22812 mortar elements after Gauss distribution (a) with $\bar{\sigma}_{s0} = 0.6$ MPa, $\sigma_{\sigma_{s0}} = 0.3$ MPa and after Weibull distribution (b) with $k = 1.5$ MPa, $\lambda = 1$ MPa.

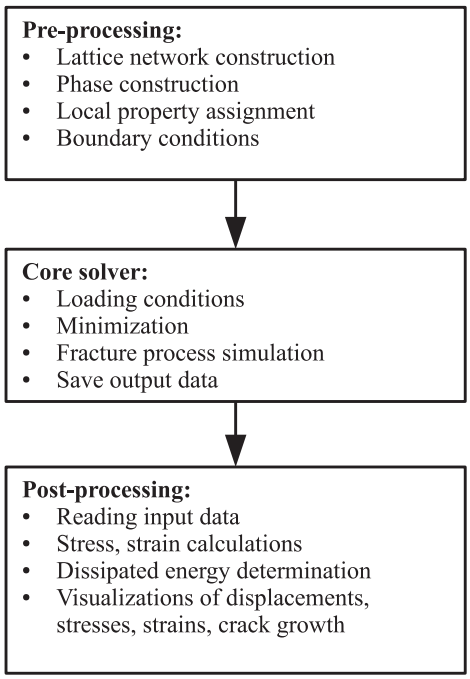

Figure 2.28 – Three modules of the calculation code.

2.4 Post-processing treatment

To analyze the behavior of the material at the mesoscale using the lattice model, the stress and strain should be computed from the lattice network. There are two methods for calculating the tress. By the first one, the stress tensor is computed based on the equivalence of strain energy stored in a cell of volume V. In the second one, stress in some direction is a measure of the resulting force on a surface perpendicular to that direction divided by area of that surface. The resulting force is calculated by defining a cutting plane and summing the force vector of all elements "cut" by that cutting plane. The strain tensor is computed by averaging the displacement gradient over a volume V. Otherwise, strain in some direction can be calculated by measuring the displacement in that direction by means of LVDT-type (linear variable differential transformer) transformer. Thereafter, estimates of local stress and strain fields are obtained.

2.4.1 Stress calculation

2.4.1.1 Mean stress

The Cauchy stress tensor in a discrete medium can be calculated from the contact forces (here the forces of lattice elements) and the geometrical characteristics of the lattice. For the specimen with a volume V, the stress tensor is calculated by (Bathurst and Rothenburg, 1990; Bagi, 1996)

$$\boldsymbol{\sigma} = \frac{1}{V}\sum_{k=1}^{N_c} \mathbf{f}^k \otimes \mathbf{l}^k \tag{2.70}$$

in which, $\otimes$ denotes the outer product. The sum is with respect to all remaining elements (unbroken elements) within the volume V. $\mathbf{f}^k$ and $\mathbf{l}^k$ are the force and contact vectors, respectively, of element k with the Cartesian components

$$\begin{array}{rcl} \mathbf{f}^k & = & f_n^k \mathbf{n}^k + f_s^k \mathbf{s}^k + f_t^k \mathbf{t}^k \quad = \quad f_x^k \mathbf{i} + f_y^k \mathbf{j} + f_z^k \mathbf{k} \\ \mathbf{l}^k & = & l_x^k \mathbf{i} + l_y^k \mathbf{j} + l_z^k \mathbf{k} \end{array} \tag{2.71}$$

in which, $\mathbf{n}^k$, $\mathbf{s}^k$, $\mathbf{t}^k$ are the three unit basic vectors of the local coordinate system of element k.

It is noted that for problems in which a concentration of stress occurs, the mean stress obtained by Equation (2.70) over the whole specimen volume V does not reflect that concentration. Instead one can define a subdomain with volume V_s around the stress concentration zone and the stress tensor is computed by averaging on that volume

$$\boldsymbol{\sigma} = \frac{1}{V_s}\sum_{k\in V_s} \mathbf{f}^k \otimes \mathbf{l}^k \tag{2.72}$$

Note that if the chosen volume V_s is too large compared to the volume of the concentration zone, the concentration of stress is lost, whereas if it is too small, the sum in Equation (2.72) is not "stable".

Alternative to Equation (2.72), the stress in some direction can be induced by the resulting forces on a cutting plane. This is presented in the next section.

2.4.1.2 Stress measure by resulting forces on a cutting plane

Defining a cutting plane (cp) with normal vector $\mathbf{N}$ which separates system into two parts as shown in Figure 2.29, the resulting force vector is obtained by summing up all the force vectors of the elements cut by this plane

$$\mathbf{F} = \sum_{k\cap\,(cp)\neq 0} \left(f_n^k \mathbf{n}^k + f_s^k \mathbf{s}^k + f_t^k \mathbf{t}^k\right) \tag{2.73}$$

The stress is then computed by averaging the resulting force over an area S of the intersection surface defined between the cutting plane and the specimen

$$\boldsymbol{\sigma} = \frac{\mathbf{F}}{S} \tag{2.74}$$

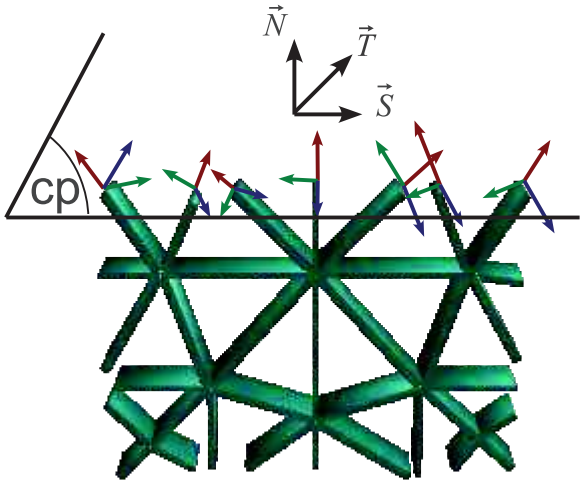

Figure 2.29 – Cutting plane.

It is worth noting that, for problems in which the stress is nearly homogeneous, the stress in a certain direction given by Equation (2.74) and the stress in that direction derived from the stress tensor given by Equation (2.70) are the same. This is verified by our simulations. For problems in which the strong concentration of stress occurs, by defining an appropriate volume V_s, the stress in the concentration zone can be measured by Equation (2.72) whereas the average stress over the specimen's cross-section (in the localization zone) along a direction can be easily, in practice, computed by using Equation (2.74). Two methods for measurement of stress are implemented in the computational code. Depending on the situation, they can be used alternatively.

2.4.2 Strain calculation

2.4.2.1 Mean strain

Similarly to the relationship between mesoscopic forces and macroscopic stress as described in Equation (2.70), the macroscopic strain is related to the mesoscopic displacements by (see Bagi (1996))

$$\boldsymbol{\varepsilon} = \frac{1}{V}\sum_{k=1}^{N_c}\left(\mathbf{u}_j^k - \mathbf{u}_i^k\right) \otimes \mathbf{a}^{ij} \tag{2.75}$$

in which, $\mathbf{u}_i^k$ and $\mathbf{u}_j^k$ are the displacements of element kth at the endpoints i and j respectively; the area vector, $\mathbf{a}^{ij}$, is defined as the vector directed from the end i to the end j of the element kth with its magnitude is equal to the area of the element k, see Figure 2.30. This macroscopic strain tensor is calculated by averaging over a volume V with respect to all elements having not broken yet.

The mean strain tensor computed by Equation (2.75) is only adapted for problems in which the strain is rather homogeneous. For problems in which the strong localization of strains occurs within certain zones, the average strain over the whole specimen size does not make sense. Similar to the way to compute the stress tensor, a subvolume V_s of the localization zone can be defined and the mean strain is computed over it

$$\boldsymbol{\varepsilon} = \frac{1}{V_s}\sum_{k\in V_s}\left(\mathbf{u}_j^k - \mathbf{u}_i^k\right) \otimes \mathbf{a}^{ij} \tag{2.76}$$

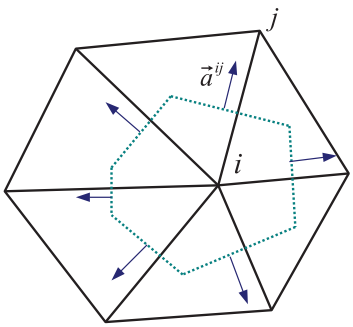

Figure 2.30 – Three modules of the calculation code.

Alternatively, the strain in certain direction can be induced by directly measuring the displacement in that direction. This is presented in the next section.

2.4.2.2 Strain induced by displacement measurement

The displacements can be also measured by defining a LVDT-type sensor as in experiments. The sensor is defined by $P_i P_j$ with the length L_0 as shown in Figure 2.31, where P_i belongs to triangle i and P_j belongs to triangle j of the lattice mesh. After deformation, the positions of P_i and P_j are determined by the interpolation from the positions of triangles i and j using the shape function

$$P_k = \sum_{n=1}^{3} N_n^k P_n^k \quad \text{with } k = i, j \tag{2.77}$$

here, $N_n^k, n = 1, 2, 3$ are the shape functions of triangle k ($k = 1, 2$); $P_n^k, n = 1, 2, 3$ are the position of three vertices of triangle k. The new length L of this sensor will be defined as the distance between P_i and P_j. The relative displacement and strain measured by this sensor are

$$\begin{aligned} u &= L - L_0 \\ \varepsilon &= \frac{u}{L_0} \end{aligned} \tag{2.78}$$

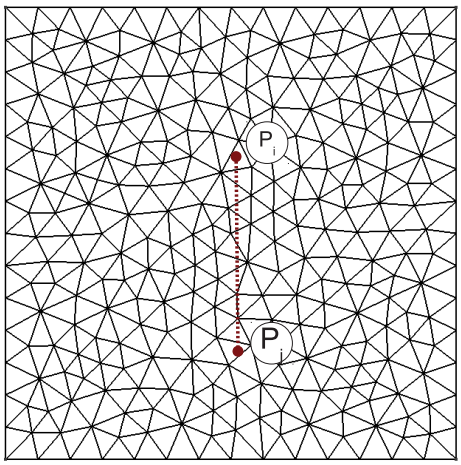

Figure 2.31 – LVDT-type sensor.

2.4.3 Envelope of global behavior curves

After simulating the fracture process of a specimen using the lattice model, the global behavior of the specimen can be determined by means of a force-displacement or a stress-strain curve. A

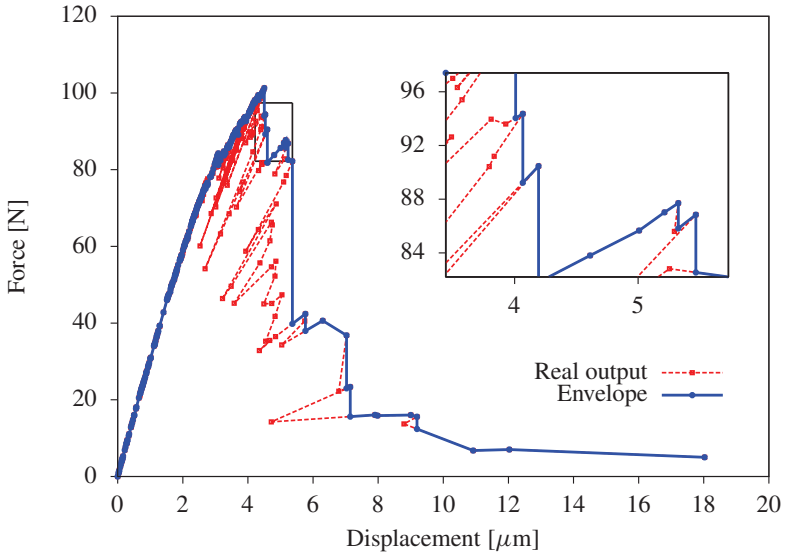

Figure 2.32 – Force-displacement curve obtained from an uniaxial tensile simulation.

force-displacement curve of an uniaxial tensile test is shown in Figure 2.32. As described above, the fracture process is simulated by removing the elements whose stress states exceed the critical value. Since the failure of lattice elements is brittle, a sudden decrease of the measured load and possibly the accompanying displacement is observed see Figure 2.32. Each point of the force-displacement curve represents the state of the specimen when removing a lattice element. Connecting these points leads to the global behavior curve. However, it differs from the experiments in which the displacement is controlled. In fact, the last one is characterized by a monotonic increase of the displacement. Therefore, in order to have a corresponding response, the "envelope" of the numerical curve should be taken. The envelope curve is obtained by the so-called smoothing procedure. The procedure is described as follows. By connecting from the first to the last point that describes the specimen state and as soon as a decrease of the displacement is observed, the decrease of the computed load is kept vertically until an intersection with the original curve is observed. The envelope curve then follows the original curve until the new decrease of the displacement is met again and the procedure is repeated. The zoom-in figure in Figure 2.32 shows the procedure.

Note that envelope curves were also proposed by Arslan et al. (1995) and Vervuurt (1997). However, when using the envelope curve alone, some essential information may be lost such as a possible snap-back. Also the area under the envelope curve is overestimated.

2.5 Numerical applications

2.5.1 Identification of elastic parameters

Depending on the type of the lattice model used (the beam or normal-shear spring model), the corresponding parameters should be identified so that the model can represent the "macroscopic homogeneous" material with the elastic properties: Young's modulus E and Poisson's ratio ν. Since almost all simulations performed in the thesis are in two dimensions, the following identification procedure of model parameters is only valid for 2D lattice model.

To determine the model parameters, elastic analyses are carried out with different model parameters and the corresponding macroscopic elastic properties E and ν are computed. The procedure to compute E et ν is described in Section 2.2.3.3. From that a relation between the model parameters and the macroscopic elastic properties can be deduced. The elastic analyses are performed on the mesh whose element size is satisfied the condition $B/l_m \geq 40$ as discussed in Section 2.2.3.3. The mesh with $B/l_{\mathrm{m}} = 60$ was used in our studies.

2.5.1.1 Beam lattice model

To distinguish the macroscopic and the local elastic property notations, all the elastic properties of the beam elements are written with a subscript b. As shown in Section 2.2.2, the local properties of the beam elements, with the subscript b standing for "beam", are: the Young's modulus E_b, the cross-section area A_b, the beam length l_b and the second moment of area I_b. Note that the polar second moment of area $I_{b1} = 2I_b$ for the circular section. Since the torsional moments of the beam elements are generally small under mode-I of failure, the shear modulus nearly has no influence on the material behavior. The Poisson's ratio of the beam elements ν_b is set at 0.2, arbitrarily, through the lattice geometry. Two parameters A_b and l_b are imposed by the mesh geometry. Two remaining parameters E_b and I_b are related to the macroscopic parameters E et ν. Similar to Delaplace and Desmorat (2007), an adimensional parameter $\lambda = 64I_b/(\pi D_s^4)$ with D_s the equivalent diameter of the cross section (see Equation (2.29)) is used instead of I_b. The model parameters are now E_b and λ.

Uniaxial tensile simulations are performed with varying the model parameter λ as in Table 2.5. For each value of λ, eight uniaxial tensile simulations corresponding to eight values of E_b taken from Table 2.5 are carried out. There are 104 cases in total of elastic analysis performed. The Young's modulus E and Poisson's ratio ν are computed for each case. An interesting observation is that when keeping λ constant and varying E_b, the computed values of ν and E/E_b do not change, refer to Figure 2.33 in which the evolutions of ν and E/E_b with respect to E_b for two values of λ (0.1 and 1) are shown. This means that ν and E/E_b are only proportional to the parameter λ.

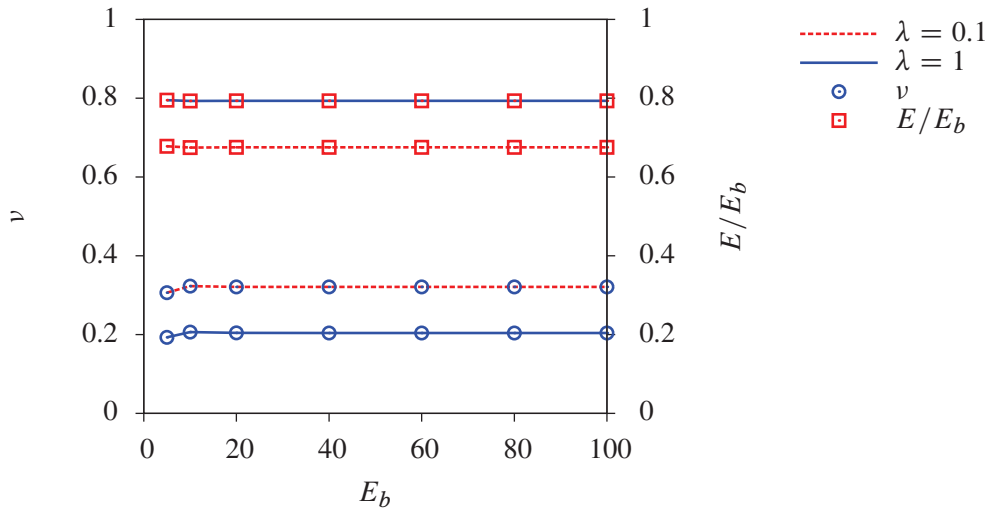

Figure 2.33 – Evolutions of ν and E/E_b with respect to E_b when λ equals to 0.1 and 1.

Table 2.5 – Varying of beam model parameters.

λ [-]	0	0.05	0.1	0.2	0.4	0.6	0.8	1.0	1.5	2.0	2.5	3.0	4.0
E_b [GPa]	5	10	20	40	60	80	100						

The evolution of ν with respect to λ is shown in Figure 2.34a while that between E/E_b and λ is shown in Figure 2.34b.

Moreover, the fitted relations which describe the evolutions of ν and E/E_b with respect to λ are

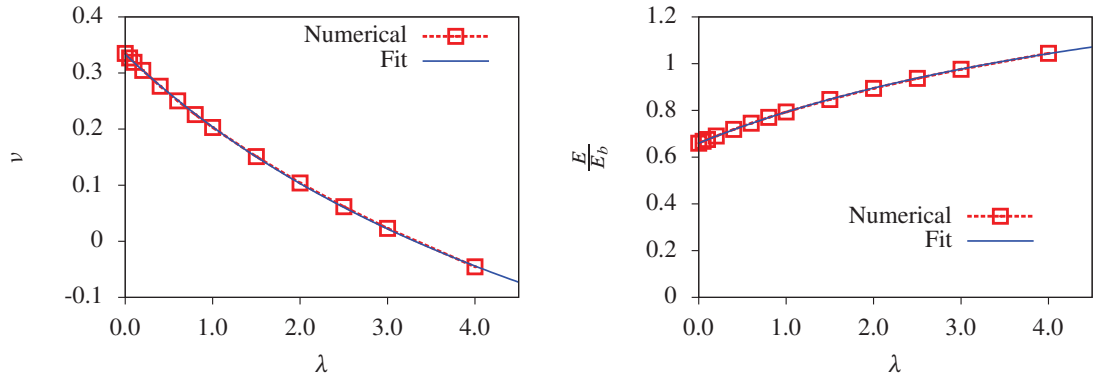

Figure 2.34 – Evolution of elastic properties with respect to the beam model parameters: Poisson's ration ν (a) and normalized Young's modulus E/E_b (b) depend on the parameter λ.

given as

$$\nu = \frac{1 - a\lambda}{3 + b\lambda} \tag{2.79a}$$

$$\frac{E}{E_b} = \frac{1 + c\lambda}{1.52 + d\lambda} \tag{2.79b}$$

in which $a = 0.3$, $b = 0.425$, $c = 0.38$, and $d = 0.23$. The plots of the numerical and fitted relations of ν and E/E_b with respect to λ are also shown in Figure 2.34. For example, to represent a homogeneous material with $E = 30$ GPa and $\nu = 0.2$, the beam model parameters are $E_b = 37.88$ GPa and $\lambda = 1.03$.

2.5.1.2 Normal-shear spring lattice model

The normal-shear spring lattice model is characterized by the local elastic properties of the elements: the normal and shear moduli E_n and E_s, the cross-section area A and the element length l. Parameters A and l are imposed from the mesh. Two remaining parameters E_n and E_s are identified to have the macroscopic homogeneous elastic parameters E and ν of the material. To this end, different simulations are performed by varying the value of the parameter E_n as shown in Table 2.6. For each value of E_n, different values of E_s/E_n ratio in Table 2.6 are also assigned to the simulations. There are totally 36 simulations carried out.

Table 2.6 – Varying the parameters of the normal-shear spring model.

E_s/E_n [-]	0.1	0.2	0.4	0.6	0.8	1.0
E_n [GPa]	1	20	40	60	80	100

The main observation is that the computed values of Poisson's ratio ν and of the E/E_n ratio do not change when keeping the ratio E_s/E_n constant and varying E_n, see Figure 2.35 in which the evolutions of ν and E/E_n with respect to E_n corresponding to two values of E_s/E_n (0.1 and 0.8) are shown. This means that ν and E/E_n are only proportional to the ratio E_s/E_n and not to the individual values of E_n or E_s. The evolutions of ν and E/E_n with respect to the ratio E_s/E_n are shown in Figure 2.36.

Similar to the previous section, the fitted relations that relate macroscopic elastic properties and

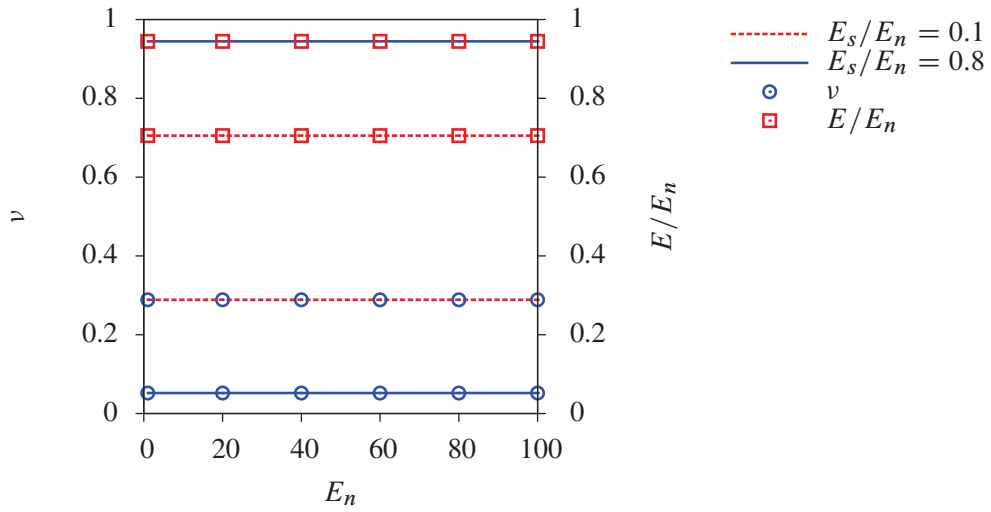

Figure 2.35 – Evolutions of ν and E/E_n with respect to E_n when E_s/E_n equals to 0.1 and 0.8.

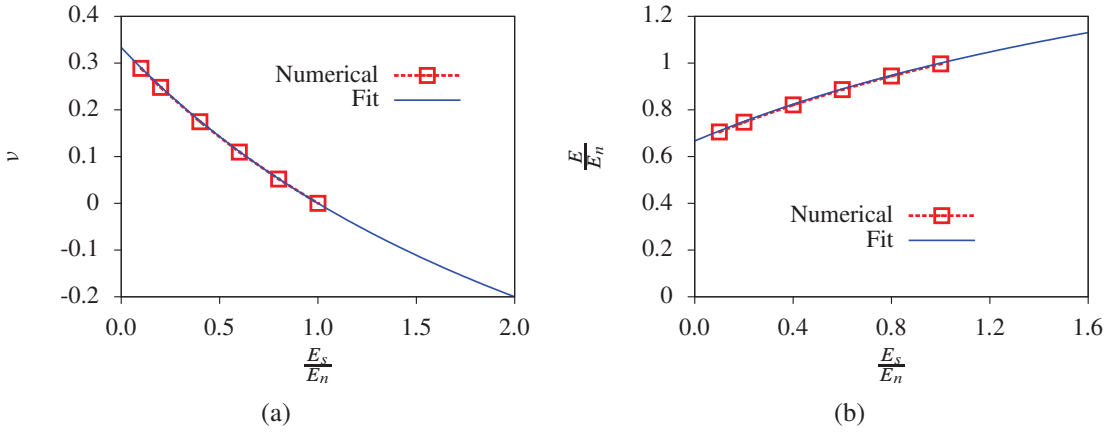

Figure 2.36 – Evolution of elastic properties with respect to the normal-shear spring model parameters: Poisson's ratio ν (a) and normalized Young's modulus E/E_n (b) depend on the ratio E_s/E_n.

the model parameters are given by

$$\nu = \frac{1 - E_s/E_n}{3 + E_s/E_n} \tag{2.80a}$$

$$\frac{E}{E_n} = \frac{2(1 + E_s/E_n)}{3 + E_s/E_n} \tag{2.80b}$$

or equivalently by

$$E_n = \frac{E}{1 - \nu} \tag{2.81a}$$

$$E_s = \frac{E(1 - 3\nu)}{1 - \nu^2} \tag{2.81b}$$

Note that the relation (2.80a) is exactly the same as that of the analytical analysis, see Chang et al. (2002b). While the ratio E/E_n of the relation (2.80b) is less than that of the analytical analysis a factor of $\sqrt{3}$. The difference is probably explained by the randomness of the lattice model because the analytical relation is obtained from the regular triangular lattice with periodic boundary conditions. As an example, to represent the homogeneous material with $E = 30$ GPa and $\nu = 0.2$, the identified parameters of the normal-shear spring lattice model are: $E_n = 37.5$ GPa and $E_s = 12.5$ GPa.

2.5.2 Identification of failure parameters

When using the fracture criterion (2.37) with $n = 5$, two parameters the local normal and shear strengths, σ_{n0} and σ_{s0}, have to be identified such that the material strengths are obtained correctly. It is recalled that whether the fine aggregates are introduced in the lattice model, values of these two parameters are randomly assigned to the lattice elements or are taken as the same for all elements. First, we present the procedure to identify σ_{n0} and σ_{s0} when disregarding the influence of fine aggregates. The identification procedure when taking into account the fine aggregates is presented in the next paragraph. Generally speaking, the two parameters σ_{n0} and σ_{s0} are identified from two material strengths, the tensile and compressive strengths, f_t and f_c, respectively. However, the thesis is only focused on tensile failure of the material. So, the local normal strength σ_{n0} is identified from the material tensile strength f_t and a study on the influence of the local shear strength σ_{s0} on f_t will be analyzed. To this end, the uniaxial tensile test on the lattice 100×100 mm^2 with the relative size $B/l_{\mathrm{m}} = 60$ is carried out by varying the values of σ_{n0} and σ_{s0} as in Table 2.7. For each value of σ_{n0}, the value of σ_{s0} is assigned to the lattice elements depending on the ratio σ_{s0}/σ_{n0} as in Table 2.7. Consequently, there are 30 simulations in total. The tensile strength of the material is calculated as the maximum tensile stress.

Table 2.7 – Varying the parameters of σ_{n0} and σ_{s0}.

σ_{n0} [MPa]	1	3	5	7	9	
σ_{s0}/σ_{n0} [-]	0.1	0.5	1	1.5	2	4

The main observation is that f_t is only influenced by σ_{n0} and the relation is linear, see Figure 2.37a. When keeping a certain value of σ_{n0} constant, varying σ_{s0} does hardly influence on f_t, see Figure 2.37b. Therefore, σ_{n0} can be directly identified from the tensile strength of the material. The value of σ_{s0}, however, should be identified from the compressive test. However, this is out of the scope of the thesis. For the following, the local shear strength σ_{s0} is taken as two or three times greater than the normal one which seems reliable (Grassl and Jirásek, 2010). As an example, to obtain $f_t = 3$ MPa, the identified value of σ_{n0} after Figure 2.37a is of 4.4 MPa.

When taking into account the fine aggregates, the local normal and shear strengths are randomly assigned to the lattice elements with the corresponding mean and standard deviation values $\bar{\sigma}_{n0}$, $\sigma_{\sigma_{n0}}$, $\bar{\sigma}_{s0}$ and $\sigma_{\sigma_{s0}}$. As above, the material tensile strength f_t allows to identify the mean value

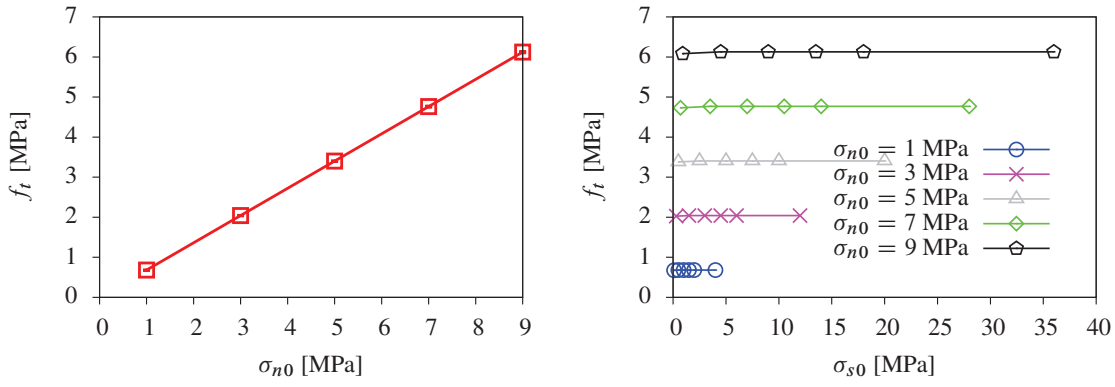

Figure 2.37 – Evolution of the tensile strength f_t of the material with respect to σ_{n0} (a) and evolution of f_t with respect to σ_{s0} when keeping σ_{n0} constants (b).

$\bar{\sigma}_{n0}$ whereas the assumed value of $\bar{\sigma_{s0}}$, does not affect mode I failure. To study the evolution of the material tensile strength with respect to the mean value $\bar{\sigma}_{n0}$ and the standard deviations $\sigma_{\sigma_{n0}}$, $\sigma_{\sigma_{s0}}$, a series of uniaxial tensile tests on the above specimen is performed by varying the parameters taken in Table 2.8. The mean value $\bar{\sigma}_{s0}$ is taken 5 MPa for all simulations. Moreover, The standard deviations of σ_{n0} and σ_{s0} are taken equal. For each value of $\bar{\sigma}_{n0}$, the standard deviation is varied 0.5, 1.5 and 3.0 MPa. There are 18 cases of simulations.

Table 2.8 – Varying the mean value of σ_{n0} and the standard deviation of σ_{n0}, σ_{s0} when keeping the mean value of $\sigma_{s0} = 5$ MPa.

$\bar{\sigma}_{n0}$ [MPa]	1	3	5	7	9
$\bar{\sigma}_{s0}$ [MPa]	5				
$\sigma_{\sigma_{n0},\sigma_{s0}}$ [MPa]	0.5	1.5	3.0		

Figure 2.38 shows the evolutions of f_t with respect to $\bar{\sigma}_{n0}$. The relation is linear when the value of the standard deviation is less than the values of $\bar{\sigma}_{n0}$ (the case of the standard deviation equals to 0.5 MPa). When increasing the value of the standard deviation, the material tensile strength f_t decreases whereas its standard deviation increases. It is excepted for the case in which the value of the mean is less than that of the standard deviation (cases $\bar{\sigma}_{n0} = 1$ MPa and the standard deviation $= 1.5, 3.0$ MPa) since all the negative generated values are replaced by the generated positive ones, see Section 2.3.1.2. This leads to more elements are assigned with larger values of σ_{n0} when increasing the value of the standard deviation. This also causes the nonlinear evolution between f_t and $\bar{\sigma}_{n0}$ close to the point in which the standard deviation is greater than the mean value. However, going far from that point, the relation becomes again linear. The maximum standard deviation of f_t is of 0.2 MPa for the case in which the standard deviations of σ_{n0} and σ_{s0} are of 3.0 MPa. Whereas they are of 0.1 MPa and 0.08 MPa for the cases in which $\sigma_{\sigma_{n0}} = \sigma_{\sigma_{s0}} = 1.5$ and 0.5 MPa, respectively.

To identify the values of the mean and the standard deviation of the local strengths, experimental data of multiple tests in which the mean and the standard deviation of the strength of the material has to be provided. In the lattice model, the material tensile strength $f_t = 3$ MPa is obtained with a standard deviation of 0.2 MPa with the parameters $\bar{\sigma}_{n0} = 6.9$ MPa and $\sigma_{\sigma_{n0}} = \sigma_{\sigma_{s0}} = 3$ MPa.

2.5.3 Model parameters for heterogeneous materials

If the generated grain structure is used to implement heterogeneity, different strengths and stiffnesses are assigned to the lattice elements according to their position. The ratios of the different

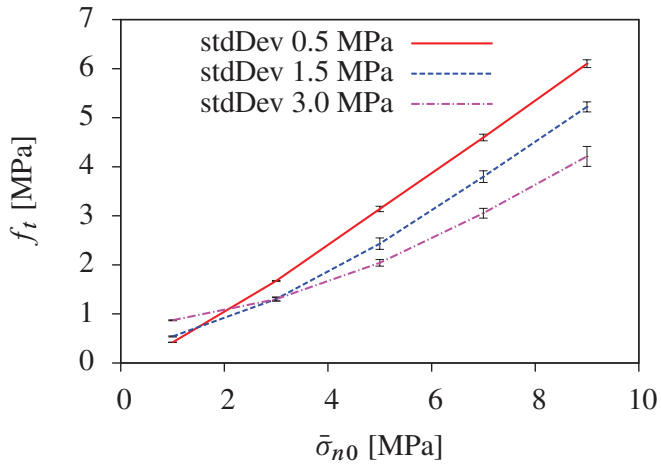

Figure 2.38 – Evolution of the tensile strength f_t of the material with respect to $\bar{\sigma}_{n0}$.

stiffnesses and strengths between the phases (aggregate, matrix and ITZ) are important. These ratios can be related to experiments. The stiffness and strengths of the matrix phase can be regarded as reference values. Once the reference values are known, the values of stiffnesses and strengths of the other phases can be easily deduced from the ratios of stiffnesses and of strengths between the corresponding phase (aggregate or ITZ) and the matrix phase, respectively.

A tensile test can be carried out on a specimen with an explicit representation of the generated grain structure in order to identify the reference values of stiffnesses and strengths of the matrix phase such that the specimen can represent a material with given macroscopic properties such as Young's modulus, Poisson's ratio and material tensile strength.

It is clear that when the ratios of the different stiffnesses and strengths between the material phases change, other values of the identified parameters will be obtained. Therefore, it does not exist a unique set of parameters for a given macroscopic properties.

The following example shows a procedure to identify the parameters of the normal-shear spring lattice model so that the modeled material can represent the heterogeneous material with the macroscopic properties: Young's modulus $E = 30$ GPa, Poisson's ratio $\nu = 0.2$, and tensile strength $f_t = 2.4$ MPa. The composition of the grain structure with $d_{\max} = 12.5$ mm is shown in Table 2.9 with the total volume fraction of grain is of 45%. The tensile test is carried out on the specimen 100×100 mm^2 with the notch of 10×2 mm^2, see Figure 2.39. The ratios of the different stiffnesses and strengths between the matrix (M), the aggregate (grain) (A) and the ITZ (I) are given in Table 2.10. The values of these ratios are chosen in the same order of magnitude of the differences of stiffnesses and strengths between the aggregate, mortar and ITZ of concrete material, see, e.g., Hsu and Slate (1963). With these assumed ratios, the parameters of the lattice model are only the stiffnesses and strengths of the matrix phase.

The tensile test is carried out using the normal-shear spring lattice model with the fracture law (2.37) with $n = 5$ and the used mesh has the size ratio $B/l_{\mathrm{m}} = 100$ with B the specimen width and l_{m} the mean length of the elements. The identified parameters of the matrix phase are: $E_n = 24.5$ GPa, $E_s = 6.5$ GPa, $\sigma_{n0} = 13.5$ MPa, $\sigma_{s0} = 27$ MPa in order to have the macroscopic properties $E = 30$ GPa, $\nu = 0.2$, and $f_t = 2.4$ MPa. The corresponding values of the aggregate and ITZ phases can be easily deduced from Table 2.10.

2.5.4 3D tensile test of homogeneous material

The uniaxial tensile test is carried on the cubic specimen of $100 \times 100 \times 100$ mm^3 using the normal-shear spring lattice model with the parameters given in Table 2.11. The corresponding macroscopic properties and tensile strength are: $E = 19.5$ GPa, $\nu = 0.25$ and $f_t = 3$ MPa. The specimen

Table 2.9 – Volume fraction of each aggregate segment of the aggregate structure obtained from the Fuller's grading.

$d_{\max}$ [mm]	Aggregate segment [mm]	Sieve size [mm]	Sieve passing [%]	V_{Agg} [%]	$V_{\text{Agg}}^{\text{abs}}$ [%]
	0–3.15	3.15	0	0	0
	3.15–4	4	30.15	30.15	13.57
	4–5	5	44.48	14.33	6.45
12.5	5–6.3	6.3	58.04	13.56	6.10
	6.3–8	8	72.02	13.98	6.29
	8–10	10	85.59	13.57	6.11
	10–12.5	12.5	100	14.41	6.48

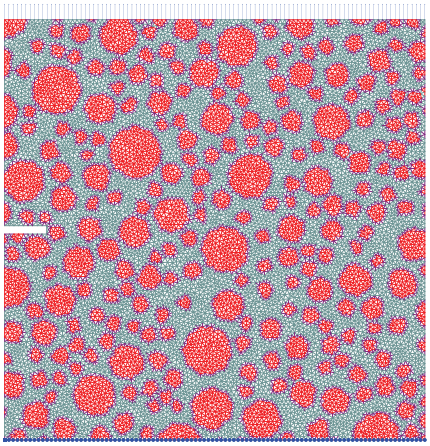

Figure 2.39 – Tensile test on the specimen 100×100 mm^2 with the notch of 10×2 mm^2.

Table 2.10 – Ratios of the different stiffnesses and of strengths between the matrix phase (M), aggregate phase (A) and the ITZ (I).

	E_n, E_s	σ_{n0}, σ_{s0}
$\frac{A}{M}$ ratios	3	2
$\frac{I}{M}$ ratios	1.5	0.33

is loaded by imposing the vertical displacement increment to the nodes on its top boundary while vertically fixing the nodes on the bottom boundary. This simulates the loading due to the non-rotating end platens. Since the computational effort increases considerably in 3D simulations, a coarse mesh with $B/l_{\mathrm{m}} = 20$, where B stands for the specimen size and l_{m} is the mean length of the lattice elements, is used. Neither generated grain structure nor random field of strengths is introduced in the description of the material. The fracture law expressed by Equation (2.37) with $n = 5$ is used in the simulation.

Table 2.11 – Input parameters for 3D simulation.

E_n [GPa]	E_s [GPa]	σ_{n0} [MPa]	σ_{s0} [MPa]
33.5	11	6	12

The development of cracks in the specimen is shown by plotting crack history at different stages, see Figure 2.40. The labels in Figure 2.40 indicate the corresponding positions in the load-displacement curve (see Figure 2.41). Figure 2.41 shows the load-displacement curve of the simulation. The envelope of the load-displacement curve is shown as well. The displacement is measured by the LVDT-type sensor with the length of 60 mm mounted along the vertical direction in the middle of the specimen volume. It is seen that the microcracks develop before the peak load is reached. It is in agreement with the observation in concrete material, see e.g., Prado and van Mier (2003) and van Mier (2008).

Moreover, it is observed that the load-displacement response is more brittle than the response usually observed for concrete material. The reason here is that the element length is very large and, as a result, small material bridges could not be obtained, in conjunction with the brittle elastic parameters used. Nevertheless, the load-displacement response should be less brittle when the heterogeneity of the material is introduced by including a grain structure in the model.

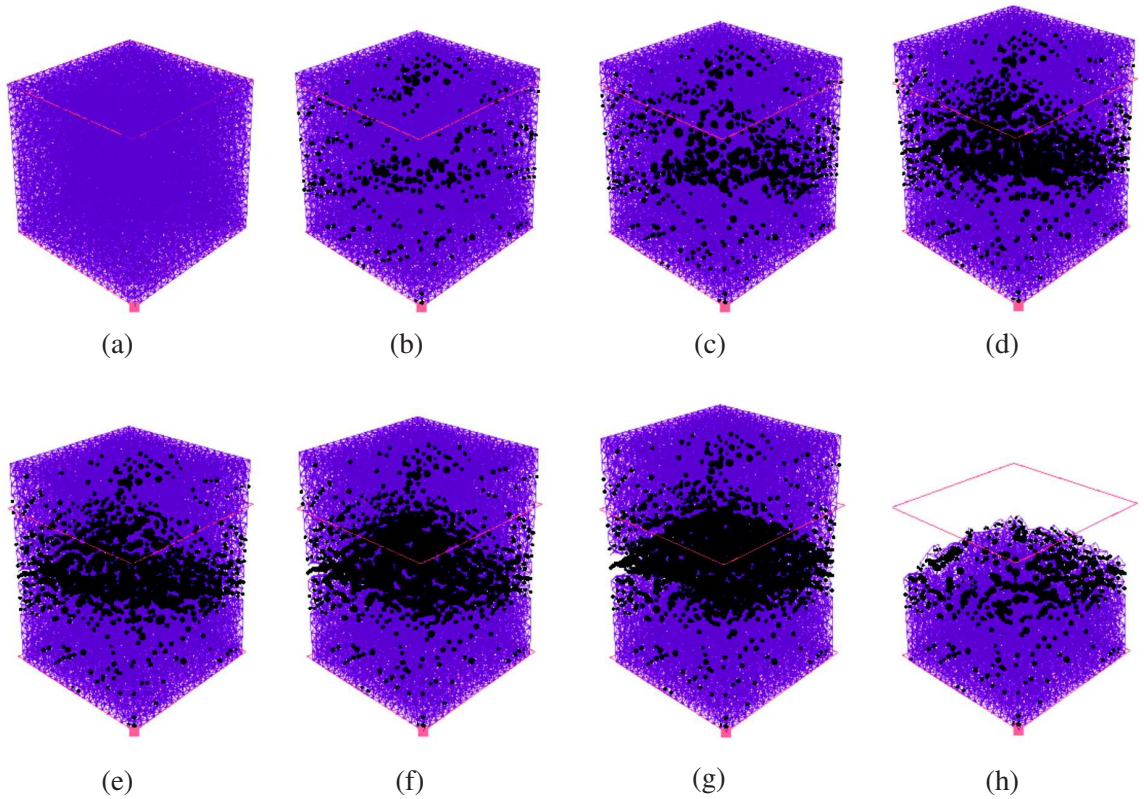

Figure 2.40 – Development of cracks in homogeneous material using the 3D lattice simulation.

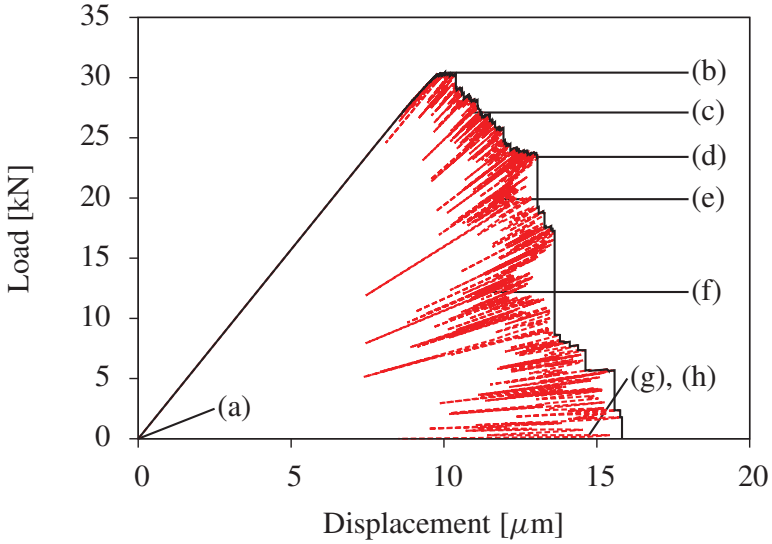

Figure 2.41 – Load-displacement curve of the homogeneous material at the different stages corresponding to the labels shown in Figure 2.40.

2.5.5 3D tensile test of heterogeneous material

The same specimen geometry and boundary conditions as in the previous section are used here for studying the cracking process of heterogeneous material. Only three grain particles with diameters equal to 26, 40, 26 mm are introduced in the simulation, see Figure 2.42a. The same mesh as the previous section is used. The material is modeled as the three-phase material with the weak ITZ (I) in-between the matrix (M) and aggregate (A) phases. The ratios of the different stiffnesses and strengths between the matrix, the aggregate, and the ITZ are given in Table 2.10, see Section 2.5.3. For a comparison with the homogeneous material case in terms of the load-displacement curve (Figure 2.41), the parameters of the model for the heterogeneous material are identified such that the load-displacement curve has the same initial slope and the peak load as those of the homogeneous material. The identified parameters of the matrix phase are: $E_n = 30$ GPa, $E_s = 8$ GPa, $\sigma_{n0} = 7.4$ MPa, $\sigma_{s0} = 14.7$ MPa.

Figure 2.42 shows the development of cracking process in the heterogeneous material. The labels of the crack patterns indicate the corresponding position in the load-displacement curve (see Figure 2.43). Figure 2.43 shows the load-displacement curve of the simulation together with its envelope. The displacement is again measured by the LVDT-type sensor with the length of 60 mm mounted along the y-direction in the middle of the specimen volume like in the simulation of the homogeneous material. The main observation is that the crack is initiated at the ITZs which are the weakest links of the material (Figure 2.42b). Then, the microcracks develop also in the matrix phase before the peak load is reached (Figure 2.42c). After that, upon the loading increase, the microcracks appear more and more and coalesce to form a curved crack surface, making the load-carrying capacity decreases gradually. This accounts for the softening behavior in the post-peak regime.

By plotting the envelopes of the load-displacement curves of both the homogeneous and heterogeneous materials in the same diagram, cf. Figure 2.44, it is seen that the load-displacement response of the heterogeneous material is less brittle than that of the homogeneous material. Quite obviously, this is due to the effect of the grain particles that make the crack surface more tortuous, which leads to the roughness of the crack faces (cf. Figure 2.42h compared to Figure 2.40h). It leads to the conclusion that when more small grain particles are introduced in the model, the brittleness of the load-displacement response should be decreased. However, doing so, the mesh size is needed to be reduced as well, which leads to a massive computational effort.

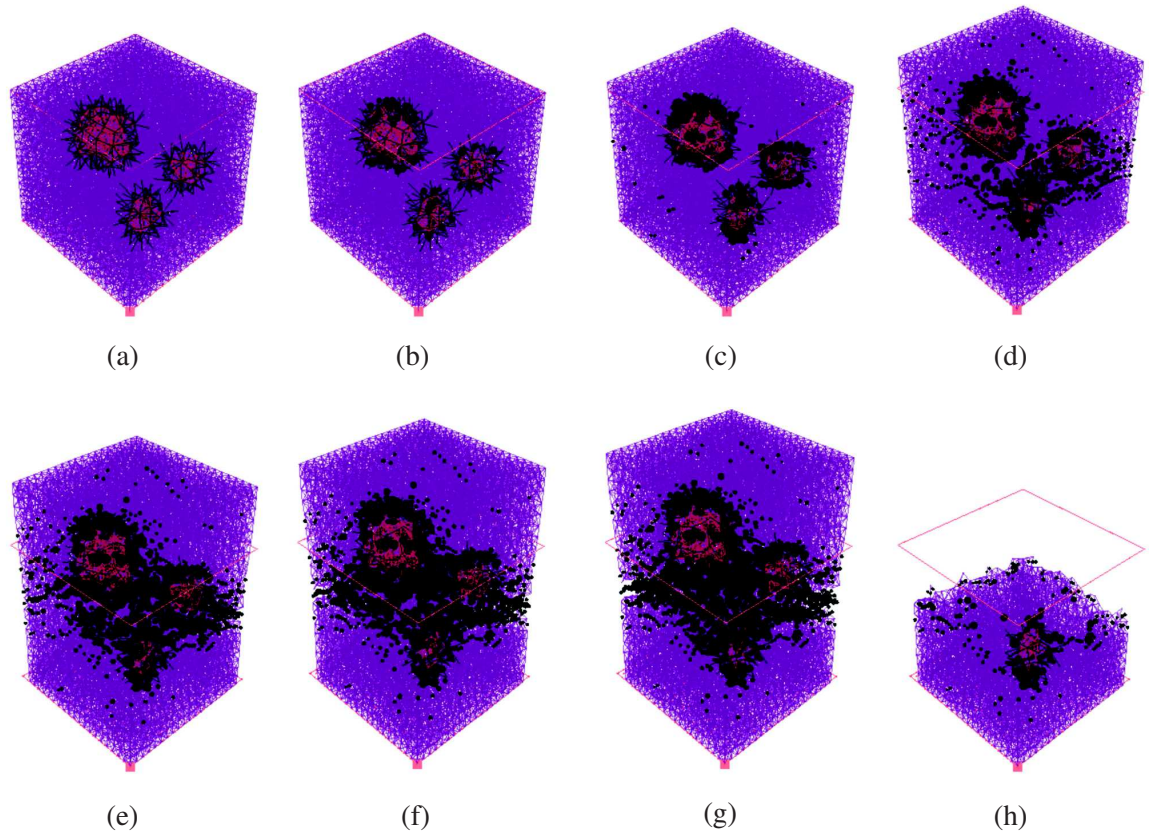

Figure 2.42 – Development of cracks of the heterogeneous material using 3D simulation.

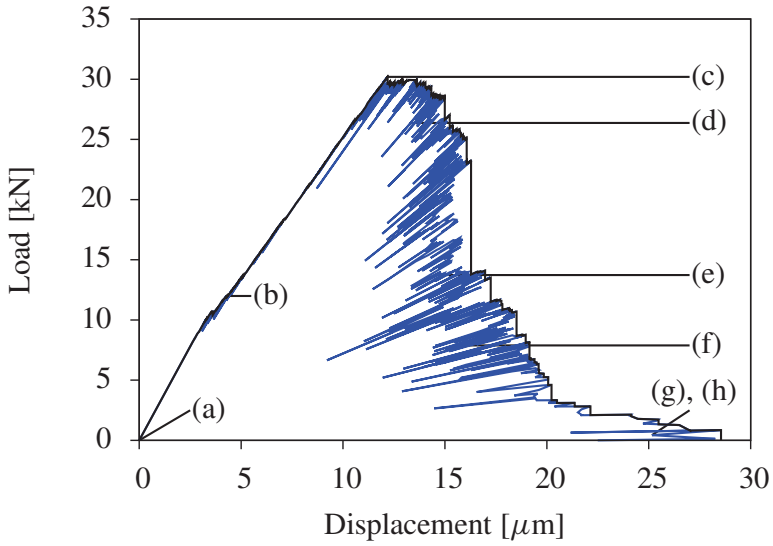

Figure 2.43 – Load-displacement curve of the heterogeneous material at the different stages corresponding to the labels shown in Figure 2.42.

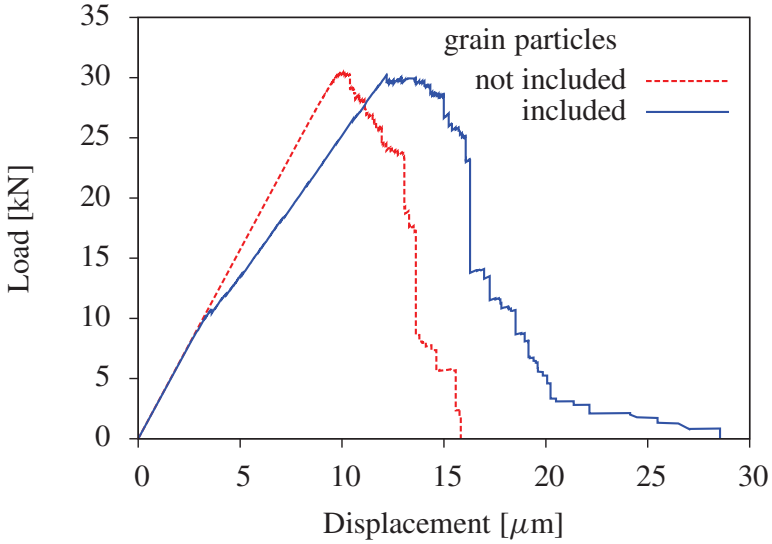

Figure 2.44 – Load-displacement responses of the homogeneous (grain particles are not included) and heterogeneous (grain particles are included) materials.

2.5.6 2D single-edge-notched tensile test

The single-edge-notched (SEN) specimen used to identify the model parameters for heterogeneous material, see Section 2.5.3, is reused in this section for performing the tensile test. The specimen dimension is 100×100 mm^2 with the notch of 10×2 mm^2. The simulation is carried out using the normal-shear spring lattice model with the parameters, the mesh used and the grain structure with $d_{\max} = 12.5$ mm, described in Section 2.5.3. The material is modeled as the three-phase material. The specimen is pulled out by imposing the vertical displacement on the nodes on the top boundary while vertically fixing all the nodes of the bottom boundary.

Figure 2.45 shows the load-displacement response of the specimen and its envelope. The displacement is computed by the LVDT-type sensor with the length of 35 mm mounted along the vertical direction in the middle of the specimen. The crack patterns corresponding to the positions (a), (b), (c) and (d) of the load-displacement curve are shown in Figure 2.46. It is seen again that the microcracks appear at the ITZ positions before the peak load is reached. From the peak load to the (c) position, the load-carrying capacity of the specimen decreases with respect to the increase of the measured vertical displacement. At the (c) position, two main separated cracks are formed, cf. Figure 2.46c. There is no doubt that the heterogeneity of the material increases due to these two cracks. From the (c) position, under the prescribed displacement, it is quite possible that the material is rotated in the middle of the bridge between these two cracks. This leads to the fact that the load-carrying capacity of the specimen increases upon crack bridging. After finishing the bridging process, only one main crack is finally formed and crosses the specimen section, cf. Figure 2.46d.

The broken elements of the final crack pattern shown by black dots in Figure 2.46d can be separated by the elements with largest opening, shown by the black dots in Figure 2.47a, and the remaining broken elements shown by the blue dots. The black and blue dots can be read as the macrocrack and the microcracks, respectively. The cumulative fracture energy dissipated (Nm) by these broken elements is shown by the colormap in Figure 2.47b.

2.6 Conclusions

The concept of the lattice model has been presented in this chapter. Local fracture of elements is brittle. Different fracture criteria are implemented for studying their influence on the failure behavior of the material. From that, one fracture criterion which is appropriate for mode I failure

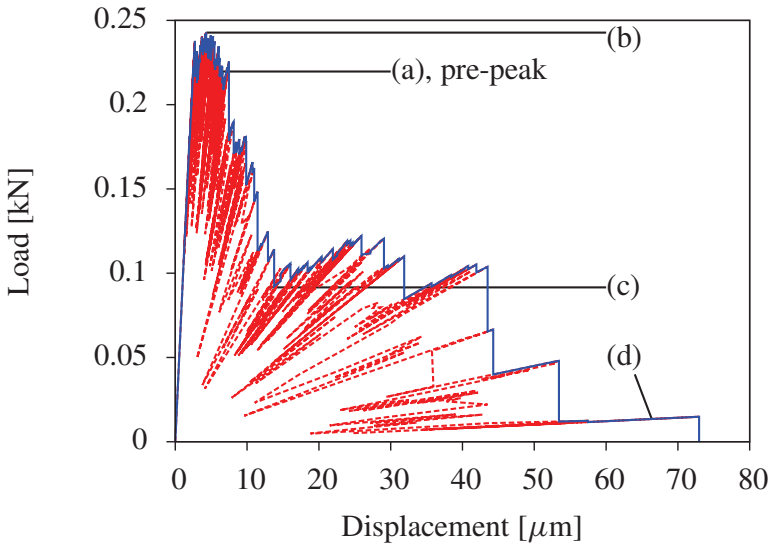

Figure 2.45 – Load-displacement response of the SEN tension test.

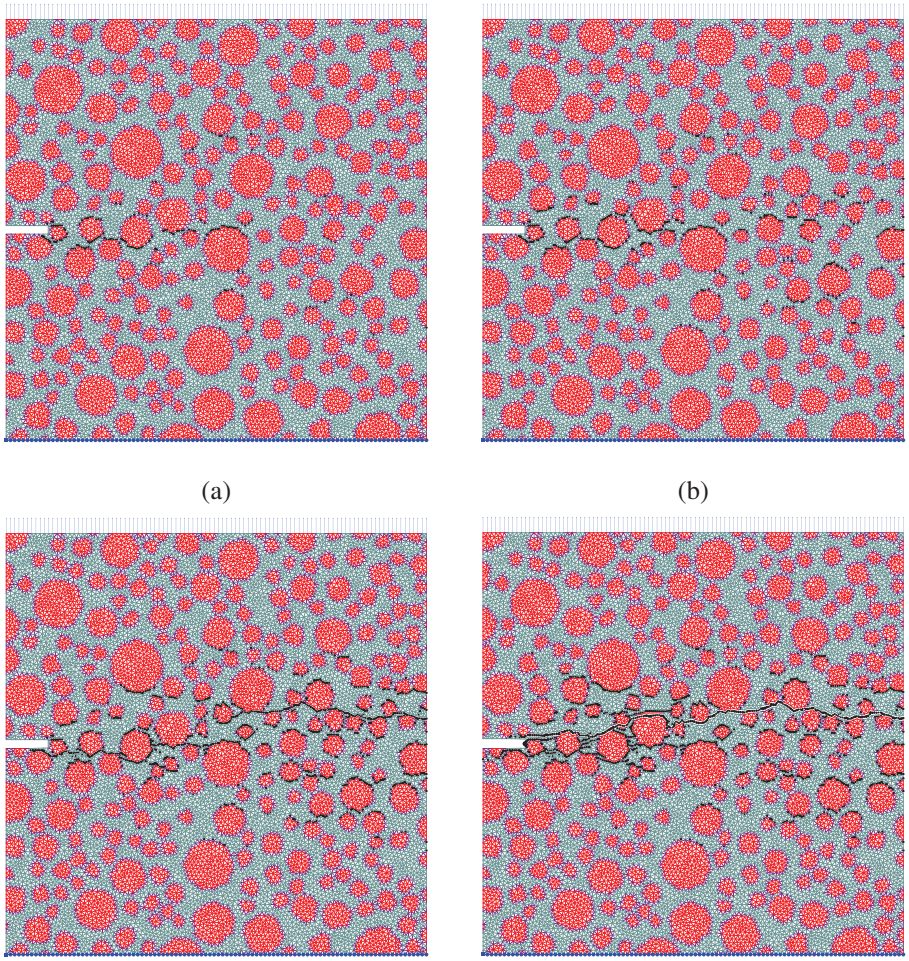

Figure 2.46 – Cracks develop in the specimen at different stages with the labels corresponding to the positions of the load-displacement response shown in Figure 2.45.

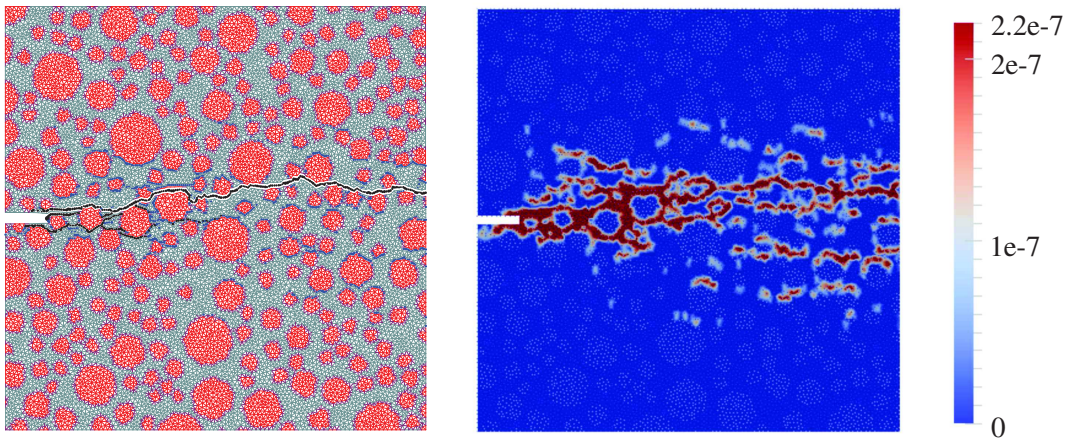

(a) (b)

Figure 2.47 – The black dots indicate broken elements with the largest opening – read as the macrocrack – while the blue dots stand for the remaining broken elements – read as the microcrack (a); Colormap of the cumulative fracture energy of the elements (Nm), the grain structure is superimposed and represented by the light gray dots (b).

is adopted for later simulations. Methods used to implement the heterogeneity of the material are also presented in details. The determination of the size of lattice elements is discussed as well. The parameter study is performed to identify the model parameters so that the lattice model can simulate a material with given elastic properties and failure strength. Several tensile tests on 2D and 3D specimens are performed to show the capacity of the lattice model. The following conclusions can be drawn:

- The model is extremely simple since it only makes use of a linear elastic analysis.
- The lattice model is very suitable for studying of cracking process in heterogeneous material.
- Even though only the brittle elastic parameters are used, a global ductile behavior can be obtained by implementing the heterogeneity of the material.

Chapter 3

Studying the origin of characteristic length and FPZ size

Contents

This chapter deals with agents at the mesoscopic scale such as size, volume fraction, size dispersion of the aggregate structure as well as at the macroscopic scale like stress gradient, boundary conditions etc., that affect the resulting size of the Fracture Process Zone (FPZ) and the characteristic length of concrete-like material. The reason for that study is addressed first. Methods for the assessment of the FPZ size and the characteristic length of the material are next presented. Then, parameters that control the aggregate structure of the material are shown, followed by an extensive study of their effects on the FPZ size and characteristic length of the material. The chapter is closed by some drawing conclusions.

3.1 Introduction

Fracture of quasi-brittle materials is characterized by a zone with a finite size around and ahead the crack tip, in which damage occurs and causes the softening behavior of the materials. This is the fracture process zone (FPZ). For concrete, as stated before, the size (width) of the FPZ, denoted by ℓ_{FPZ} hereafter, is believed to be proportional to the maximum aggregate size $d_{\max}$, see, e.g., Bažant and Oh (1983) and Pijaudier-Cabot and Bažant (1987). Therefore, in nonlocal models (gradient or integral form), the FPZ size which only depends on the internal length ℓ_{c} introduced, depends on (is proportional to) the maximum aggregate size. Accordingly, neither loading nor structural effect is considered to affect the resulting size of the FPZ except in the latest integral nonlocal model proposed by Giry et al. (2011). However, in the latter, the internal length parameter is related to the maximum aggregate size and also depends on the stress state. Figure 3.1 shows a schematic representation of modeling procedure using a nonlocal model.

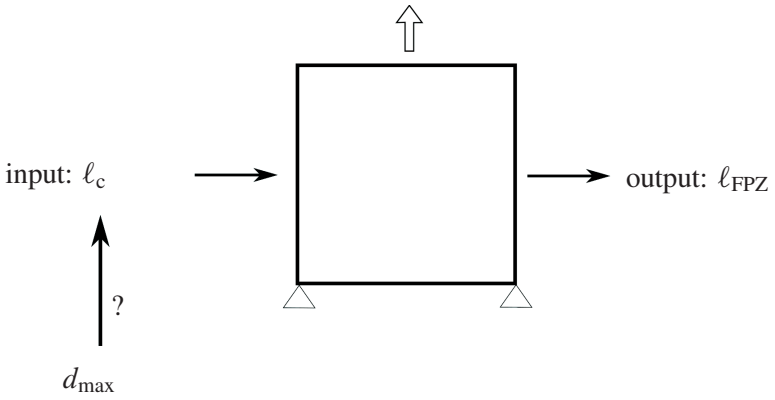

Figure 3.1 – Based on the maximum aggregate size $d_{\max}$, a value of ℓ_{c} is chosen as an input of a nonlocal model for fracture analysis which provides a FPZ size ℓ_{FPZ}.

The literature often reports a linear or affine relation between ℓ_{c} and $d_{\max}$, see, e.g., Bažant and Pijaudier-Cabot (1989) and Otsuka and Date (2000). But actually, varying $d_{\max}$ in experiments may lead to a number of changes in the aggregate structure characterized by other parameters such as the volume fraction of aggregate, their size dispersion, their fabric or connectivity. Basic questions may be raised: what does affect the internal length of a nonlocal model? Is it only the maximum size of aggregates or some less obvious parameter(s)? Does the loading or the structure size itself play a role in the internal length?

To address these questions, numerical simulations of uniaxial tensile tests are carried out using the lattice model in which the geometry and mechanical properties of the material mesostructure are explicitly introduced. The output of the simulations is the FPZ size ℓ_{FPZ} and the characteristic length of the material. The characteristic length is *a priori* regarded as the internal length that would be introduced in nonlocal models. The same notation ℓ_{c} is thus used in the following. From the lattice simulations, we would like to find out the relation between the two lengths ℓ_{FPZ} and ℓ_{c}, and some relevant characteristics of the material mesostructure. The study is restricted to the case of

two-dimensional analysis of a brittle elastic model material with circular inclusions. The presence of a weak interfacial transition zone (ITZ) in-between inclusions and matrix is whether considered or not.

It is important to stress before reading the following that the inclusions and matrix have a brittle elastic behavior together with highly simplified geometry. Since we are on the way to approach the behavior of concrete material, the terms inclusions and matrix are often willingly replaced by aggregates and mortar, respectively, just like in concrete. We are aware that this is a misnomer given the complexity of real concrete mesostructure, but it allows one to keep in mind the primary goals of the study. As a consequence, our observations and conclusions must be translated with caution to the case of real concrete.

3.2 Determination of FPZ size and material characteristic length

3.2.1 Fracture process zone size

In the model, the overall energy is stored in the form of elastic energy in each element. The fracture energy of the entire material is the sum of all elastic energy dissipated by the rupture of each element. A density map of the dissipated elastic energy can thus be drawn. Based on this map, the size of the FPZ can be determined by analyzing the density distribution of dissipated energy around the macrocrack. This distribution, when represented as a probability density function (pdf), can be fitted by a Gaussian distribution in order to extract a width. Rather than that, we choose to rely on the cumulative density function (cdf) of the dissipated energy to determine the size of the FPZ since that curve can be more smoothly defined by sorting the dissipated energy along a direction. The direction chosen here is the one perpendicular to the mean direction of the final crack which may not be strictly perpendicular to the loading direction depending on the microstructure setting. As shown in Figure 3.2, the cdf will be generated along the y_1-direction set perpendicular to the mean direction x_1 of the final crack. Doing so, the difference in y-direction between two end points of the final crack is not taken into account in the resulting fracture process size.

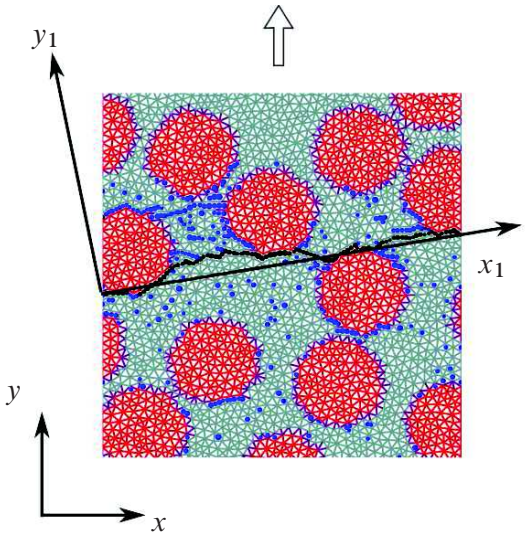

Figure 3.2 – The mean direction of the final crack.

The cumulative form of the dissipated energy density is then fitted by the cdf of a normal distribution expressed as

$$F(x) = \frac{1}{2}\left[1 + \mathrm{erf}\left(\frac{x-\mu}{\sigma\sqrt{2}}\right)\right] \tag{3.1}$$

where 'erf' stands for the Gauss error function defined by two parameters: the mean μ and the standard deviation σ. The width of the FPZ is hence estimated four times larger than the value of

the standard deviation σ. This approximation provides a width of the zone that contains about 95% of the dissipated energy. An example to determine the FPZ size based on the lattice simulation is presented in Section 3.2.4.

3.2.2 Material characteristic length

As stated in Chapter 1 a length parameter (internal length), denoted as ℓ_c, is required for simulating the failure of the heterogeneous material using continuum nonlocal models. This length is required for reproducing the heterogeneity of the material. This length is directly related to the characteristic length of the material. However, it is not simple to deduce the value of the internal length from the characteristics of the material such as the size and the distribution of the constituents at the material scale, e.g., the aggregate scale. To better understand the correlation between the internal length and the characteristic of the material mesostructure, numerical simulations using the lattice model are proposed since the variation of the size and the distribution of the material constituents can be explicitly and easily introduced for verifying their influence on the internal length. To estimate the value of the internal length of the material which is modeled by the lattice model, we use the method proposed by Bažant and Pijaudier-Cabot (1989). The basic idea is that the internal length of the material is approximated as the *effective* width h of the zone in which the fracture energy of the material is dissipated. This effective width is defined as the ratio of the fracture energy G_f (energy per unit area of crack surface) dissipated by the cracking that localizes in a narrow band of the specimen in one type of the tensile test and the *energy density* W_s dissipated by the cracking that is nearly homogeneously distributed in the whole volume of the specimen of the same material in another type of tensile test. Finally, the internal length of the material is given by

$$\ell_c \simeq h = \frac{G_f}{W_s} \tag{3.2}$$

To evaluate ℓ_c by the lattice model, both numerical tensile tests have to be performed to determine G_f and W_s. G_f is determine from the tensile test performed on a notched specimen so that the damage can be localized whereas W_s has to be determined from the tensile test carried out on an unnotched specimen such that the damage is as homogeneously as possible distributed in the specimen volume. To this end, the numerical simulations of tensile tests using the lattice model can be performed in which the tensile loading is indirectly applied to the notched and unnotched specimens by elongating the steel bars "glued" to the specimens as proposed by Bažant and Pijaudier-Cabot (1989), see Figure 3.3. The main difference between the two types of tensile tests is that the steel bars are only glued to the ends of the notched specimen within a certain length while they are entirely glued to the unnotched specimen within the whole height of the specimen. For the following, the tensile tests performed on notched specimens, where the **L**ocation of **D**amage is forced, are referred to as LD-tests. The tensile tests performed on unnotched specimens, designed to identify **D**istributed **D**amage, are mentioned as the DD-tests. These tests are known as the PIED (Pour Identifier l'Endommagement Diffus) tests in the French community, as introduced by Fokwa (1992). Note however that a diffused damage is actually not achievable, that is why we prefer to talk about distributed rather than diffused damage. In the lattice simulations, the steel bars are also discretized by the lattice elements but their stiffnesses are set 10 times greater than those of the material tested and they always have an elastic behavior. An example to point out the measurement of the internal length ℓ_c by lattice simulations is presented in Section 3.2.4.

3.2.3 Numerical samples and mechanical parameters

Tensile tests using the lattice model are carried out to determine the FPZ size ℓ_{FPZ} and the material characteristic length ℓ_c. The FPZ size ℓ_{FPZ} is determined by fitting the cumulative density curve of the dissipated energy of a localized tensile test while the characteristic length ℓ_c is assessed from the dissipated energies of both localized and distributed tensile tests on notched and unnotched

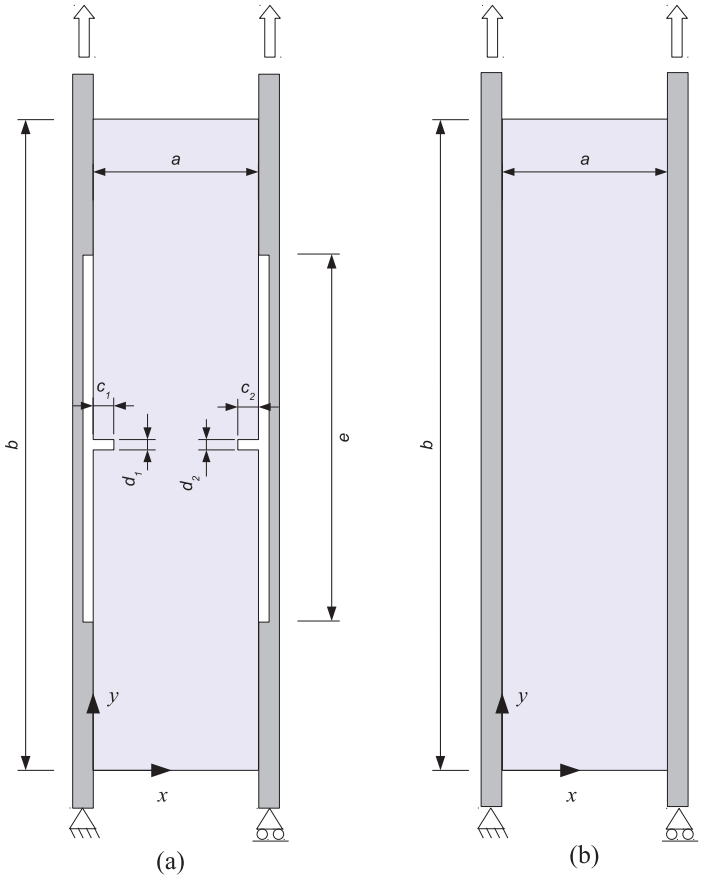

Figure 3.3 – The tensile test performed on the notched specimen to obtain the localized cracking process (a) and on the unnotched specimen to obtain the distributed cracking process (b).

specimens, respectively. Figure 3.3 shows the configuration of the specimens used in the study. Six types of localized tensile tests, A-type, B-type, B1-type, C-type, C1-type and D-type, in which there are differences in specimen size, notch types (two or only one notch), loading equipment (with or without steel bars) are performed to examine the effect of specimen size and boundary conditions on ℓ_{FPZ}, with the dimensions given in Table 3.1. Only A-type tensile tests are carried out by elongating the steel bars glued to the specimen. B-, B1-, C-, C1- and D-type specimens are loaded in tension by directly imposing the vertical displacement increment on the nodes of the top boundary of the specimens while vertically fixing the nodes of their bottom boundaries. C1- and D1-type specimens have only one notch on the left side whereas A-, B-, C- and D-type specimens have two symmetric notches on left and right sides. The six types of LD-tests are schematically shown in Figure 3.4. The characteristic material length ℓ_c is determined from the A-type localized tensile tests and the distributed tensile tests (Figure 3.3b).

Table 3.1 – Specimen dimensions [mm].

Tests designed for:		Localized damage						Distributed damage
		A-type	B-type	B1-type	C-type	C1-type	D-type	
Sizes	a	40	40	40	40	40	40	40
	b	160	160	160	40	40	20	160
Left notch	c_1	5	5	5	5	5	5	0
	d_1	1	1	1	1	1	1	0
Right notch	c_2	5	5	0	5	0	5	0
	d_2	1	1	0	1	0	1	0
Unglued height	e	90	–	–	–	–	–	0

As presented in Chapter 2, in the mode-I failure, the normal-shear spring model can be used instead of the beam model to gain in computational time. The model parameters are shown in Table 3.2. It is noted that we are only interested in the influence of the size and the distribution of the aggregate particles of concrete-like material on the resulting FPZ size and characteristic length. The stiffnesses and strengths of the aggregates are taken 10 times higher than those of the matrix while in turn the stiffnesses and strengths of the matrix are twice greater than those of the ITZ. These relative magnitudes of the stiffnesses and strengths are used for the following studies even though the relative stiffnesses and strengths between aggregates and matrix are higher than those of a real concrete. Using the parameters given in Table 3.2, a tensile test performed on the A-type specimen made of the three-phase material defined by explicitly generating a monodisperse aggregate structure with the size and volume fraction of aggregate particles are 6 mm and 45%, respectively, provides the macroscopic properties of the modeled material being: $E = 25$ GPa, $\nu = 0.2$ and the tensile strength $f_t = 2.4$ MPa.

Table 3.2 – Elastic and strength parameters used in the bulk of each phase.

	Matrix	Aggregates	Interface
E_n [GPa]	16.50	165.00	8.25
E_s [GPa]	5.10	51.00	2.55
σ_{n0} [MPa]	6.07	60.70	3.04
σ_{s0} [MPa]	18.21	182.10	9.11

3.2.4 Practical examples for the assessment of FPZ size and characteristic length

The aggregate structure used in this section has the monodisperse distribution with the aggregate size $d = 6$ mm. The reference volume fraction of aggregates is 45%. The A-type localized tensile test and the distributed one are used. The tested specimens are discretized with the mean length

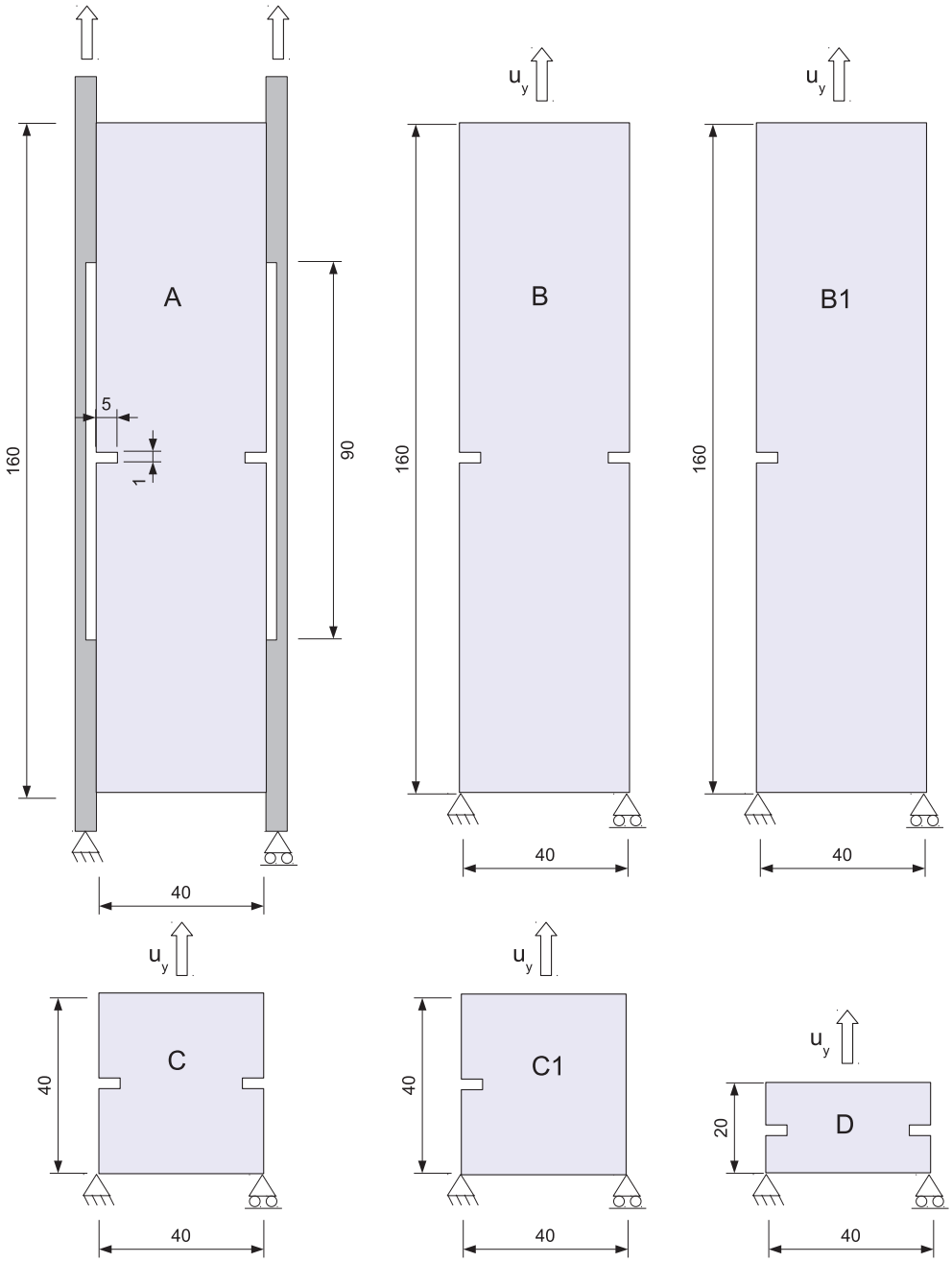

Figure 3.4 – Six types, A-, B-, B1-, C-, C1- and D-type, of localized tensile tests used to study the influence of the stress gradient applied to the tested specimens on the resulting FPZ size ℓ_{FPZ}.

of the lattice elements is of $l_{\mathrm{m}} = 0.95$ mm. The material is modeled as the three-phase one and no random field of strengths is introduced in the mortar phase. For stress and strain analysis, the out-of-plane dimension is unity, i.e. 1 mm.

Figure 3.5 shows the force-displacement curve obtained from the localized tensile test and the stress-strain curve given by the distributed tensile test. The corresponding crack patterns are also presented. It is seen that there is only one macro crack which traverses the notched specimen while about fifteen macro cracks cross over the unnotched specimen. The FPZ size ℓ_{FPZ} is obtained by fitting the cumulative density curve of the dissipated energy of the localized tensile test as shown in Figure 3.6. It is noteworthy that the cumulative dissipated energy is normalized between 0 and 1 in order to be fitted by a cdf of the Guassian distribution. The FPZ size is taken as 4 times the fitted standard deviation resulting in $\ell_{\mathrm{FPZ}} = 4.92$ mm.

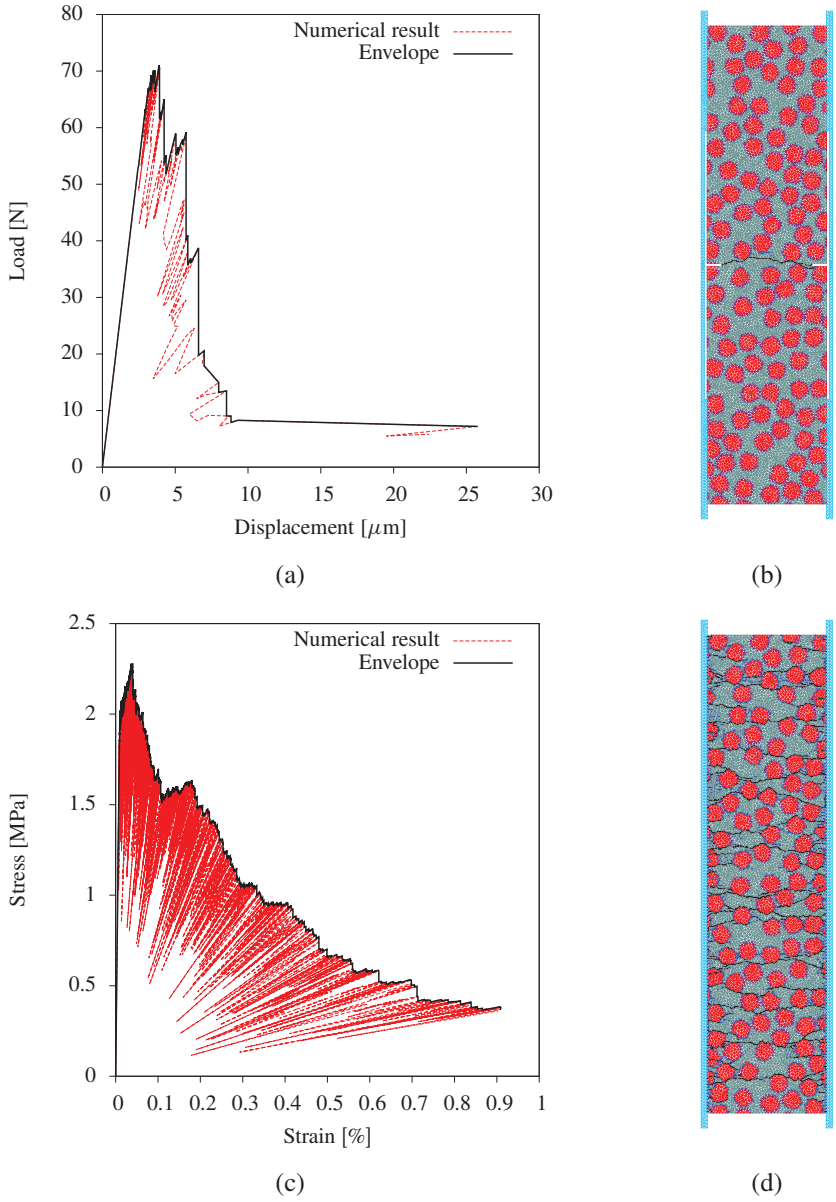

Figure 3.5 – The force-displacement curve (a) and the corresponding crack pattern (b) of the localized tensile test on the notched specimen; the stress-strain curve (c) and the crack pattern (d) of the distributed tensile test on the unnotched specimen.

The characteristic length ℓ_{c} of the material is evaluated from the dissipated energy per unit area of crack surface G_f and from the dissipated energy density W_s of the localized and distributed tensile

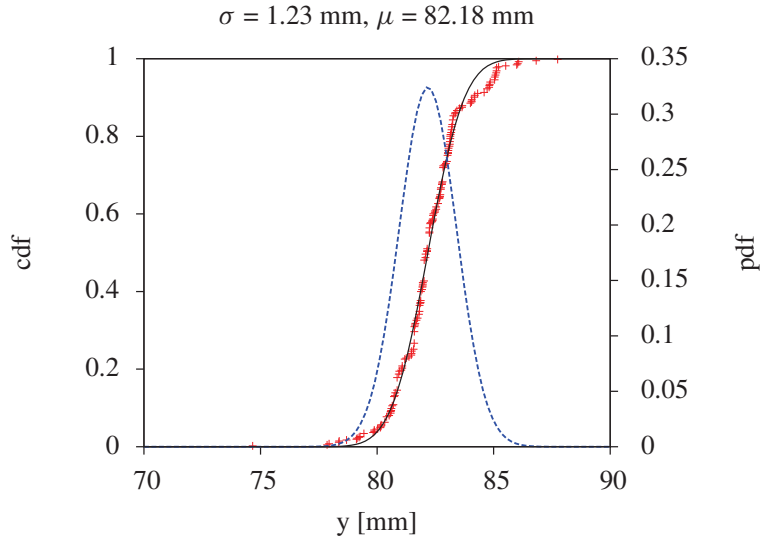

Figure 3.6 – Fitting the cumulative density curve of the dissipated energy of the notched specimen by the cdf of Guassian distribution with two parameters $\mu = 82.17$ mm and $\sigma = 1.23$ mm; the corresponding probability density function (pdf) is also shown.

tests, respectively. The values of G_f and W_s are 3.95 N/m and 809.43 N/m^2, respectively, which result in the value of ℓ_c to be 4.88 mm. Note that the values of G_f and W_s should not be taken from the corresponding areas under the macroscopic force-displacement and stress-strain curves since the last ones often overestimate the values of G_f and W_s. G_f and W_s were directly computed from the stored elastic energies of the broken elements instead.

It is, however, necessary to point out that the FPZ size ℓ_{FPZ} and the characteristic length of the material ℓ_c also result from the mesh size, i.e. the lattice element size. In fact, the non-null values of ℓ_{FPZ} and ℓ_c are obtained from the localized and distributed tensile tests in which the same parameters as before are used except that no aggregate structure is introduced, i.e., the material is modeled as homogeneous with only one matrix phase. The behavior curves and the corresponding crack patterns of the localized and distributed tensile tests are shown in Figure 3.7. It is observed that the straighter macrocrack is obtained for the localized tensile test and there are about 18 macrocracks crossing over the specimen of the distributed tensile test. Using the same method as before, one gets $\ell_{FPZ} = 2.11$ mm and $\ell_c = 2.34$ mm. As expected, these values are smaller than the values of the heterogeneous material. In the case of homogeneous material, the FPZ size and the characteristic length are proportional to the mesh size which has a finite value. This is a transparent problem and is acceptable because of the non-null size of the lattice elements. However, it is expected that the FPZ size and the characteristic length due to the mesh do statistically tend to zero under mesh refinement. An analysis of the mesh-size influence on the FPZ size is presented in Section 3.2.5.

3.2.5 Mesh-size induced length

To analyze the influence of lattice element sizes on the FPZ size, a series of tensile tests on the notched specimen (Figure 3.3a) is performed in which the specimen is discretized with five different mean values of the mesh size l_m. Furthermore, for each discretization, five independent meshes are generated by randomly moving the nodes using the procedure presented in Section 2.2.3.1 to take into consideration of mesh orientation effect on ℓ_{FPZ}. Accordingly, it results in 25 generated meshes that are used for the simulations of tensile tests. The same model parameters are used as above and the material is modeled as homogeneous with the matrix phase. The tensile tests are carried out and then the cumulative density curve of the dissipated energy of each tensile test is fitted by the cdf of a Gaussian distribution in order to determine ℓ_{FPZ}.

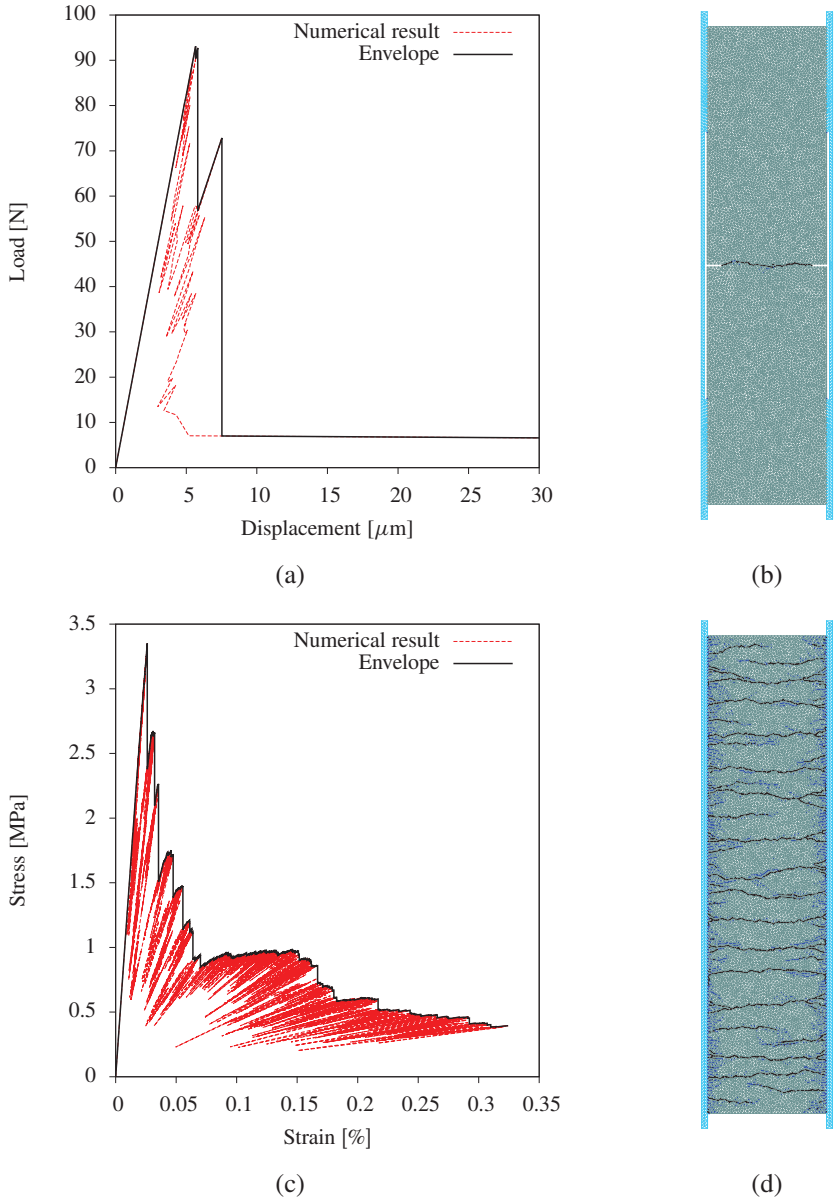

Figure 3.7 – The force-displacement curve (a) and the corresponding crack pattern (b) of the A-type localized tensile test on the notched specimen; the stress-strain curve (c) and the crack pattern (d) of the distributed tensile test on the unnotched specimen.

Figure 3.8 shows the dependence of the PFZ size ℓ_{FPZ} on the mesh size. $\bar{l}_{\mathrm{m}}$ is the average value of the discretization size. The best linear fit of the variation of the ℓ_{FPZ} with respect to the mesh size is also illustrated. As expected, the FPZ size does statistically tend to "zero" upon mesh refinement. Note however that the intercept of the fit is not exactly zero, its value is of 0.18. This is probably due to the fact that there are only five discretizations were used and there was not any mesh finer than 1 mm to be generated for the sake of saving computational time.

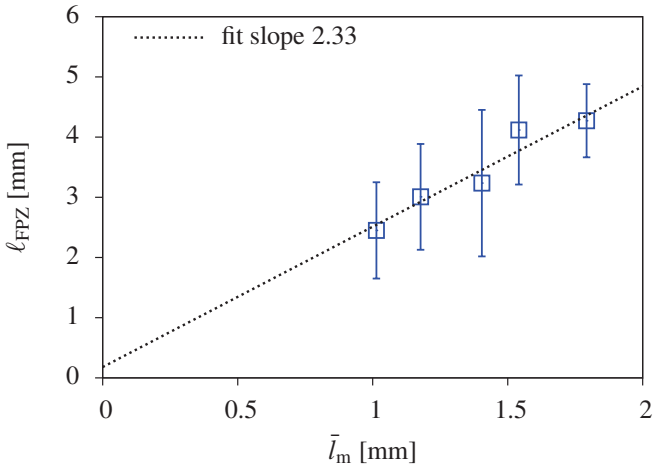

Figure 3.8 – Evaluation of the FPZ size with respect to mesh size: the FPZ size ℓ_{FPZ} does statistically vanish under mesh refinement.

3.3 Parameters controlling the aggregate structure

As mentioned in Section 1.1.1, concrete has a complex aggregate structure with a wide range of particle sizes. Moreover, going from one type of concrete to the other, many characteristics of the aggregate structure may change such as aggregate volume fraction, particle size, aggregate grading and of course aggregate distribution (spacial distribution). Accordingly, directly taking all of these variations to analyze their influences on the FPZ size as well as the material characteristic length of a concrete-like material by a numerical model can make complicated the situation. The better way to study the influences of the aggregate structure on the PFZ size ℓ_{FPZ} or the characteristic length ℓ_{c} is to separate its individual characteristics. This makes easy to understand the effect of each characteristic of the complex structure. Besides, from the numerical point of view, one can first consider a monodisperse structure of aggregates for the sake of simplicity and then may approach to a polydisperse one like that of the real concrete material.

3.3.1 Monodisperse distribution

In the first approach, we consider the monodisperse distribution of aggregate structures. In order to study the effects of the size d and the volume fraction P_{a} of aggregates on the FPZ size, three variations of aggregate structures are considered as schematically shown in Figure 3.9:

(I) varying d while the positions and the number of aggregates remain the same;

(II) varying d while P_{a} is kept at 45%;

(III) varying P_{a} for a given aggregate diameter $d = 8$ mm.

It must be recognized that the volume (surface) fraction of aggregates that is kept at 45% is the ratio of the area occupied by all aggregate particles and the total area of the specimen (by the

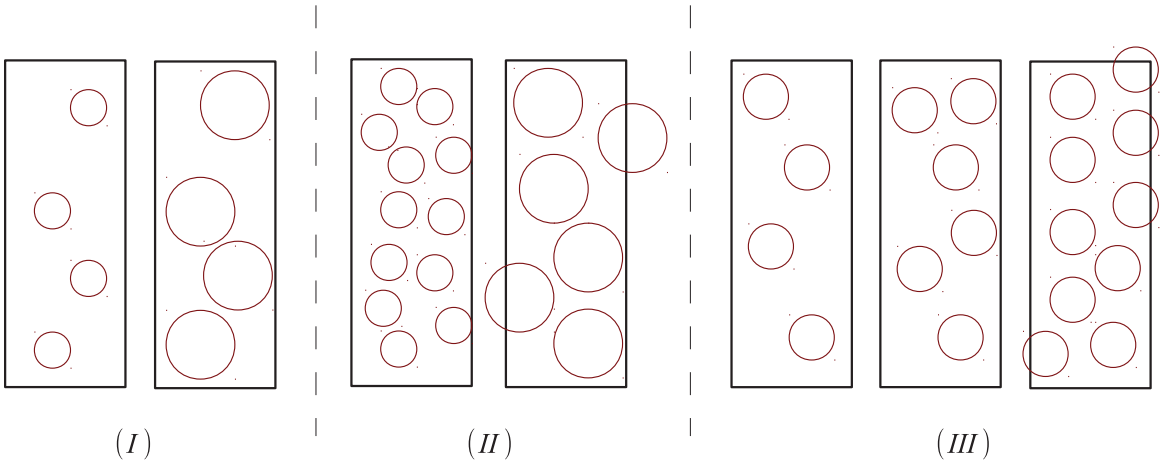

Figure 3.9 – Schematic representation of three variations of the aggregates.

continuous manner). This is mentioned as the "reference" value of P_a. However, when the aggregate particles are introduced in the lattice model, P_a is recomputed as the ratio of the number of elements representing the aggregates and the total number of elements. As a result, the obtained value of P_a is smaller than the reference value but tends to it under mesh refinement.

Aggregate structures have to be generated from these three aggregate variations and are introduced to the lattice model for an individual study. In addition to the variation of particle structure, a weak interfacial transition zone (ITZ) between aggregate and matrix phases can be introduced in the model and this will be explicitly mentioned for the individual studies in which the ITZ is whether or not defined. Without weak ITZ, only two phases (2φ) were modeled in the sense that the properties are either those of aggregates or of matrix. With weak ITZ, a weaker and less stiff thin phase (one element) is added in-between aggregates and matrix, bringing the number of phases to three (3φ).

In the studies presented in the following sections, d is varied by taking the values of 4, 6, 8 and 10 mm. The generated aggregate structures are mapped on the lattice mesh used in the simulations thereafter to define the material phases. And when the ITZ is introduced between the aggregates and the matrix (3φ), the three above variations, (*I*), (*II*) and (*III*), of aggregate size and volume fraction are represented by three variation paths in the ($P_a - d$) parameter space as in Figure 3.10. Without introducing the ITZ (2φ), the path (*I*) is also shown in Figure 3.10. Note that only the path (*I*) is shown here for the two-phase material since it will be used later to study the influence of the presence of the ITZ on the FPZ size. It is seen that P_a varies roughly like d^2 for the variation path (*I*). Note however that the volume fraction is not exactly kept constant at 40%[1] for the variation path (*II*) when changing the particle size. This is because of the fact that the smaller the particle size, the greater the number of particles are needed, resulting in a greater number of the ITZ elements and consequently leading to a smaller number of aggregate elements.

3.3.2 Polydisperse distribution

In order to better match the aggregate structure of a real concrete, a polydisperse distribution of the particle structure is used in the second approach. As mentioned in the literature that the FPZ size may only be proportional to the size of the largest aggregates, therefore to study the influences of the aggregate sizes on the FPZ size ℓ_{FPZ}, we vary the maximum aggregate size d_{max} of a polydisperse aggregate structure as schematically shown in Figure 3.11. To this end, four types of aggregate structures are generated using the Fuller's grading in which the minimum aggregate size $d_{min} = 3.15$ mm and the maximum aggregate size d_{max} is varied by taking the values of 6.3,

[1] It is noted that, in reality, the "real" aggregate volume fraction P_a is determined by the ratio of the aggregate elements and the total number of elements, which is smaller than the "reference value" of the aggregate fraction (45%). The real aggregate volume fraction tends to the reference value upon mesh refinement.

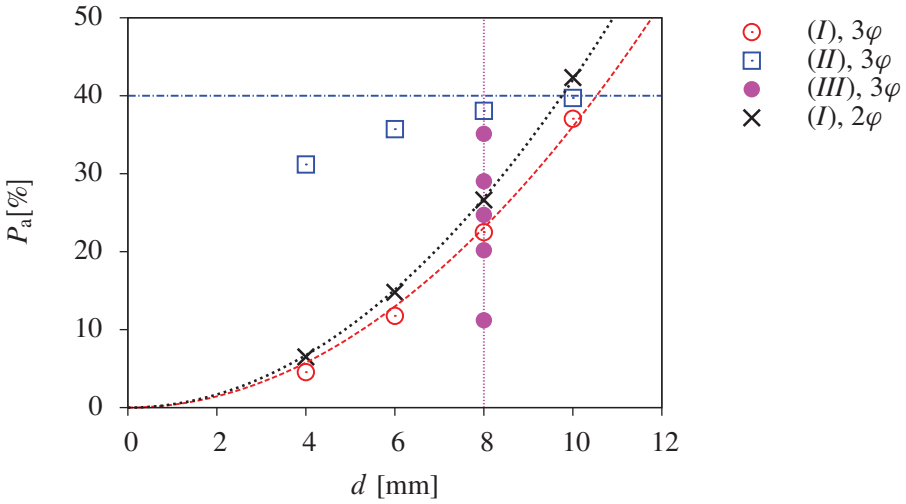

Figure 3.10 – Three variation paths (*I*), (*II*) and (*III*) for three-phase material (3φ) and the variation path (*I*) for two-phase material (2φ) in the (P_a – d) parameter space for the monodisperse distribution of aggregate particles.

8, 10 and 12.5 mm while keeping the "reference" volume fraction of aggregates constant at 45%. This aggregate size variation is denoted as the variation (*IV*). Table 3.3 shows the volume fraction of each aggregate segment of the four types of aggregate structures obtained from the Fuller's grading, in which $V_{Agg}^{abs} = 45\% \times V_{Agg}$ is the absolute volume fraction of aggregates with V_{Agg} the volume fraction of each aggregate segment, generated by the Fuller's grading.

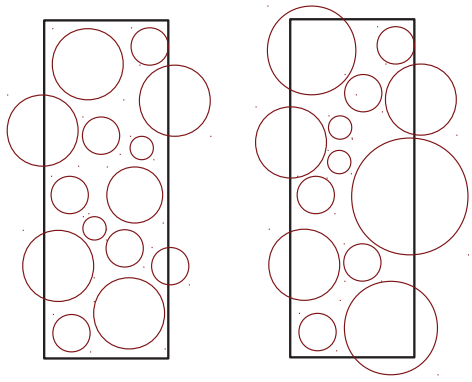

Figure 3.11 – Schematic representation of the mesostructure variation by varying the size of the largest aggregate particles while keeping the size of the fine particles nearly the same from a polydisperse aggregate structure to the other.

As for the monodisperse aggregate distribution, generated aggregate structures from the variation (*IV*) are mapped on the used mesh to define material phases for the studies thereafter. In the case of taking into account the ITZ between the aggregate and matrix phases, the aggregate size variation (*IV*) is shown in the (P_a – d_{max}) parameter space in Figure 3.12. Similarly, the obtained volume fractions of aggregates are smaller than the reference value (45%) and they are not exactly kept constant as expected due to the fact that the number of aggregates increases for the smaller d_{max} value leading to an increase of the number of ITZ elements and thus a decrease of the number of aggregate elements.

Table 3.3 – Volume fraction of each aggregate segment of four types of aggregate structures of the variation (*IV*) obtained from the Fuller's grading.

d_{max} [mm]	Aggregate segment [mm]	Sieve size [mm]	Sieve passing [%]	V_{Agg} [%]	V_{Agg}^{abs} [%]
6.3	0–3.15	3.15	0	0	0
	3.15–4	4	51.95	51.95	23.38
	4–5	5	76.64	24.69	11.11
	5–6.3	6.3	100	23.36	10.51
8	0–3.15	3.15	0	0	0
	3.15–4	4	41.86	41.86	18.84
	4–5	5	61.76	19.90	8.95
	5–6.3	6.3	80.59	18.83	8.47
	6.3–8	8	100	19.41	8.73
10	0–3.15	3.15	0	0	0
	3.15–4	4	35.23	35.23	15.85
	4–5	5	51.97	16.74	7.53
	5–6.3	6.3	67.81	15.84	7.13
	6.3–8	8	84.14	16.33	7.35
	8–10	10	100	15.86	7.13
12.5	0–3.15	3.15	0	0	0
	3.15–4	4	30.15	30.15	13.57
	4–5	5	44.48	14.33	6.45
	5–6.3	6.3	58.04	13.56	6.10
	6.3–8	8	72.02	13.98	6.29
	8–10	10	85.59	13.57	6.11
	10–12.5	12.5	100	14.41	6.48

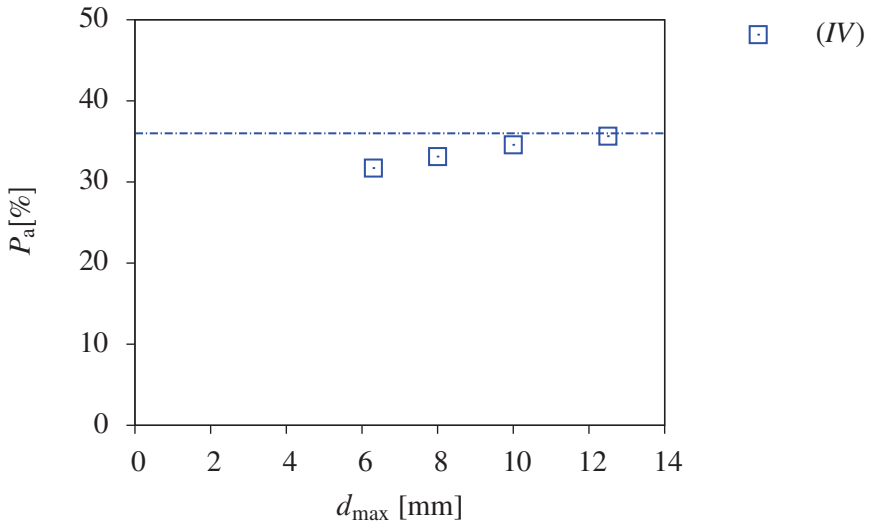

Figure 3.12 – The variation path (*IV*) in the (P_a – d_{max}) parameter space for the polydisperse distribution of aggregate particles.

3.4 Key features that may influence the FPZ size

To study key features that may influence the FPZ size, numerical tensile tests are performed using the normal-shear spring lattice model, presented in the following sections. The mesostructure of the material is modeled by explicitly introducing an aggregate structure. The mesostructure is varied according to the variation paths (*I*), (*II*), (*III*) for the case of monodisperse aggregate size distribution and the path (*IV*) for the case of polydisperse one, refer to Section 3.3. Five independent uniformly random distributions of aggregate positions are generated for each considered case of the mesostructure. The FPZ size will be assessed for each considered tensile test. Evolutions of the mean value of the FPZ size ℓ_{FPZ} (the average value of ℓ_{FPZ} over five realizations of aggregate positions) with respect to the aggregate size d (or $d_{\max}$ for polydisperse size distributions), or to the volume fraction of aggregates P_{a}, will be shown. The standard deviations of ℓ_{FPZ} obtained from five realizations of aggregate positions will also given by means of the vertical bars attached to the mean values of ℓ_{FPZ} in each plot.

The model parameters shown in Table 3.2 are used in the simulations hereafter. Note that no random field of strengths is introduced in the matrix phase such that one could study only the influences of coarse aggregates on ℓ_{FPZ}. Only in Section 3.4.2, a random field of strengths is introduced in the matrix phase to mimic the effect of fine aggregate particles. When fine aggregates are introduced by a random field of the failure parameters in the matrix phase, the values of σ_{n0} and σ_{s0} of the matrix phase given in Table 3.2 are taken as the mean values and the corresponding values of the standard deviation will be pointed out in Section 3.4.2.

3.4.1 Interfacial transition zone

The interfacial transition zone (ITZ) between the aggregate particles and the matrix, plays an important role in the size of the FPZ. As known, for concrete-like materials, the ITZ has the weakest strength compared to that of the aggregate particles and the matrix. Therefore, the failure of that kind of materials, and thus the FPZ size, is driven by the ITZ.

To study the effect of the bond strength and to verify whether the ITZ has an influence on the size of the FPZ, the following numerical campaign of uniaxial tensile tests is performed. In this campaign, the tensile tests performed on the specimen of A-type are carried out. Two cases are considered. The first concerns the specimen made of the three-phase material in which the ITZ is considered as the third phase in addition to the aggregate and matrix phases. The ITZ is introduced in the model by the procedure described in Section 2.3.1.1. In the second case, the ITZ is excluded in the description of the material and the specimen is made of two phases. For each case of the two-phase and three-phase materials, the aggregate structure is also varied to account for the variation of aggregate volume fraction and aggregate size. The aggregate structures of the path (*I*) of variation are used in the study, i.e., varying the size d while the positions and the number of aggregates remain the same.

The model parameters shown in Table 3.2 are used in the simulations. Note that no random field of strengths is introduced in the matrix phase such that one could study the individual influences of coarse aggregates on ℓ_{FPZ}.

Figure 3.13 shows the evolution of the FPZ size ℓ_{FPZ} with respect to the size of the aggregate particles d, in which each point corresponds to the mean of ℓ_{FPZ} of 5 uniformly random distributions of the position of the aggregate particles. The corresponding standard deviations are also shown by means of a vertical bar attached to it. As presented in Section 3.2.5, the size of the lattice elements also provide a non null ℓ_{FPZ}. The value of ℓ_{FPZ} due to the lattice elements' size can be calculated from the "homogeneous" tensile test in which no aggregate structure is introduced. The lattice mesh used in the simulations provides a width of the FPZ equals to 2.1 mm. Besides, the best fits of the variation of the mean value of ℓ_{FPZ} with respect to the aggregate size d for the two- and three-phase materials are shown in the figure as well. It is noted that these fits are calculated only from the mean values of ℓ_{FPZ} in the cases of aggregate particles are introduced, so the value of ℓ_{FPZ} of the

homogeneous material is not taken into consideration in the fits. Also, the displayed fitted lines do not necessary mean that an affine relation is enlightened. It must rather be seen as a rough tendency since the data presents significant variations. As a consequence, the intersection of the fitted line with the vertical axis has no particular meaning.

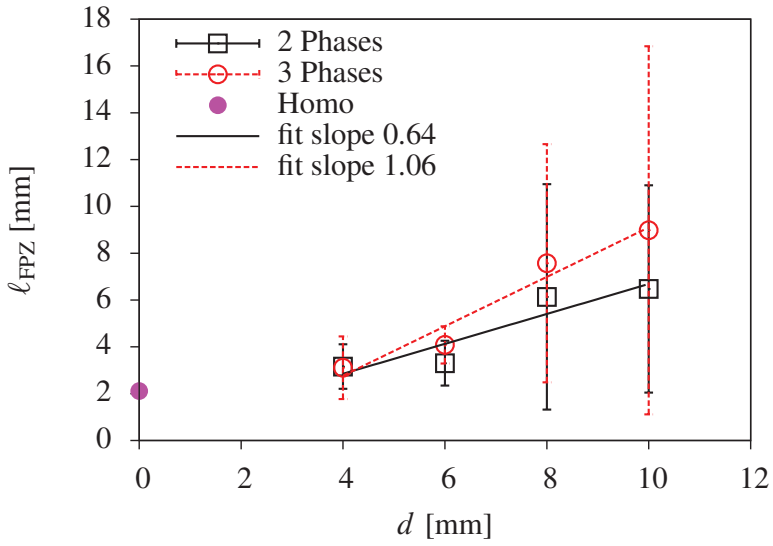

Figure 3.13 – Effect of the weak interface zone between the aggregates and the matrix on the FPZ size.

The main observation from the Figure 3.13 is that when the aggregates are introduced, they have a strong effect on the FPZ size in both two- and three-phase materials. First, the mean values of ℓ_{FPZ} in the case of heterogeneous material are greater then the value of ℓ_{FPZ} in the case of homogeneous one. Second, in the case of aggregate particles are introduced, the fitted slope of the mean values of ℓ_{FPZ} of the three-phase material is greater than that of the two-phase material. This means that when the ITZ is taken into account, the aggregate size plays a stronger effect on the variation of ℓ_{FPZ} than the case in which the ITZ is not taken into consideration. Moreover, it reveals that the greater the value of the aggregate size, the higher the difference of the mean value of ℓ_{FPZ} between the two- and three-phase materials is. This is probably explained by the increase of the ITZ fraction when increasing the aggregate size of the three-phase material, see Figure 3.14. Here, the ITZ plays a role of attractive zones for the crack propagation. Accordingly, the greater fraction of the ITZ results in the larger mean value of ℓ_{FPZ} compared to the mean value of ℓ_{FPZ} of the two-phase material (in which the ITZ fraction is zero). In the case of $d = 4$ mm, the mean value of ℓ_{FPZ} of the three-phase material does not differ from that of the two-phase one. This is related to the fact that the matrix prevails in the mesostructure in the case of $d = 4$ mm, as shown in Figure 3.14, and thus few aggregate particles are found on the crack path, see Figure 3.15.

Furthermore, bigger values of the standard deviations are observed when increasing the particle size of the three-phase material as well as of the two-phase one even though this is less clearly observed in the two-phase material than the three-phase one. This is probably due to the fact that increasing the aggregate size results in the increase of the aggregate fraction and as a result, the spacial distribution of aggregate particles plays a stronger role in the resulting value of ℓ_{FPZ}. In two-phase material, by comparison between $d = 8$ mm and $d = 10$ mm, the standard deviation of ℓ_{FPZ} does not significantly change. This is due to the fact that from $d = 8$ mm, the aggregate particles get dense in the mesostructure of the material, which leads to the fact that a change of the position of the aggregate particles does not have a strong effect on the value of ℓ_{FPZ}. However, in three-phase material, the spacial distribution of aggregate particles still make sense on the variation of ℓ_{FPZ} even though the aggregate particles get dense. This is reflected by the greater value of the standard deviation of ℓ_{FPZ} in the case of $d = 10$ mm than that in the case of $d = 8$ mm, of the

three-phase material. There is no doubt that this is due to the effect of the ITZ.

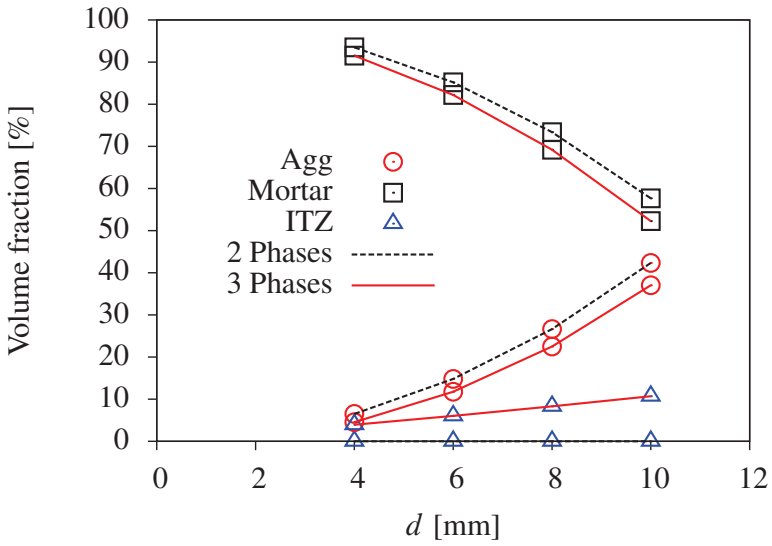

Figure 3.14 – Evaluation of volume fraction of each phase.

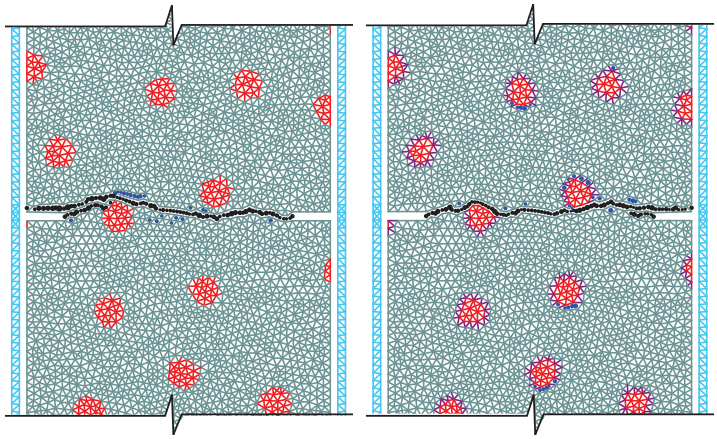

(a) $\ell_{FPZ} = 3.37$ (b) $\ell_{FPZ} = 2.12$

Figure 3.15 – Crack patterns and the corresponding value of ℓ_{FPZ} of the two-phase (a) and three-phase (b) materials with a random distribution of aggregate structure of $d = 4$ mm.

For the sake of clarity when accounting for the standard deviation of ℓ_{FPZ}, the crack patterns of two different random positions of the aggregate structure with $d = 8$ mm in the case of two-phase material are shown in Figure 3.16. The corresponding fits of the cumulative energy dissipation after the normal distribution are shown in Figure 3.17. It is shown that depending on the distribution of the aggregates in the specimen, the resulting FPZ has the different size. Since there is no aggregate along the line joining the two notches in the case shown in Figure 3.16a, the final crack can easily cross the specimen through the narrow band between the aggregates and connects the two notches. In this case, it seems that the aggregates play a role as a blocking against the development of microcracks. Whereas an aggregate is found in front of the notches in the case of Figure 3.16b, and thus, the failure of the specimen is characterized by the crack that has to dodge the aggregate to find enough space for the development of microcracks. Consequently, a much larger FPZ is obtained compared to the case of Figure 3.16a, leading to the high value of the standard deviation for this aggregate structure.

It is worth noting that the difference of the size of the FPZ between the two- and three-phase

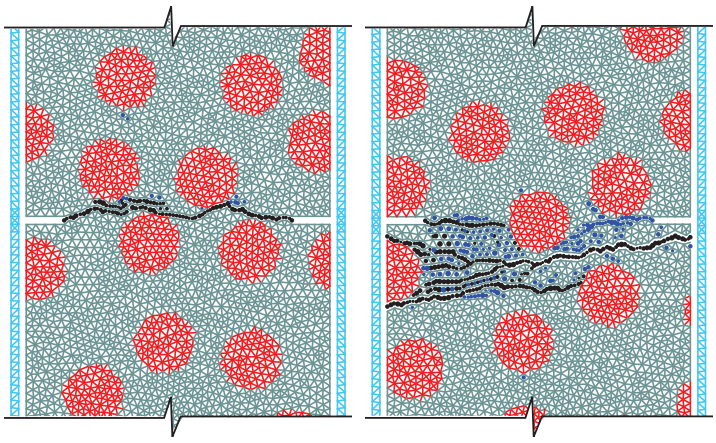

(a) $\ell_{\mathrm{FPZ}} = 3.29$ (b) $\ell_{\mathrm{FPZ}} = 14.27$

Figure 3.16 – Crack patterns of the two-phase material with different distributions of the aggregate structure of $d = 8$ mm.

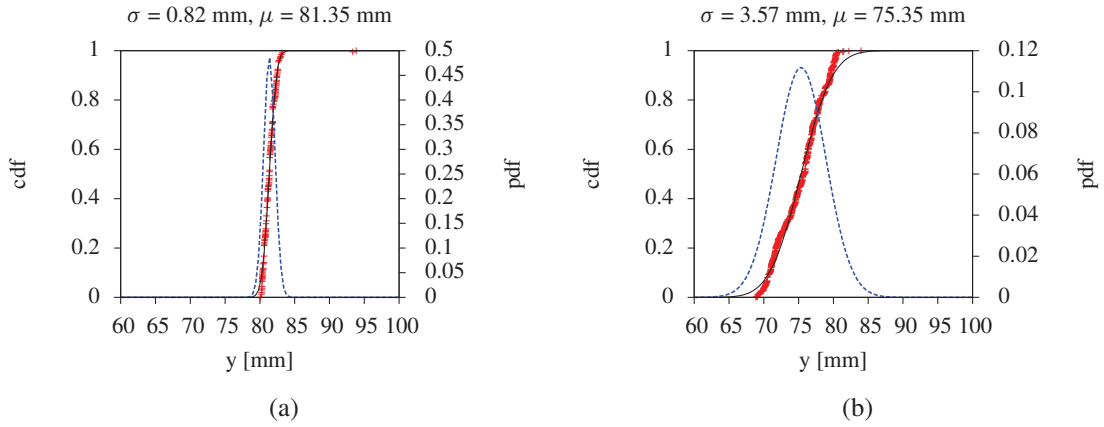

(a) (b)

Figure 3.17 – The best fit of the cumulative energy dissipation after the cumulative distribution function of the normal distribution.

materials strongly depends on the relative position of the aggregate particles with respect to the position of the notches. Indeed, as shown in Figure 3.18, the value of ℓ_{FPZ} of the three-phase material is smaller than that of the two-phase material of the same aggregate structure (the same size and position of aggregate particles). This is simply due to the fact that the aggregate particle without the ITZ in two-phase material, found in front of the notches, plays a role as a blocking against the development of the FPZ whereas this particle with the ITZ being more or less aligned with the notches in three-phase material plays a role as an attraction to the crack. Accordingly, the crack can cross the specimen section with a straighter path in three-phase material than in two-phase one. Nevertheless, as shown in Figure 3.19, when the position of the aggregate particles changes, which leads to a change of the relative position between the aggregate particles and the notches, the value of ℓ_{FPZ} in three-phase material is now greater than that in two-phase material.

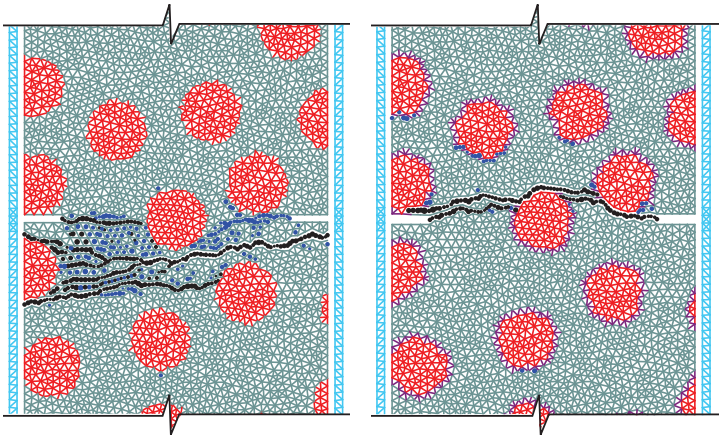

(a) $\ell_{\text{FPZ}} = 14.27$ (b) $\ell_{\text{FPZ}} = 5.90$

Figure 3.18 – Crack patterns of the two-phase (a) and three-phase (b) materials for the same aggregate distribution of the aggregate size $d = 8$ mm.

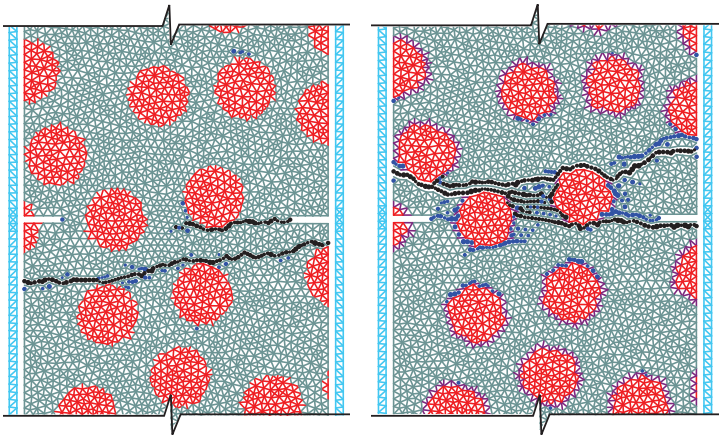

(a) $\ell_{\text{FPZ}} = 2.91$ (b) $\ell_{\text{FPZ}} = 16.16$

Figure 3.19 – Crack patterns of the two-phase (a) and three-phase (b) materials for the same aggregate distribution of the aggregate size $d = 8$ mm but differs from the aggregate distribution shown in Figure 3.18.

Compared with Figure 3.18a, in Figure 3.19a there are now two aggregate particles located along the line joining the two notches that play a role as a strong obstacle, and this explains for the fact that the crack is initiated at the right notch but finally it cannot propagate to cross the specimen section and another straight crack eventually extends over the specimen section. It is in contrast to Figure 3.18a in which there is only one obstacle particle, so the crack initiated at the right notch

tries to elude the particle and join the other notch. In the end the crack fails to join the left notch but this try leads to the greater value of ℓ_{FPZ}. In the case of three-phase material, two obstacle particles shown in Figure 3.19b now allows of the development of microcracks *around* them via the ITZ, which leads to a larger value of ℓ_{FPZ} compared to that shown in Figure 3.18b.

3.4.2 Fine aggregates (matrix heterogeneity)

As known, in the lattice model, the heterogeneity due to fine aggregates can be modeled by a random distribution of the failure parameters. The procedure to identify the random parameters is presented in Section 2.5.2. Here we focus on the effect of the fine aggregates introduced by the random field in the matrix to the size and the variation of the FPZ. To this end, the uniaxial tensile tests are performed on specimens made of the material in which the mesostructure is modeled by two manners. In the first one, only the coarse aggregates are directly introduced by mapping the aggregate particles on the lattice mesh. The uniaxial tests performed on specimens made of the material modeled by this manner are denoted as "NFA" series. In the second manner, the random fields of the failure parameters are introduced in addition to the coarse aggregates to simulate the effect of fine aggregates of the material mesostructure. The uniaxial tensile tests performed on the specimens made of the material modeled by the second manner are denoted as "FA" series. In both series, the influence of the coarse aggregates is studied by varying the size of the aggregate particles.

The numerical simulations of tensile tests in this section are performed on the specimen of A-type. The material is modeled as the three-phase one with the weak ITZ phase in-between aggregate and matrix phases. The same model parameters as before are used, see Table 3.2. Only for the FA series of tensile tests, two additional parameters being the standard deviations of the failure parameters: σ_{n0} and σ_{s0}, denoted by $\sigma_{\sigma_{n0}}$ and $\sigma_{\sigma_{s0}}$, are used to generate random fields in the matrix phase. In the study, the value of $\sigma_{\sigma_{n0}}$ and $\sigma_{\sigma_{s0}}$ is of 2 MPa. Note that the value of $\sigma_{\sigma_{n0}}$ and $\sigma_{\sigma_{s0}}$ should not be too large to ensure the fact that no matrix element has the generated values of σ_{n0} and σ_{s0} which are smaller than the corresponding values of ITZ elements. If not, the physical meaning of the mesostructure is lost. That is why the value of 2 MPa but not a larger value is used for $\sigma_{\sigma_{n0}}$ and $\sigma_{\sigma_{s0}}$. The aggregate size is varied while keeping the number of aggregate particles and their position unchanged. This concerns the path (I) variation of the aggregate structure. Five independently random distributions of aggregate particles are generated for each aggregate size.

Figure 3.20 demonstrates the relations of the FPZ size and the size of the aggregate particles for two series tests. The best fits of these relations are shown as well. The standard deviations of ℓ_{FPZ} obtained from five realizations of aggregate distributions are also given by means of the vertical bars attached to the mean values of ℓ_{FPZ}. It exhibits that the mean value of ℓ_{FPZ} of the FA tests is always greater than that of the NFA tests disregarding the size of the coarse aggregates. This is of course due to the effect of the fine aggregates considered dissolved in the matrix. The fine aggregates not only show the effect on the size of the FPZ for a certain size of the coarse aggregates but also on the variation of the FPZ size in respect of the coarse aggregates' size. Indeed, the slope of the fit of the FA tests is about 30% greater than that of the NFA tests. In consequence, a stronger effect of the coarse aggregates' size on the FPZ is obtained when the fine aggregates are taken into account in the model. This result may lead us to think, by extrapolation, that if the material is modeled with more complex mesostructure, the effect of the coarse aggregates to the FPZ size could be even greater.

It reveals again in the "FA" series tests that increasing the aggregate size leads to an increase of the standard deviation of the mean value of ℓ_{FPZ} as in the "NFA" series observed previously. The reason for that is still the same: increasing aggregate size leads to an increase of the volume fraction of aggregates, and obviously the sensitivity of ℓ_{FPZ} to the distribution of aggregate particles becomes more important.

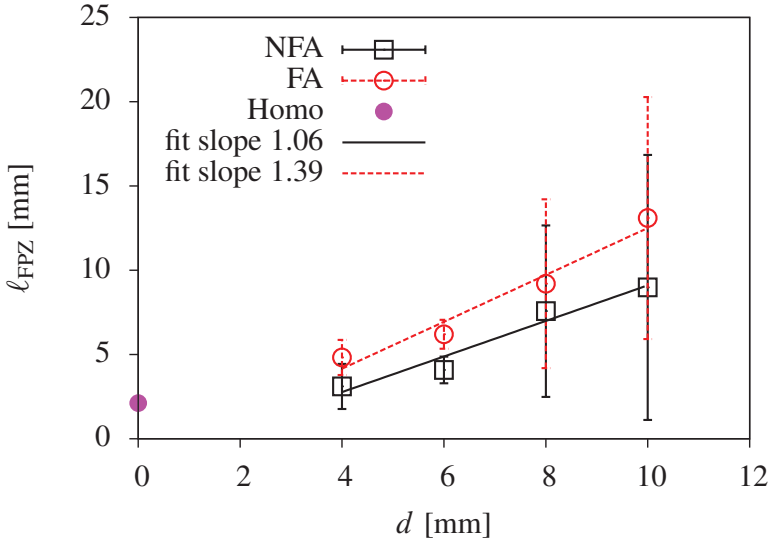

Figure 3.20 – Evolution of ℓ_{FPZ} with respect to d of three-phase concrete-like material.

3.4.3 Stress gradient and material rotation

The above studies are related to the influence of the material characteristics on the FPZ size. They were performed through the uniaxial tensile tests on the specimen of the A-type by changing the material properties. An interesting question is that whether the size of the FPZ and its variation related to the changes of the aggregates' size are also driven by the stress gradient due to the boundary conditions. In order to provide an answer to that question, the following campaign are carried out, in which the stress gradient applied to tested specimens is varied by either changing the specimen size to make the boundary conditions closer to or further from the notch position, or changing the type of the boundary conditions such as loading equipments or notch types (symmetric or not). The test campaign consists of uniaxial localized tensile tests performed on six different-sized specimens and boundary conditions. They are labeled as A-, B-, B1-, C-, C1- and D-types. The dimensions as well as the boundary conditions of these types of localized tensile tests are clearly described in Section 3.2.3.

For each A-, B- and B1-type tensile test, the aggregate size is varied as the set of variation (I) of aggregates (i.e. changing the aggregate size d while keeping the position and the number of aggregates constants) described in Section 3.3.1. The aggregate structures of the C-, C1- and D-type tests are exactly the same as those of A-, B1- and B-type tests such that one can imagine that the C-, C1- and D-type specimens are created by sawing the specimens of the A-, B1- and B-type tests, respectively, in the zone around the notches. The model parameters are always taken as above and the material is model as three-phase one with a weak ITZ between the aggregate and the matrix phases. Here, no random field of strengths is introduced in the matrix phase such that one can study the individual influences of coarse aggregates on ℓ_{FPZ}.

Figure 3.21 shows the relations between the mean of ℓ_{FPZ} and the aggregate volume fraction P_a for the six types of tensile tests. The best fits for each relations are also presented. Note that the dimension of the fitted slopes is mm/%, i.e. when the aggregate volume fraction changes 1%, it leads to the change of ℓ_{FPZ} of the quantity being equal to the value of slope times 1 mm. So, do not surprise for the small values of the fitted slopes shown in Figure 3.21. The figure reveals that the stress gradient via changing the type of boundary conditions and specimen size has a strong effect on the variation of ℓ_{FPZ} with respect to the aggregate volume fraction which in turn is proportional the aggregate size d. Indeed, the fitted slope of the B1-type tests has the maximum value compared to that of other type tests. For the B-, C- and D-type tests, the larger the value of specimen height, the greater the value of the fitted slope is. Between the B- and B1-type tests or between the C- and

C1-type tests, the fitted slope of the one-notch specimens, B1- and C1-type, is higher than that of the corresponding two-notch specimens, B- and C-type, respectively. For the specimens of the same size and the same number of notches, by comparison with the fitted slope of the B-type tensile tests, the fitted slope of the A-type ones has a greater value.

These observations mean that the relation between the FPZ size and the aggregate size/ratio is also influenced by the specimen size or generally the boundary conditions that result in different stress gradient and material rotation fields. The effect of the boundary conditions on the FPZ size might be explained by the fact that the intensity of the stress gradient and the nonuniformity of the strain across the specimens is more or less important. Actually, when it exists an intense stress gradient that involves in the specimens, the failure position is strongly imposed which brings the FPZ into being narrower than in the case of a weak stress gradient. And when the nonuniformity of the strain is important through the cross section of the specimens, it results in a relative rotation of the upper and the lower parts of the specimens separated by the macrocrack and thus this provokes the change of the principal direction of the loading that probably allows the FPZ evolves in a wider zone.

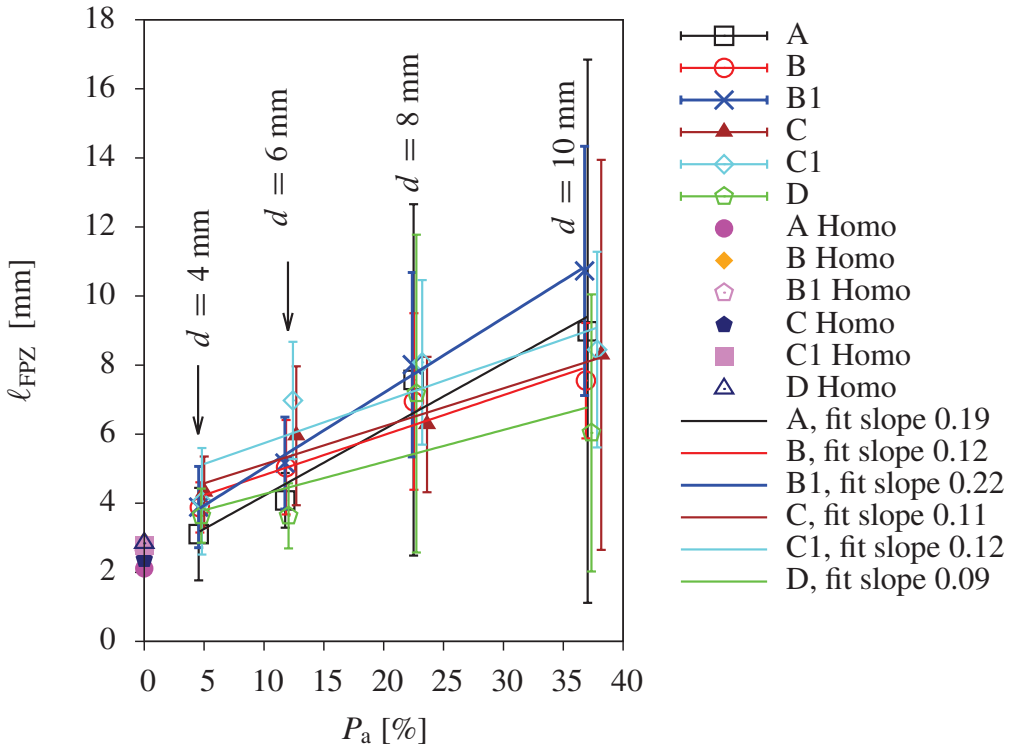

Figure 3.21 – Influence of the stress gradient, when changing whether the specimen sizes or the type of boundary conditions, on the values and variations of ℓ_{FPZ} with respect to the aggregate volume fraction P_a.

Figure 3.22 shows the distribution of the "mesoscopic force", i.e. the resultant force of the stress over an area being equal to the cross-sectional area of the lattice elements, through the cross section of the B-, C- and D-type specimens in the vertical direction just before complete failure. It unveils that the distribution of stress in the C- and D-type specimens is more varied from the left side to the right side than that in the B-type specimen. This means that the stress in C- and D-type specimen is not as uniform as in the B-type one, and thus the stress gradient through the specimen cross-section must be accounted for the smaller value of the FPZ size ℓ_{FPZ} and for the weaker influence on the variation of ℓ_{FPZ} with respect to aggregate sizes. Moreover, some negative mesoscopic forces are found in C- and D-type specimen which means that the principal direction of loading is *locally* changed and the elements undergoing the negative forces probably play the role as a blocking against the development of the FPZ. By comparison between the mean values of ℓ_{FPZ} and their variations

with respect to the aggregate size d of the B-, C- and D-type specimens, it is worth stressing that the difference of stress gradient seems to play a higher role in the variation of ℓ_{FPZ} with respect to d than in the mean value of ℓ_{FPZ} between the B- and C-type specimens whereas it plays an important role in both the values and the variations of ℓ_{FPZ} between B- and D-type specimens, see Figure 3.21. This may come from the fact that there is not enough space for the FPZ to develop in the D-type specimens.

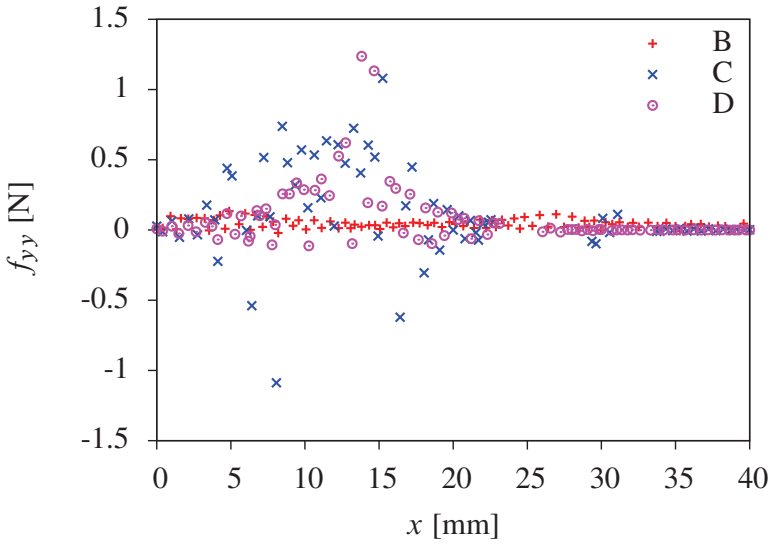

Figure 3.22 – Distribution of the vertical force f_{yy} through the specimen section at the position of 10 mm above the notch position of the B-, C- and D-type specimen made of the material with $d = 8$ mm.

Figure 3.23 shows the plot of strains measured by LVDT gages mounted on the left and right sides (in the middle of the vertical direction) of each type of specimens. Here the case of the aggregate structure $d = 8$ mm is presented and the corresponding crack patterns of a random distribution of the aggregates are shown in Figure 3.25. The length of the LVDT gages of the A-, B-, B1-, C- and C1-type specimens is 30 mm while that of the D-type specimen is 15 mm since the height of the D-type specimen is only of 20 mm. It is seen that the nonuniformity of the strain is found to be the most important for the B1-type specimen and then for the A-type specimen. The important difference of these strains of the A- and B1-type specimens means that the material undergoes bending. For the A-type specimen, this is because the tension was indirectly applied to the specimen through the steel bars that allows the relative rotations between the top and bottom boundaries of the specimen in the softening regime. For the B1-type specimen, even though the way in which the tension was applied at the top and bottom boundaries prevented in advance a rotation possibility between these boundaries, there is no doubt that the asymmetry of the specimen geometry due to the notch motivates a relative rotation between the upper and the lower parts of the specimen around the notch along with the development of the macrocrack. Whereas the prevention of a rotation between the top and bottom boundaries of the B-, C- and D-type tests accompanying with the symmetry of the specimen geometries prevent any bending effect in the specimens. However, when the specimen is long i.e. the boundary effect is far from the notches, the presence of the rotation effect is more important than in the short specimen. It is shown that the asymmetry of the strains in the B-type specimen is more notable than in C- and D-type specimens. The asymmetry of the strains is again observed more notable in C-type specimen than in the D-type one.

It is interesting to point out that the distribution of the aggregate structure plays an important role on the nonuniformity of the strains measured in the material. Figure 3.24 shows a plot of strains in the vertical direction measured by LVDT gages with the length of 30 mm mounted in the left and right sides, normalized by the maximum strain $\varepsilon_{\max}$, of the B1-type specimens made of the homogeneous material and the heterogeneous material with two different random distributions of

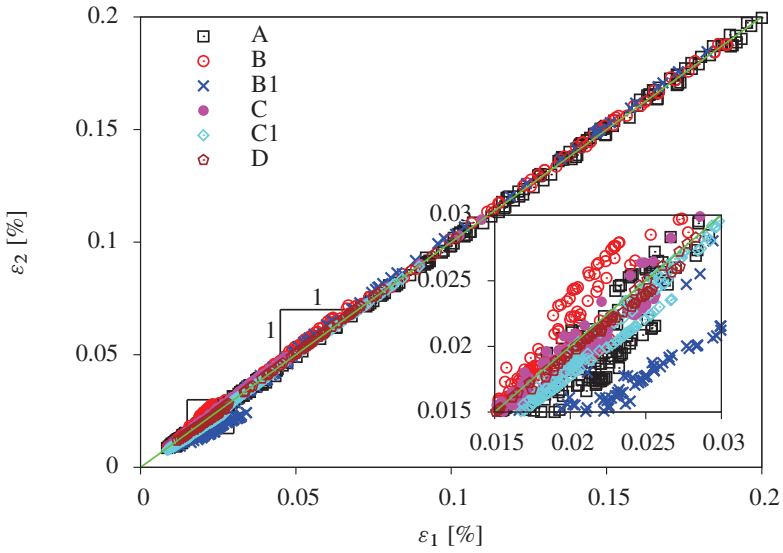

Figure 3.23 – Nonuniformity of strains in each side of the specimens.

aggregate structure with $d = 8$ mm (a and b). The homogeneous material is modeled as one-phase material with the matrix phase while the heterogeneous material is modeled as the three-phase one. It is seen that the nonuniformity of strains has not the same magnitude. Indeed, for the heterogeneous material, depending on the distribution (the position) of the aggregates with respect to the notch position, the crack is initiated at the ITZ phase at the different positions and thus propagated in different ways which result in a different degree of nonuniformity of strains measured in the specimens. For the case of the homogeneous material, the crack is exactly initiated at the notch and propagated forward to the other side of the specimen, which obviously reproduces the highest value of the strain nonuniformity. It all accounts for the fact that not only does the FPZ size vary with the boundary conditions but also with the aggregate position for a fixed aggregate size and of course with the aggregate size itself.

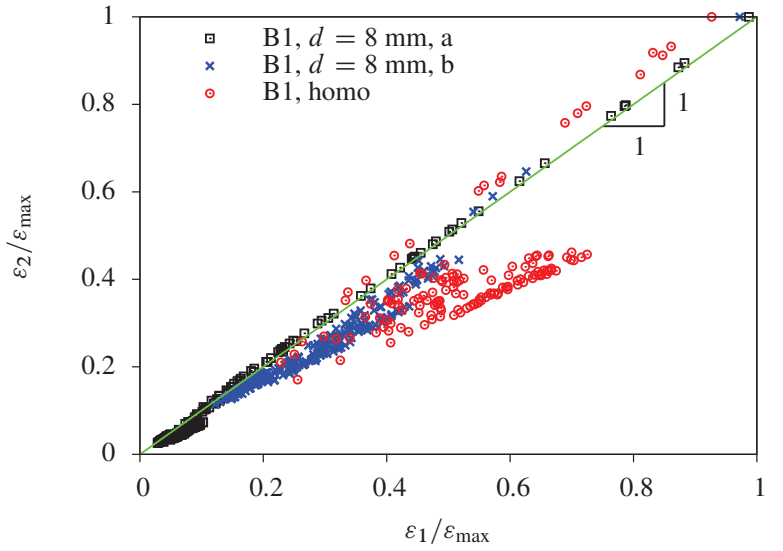

Figure 3.24 – Nonuniformity of strains in the left and right sides of the B1-type specimens.

In short, the results highlight the dependence of the size and of the variation of the FPZ with respect to the size/volume fraction of the aggregates on both the stress gradient and the rotation effect. Nevertheless, it is shown that the influence of the rotation effect on ℓ_{FPZ} can be different

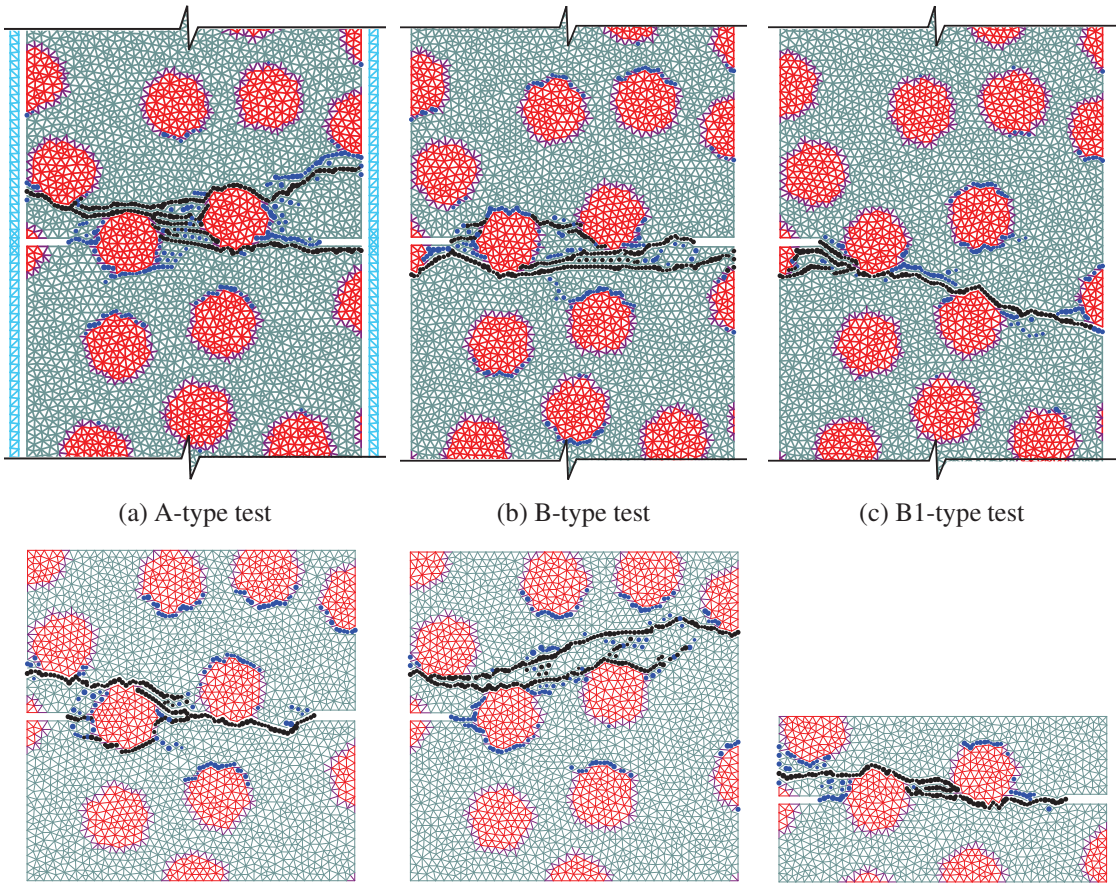

(a) A-type test (b) B-type test (c) B1-type test

(d) C-type test (e) C1-type test (f) D-type test

Figure 3.25 – Crack patterns of the different types of tensile test with the aggregate structure $d = 8$ mm.

in the specimens with different values of the stress gradient. It is observed from Figure 3.21, by comparison the B- and B1-type tests with the C- and C1-type tests, that when the stress gradient is less important in the B- and B1-type specimens (since the specimens are longer than in the C- and C1-type specimen), the rotation effect becomes dominant and strongly influences on the variation of ℓ_{FPZ}. This is exposed by the fitted slope of the B1-type tests is clearly higher than that of the B-type ones. Whereas, in the C- and C1-type tests, the stress gradient is more important since the tested specimens are shorter than those of the B- and B1-type tests, leading to the fact that the high stress gradient seems to decrease the influence of the rotation effect on the variation of ℓ_{FPZ}. This is shown by the slightly higher value of the fitted slope of the C1-type tests compared with that of the C-type tests.

An important observation from the Figure 3.21 is that the effect of the boundary conditions on the FPZ size becomes more remarkable when the aggregate size increases. Actually, it is seen that for a fixed greater value of the aggregate size d, changing the boundary conditions leads to a wider deviation of the values of the FPZ size ℓ_{FPZ}. This is simply explained by the fact that within the aggregate structure with higher aggregates' size, the higher volume fraction of the aggregates is found leading to the greater area of the weak ITZ, and thus, the rotation effect due to the boundary conditions plays a more significant role in the failure of the material.

3.4.4 Aggregate size with fixed volume fraction

To evaluate the influence of the aggregate structure on the FPZ size ℓ_{FPZ}, the above studies were related to the path (*I*) of variation, i.e., the aggregate size d is varied while the positions and the number of aggregates remain unchanged in the numerical simulations. This results in changing the size and the volume fraction of aggregates at the same time. In the present section, we are addressing the question of the influence of the aggregate size d on the FPZ size ℓ_{FPZ} when only the size d of aggregates is varied whereas the volume fraction of aggregates is kept as constant as possible. The reason of this choice relies on the fact that the fundamental role of aggregate size d must be checked while keeping other parameters unchanged to suppress their possible effect. Furthermore, in experiments with real concrete, the admixture formulation targets a given compressive strength usually controlled by the water/cement ratio and maximum aggregate size. Consequently, the volume fraction of aggregates is not explicitly controlled. However, we believe that the volume fraction of aggregates might not be significantly changed when varying maximum aggregate size in real concrete admixture. In other words, the volume fraction of coarse aggregates hardly changes in reality. Therefore, the path (*II*) of variation (see Section 3.3.1) is used in this section to study the influence of the aggregate size d on the FPZ size ℓ_{FPZ}, in which the "reference" aggregate volume fraction is kept constant at 45% when changing the aggregate size.

The numerical simulations of tensile tests in this section are performed on the specimen of A-type. The same model parameters as before are used. The material is modeled as the three-phase one with the weak ITZ phase in-between the aggregate and matrix phases. In addition, no random field of strengths is introduced in the matrix phase such that one could study the individual influences of coarse aggregates on ℓ_{FPZ}.

Figure 3.26 shows the plot of the mean value of the FPZ size ℓ_{FPZ} with respect to the size d of aggregates of the path (*II*) of variation. For the sake of comparison, the same plot of the path (*I*) is shown as well. Each point corresponds to the mean value of five values of ℓ_{FPZ} with five independently random distributions of the aggregates in the specimen. The standard deviation of each mean value is also presented. Surprisingly, it exhibits that the mean value of the FPZ size does not depend on the aggregate size for the path (*II*) of variation. It means that the FPZ size developed in this type of model material (brittle elastic) may not always be related to the aggregate size itself as usually observed in the literature. The observation is in agreement with that of Skarżyński et al. (2011), in which the width of the FPZ was experimentally measured on the surface of concrete specimens using a Digital Image Correlation (DIC) technique. However, it is in contrast to the results of Mihashi and Nomura (1996) and Otsuka and Date (2000) for concrete material, in which

the experiments were carried out with X-rays and three-dimensional Acoustic Emission techniques leading to the conclusion that the width of the FPZ increases with the increase of the maximum aggregate size. But for the path (*I*) of variation, as previously shown, it is seen that the mean values of ℓ_{FPZ} increases with the increase of aggregate size d that also results in the increase of the aggregate volume fraction.

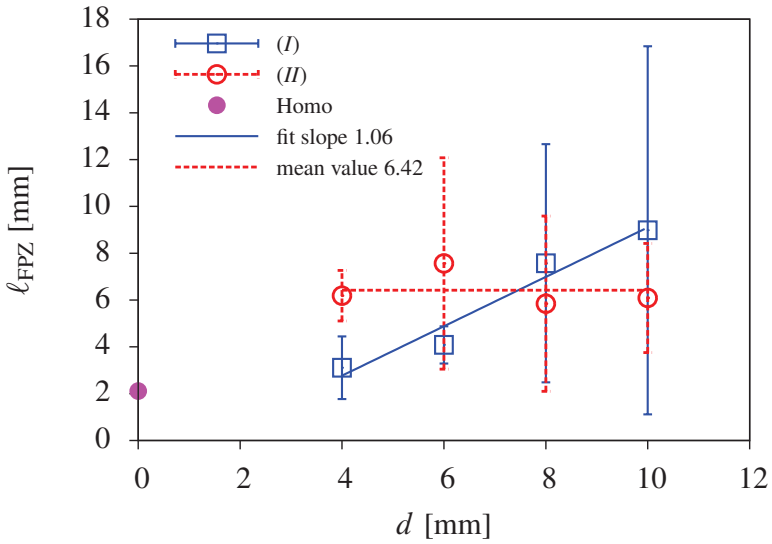

Figure 3.26 – Relation between the FPZ size ℓ_{FPZ} and aggregate size d with respect to the variation paths (*I*) and (*II*).

Figure 3.27 shows the crack patterns and the corresponding value of ℓ_{FPZ} obtained when changing the aggregate size d within the variation path (*II*). The figure shows for each aggregate size d only one random distribution of aggregates in the specimen. It seems that the position of aggregates around the notches have an essential role on the resulting FPZ size. In fact, the crack is always initiated at the weak ITZ between the aggregate and matrix phases. With regard to the position of a notch – that can also be seen as a "weak link" – the crack is then propagated *via* the development of microcracks and at the end the macrocrack is formed by connecting the notch(es) and the broken elements (mainly in the ITZs). However, sometimes an aggregate is found just in front of the notch(es) and it plays a role of an obstacle that prevents the rupture of elements in the vicinity of the notch(es) and consequently, disconnects the macrocrack from the notch(es). In this case, the macrocrack is finally formed by mainly connecting the broken ITZ elements. Therefore, the spacial distribution (positions) of the aggregate particles actually have an important role on the FPZ size in conjunction with the size of the aggregate particles. Nevertheless, for the case where the reference volume fraction of aggregate is kept almost constant (path (*II*)), the spacing between the aggregate particles seems to be constant regardless of the size of the particles, and thus the spacial distribution of the particles prevails more and more on their size in the resulting FPZ size ℓ_{FPZ}. Actually, as shown in Figure 3.28 in which four different sets of aggregate positions with the diameter being 6 mm, the values of ℓ_{FPZ} are finally different depending on the spacial distribution of the aggregate particles with regard to the notch position. This explains why changing the size of the aggregate particles according to the path (*II*) does not change the value of ℓ_{FPZ} averaged over five random spacial distributions of aggregate particles. On the contrary, within the path (*I*) of variation, changing the aggregate size leads to a change in the aggregate volume fraction together with the spacing between aggregate particles, and the FPZ size is affected by not only the size of aggregate particles but also the other structuring parameters (position and volume fraction of aggregates in our case). Still, the smaller the aggregate particle size, the larger the spacing between the particles is in the path (*I*). This leads to the weaker influence of the spacial distribution of aggregate particles observed on the FPZ size. It is revealed in Figure 3.26 by the value of the standard deviation that is increased with

the aggregate size.

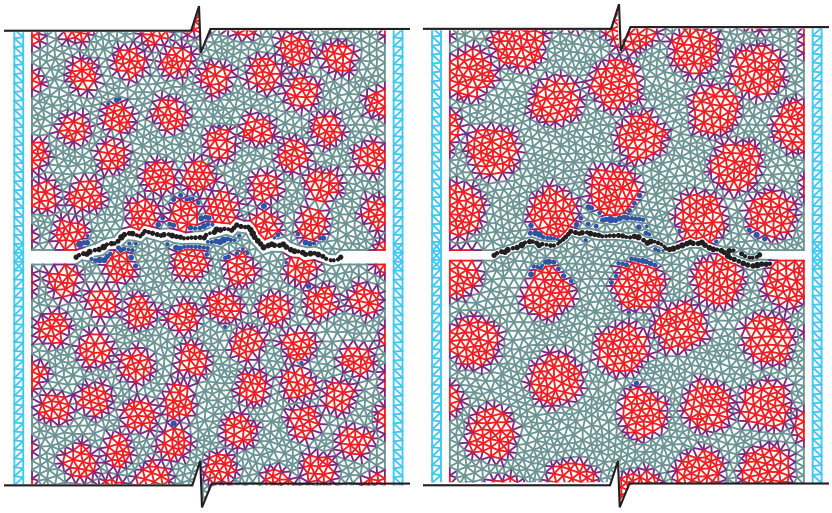

(a) $d = 4$, $\ell_{\text{FPZ}} = 5.47$ (b) $d = 6$, $\ell_{\text{FPZ}} = 4.94$

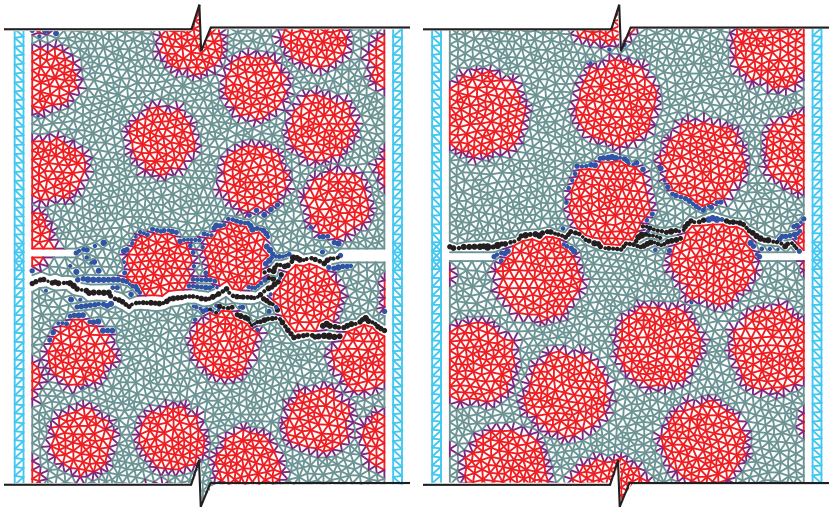

(c) $d = 8$, $\ell_{\text{FPZ}} = 12.46$ (d) $d = 10$, $\ell_{\text{FPZ}} = 4.75$

Figure 3.27 – Crack patterns and the corresponding FPZ size ℓ_{FPZ} [mm] of the A-type tensile tests on the specimen made of the material with different aggregate size d [mm] of the variation path (*II*).

In summary, after the study of tensile tests on a fixed-size specimen made of a brittle elastic model material with aggregate particles (inclusions), the results highlight that the FPZ size ℓ_{FPZ} is related to the characteristics of the aggregate structure including aggregate size, aggregate distribution/position, aggregate volume fraction as well as aggregate spacing. Depending on the situation, one of the characteristics prevails. Anyway, the spacial distribution of aggregates always impacts ℓ_{FPZ}, and this is exposed *via* the non-null standard deviation in the above studies. If the aggregate spacing is kept constant by keeping the reference volume fraction of aggregate particles unchanged while changing the size of the aggregate particles, the mean value of ℓ_{FPZ} seems to be independent from the aggregate size. When the aggregate volume fraction/spacing changes due to the change of aggregate size while keeping the same position for different aggregate sizes, the mean value of ℓ_{FPZ}, taken by averaging the FPZ sizes of several (five in the study) random distributions of aggregates of the same size, increases with the increase of the aggregate size. Now, it remains to be seen the influence of the aggregate structure on ℓ_{FPZ} when keeping the aggregate size constant and changing the aggregate volume fraction that leads to the change of the aggregate spacing. This study is outlined in the next section.

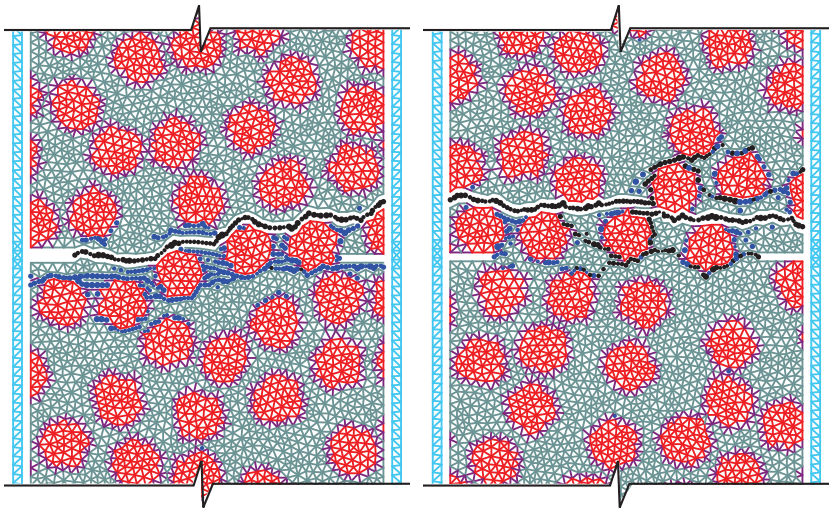

(a) $\ell_{\mathrm{FPZ}} = 10.60$ (b) $\ell_{\mathrm{FPZ}} = 14.01$

(c) $\ell_{\mathrm{FPZ}} = 3.81$ (d) $\ell_{\mathrm{FPZ}} = 4.94$

Figure 3.28 – Crack patterns and the corresponding FPZ size ℓ_{FPZ} [mm] of the A-type tensile tests on the specimen made of the material with aggregate size $d = 6$ mm with four different distributions of the aggregate particles.

3.4.5 Fraction of aggregates with fixed size

In order to evaluate the only influence of the aggregate volume fraction (or equivalently the aggregate spacing, since the latter is inversely proportional to the former) on the FPZ size ℓ_{FPZ}, numerical tensile tests are carried out on the specimen made of the brittle elastic model material in which the aggregate volume fraction is varied while keeping the aggregate size constant. This concerns the path (*III*) of variation in which the size of aggregates is held constant at 8 mm. Moreover, for each value of the aggregate volume fraction, five independently random distributions of aggregate positions are generated so that the mean value of ℓ_{FPZ} is utilized for studying the effect of the aggregate volume fraction.

The numerical simulations of tensile tests in this section are performed on the specimen of A-type. We use the same model parameters as before. The material is modeled as the three-phase one with the weak ITZ phase in-between aggregate and matrix phases. In addition, no random field of strengths is introduced in the matrix phase such that one could study only the influence of coarse aggregates on ℓ_{FPZ}.

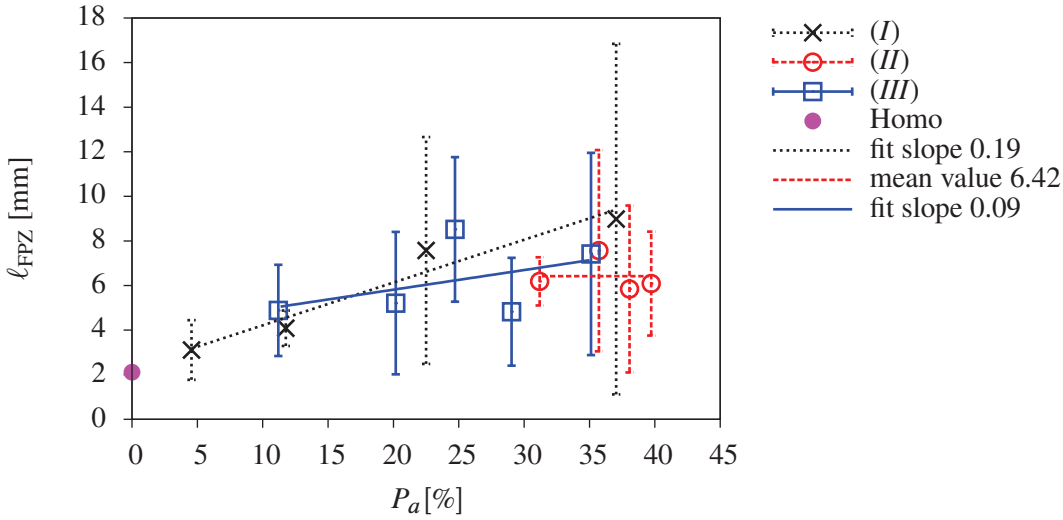

Figure 3.29 – Variation of ℓ_{FPZ} according to the aggregate volume fraction P_{a} of the three variation paths (*I*), (*II*) and (*III*) of aggregate variations.

Figure 3.29 shows the variation of the mean value of ℓ_{FPZ} with respect to the aggregate volume fraction P_{a} when changing the aggregate volume fraction according to the path (*III*) of variation (hold the aggregate size $d = 8$ mm). For the sake of comparison, the results of above studies for the variation paths (*I*) and (*II*) are plotted as well, but in the (ℓ_{FPZ}–P_{a}) space. For each size of aggregate particles, five independently random distributions of positions are generated and used in the numerical simulations. Figure 3.29 also shows the best fits of the variation of ℓ_{FPZ} corresponding to the three variation paths (*I*), (*II*) and (*III*). The main observation is that the mean value of ℓ_{FPZ} of the path (*I*) and the path (*III*) does increase with the increase of the aggregate volume fraction P_{a}, whereas that of the path (*II*) does not change. This is simply explained by the fact that the spacing between aggregate particles decreases with the increase of the aggregate volume fraction within the variation paths (*I*) and (*III*), whereas it seems to be "constant" (or slightly changed) within the path (*II*). By comparison the path (*III*) with the path (*I*), it is observed, however, that the increase rate of ℓ_{FPZ} with respect to P_{a}, which is represented by the fitted slope, of the path (*III*) is smaller than that of the path (*I*). A suitable explanation for this observation is that within the path (*I*), the size of and the spacing between the aggregate particles do change (increase and decrease, respectively) at the same time with respect to the increase of P_{a} whereas only the spacing of the aggregate particles does decrease with respect to the increase of P_{a} within the path (*III*).

Therefore, the observation could lead to the evidence that the FPZ size depends on both the

aggregate spacing (which is just a consequence of the aggregate volume fraction) and aggregate size.

Figure 3.30 shows the crack patterns and the corresponding values of ℓ_{FPZ} of four different values of P_a in the path (*III*) with $d = 8$ mm. By comparison between Figures 3.30b and 3.30c, it is however seen that the aggregate volume fraction and the FPZ size are not always in direct correlation (even if an affine relationship with positive slope is actually observed when averaging over several realizations of specimens). In fact, the value of P_a in Figure 3.30b is smaller than that in Figure 3.30c but the value of ℓ_{FPZ} of Figure 3.30b is greater than that of Figure 3.30c. In this case, again, the relative position of the aggregate particles and the notches seems to have important sense. Similarly, as shown in Figure 3.31, in which the total number of aggregate particles is kept constant

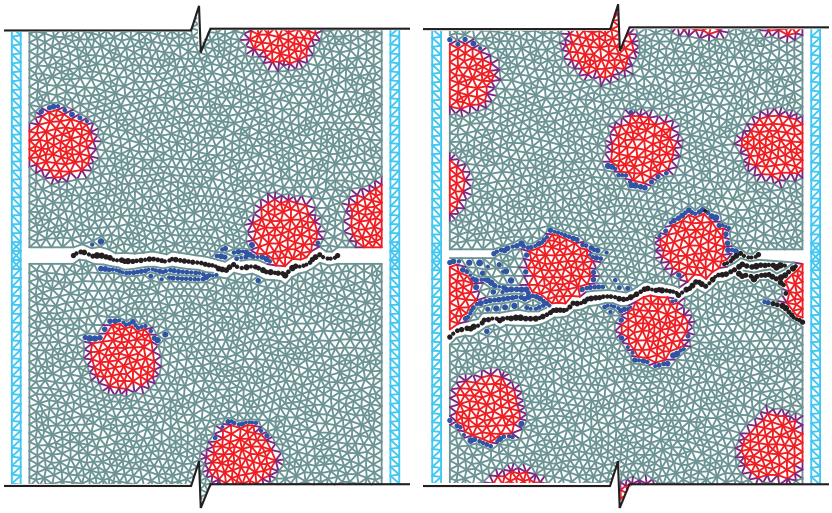

(a) $P_a = 10.52$, $\ell_{FPZ} = 3.60$ (b) $P_a = 22.49$, $\ell_{FPZ} = 11.92$

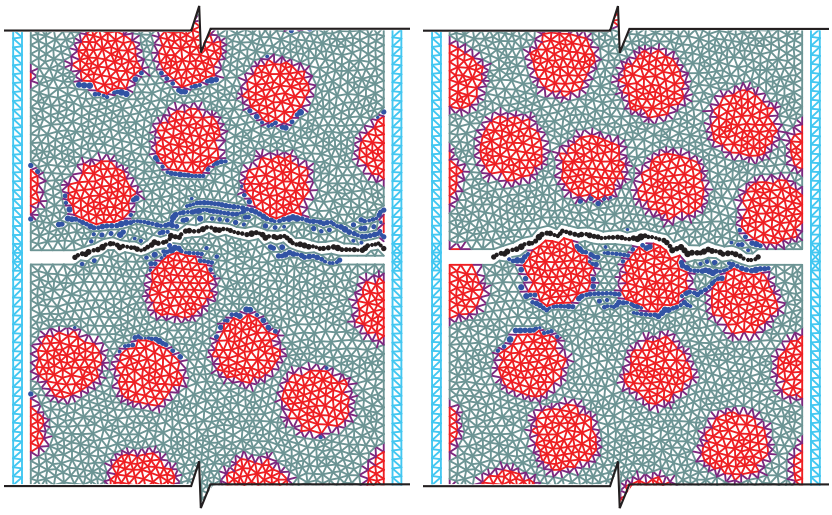

(c) $P_a = 27.57$, $\ell_{FPZ} = 8.60$ (d) $P_a = 33.72$, $\ell_{FPZ} = 8.44$

Figure 3.30 – Crack patterns and the corresponding FPZ size ℓ_{FPZ} [mm] of the A-type tensile tests on the specimen made of the material with different aggregate volume fraction P_a [%] and the aggregate size is of 8 mm of the variation path (*III*).

at 50 particles within the path (*III*) so that the reference aggregate volume fraction is held almost constant, different values of ℓ_{FPZ} are obtained with regard to the relative position of the aggregate particles and the notches. These all account for the standard deviations of ℓ_{FPZ} shown in Figure 3.29.

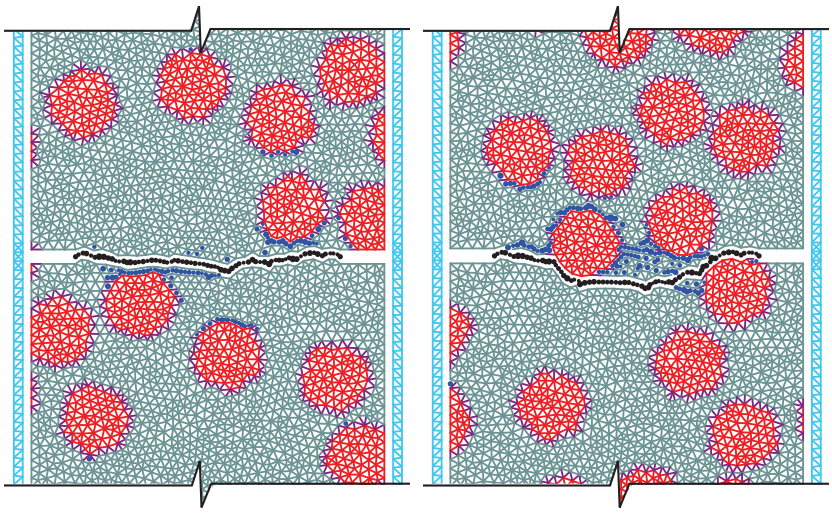

(a) $P_a = 25.17$, $\ell_{FPZ} = 4.20$ (b) $P_a = 24.96$, $\ell_{FPZ} = 7.90$

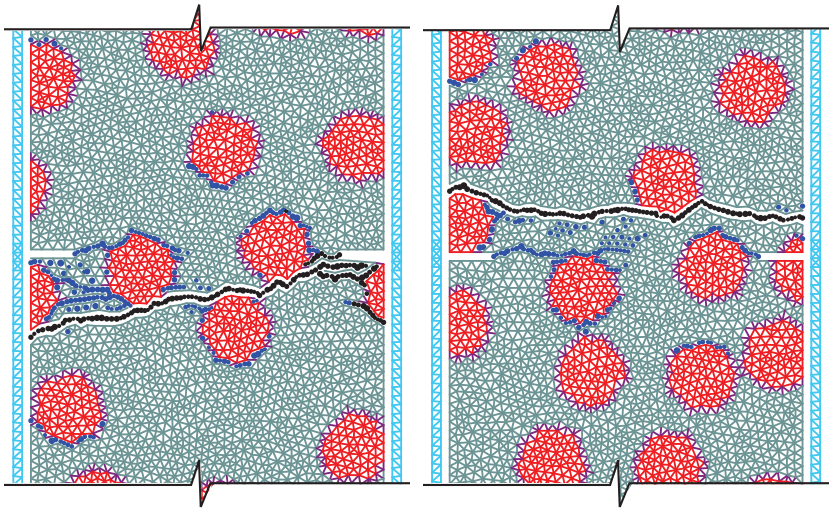

(c) $P_a = 22.49$, $\ell_{FPZ} = 11.92$ (d) $P_a = 25.96$, $\ell_{FPZ} = 11.56$

Figure 3.31 – Crack patterns and the corresponding FPZ size ℓ_{FPZ} [mm] of the A-type tensile tests on the specimen made of the material with aggregate size $d = 8$ mm with four different distributions of the aggregate particles with the corresponding aggregate volume fraction P_a [%].

3.4.6 Aggregate size dispersion at constant volume fraction

The previous studies concern the influence of the aggregate structure on the FPZ size. However, the aggregate structure was restricted to the case of monodispersion. In the present study, an approach to a more realistic aggregate structure of concrete is performed in which a polydisperse aggregate structure is generated for studying the influence of the maximum aggregate size on the FPZ size. For this end, the variation path (*IV*), see Section 3.3.2, in which an aggregate structure is generated using the Fuller's grading, is utilized for numerical simulations of tensile tests by changing the maximum aggregate size $d_{\max}$ to 6.3, 8, 10, 12.5 mm. The minimum aggregate size is 3.5 mm. The reference aggregate volume fraction is kept constant at 45% while changing $d_{\max}$. Furthermore, for each aggregate structure with a value of $d_{\max}$, five independently random distributions are generated so that the mean value of ℓ_{FPZ} is adopted for studying the effect of the maximum aggregate size.

The numerical simulations of tensile tests in this section are performed on the specimen of A-type. We use the same model parameters as before. The material is modeled as the three-phase one with the weak ITZ phase in-between aggregate and matrix phases. In addition, no random field of strengths is introduced in the matrix phase such that one could study only the influences of coarse aggregates on ℓ_{FPZ}.

Figure 3.32 shows the variation of the mean value of the FPZ size ℓ_{FPZ} of the polydisperse aggregate structures of the path (*IV*) variation. For sake of comparison, the result of the monodisperse aggregate structures when varying the aggregate size d and holding the reference aggregate volume fraction constant at 45% (the variation path (*II*)) is also presented. It is seen that, similar to the monodisperse aggregate distribution, when keeping the reference aggregate volume fraction constant and varying the maximum aggregate size $d_{\max}$ of the polydisperse aggregate structure, the mean value of ℓ_{FPZ} does not seem to change significantly with respect to $d_{\max}$. However, the mean value of ℓ_{FPZ} for the polydisperse aggregate structure is found to be slightly higher than that of the monodisperse one. It is likely due to the fact that for reaching the reference aggregate volume fraction 45%, a greater number of aggregate particles is needed for the polydisperse structure than for the monodisperse one. It results in a greater number of ITZ elements in the polydispersion case (see Figure 3.33 for evidence), which in turn obviously has a significant effect on the FPZ size.

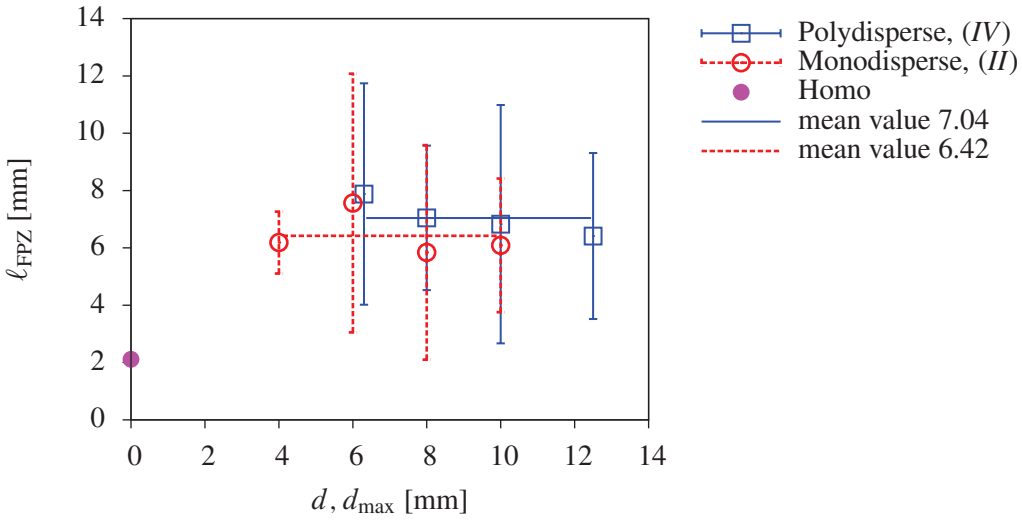

Figure 3.32 – Influence of the dispersion of the aggregate structure on the FPZ size ℓ_{FPZ} when keeping the reference aggregate volume fraction constant at 45% and changing the aggregate size d for the monodisperse or $d_{\max}$ for the polydisperse distributions of aggregate particles.

Figure 3.34 shows the crack patterns and the corresponding values of ℓ_{FPZ} for four aggregate structures with different values of $d_{\max}$ within the variation path (*IV*). Besides, Figure 3.35 shows the crack patterns and the corresponding values of ℓ_{FPZ} for four independently random distributions

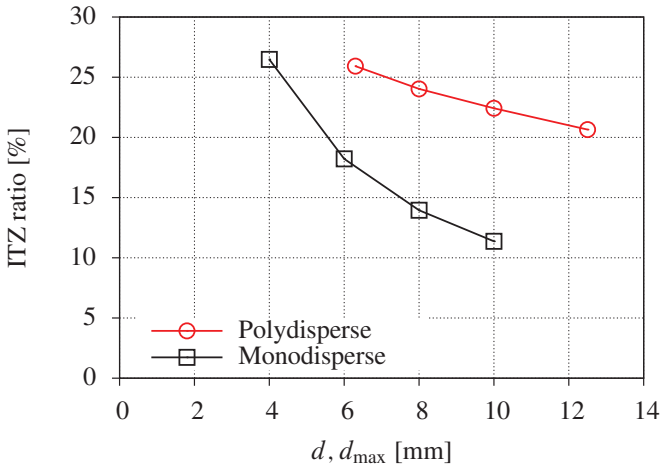

Figure 3.33 – To achieve the same reference aggregate volume fraction (45%), the polydisperse structure results in a greater ratio of ITZ elements than the monodisperse structure when comparing for the same value of d_{max} and d.

of aggregate particles of the polydisperse structure with $d_{max} = 12.5$ mm. It is seen again that the relative positions between the aggregate particles and the notches have a significant effect on the value of ℓ_{FPZ}. As shown in Figure 3.35 for a fixed value of d_{max}, it strongly depends on the position of the aggregate particles with respect to the position of the notches, a wide range of ℓ_{FPZ} can be obtained. It is, however, noted that the maximum-size aggregates are not always found around the notches since the specimen is slender, and of course this is considered as a drawback for an attempt to correlate the FPZ size and the maximum aggregate size. This leads us to think that it would be better if the study is performed on a square specimen so that the maximum-size aggregates can be more "representatively" distributed along the crack path within the specimen. We will refer to the length of that crack path across the specimen as the ligament size. Furthermore, to extend the study of the influence of the aggregate size dispersion on ℓ_{FPZ}, the ligament size between the notches should be enlarged so that more "biggest aggregates" can be represented within the ligament.

3.4.7 Ligament size

Since the above studies are performed on slender specimens (small ligament size compared with d_{max}, in the order of $3 \times d_{max}$) which causes a less frequent occurrence of the maximum-size aggregates in the zone of interest around the FPZ, tensile tests are carried out, this time, on square specimens. In this way, the ligament size is increased while the slenderness is reduced to 1 in order to limit the number of elements. The maximum-size aggregates can more systematically be found around the notch position and play their influences on the FPZ size. In addition, the influence of the ligament size on the value and the variation of the FPZ size ℓ_{FPZ} with respect to the maximum aggregate size d_{max} is pointed out as well.

The specimen geometry is shown in Figure 3.36 and the dimensions of the specimens used in the test are given in Table 3.4, with the same size but with different notch length that results in different ligament length: 90, 80, 65 and 50 mm. They are labeled by L, M, S and XS respectively for convenience.

In order to study the influence of the maximum aggregate size d_{max} on the FPZ size, the tensile tests are performed on the specimens made of the material with a polydisperse aggregate structure with d_{max} being 6.3, 8, 10, 12.5 and 16 mm and the reference aggregate volume fraction is kept constant at 45%. The aggregate structures with d_{max} being 6.3, 8, 10, 12.5 mm have the same aggregate grading of that of the path (*IV*) presented in Section 3.3.2. The additional aggregate grading with $d_{max} = 16$ mm is shown in Table 3.5. All the aggregate gradings are generated by

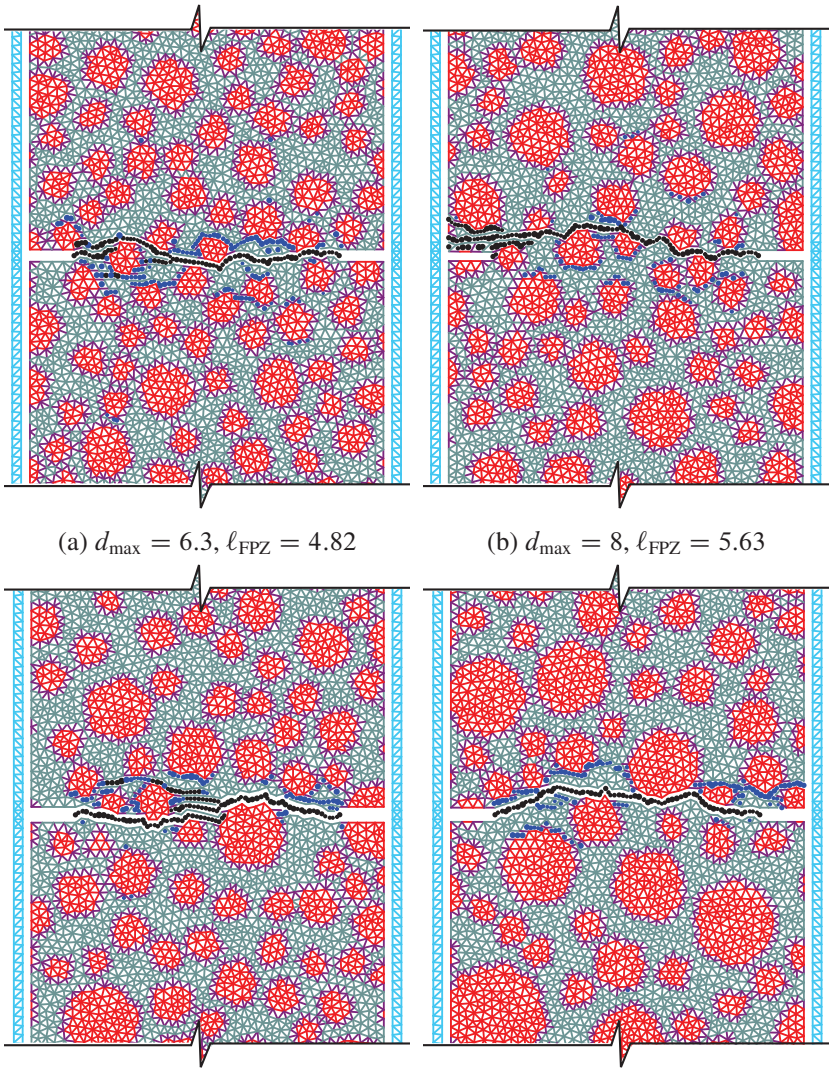

(a) $d_{\max} = 6.3$, $\ell_{\text{FPZ}} = 4.82$ (b) $d_{\max} = 8$, $\ell_{\text{FPZ}} = 5.63$

(c) $d_{\max} = 10$, $\ell_{\text{FPZ}} = 5.15$ (d) $d_{\max} = 12.5$, $\ell_{\text{FPZ}} = 4.71$

Figure 3.34 – Crack patterns and the corresponding FPZ size ℓ_{FPZ} [mm] of the A-type tensile tests on the specimen made of the material with different maximum aggregate size $d_{\max}$ [mm] of the polydisperse aggregate structure of the variation path (*IV*).

Table 3.4 – Specimen dimensions [mm].

Ligament size	Long (L)	Medium (M)	Small (S)	eXtra Small (XS)
Specimen size: a	100	100	100	100
Notch length: c	10	20	35	50
Notch width: d	2	2	2	2
Ligament length: $a - c$	90	80	65	50

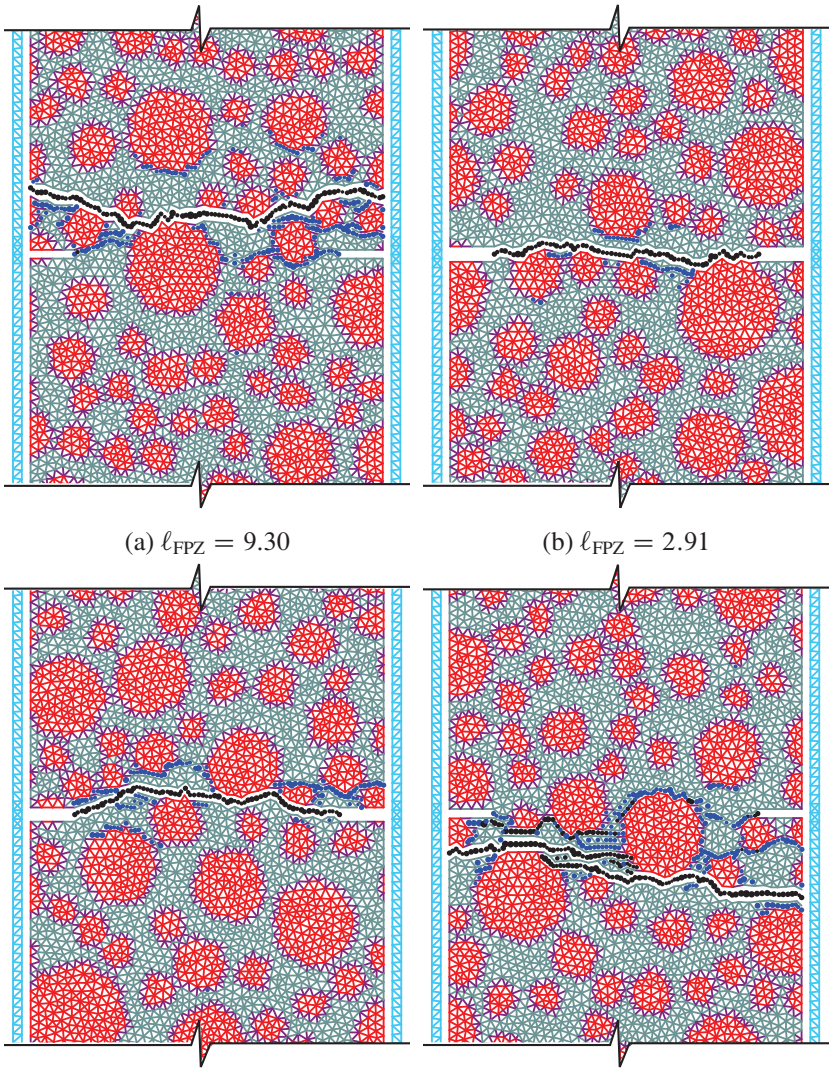

(a) $\ell_{\mathrm{FPZ}} = 9.30$ (b) $\ell_{\mathrm{FPZ}} = 2.91$

(c) $\ell_{\mathrm{FPZ}} = 4.71$ (d) $\ell_{\mathrm{FPZ}} = 9.49$

Figure 3.35 – Crack patterns and the corresponding FPZ size ℓ_{FPZ} [mm] of the A-type tensile tests on the specimen made of the material with the maximum aggregate size $d_{\max} = 12.5$ mm with four independently random distributions of aggregate particles.

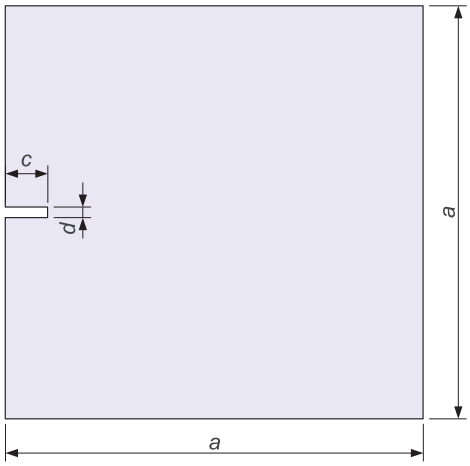

Figure 3.36 – Specimen geometry.

the Fuller's curve. In the study, for each aggregate grading up to $d_{\max}$, five aggregate structure realizations are generated with independently random distribution of aggregate positions.

Table 3.5 – Volume fraction of each aggregate segment of the aggregate structure with $d_{\max} = 16$ mm obtained from the Fuller's grading.

$d_{\max}$ [mm]	Aggregate segment [mm]	Sieve size [mm]	Sieve passing [%]	V_{Agg} [%]	$V_{\text{Agg}}^{\text{abs}}$ [%]
16	0–3.15	3.15	0	0	0
	3.15–4	4	25.72	25.72	11.57
	4–5	5	37.94	12.22	5.50
	5–6.3	6.3	49.51	11.57	5.21
	6.3–8	8	61.44	11.92	5.36
	8–10	10	73.01	11.58	5.21
	10–12.5	12.5	85.30	12.29	5.53
	12.5–15	15	96.03	10.73	4.83
	15–16	16	100	3.97	1.79

The numerical simulations of tensile tests are performed using the lattice model with the same model parameters as before. The material is modeled as the three-phase one with the weak ITZ phase in-between aggregate and matrix phases. In addition, no random field of strengths is introduced in the matrix phase such that one could study only the influences of coarse aggregates on ℓ_{FPZ}. The specimens are loaded in tension by directly imposing the vertical displacement increment on the nodes of the top boundary of the specimens while vertically fixing the nodes of their bottom boundaries.

Figure 3.37 shows the relationship between the FPZ size ℓ_{FPZ} with respect to the maximum aggregate size $d_{\max}$ for the specimens corresponding to four ligament lengths L, M, S and XS. The figure also shows the FPZ size of L, M, S, XS specimens in which no aggregate structure has been introduced and the material is modeled "homogeneously" by only the matrix phase. It is seen that, when the aggregate structures are introduced, it always results in a larger FPZ size computed with the homogeneous cases. For given value of $d_{\max}$, the mean value of ℓ_{FPZ} is systematically increased when the ligament size is increased. In addition, the increase rate of ℓ_{FPZ} is also increased with $d_{\max}$. It results in an higher slope of variation of ℓ_{FPZ} as a function of $d_{\max}$ for a larger ligament size. This is shown in Figure 3.38 where the increase factor of ℓ_{FPZ} (slopes in Figure 3.37) is plotted as a function of the ligament ratio, that is ligament size compared to the specimen width. The dotted line in Figure 3.38 is used as a guide that extrapolates the slope variation over all the possible values of ligament ratio. Interestingly, with the specimen dimensions used, a stabilized value of variation slope of ℓ_{FPZ} is achieved only for ligament size in the order of specimen width. *For ligament size below a half of specimen width, the variation slope is negligible, which means that the aggregate size appears to have no influence on the mean value of ℓ_{FPZ}. Between these limits, the slope variation evolves progressively, indicating that both the aggregate structure and the specimen dimension itself can play a role on the FPZ size. It all may suggest that the FPZ is not completely developed within the specimens with "too short" ligament length*. The maximum-aggregate-size independence of ℓ_{FPZ} of the specimens with too short ligament length is in agreement with the previous study performed on the A-type specimen which also has a short ligament length.

Figure 3.39 shows the crack patterns (selected among several realizations of aggregate positions) and the value of ℓ_{FPZ} corresponding to the smallest aggregate sizes ($d_{\max} = 6.3$ mm) and the biggest ones ($d_{\max} = 16$ mm) for the two extremum ligament lengths (XS and L). In the case of XS specimens (Figures 3.39a and 3.39c), whatever the maximum aggregate size, a crack without bifurcation crosses the ligament by connecting ITZ elements with a path that seems to be the shortest. Whereas, in the case of L specimens (Figures 3.39b and 3.39d), even if only one crack finally crosses the

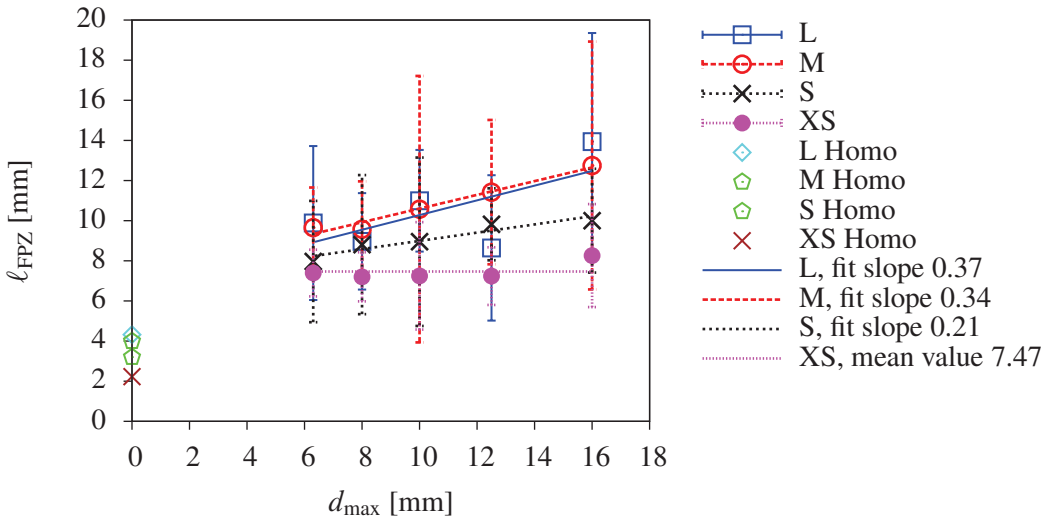

Figure 3.37 – Influence of the ligament length on the variation of the FPZ size ℓ_{FPZ} with respect to the maximum aggregate size d_{max}: L (long ligament), M (medium ligament), S (small ligament), XS (extra small ligament).

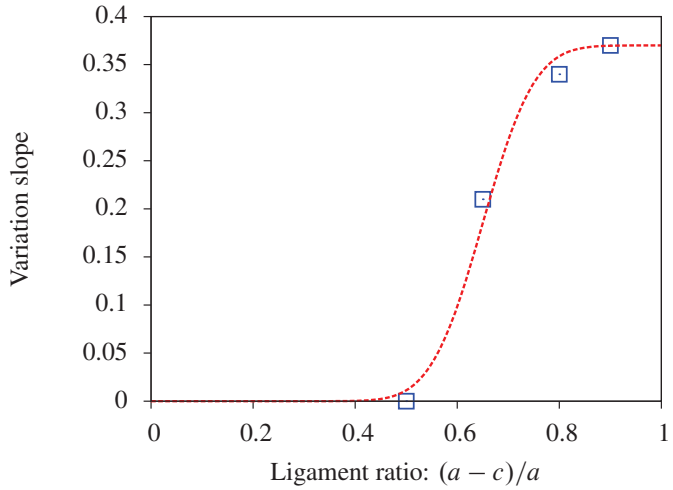

Figure 3.38 – Variation slope of ℓ_{FPZ} with respect to d_{max} as a function of the ligament ratio (ligament size divided by the specimen width).

ligament, a number of bifurcations occur either side of the aggregates. As a consequence, the FPZ size is in direct proportion with the maximum aggregate size in the latter case. *This is one more time an illustration of the possible predominant effect of the stress gradient on the development of the FPZ that can partly hide the influence of the aggregate structure.*

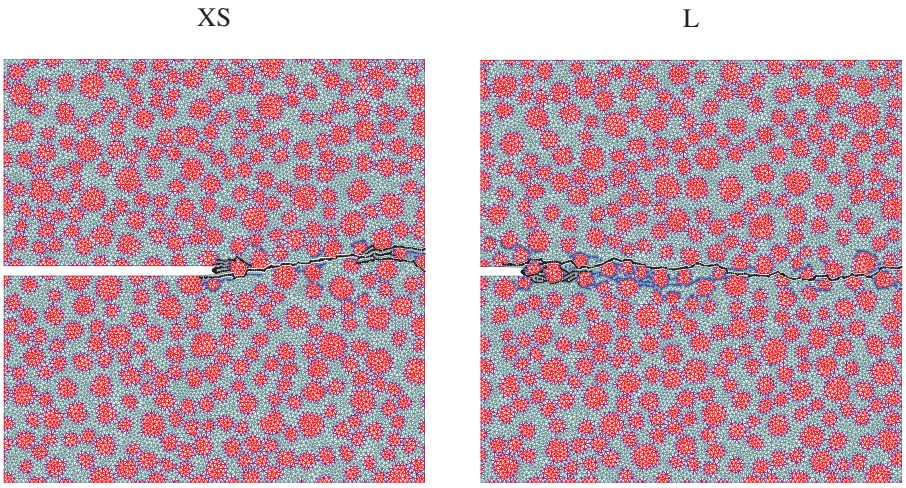

(a) $d_{\max} = 6.3$, $\ell_{\text{FPZ}} = 7.97$ (b) $d_{\max} = 6.3$, $\ell_{\text{FPZ}} = 8.57$

(c) $d_{\max} = 16$, $\ell_{\text{FPZ}} = 8.27$ (d) $d_{\max} = 16$, $\ell_{\text{FPZ}} = 16.60$

Figure 3.39 – Crack patterns and the corresponding FPZ size ℓ_{FPZ} [mm] of the XS specimens (left) and the L specimens (right), both made of the material with $d_{\max} = 6.3$ mm (top) and $d_{\max} = 16$ mm (bottom). The black dots indicate broken elements with the largest opening – read as the macrocrack – while the blue dots stand for the remaining broken elements – read as the microcrack.

3.5 Material characteristic length *versus* FPZ size

In Section 3.4, the influence of the material mesostructure on the FPZ size has been studied. The aim is now to question whether the same influence can be observed on the characteristic length of the material. Although many simulations were carried out to answer this question, we only focus herein on two mesoscopic features that may influence the characteristic length ℓ_{c}, the aggregate size with (i) fixed position and (ii) fixed volume fraction.

A practical example for the assessment of the characteristic length of the material using the lattice model is presented in Section 3.2.4 in which the LD and DD tensile tests are performed to determine the fracture energy G_f and dissipation energy density W_s, respectively, and the charac-

teristic length is determined by Equation (3.2).

In this section, the numerical simulations of LD tensile tests are performed on the specimen of A-type. The dimensions of LD and DD specimens tested are shown in Table 3.1. The same model parameters as previous are used, see Table 3.2. The material is modeled as the three-phase one with a weak ITZ phase in-between aggregate and matrix phases. In addition, no random field of strengths is introduced in the matrix phase such that the influence of coarse aggregates on ℓ_c can be individually studied.

3.5.1 Aggregate size with fixed positions

First, the lattice simulations are performed by varying the aggregate size while both the positions and the number of aggregates remain unchanged. This concerns the path (I) of mesostructure variation in which the monodisperse diameter of aggregates is changed by setting their values to 4, 6, 8, and then 10 mm. Five independent realizations of aggregate positions are performed for each aggregate size.

Figure 3.40 shows the relation between the characteristic length ℓ_c and the aggregate size d. For a comparison with the FPZ size ℓ_{FPZ}, the relation between ℓ_{FPZ}, computed from the LD tests, and the aggregate size is shown as well. The standard deviations of ℓ_c and ℓ_{FPZ} are always shown by the vertical bars attached to the corresponding mean values.

The main observation is that ℓ_c and ℓ_{FPZ} have the same order of magnitude and trend with respect to the aggregate size.

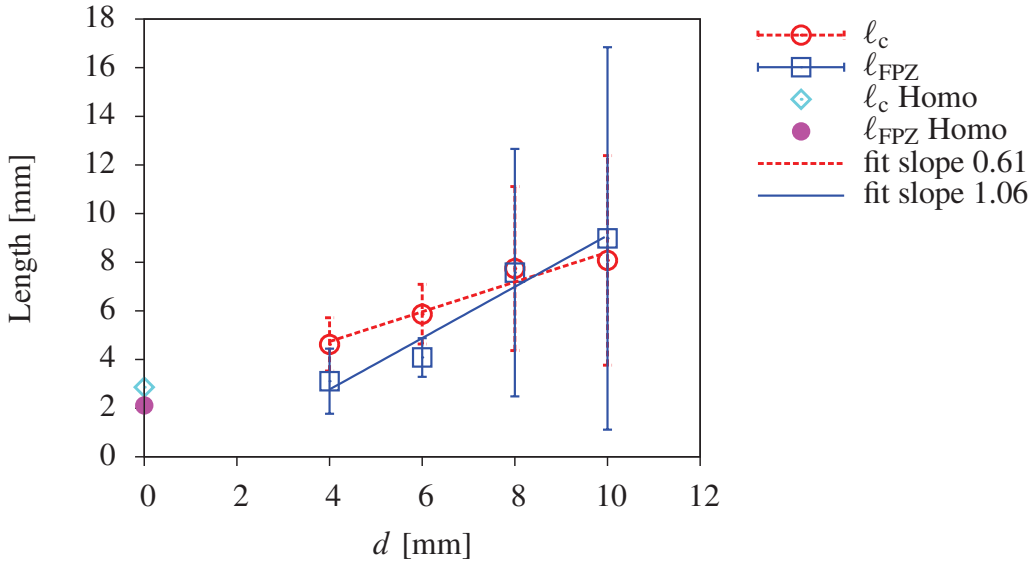

Figure 3.40 – Variation of the internal length of the material ℓ_c and the FPZ size ℓ_{FPZ} with respect to the aggregate size d within the path (I) of variation.

The increase in d results in an increase of standard deviations of ℓ_c as previously observed in the variation of the FPZ size ℓ_{FPZ}. The reason may still be related to the fact that upon the aggregate size increase, the volume fraction of aggregate particles, and thus the number of ITZ elements, increases and as a consequence, the spacial distribution of aggregate particles with respect to the notch position has a more important role in the resulting characteristic length of the material. This remark highlights the fact that not only the aggregate size but also other less obvious features, affected themselves by the aggregate size, influences ℓ_c (idem for ℓ_{FPZ}).

3.5.2 Aggregate size with fixed volume fraction

Now the question is whether the variation of the characteristic length ℓ_c with respect to the aggregate size d still follows the variation of the FPZ size ℓ_{FPZ} with respect to d if we only do vary the size d of aggregates while keeping the volume fraction of aggregates as constant as possible? For this end, the path (*II*) of the mesostructure variation (see Section 3.3.1) is used to study the influence of the aggregate size d on the characteristic length ℓ_c, in which the "reference" volume fraction of aggregates is kept at 45% when changing the aggregate size.

Figure 3.41 shows the characteristic length of the material ℓ_c as a function of the aggregate size d. The plot between the FPZ size ℓ_{FPZ} and d is shown as well. It exhibits that increasing d does not lead to an increase of ℓ_c, as previously observed in the case of ℓ_{FPZ}. With a fixed value of the aggregate size, the resulting characteristic length of the material varies upon the spacial distribution of aggregate particles. However, the mean value of the characteristic length with respect to the spacial distribution of aggregate particles seems to be unchanged upon the increase of the aggregate size. The reason for this non-sensitivity may be related to the fact that the spacing between the aggregate particles, thus the spacing between the ITZs, seems to be insignificantly changed when the aggregate size is increased, as previously shown for the case of the FPZ size, see Section 3.4.4.

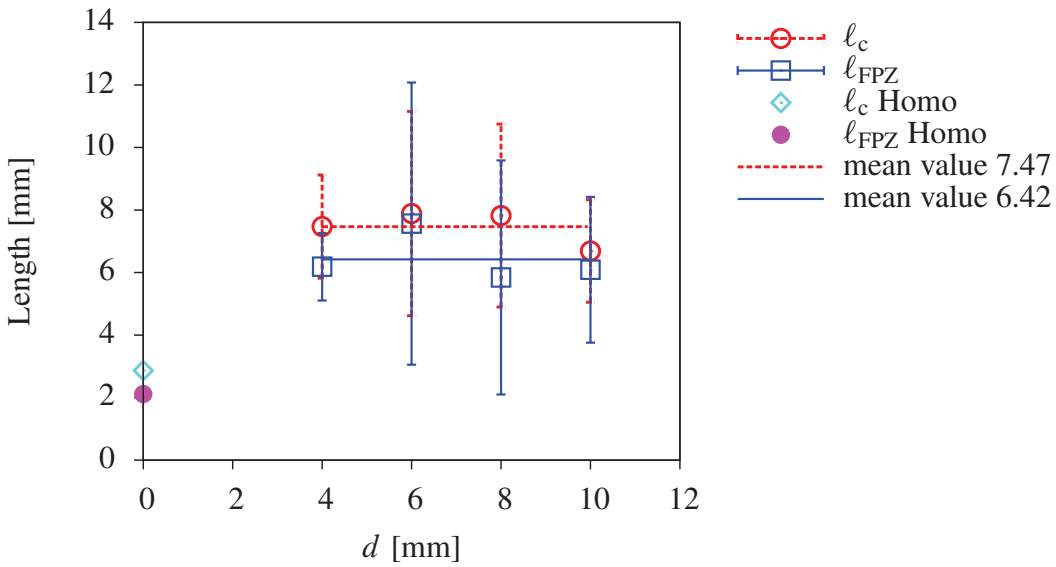

Figure 3.41 – Variation of the internal length of the material ℓ_c and the FPZ size ℓ_{FPZ} with respect to the aggregate size d within the path (*II*) of variation.

In addition, the standard deviations of ℓ_c behave in the same way as that of ℓ_{FPZ}. This means that if ℓ_{FPZ} varies within a wide range then the range of deviation of ℓ_c is also wide and of the same order. This remark stands also for small standard deviations of ℓ_{FPZ} and ℓ_c. *It illustrates once more that a certain equivalence exists between* ℓ_{FPZ} *and* ℓ_c. The difference is that the assessment of ℓ_{FPZ} only requires one LD test whereas the assessment of ℓ_c requires both LD and "diffused damage" tests; but unfortunately the latter cannot be practically performed, at best the damage is distributed in the form of cracks overall the specimen in the so-called DD tests. For this reason, and given that ℓ_{FPZ} and ℓ_c have been shown to behave similarly (in spite of a small difference in their values), the conclusions drawn in Section 3.4 for ℓ_{FPZ} can be extrapolated for ℓ_c.

3.6 Conclusions

Two types of tensile tests were performed to study the key features that influence the FPZ size ℓ_{FPZ} and the material characteristic length ℓ_c. The assessment of ℓ_{FPZ} is achieved via localized damage

(LD) tests while ℓ_c is measured via both LD tests and distributed damage (DD) tests. The numerical simulations are performed on the brittle elastic model material with inclusions which are called aggregates. The material is then modeled as the two-phase material with the aggregate and matrix phases that constitute the mesostructure of the material or as the three-phase one with the interfacial transition zone (ITZ) is defined in addition in-between aggregate and matrix phases. Not only the mesostructure of the material but also the specimen geometry and boundary conditions are varied in order to analyze their effect on the resulting FPZ size and material characteristic length. Five independent realizations of aggregate positions are generated for each case of the mesostructure so that the average values of ℓ_{FPZ} and of ℓ_c over that five realizations are used to analyze the effect of the mesostructure. The study has been pointed out the influences of: the ITZs, the fine aggregate particles, the applied stress gradient and material rotation, the aggregate size with fixed volume fraction, the aggregate volume fraction with fixed size, the aggregate size dispersion and the ligament size of the specimen on ℓ_{FPZ} and ℓ_c.

From that extensive study, the following conclusions can be drawn:

- It appears that not basically the size, but other parameters that characterize the aggregate structure of the material such as the volume fraction, the size dispersion, the fabric, the connectivity, and interface properties... strongly affects the size of the FPZ, and thus the characteristic length of the material.

- The measured value of the FPZ size is also dependent on the local stress level and/or on the stress gradient which may be related to the specimen geometry or the boundary conditions for instance. Therefore, it is difficult to avoid the conclusion that the FPZ size is *not* an intrinsic property of the material as usually believed. However, it seems true that the FPZ size remains in the same order when the tested system is the same (mesostructure, global geometry and dimensions, loading conditions...).

- The assessment of the characteristic length of the material is essential for using its value as the internal length in nonlocal models. However, just like the FPZ size, it is difficult to avoid structural effects in the method of measurement of the characteristic length.

Chapter 4

Multiscale coupling

Contents

This chapter deals with the coupling between the numerical continuum-based approach and discontinuous approach for simulation of the fracture process of quasi-brittle materials. The numerical methods used for continuum based model and discrete model are the Finite Element Method (FEM) and the Lattice Element Method (LEM), respectively. The reasons for this coupling are discussed in the first section. Then, a selection of an algorithm for the coupling is proposed. The algorithm of the proposed algorithm will be presented in details before dealing with the numerical implementation. The chapter is closed by some applications and conclusions.

4.1 Introduction

Numerical simulations are an indispensable part of the current engineering and science development. Modeling of fracture of heterogeneous quasi-brittle materials (concrete, rocks, ceramics) is evolving over the past twenty years. The lattice element method (LEM) has become a useful tool for studying the fracture of heterogeneous materials. In fact, the lattice approach is very suitable for simulation of fracture process because firstly the discontinuous displacement field is well captured thanks to the intrinsic discrete feature of the model. Secondly, the crack patterns and crack opening are explicitly produced at the mesoscale when the heterogeneity of the material is introduced by generating the material constituents, see Chapter 2. In contrast, the continuum-based approaches used at the macroscale are unsuitable (or, not easy because of complex constitutive laws as, for example, shown in Bažant and Planas (1998) and Jirasek and Bažant (2002)) to capture the post-peak stage in terms of stress-strain curves, crack patterns and crack opening. However, simulations with the lattice model at the mesoscale require fine resolutions of the discretized mesh, leading to the model with a large number of degrees of freedom in particular for three-dimensional analyses. Indeed, three-dimensional analyses by the lattice model seem to be necessary since the two-dimensional ones may misrepresent important aspects of three-dimensional fracture process such as the ductility in the post-peak regime. Therefore, the analysis of realistic large structures only with the lattice model at the mesoscale with a vast number of degrees of freedom is not feasible (or, not economic if it is feasible). So, it seems that an appropriate combination of discrete approach at the mesoscale dealt by the lattice model and continuous approach at the macroscale treated by the finite element method (FEM), which results in a multiscale approach, is essential. Using the multiscale approach, average values of variables at the structural level are available and where needed, we have the possibility to zoom in and get a fine resolution of the crack topology at the mesoscale. This will be of a great interest both for graphical simulation and for transfer properties analysis in a post-treatment procedure, e.g., analyzing the interaction between material damage and transport properties of concrete (Pijaudier-Cabot et al., 2009). In addition, this approach may provide a direct tool in durability analyses of (concrete) structures since crack propagation and crack opening are directly furnished instead of estimating them from the continuum-based approach (Dufour et al., 2012).

The key issue of the multiscale approach proposed in this study is that the macroscopic approach by FEM and mesoscopic approach by LEM are coupled within an *adaptive* multiscale procedure to model large-scale structures with localized fracture processes. This means that only the fracture process zone and its immediate vicinity are modeled by the lattice model at the mesoscale. The material surrounding the lattice network is represented by finite elements (FE) and is assumed to be linear elastic at the macroscale. As the fracture process evolves, the coupling model is updated by a zoom-in procedure in which certain zones represented by the FE, satisfying a specific criterion (which is defined later), are switched to be represented by the lattice model at the mesoscale.

Despite the attractiveness of the multiscale approach in terms of computational cost, dealing with a (very) fine resolution even on a reduced area (near the crack front) require high levels of performance to process a large simulation in three dimensions. Therefore, parallel computation should be anticipated for the LEM-FEM multiscale coupling. It accounts for the implementation of the coupling procedure into SOFA architecture presented hereafter. The coupling is restricted to small deformations under quasi-static loading conditions.

4.2 Selection of an algorithm

4.2.1 A conspicuous algorithm

If the stiffness of a lattice cell is equivalent to that of a FE, the coupling procedure LEM-FEM can be conceptually performed as follows. The structure is initially modeled by FEM with linear elastic elements. As the load increases, the FE that satisfies a specific criterion, e.g. based on stress/strain quantity, is supposed to behave nonlinearly. And just before the criterion is verified, that FE is replaced by a lattice network of the same size and the coupling is performed by restraining the boundary nodes of the lattice network by the displacement field at the boundaries of the FEs at the moment of replacement. The simulation is continued by performing nonlinear analysis on the lattice network and then transferring the stress field at the boundary nodes of the lattice network to the neighboring FEs, see Figure 4.1. The simulation is pursued so that the next FE fulfills the criterion of nonlinearity and is replaced by another lattice network. The above procedure is repeated until complete failure of the structure.

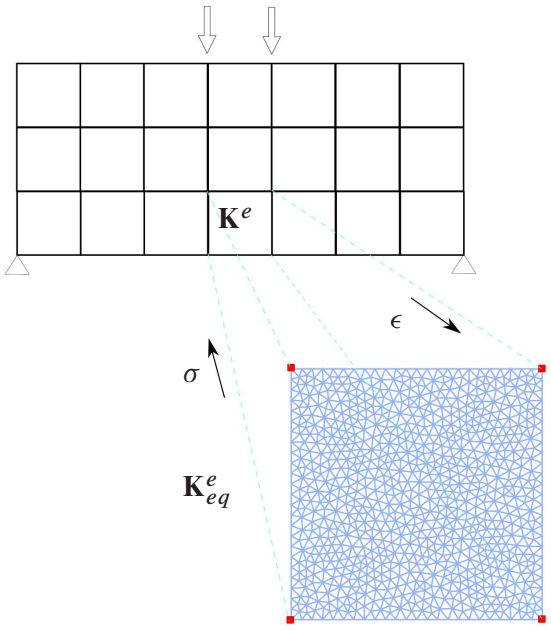

Figure 4.1 – Replacing a FE by a lattice cell of the same size.

However, the coupling procedure is only valid if and only if the lattice network and the replaced FE have the same Young's modulus, Poisson's ratio and elementary stiffness matrix, i.e., they are representing the same material. In order to verify whether a lattice network can represent the same material represented by a FE, the following test is carried out. For the sake of simplicity, the simplest FE which is a four-node quadrilateral element (QUA4) with 8 degrees of freedom and the normal-shear spring lattice network are used in the test. The size of the FE and the lattice cell are 1×1 mm^2. The lattice cell is discretized so that the isotropy requirement is satisfied, i.e., the macroscopic Young's modulus and Poisson's ratio obtained from the lattice cell in x- and y-direction are not significantly different, see Section 2.2.3.3. This accounts for the ratio $B/l_m = 60$ is used in the study with $B = 1$ mm the size of the cell and l_m the mean size of the lattice elements. The material is used in the test with the Young's modulus $E = 30$ GPa and the Poisson's ratio $\nu = 0.2$. First the parameters of the lattice network E_n, E_s are identified so that the macroscopic Young's modulus and Poisson's ratio obtained from the lattice cell are 30 GPa and 0.2 respectively. This leads to $E_n = 37.5$ GPa and $E_s = 12.5$ GPa. The FE QUA4 which represents the continuum with two parameters $E = 30$ GPa and $\nu = 0.2$ has its individual stiffness matrix. The remaining problem is to check whether the lattice cell has the same stiffness matrix with the FE QUA4 in order to ensure

that they are modeling the same material.

Figure 4.2a shows the FE QUA4 1×1 mm^2 with four nodes 1, 2, 3, and 4. The lattice cell of the same size with four macroscopic nodes 1, 2, 3, and 4 are shown in Figure 4.2b. Since the displacement field in the FE QUA4 is bilinear, so in order to compare the stiffness matrix of the FE with the *equivalent stiffness matrix* of the lattice cell with respect to the four macroscopic nodes, the latter has to be determined by the way such that the displacement field of the lattice cell is also linear. It is numerically determined as follows. First, the elastic analysis is performed on the lattice cell by imposing the unit displacements at the macroscopic nodes, one by one, with respect to the degrees of freedom in x- and y-direction, and also linearly imposing the displacements to the nodes located on the boundaries containing the current macroscopic node with respect to the unit displacement imposed on the current macroscopic node and the zero displacements on the neighboring macroscopic nodes, while fixing all remaining nodes located on the boundaries that do not contain the current macroscopic node in the same direction with the unit displacement. For example, to compute the equivalent stiffness with respect to the degree of freedom u_1, one imposes the unit displacement at the macroscopic node 1 in the x-direction and all nodes belonging to the boundaries 1-4 and 1-2 are linearly imposed also in the x-direction from the unit displacement at node 1 to the zero displacements at nodes 4 and 2, see Figure 4.2b, while all nodes located on the boundaries 2-3 and 3-4 are fixed in x-direction for the elastic analysis. Then, the forces are measured at the macroscopic nodes 1, 2, 3 and 4 in x- and y-direction which are the components of the equivalent stiffness matrix. By doing so, the equivalent stiffness matrix of the lattice cell is

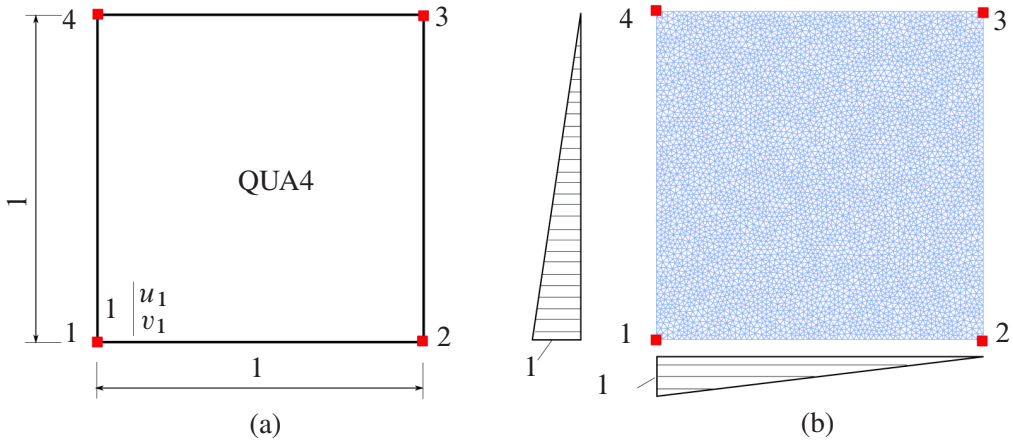

Figure 4.2 – Continuum medium represented by a FE QUA4 (a) and by a lattice network (b).

numerically given by

$$\mathbf{K}^e_{\text{LEM}} = \begin{pmatrix} 15.2562 & 2.9127 & -6.5872 & -0.0338 & -7.8768 & -2.8735 & -0.7922 & -0.0054 \\ 2.9127 & 15.2251 & -0.0494 & -0.7399 & -2.8828 & -7.8734 & 0.0194 & -6.6118 \\ -6.5872 & -0.0494 & 15.0244 & -2.7939 & -0.6519 & 0.0182 & -7.7853 & 2.8250 \\ -0.0338 & -0.7399 & -2.7939 & 15.0482 & -0.0091 & -6.5145 & 2.8368 & -7.7938 \\ -7.8768 & -2.8828 & -0.6519 & -0.0091 & 15.0555 & 2.8344 & -6.5269 & 0.0576 \\ -2.8735 & -7.8734 & 0.0182 & -6.5145 & 2.8344 & 15.0860 & 0.0209 & -0.6981 \\ -0.7922 & 0.0194 & -7.7853 & 2.8368 & -6.5269 & 0.0209 & 15.1043 & -2.8772 \\ -0.0054 & -6.6118 & 2.8250 & -7.7938 & 0.0576 & -0.6981 & -2.8772 & 15.1037 \end{pmatrix}$$

in which the unit is kN/mm. The stiffness matrix of the FE QUA4 in the case of plane strain with

two parameters $E = 30$ GPa and $\nu = 0.2$ is given by

$$\mathbf{K}^e_{\text{FEM}} = \begin{pmatrix} 15.2778 & 5.2083 & -9.0278 & -1.0417 & -7.6389 & -5.2083 & 1.3889 & 1.0417 \\ & 15.2778 & 1.0417 & 1.3889 & -5.2083 & -7.6389 & -1.0417 & -9.0278 \\ & & 15.2778 & -5.2083 & 1.3889 & -1.0417 & -7.6389 & 5.2083 \\ & & & 15.2778 & 1.0417 & -9.0278 & 5.2083 & -7.6389 \\ & & & & 15.2778 & 5.2083 & -9.0278 & -1.0417 \\ & & & & & 15.2778 & 1.0417 & 1.3889 \\ & & \text{sym} & & & & 15.2778 & -5.2083 \\ & & & & & & & 15.2778 \end{pmatrix}$$

where the unit is again kN/mm. It is shown that a significant difference between the stiffness matrix of the lattice cell and that of the FE QUA4 is observed. In particular, the non-diagonal terms of the equivalent stiffness matrix of the lattice cell is significantly smaller than those of the FE QUA4. Note that the difference between the two matrices not only is observed on the magnitude but also on the sign. Moreover, the non-equal values among diagonal terms of $\mathbf{K}^e_{\text{LEM}}$ mean that the macroscopic behavior of the lattice cell is not isotropic with respect to the directions of the macroscopic degrees of freedom. It all may be related to the discretization fineness of the used mesh and/or to the fact that the rotational degrees of freedom are not taken into account in the lattice cell.

In order to verify the effect of the discretization fineness on the equivalent stiffness matrix, an analysis with the same model parameters but on the lattice cell with a finer discretization than above is carried out. The discretization mesh with the ratio $B/l_m = 100$ is used in the present study to determine the equivalent stiffness matrix of the lattice cell. By doing the same elastic analysis as above, the equivalent stiffness matrix of the lattice cell is now given by (kN/mm)

$$\mathbf{K}^e_{\text{LEM}} = \begin{pmatrix} 15.2751 & 2.8976 & -6.7470 & 0.0494 & -7.9332 & -2.9542 & -0.5948 & 0.0072 \\ 2.8976 & 15.0072 & -0.0023 & -1.0041 & -2.9201 & -7.7446 & 0.0248 & -6.2585 \\ -6.7471 & -0.0023 & 15.6910 & -3.1273 & -0.7373 & 0.0497 & -8.2067 & 3.0798 \\ 0.0494 & -1.0041 & -3.1273 & 15.5107 & -0.0175 & -6.4283 & 3.0954 & -8.0783 \\ -7.9332 & -2.9201 & -0.7373 & -0.0175 & 15.3816 & 2.9728 & -6.7111 & -0.0352 \\ -2.9542 & -7.7446 & 0.0497 & -6.4283 & 2.9728 & 15.1588 & -0.0684 & -0.9860 \\ -0.5948 & 0.0248 & -8.2067 & 3.0954 & -6.7111 & -0.0684 & 15.5126 & -3.0518 \\ 0.0072 & -6.2585 & 3.0798 & -8.0783 & -0.0352 & -0.9860 & -3.0518 & 15.3229 \end{pmatrix}$$

It is shown again that the difference with the stiffness matrix of the FE QUA4 persists. The non-equal values of the diagonal terms of $\mathbf{K}^e_{\text{LEM}}$ are seen yet. It exhibits that a better value of the term k_{18} (0.0072) but a worse value of k_{14} (0.0494) than the values in the case of the mesh with $B/l_m = 60$ are obtained when comparing those values with the corresponding values of $\mathbf{K}^e_{\text{FEM}}$. However, the smaller magnitudes of the non-diagonal terms compared to those of the stiffness matrix of the FE QUA4 are always observed. This leads us to think that the rotational degrees of freedom, when activated, may play a vital role in the transfer of load and thus have a significant effect on the equivalent stiffness matrix of the lattice cell.

In order to take into account the rotational degrees of freedom when computing the equivalent stiffness matrix of the lattice cell, the beam lattice model is used in the elastic analysis. The beam lattice model has two elastic parameters which are the Young's modulus E_b of the beam lattice elements and an adimensional parameter λ that is related to the second moment of area, see Section 2.5. These parameters are identified so that the macroscopic Young's modulus and Poisson's ratio obtained from the lattice cell are 30 GPa and 0.2 respectively. They are $E_b = 37.88$ GPa and $\lambda = 1.03$. The mesh with the ratio $B/l_m = 100$ is used. With the same procedure as above, the elastic analyses are carried out to compute the equivalent stiffness matrix of the beam lattice cell.

The obtained stiffness matrix is given by (kN/mm)

$$\mathbf{K}^{e}_{\text{LEM}} = \begin{pmatrix} 15.2778 & 5.2023 & -9.1323 & -0.9357 & -8.6351 & -5.1308 & 2.4897 & 0.9745 \\ 5.2023 & 15.3971 & 0.9963 & 2.3980 & -5.1941 & -8.5926 & -0.9450 & -9.1966 \\ -9.1329 & 0.9457 & 15.2662 & -5.1837 & 2.5363 & -0.9811 & -8.6692 & 5.1086 \\ -0.9885 & 2.3944 & -5.1837 & 15.3528 & 0.9446 & -9.1832 & 5.1680 & -8.5697 \\ -8.6351 & -5.1705 & 2.5357 & 0.9790 & 15.3246 & 5.1519 & -9.2255 & -0.8496 \\ -5.1542 & -8.5925 & -0.9485 & -9.1809 & 5.1519 & 15.3451 & 1.0105 & 2.4344 \\ 2.4901 & -0.9775 & -8.6696 & 5.1404 & -9.2258 & 0.9599 & 15.4050 & -5.2335 \\ 0.9403 & -9.1991 & 5.1359 & -8.5699 & -0.9025 & 2.4307 & -5.2335 & 15.3319 \end{pmatrix}$$

As expected, it is seen that the smaller difference between $\mathbf{K}^{e}_{\text{LEM}}$ and $\mathbf{K}^{e}_{\text{FEM}}$ than in the case of the normal-shear spring lattice cell is obtained. The values of the non-diagonal terms are now close to those of the FE QUA4. The sign of the terms is now correctly obtained. However, the non-equal values of the diagonal terms are still observed. It again means that the macroscopic behavior of the beam lattice cell is not perfectly isotropic with respect to the directions of the macroscopic degrees of freedom. Moreover, the obtained stiffness matrix is no longer symmetric. This is clearly due to the effect of the transfer of moments and shear forces when the rotational degrees of freedom are activated.

To sum up, the above studies lead to the logical conclusion that the lattice model with the appropriate parameters can macroscopically represent the material with the given Young's modulus and Poisson's ratio as the FEM does. However, in terms of stiffness, a lattice cell reproduces a different stiffness matrix compared to that of a FE of the same size. This seems likely due to the "structural effect" of the lattice model. Nevertheless, the equivalent stiffness matrix of a lattice cell reproduced by the beam lattice model is closer to the stiffness matrix of a FE than that reproduced by the normal-spring lattice model. Quite obviously, this is due to the influence of rotational degrees of freedom on the transfer of moments and shear forces. Since the stiffness matrices of a lattice cell and of a FE are not equivalent, this leads us to use another algorithm for the LEM-FEM coupling.

4.2.2 The proposed algorithm

Since a lattice cell does not yield the same stiffness matrix as a FE of the same size even though they can macroscopically represent a material with the same elastic parameters like Young's modulus and Poisson's ratio, the above algorithm for LEM-FEM coupling is not valid. Therefore, we propose another algorithm in which the structure is also initially modeled by the FEM, however the stiffness matrix of a FE is not constructed by integration over the volume/area of that FE but it is computed by means of a *homogenization process* over a LEM cell of the same size. FEs where the behavior remains below a threshold, the material is supposed to behave elastically and the initial stiffness matrices are kept. FE, where the threshold is overtaken, is replaced by a LEM cell on which an update of the stiffness matrix is performed by means of a nonlinear analysis of the LEM cell when restraining the boundary nodes of the LEM cell by the strain field at the boundaries of the neighboring FEs. Then, the stress field at the boundaries of the LEM cell is transfered to the neighboring FEs. Since the beam lattice model produces the equivalent stiffness matrix of a LEM cell which is closer to the stiffness matrix of a FE than the normal-shear spring lattice model, the former is used in the LEM-FEM coupling.

Moreover, the algorithm of the LEM-FEM coupling should be provided for parallel computation in order to deal with large-scale structures in general purposes. In the context of continuum based approach, for dealing with large-scale system in three dimensions, the dual-primal finite element tearing and interconnecting (FETI-DP) method (Farhat et al., 2000, 2001), which are a family of domain decomposition (DD) algorithms, has been developed during the last decade for the parallel iterative solution of large-scale system of equations arising from the finite element discretization of partial differential equations. Within the dual-primal DD method, the reference problem is split into

subdomains and the coarse problem is numerically built by choosing some "corner node" degrees of freedom (DOF) as basics unknowns. The key issue of only choosing DOFs of corner nodes as unknowns is to reduce the size of the coarse problem in order to speedup the computational time compared to the basic FETI (Farhat and Roux, 1991) and FETI-2 (Farhat and Mandel, 1998) methods. The continuity between subdomains is assured by Lagrange multipliers. Parallel computing is achieved by mapping one or several subdomains onto a processor. For this reason, the method is capable of delivering a larger speedup for a larger number of processors with respect to the number of subdomains. This is the parallel scalability. For more details about the FETI-DP method and its scalability, the reader is referred to Farhat et al. (2000, 2001) and references therein.

In order to keep the parallel scalability of the LEM-FEM multiscale approach, the coupling algorithm is based on the idea of the FETI-DP methodology. The difference with the latter is that the solution of the fine scale is affected by LEM approach. Details of the LEM-FEM coupling algorithm are presented in the next section. For the sake of simplicity, demonstrations in what follows are shown by two-dimensional figures even though the algorithm is fully applied to three-dimensional problems.

4.3 Algorithm for concurrent LEM-FEM coupling

4.3.1 Meso-macro description

The starting point is that the structure is discretized by a fine mesh and is decomposed into subdomains with compatible interfaces, defined by the coarse nodes. The fineness of the mesh is determined by the lattice model described in Chapter 2. The fact that the mesh decomposition is performed is for the purpose of parallel computation. The LEM description based on the fine mesh is firstly constructed for all the subdomains with an explicit representation of aggregate structure of the material at the mesoscale, see Figure 4.3a. Then, the FEM approach is constructed on the whole structure based on the coarse mesh defined by the coarse nodes in which each macro zone is considered as a FE whose the stiffness matrix is constructed by performing a *homogenization process* over the corresponding LEM description of that macro zone, see Figure 4.3b. It is noted that by this way, the FEM description is just seen as a discrete set of macro nodes interconnecting by the homogenized stiffnesses. It is in contrast to the "real" FEM in which the stiffness matrices of FEs are constructed by numerical integration over the element volume using the shape functions and the matrix of elastic properties. It exhibits that, by this meso-macro description, each macro zone possesses its own fine mesh described by LEM approach and during the simulation, when needed, these fine zones will be activated.

The simulation is initially carried out by the FEM approach. As the loading increases, certain subdomains, in which the criterion (called the switch criterion) defined later is satisfied and the material is supposed to behave nonlinearly, are upgraded one by one to their corresponding fine resolution represented by LEM approach. Figure 4.4a shows the first mesozone which is activated to replace the corresponding FE. Subsequently, cracking process occurs in the mesozone by performing elastic analysis on that mesozone. If in the meantime, the switch criterion is fulfilled in another FE, the corresponding mesozone will be activated to substitute the FE, see Figure 4.4b. However, the fracturing process still takes place in the first mesozone. When a crack fully crosses the LEM cell, i.e., the latter is totally broken and will be deactivated. The corresponding FEM cell is reactivated but is decomposed into two FEs by the mean path of the crack in order to maintain the mass of the structure, see Figure 4.4c. The cracking process now takes place in the second mesozone. The simulation is continued by repeating the meso-macro procedure.

In short, in order to develop the multiscale coupling LEM-FEM approach, one has to tackle five issues: (i) the homogenization from the meso- to the macroscale, (ii) the connection of fine and coarse subdomains (incompatible mesh connection), (iii) the connection of fine and fine subdomains (compatible mesh connection), (iv) the transition from the macro- to the mesoscale by a zoom-in

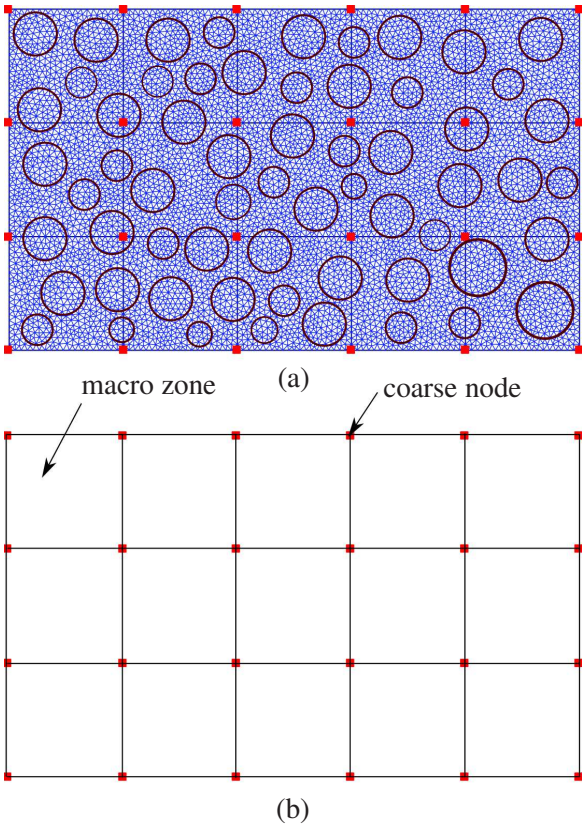

Figure 4.3 – LEM description based on the fine mesh which is decomposed into the subdomains defined by the coarse nodes (a) and FEM description based on the coarse mesh defined by the macro zones (elements) with macro (homogenized) stiffnesses computed by homogenization on the corresponding LEM description of each macro zone (b).

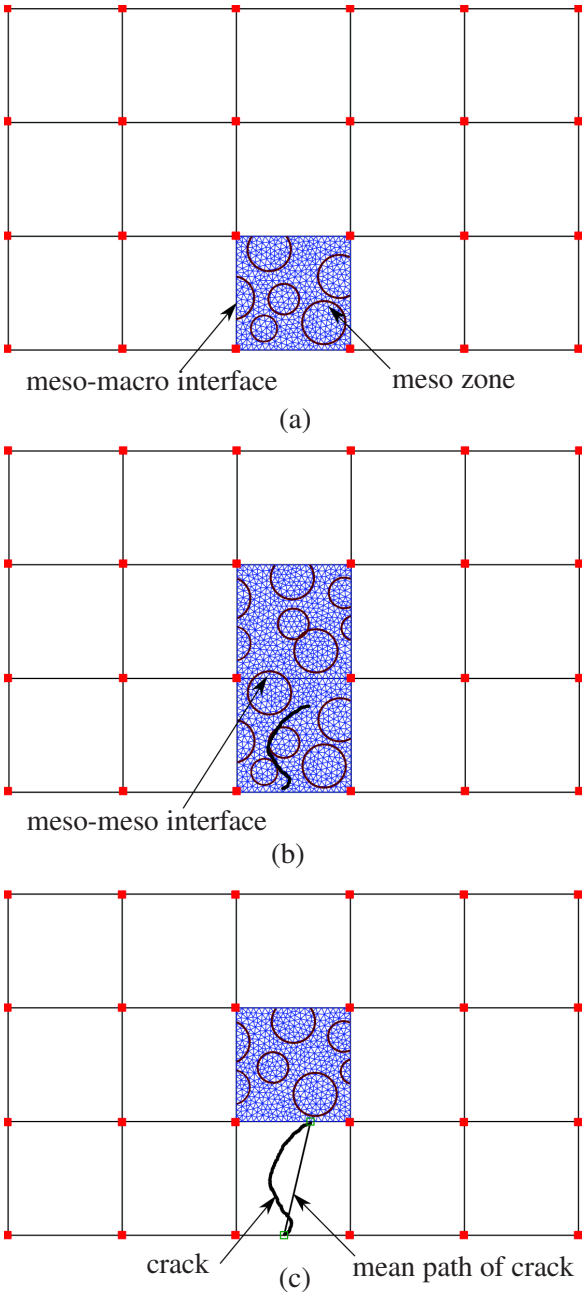

Figure 4.4 – The first mesozone is activated and the corresponding FE is deactivated (a); the second mesozone is activated if the switch criterion is fulfilled in the corresponding FE, but the cracking process still takes place in the first mesozone (b); when the first one which is completely failed, it is deactivated and the corresponding FE is reactivated but is decomposed into two FEs by the mean path of the crack to maintain the mass of the structure (c).

technique and (v) the transition from the meso- to the macroscale by a zoom-out technique applied on the LEM cells that are completely damaged. These issues will be addressed (not in the order) in the subsequent sections.

4.3.2 Subdomain connections

Two types of subdomain connections can be encountered, see Figure 4.4:

- connection of LEM and FEM subdomains
- connection of LEM and LEM subdomains

4.3.2.1 LEM and FEM connection

For the LEM-FEM coupling, it would be useful first of all to recall the continuum theory which is the basic of FEM approach. Under the small perturbation assumption, in addition to the small strain tensor which is given by

$$\boldsymbol{\varepsilon} = \frac{1}{2}(\nabla \mathbf{u} + \nabla \mathbf{u}^T) \tag{4.1}$$

with $\mathbf{u}$ the displacement field, we can also have the infinitesimal rotation tensor linked to the rigid body rotation of a body, which is solely induced by the displacement field, given by

$$\mathbf{W} = \frac{1}{2}(\nabla \mathbf{u} - \nabla \mathbf{u}^T) \tag{4.2}$$

In fact, the infinitesimal rotation tensor $\mathbf{W}$ is just the skew-symmetric part of the displacement gradient tensor. Since $\mathbf{W}$ is a skew-symmetric tensor, then for any vector $\mathrm{d}\mathbf{x}$ we have

$$\mathbf{W} \cdot \mathrm{d}\mathbf{x} = \boldsymbol{\theta} \times \mathrm{d}\mathbf{x} \tag{4.3}$$

where $\boldsymbol{\theta}$ is called the rotation vector of the skew-symmetric tensor. From Equations (4.2) and (4.3), the rotation vector can be expressed as

$$\boldsymbol{\theta} = \frac{1}{2}\nabla \times \mathbf{u} \tag{4.4}$$

In the concurrent multiscale analysis, at a certain moment LEM and FEM coexist in the same framework. A strategy is needed to assure the kinematic continuity at the interface of LEM and FEM subdomains. Let us consider two neighboring subdomains LEM and FEM, Ω^L and Ω^F respectively with the local interface Γ, see Figure 4.5. Along this interface, the FEM subdomain only shares two coarse nodes, which are common to the LEM subdomain.

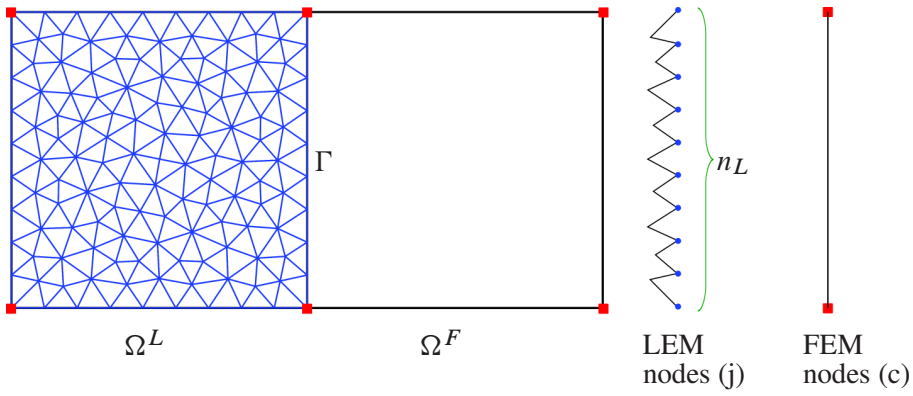

Figure 4.5 – Interface of LEM and FEM domains.

It is worth noting that the LEM nodes are equipped with translational and rotational DOFs whereas the FEM nodes have only translational DOFs. Therefore, for the continuity of kinematics, the translational DOFs of LEM nodes at the interface have to be tied to the translational DOFs of FEM nodes whereas the rotational DOFs of LEM nodes at the interface should be anchored to the rotation vector of the skew-symmetric tensor which derived from the displacement field of the FE. Let $\mathbf{u}^F$ be the displacement filed in the FEM subdomain. Let $\mathbf{u}^L$, $\boldsymbol{\theta}^L$ be the vectors of discrete displacement and of discrete rotation, respectively, of the LEM subdomain. The continuity of kinematics between LEM and FEM subdomains at the interface is expressed by following constraint equations

$$\mathbf{u}_j^L = \mathbf{u}^F(\mathbf{x}_j), \forall j = \{1, 2, \ldots, n_L\} \tag{4.5}$$

and

$$\boldsymbol{\theta}_j^L = \boldsymbol{\theta}_j^F(\mathbf{x}_j) = \frac{1}{2}\nabla \times \mathbf{u}^F(\mathbf{x}_j), \forall j = \{1, 2, \ldots, n_L\} \tag{4.6}$$

where $\mathbf{u}_j^L$ and $\boldsymbol{\theta}_j^L$ are the vector of three translations and of three rotations of the LEM node j on the interface, respectively; $\mathbf{u}^F(\mathbf{x}_j)$ is the translational displacement vector of FEM subdomain at the corresponding interface position while $\boldsymbol{\theta}^F(\mathbf{x}_j)$ is the rotation vector at the position of LEM node j of FEM subdomain linked to the rigid body rotation defined by Equation (4.4); n_L is the number of LEM nodes on the interface.

Furthermore, on the FEM domain, the coarse element is built from the coarse nodes with its shape functions $\mathbf{N} = \left[N_c(\mathbf{x})\right]$. Consequently, the displacement field $\mathbf{u}^F$ can be interpolated from the coarse node displacements $\mathbf{u}_c^F = \left\{u_c\right\}$. The Equation (4.5) is rewritten as

$$\mathbf{u}_j^L = \mathbf{N} \cdot \mathbf{u}_c^F = N_c(\mathbf{x}_j) \cdot u_c, \forall j = \{1, 2, \ldots, n_L\} \tag{4.7}$$

in which the summation notation is applied over all coarse nodes c. Likewise, the rotations $\boldsymbol{\theta}_j^L$ can be also obtained from the coarse node displacements $\mathbf{u}_c^F$ through the rotation coupling matrix $\mathbf{R} = \left[R_c(\mathbf{x})\right]$ as

$$\boldsymbol{\theta}_j^L = \mathbf{R} \cdot \mathbf{u}_c^F = R_c(\mathbf{x}_j) \cdot u_c, \forall j = \{1, 2, \ldots, n_L\} \tag{4.8}$$

where the rotation coupling matrix is derived from Equations (4.2) and (4.4) when applying the interpolation of the displacement filed $\mathbf{u}^F$ to the coarse node displacements

$$\mathbf{R} = \frac{1}{2}(\nabla\mathbf{N} - \nabla\mathbf{N}^T) \tag{4.9}$$

4.3.2.2 LEM and LEM connection

LEM subdomains might be activated and thus coexist in the same framework before the complete failure of one of them. In order to assure the continuity between these LEM subdomains, constraint conditions have also to be fulfilled.

It is recalled here that the LEM subdomains are initially built from a fine mesh, compatible on the interface. Let us consider two adjacent LEM subdomains Ω^{L_1} and Ω^{L_2} that share n_L common nodes on the interface Γ, see Figure 4.6. Assuming that the cracking process is occurring within the subdomain Ω^{L_1}.

On the compatible interface, the translation and rotation continuities simply read

$$\mathbf{u}_j^{L_2} = \mathbf{u}_j^{L_1}, \forall j = \{1, 2, \ldots, n_L\} \tag{4.10}$$

and

$$\boldsymbol{\theta}_j^{L_2} = \boldsymbol{\theta}_j^{L_1}, \forall j = \{1, 2, \ldots, n_L\} \tag{4.11}$$

which mean that the displacement vectors of the nodes on the interface of the subdomain Ω^{L_2} are imposed by the displacement vectors of the corresponding nodes on the interface of the subdomain Ω^{L_1}.

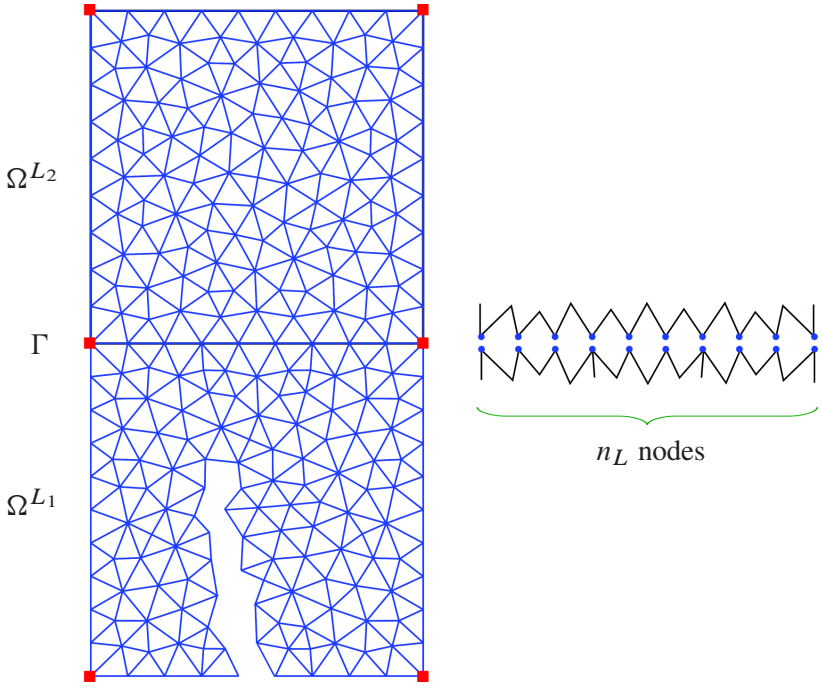

Figure 4.6 – Interface of two neighboring LEM subdomains.

4.3.3 Numerical homogenization of a fine subdomain by LEM approach

Within a concurrent multiscale approach proposed here, the discrete and continuum models provided by LEM and FEM approaches, respectively, should represent the same material on different scales. Consequently, the elastic mechanical properties of both approaches should coincide. Therefore, we adapt the geometry and material parameters of the lattice model and consider them as the parameters of the multiscale approach. The mechanical properties of the continuum model at the macroscale are deduced from a homogenization scheme. Homogenizations for each suddomains are realized in the preliminary stage for the transition from the meso-to the macroscale.

Considering a LEM subdomain Ω^s with an explicit representation of an aggregate structure at the mesoscale, see Figure 4.7. The material is described within this subdomain by the lattice model in which each lattice beam element has a stiffness matrix expressed by Equations (2.16) to (2.18). The subdomain-related nodes are classified into the corner nodes (c), the internal nodes (i) and the non-corner boundary nodes (b), refer to Figure 4.7.

The assembled stiffness matrix $\mathbf{K}^s$, the solution displacement vector (including translation and rotation DOFs) $\mathfrak{u}^s$ and the loading vector $\mathbf{f}^s$ can be partitioned as

$$\mathbf{K}^s = \begin{bmatrix} \mathbf{K}^s_{ii} & \mathbf{K}^s_{ib} & \mathbf{K}^s_{ic} \\ \mathbf{K}^s_{bi} & \mathbf{K}^s_{bb} & \mathbf{K}^s_{bc} \\ \mathbf{K}^s_{ci} & \mathbf{K}^s_{cb} & \mathbf{K}^s_{cc} \end{bmatrix}, \quad \mathfrak{u}^s = \begin{Bmatrix} \mathfrak{u}^s_i \\ \mathfrak{u}^s_b \\ \mathfrak{u}^s_c \end{Bmatrix}, \quad \mathbf{f}^s = \begin{Bmatrix} \mathbf{f}^s_i \\ \mathbf{f}^s_b \\ \mathbf{f}^s_c \end{Bmatrix} \tag{4.12}$$

The equilibrium equation of this subdomain, omitting the superscript s for the simplification, is

$$\begin{bmatrix} \mathbf{K}_{ii} & \mathbf{K}_{ib} & \mathbf{K}_{ic} \\ \mathbf{K}_{bi} & \mathbf{K}_{bb} & \mathbf{K}_{bc} \\ \mathbf{K}_{ci} & \mathbf{K}_{cb} & \mathbf{K}_{cc} \end{bmatrix} \cdot \begin{Bmatrix} \mathfrak{u}_i \\ \mathfrak{u}_b \\ \mathfrak{u}_c \end{Bmatrix} = \begin{Bmatrix} \mathbf{f}_i \\ \mathbf{f}_b \\ \mathbf{f}_c \end{Bmatrix} \tag{4.13}$$

In order to determine the stiffness matrix with respect to the corner nodes, a macroscopic field has to be applied to the mesoscopic level, i.e. one has to deal with the boundary conditions. Three classical boundary conditions are (i) linear displacement (Dirichlet), (ii) constant tractions (Neumann), and (iii) periodic displacements and antiperiodic tractions on the opposite sides (Miehe and

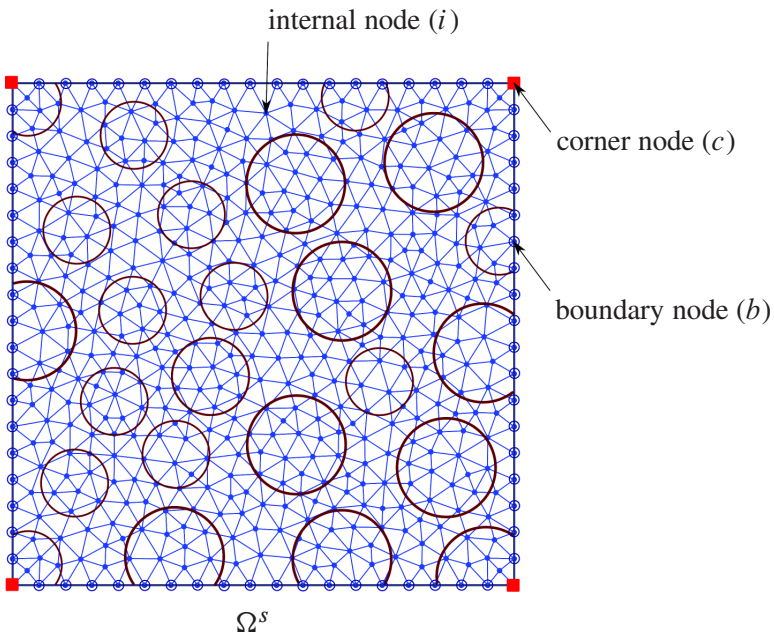

Figure 4.7 – Classification of LEM subdomain nodes.

Koch, 2002). These boundary conditions correspond to a modeling of the loadings applied by the neighboring subdomains. The main difficulty is the choice of a suited boundary condition to be applied to the LEM subdomain. However, in the multiscale framework proposed here, the transition from the meso-to the macroscale only takes into account for the corner nodes i.e. the resulting macro subdomain is linear in terms of displacement. Furthermore, the strong coupling between LEM and FEM subdomains is affected through linear interpolation as in Equation (4.7). Accordingly, the linear displacement boundary condition has to be applied for the homogenization scheme.

The linear displacement boundary condition can be defined from the constant macroscopic strain and rotation tensors, $\bar{\boldsymbol{\varepsilon}}$, $\bar{\boldsymbol{\omega}}$, respectively, at each node q of the boundaries (q includes corner nodes (c) and non-corner boundary nodes (b)) as

$$\mathbf{u}_q = \bar{\boldsymbol{\varepsilon}}\mathbf{x}_q, \quad \boldsymbol{w}_q = \bar{\boldsymbol{\omega}}\mathbf{x}_q \tag{4.14}$$

or shortly

$$\mathfrak{u}_q = \bar{\boldsymbol{\Upsilon}}\,\mathbf{x}_q \tag{4.15}$$

where $\bar{\boldsymbol{\Upsilon}}$ stands for the coupling strain-rotation tensor. By introducing a matrix $\mathbb{D}_q^T$ that depends on the coordinates of the boundary node q in the reference configuration, we may represent Equation (4.15) in the form

$$\mathfrak{u}_q = \mathbb{D}_q^T \bar{\boldsymbol{\Upsilon}} \tag{4.16}$$

It can be repartitioned as

$$\begin{Bmatrix} \mathfrak{u}_b \\ \mathfrak{u}_c \end{Bmatrix} = \begin{bmatrix} \mathbb{D}_b^T & 0 \\ 0 & \mathbb{D}_c^T \end{bmatrix} \begin{Bmatrix} \bar{\boldsymbol{\Upsilon}}_b \\ \bar{\boldsymbol{\Upsilon}}_c \end{Bmatrix} \tag{4.17}$$

Incorporating the boundary constraint (4.17) in the equilibrium equations (4.13), which leads to

$$\begin{bmatrix} \mathbf{K}_{ii} & \mathbf{K}_{ib} & \mathbf{K}_{ic} \\ \mathbf{K}_{bi} & \mathbf{K}_{bb} & \mathbf{K}_{bc} \\ \mathbf{K}_{ci} & \mathbf{K}_{cb} & \mathbf{K}_{cc} \end{bmatrix} \cdot \begin{Bmatrix} \mathfrak{u}_i \\ \mathbb{D}_b^T \bar{\boldsymbol{\Upsilon}}_b \\ \mathbb{D}_c^T \bar{\boldsymbol{\Upsilon}}_c \end{Bmatrix} = \begin{Bmatrix} \mathbf{f}_i \\ \mathbf{f}_b \\ \mathbf{f}_c \end{Bmatrix} \tag{4.18}$$

The macroscopic stiffness on the corner DOFs of the LEM subdomain is obtained by condensing the internal DOFs $\mathfrak{u}_i$, then in the second stage, $\mathbb{D}_b^T \bar{\boldsymbol{\Upsilon}}_b$ onto the corner DOFs. As a result, one

gets the following expression for the macroscopic (homogenized) stiffness $\mathbf{K}_H$ and the macroscopic (homogenized) generalized force $\mathbf{f}_H$ from (4.18):

$$\mathbf{K}_H \mathbb{D}_c^T \bar{\boldsymbol{\Upsilon}}_c = \mathbf{f}_H \tag{4.19}$$

By applying the boundary condition such that $\mathbb{D}_c^T \bar{\boldsymbol{\Upsilon}}_c$ equals unity on the corner nodes, the macroscopic stiffness on the corner DOFs amounts to the generalized force measured on the boundaries, given by

$$\mathbf{K}_H = \mathbf{f}_H \tag{4.20}$$

4.3.4 Zoom-in procedure and criterion to trigger zoom-in events

In the previous sections, the homogenization method was presented to obtain the macroscopic stiffnesses for the macro subdomains. Therewith the connection method on interfaces of LEM and FEM subdomains was also discussed. But during the analysis upon the loading increases, how are macro FEM subdomains upgraded to corresponding LEM subdomains? In this section, we deal with this transition from low resolution representation by FEM approach to high resolution one by LEM approach. This is accomplished by the so-called zoom-in procedure.

A key issue of the present multiscale framework is the assumption that a macroscopic description by FEM approach with homogenized stiffness matrices obtained from the mesoscale LEM description suffices during the linear elastic analysis. It is recalled that there is no homogenized nonlinear law introduced in the FEM approach, all nonlinearities come from the LEM approach with brittle elastic parameters. The nonlinear analysis accounted for the LEM approach only occurs in the nonlinear zone by "switching" the certain FEM subdomains to the corresponding LEM subdomains. Consequently, a criterion for this transition that are linked to the prediction of nonlinearities has to be adopted.

To this end, we monitor the evolution of an internal variable which is assumed to be representative for the linear/nonlinear character of each domain. Here, we propose to employ the nonlocal equivalent strain $\bar{\varepsilon}$ from the nonlocal damage theory (Pijaudier-Cabot and Bažant, 1987) for dictating the nonlinearities of the material in each domain. Its representative value for each domain is denoted by $\bar{\varepsilon}^{(s)}$. It is computed as the maximum value over the points that correspond to the integration points when considering each domain as a macro element:

$$\bar{\varepsilon}^{(s)} = \max_n(\bar{\varepsilon}^n) \tag{4.21}$$

At a known loading stage, only the domain that has the largest $\bar{\varepsilon}^{(s)}$ and fulfills the condition:

$$\bar{\varepsilon}^{(s)} \geq \alpha\kappa_0 \tag{4.22}$$

is switched into LEM approach. Here, κ_0 is adopted as a damage initiation threshold and α a parameter close to 1 but is always lower than 1, e.g. 0.98, that allows the zoom-in event occurs right before the damage initiates.

It should be mentioned that there always exists one and only one FEM subdomain having the largest equivalent strain for both homogeneous and nonhomogeneous loadings at a given stage. For nonhomogeneous loadings which mean that stress fields of all domains are not equal, it is obvious that there is only one domain undergoing the largest $\bar{\varepsilon}^{(s)}$. For homogeneous loadings, the macroscopic stiffness matrices of FEM subdomains are different since they are obtained from the homogenization scheme with a random distribution of the aggregate structure, which leads to the different strain field of subdomains.

When more than one LEM domains coexist, the nonlinear LEM solver is only applied for the domain in which cracks are being propagated whereas the LEM domain that has just been zoomed in is solved by the linear solver. When the former domain is completely cracked and is zoomed out

to two FEs by the mean path of the crack (see Section 4.3.5), the nonlinear LEM solver is employed for the next LEM domain.

It is noted that the proposed zoom-in condition Equation (4.22) is restricted to monotonic loading conditions. For the cyclic loadings, one should define a loading function formulated in term of the nonlocal equivalent strain and a parameter that stores the maximum value of the nonlocal equivalent strain reached at each domain to handle the hardening parameter and distinguish among linear loading, nonlinear loading and linear unloading. The reader is referred to Lloberas-Valls et al. (2012a) for more details.

4.3.5 Zoom-out procedure and criterion to trigger zoom-out events

When a LEM subdomain is completely cracked, instead of removing it from the system, it would be better to macroscopically represent the subdomain by a FEM approach in order to maintain the mass of the structure. This can be accomplished by the so-called zoom-out procedure in which the transition from high resolution representation by LEM approach to low resolution one by FEM approach that is solely done by deactivating the LEM approach of the subdomain and reactivating the corresponding FEM approach. However, we must take into account the discontinuity of the kinematics due to the crack. Within the assumption that there is only one macrocrack that traverses the LEM subdomain, the discontinuity due to the crack can be accounted for decomposing the corresponding FEM subdomain into two FEs after the mean crack path. Nevertheless, to guarantee the continuity with the crack in the neighboring subdomains, we propose to decompose the FEM subdomain into two FEs by the path that connects the starting point and the ending point of the crack in the LEM subdomain (the points A and B in Figure 4.8).

The decomposition of the FEM subdomain can be performed by adding four nodes corresponding to the position of the points A and B of the crack, see Figure 4.8b. The two new resulting FEs 1-6-5-4 and $6'$-2-3-$5'$ have the stiffness matrix that is computed by discretizing the domains represented by these two FEs with the fine resolution meshes, and then the stiffness matrix is computed by the homogenization scheme using the lattice approach. It is worth noting that by this way, the structure is not planed for a change of the loading direction since the new nodes 5 and $5'$, 6 and $6'$ can slide freely on each other. In order to assure the discontinuity due to the crack and at the same time provide for a change of loading direction inducing crack-closing, a zoom-out procedure to the macroscopic element represented by XFEM should be used.

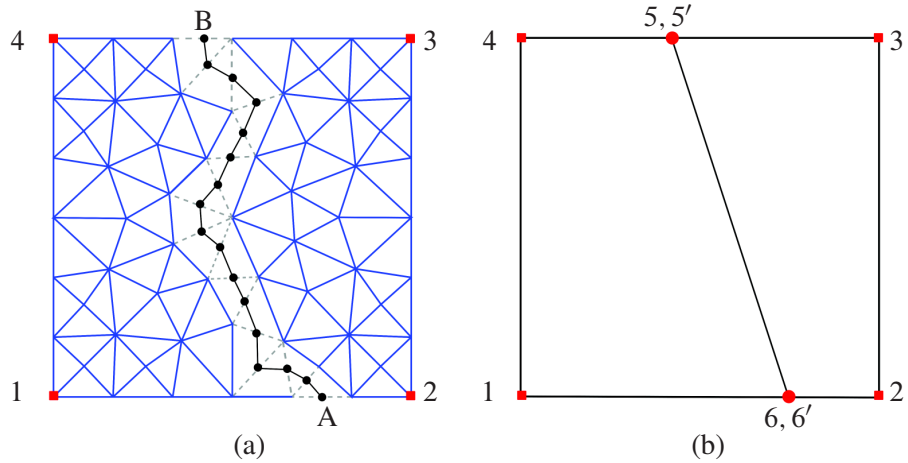

Figure 4.8 – Zoom-out procedure.

For the zoom-out procedure to be carried out, a criterion for the transition from the mesoscopic approach by LEM to the macroscopic approach by FEM, that are linked to the prediction of complete failure of a LEM subdomain, has to be adopted. This is simply accomplished by the fact that the parameter α controlling the elimination of the lattice elements is greater than a predefined constant

α_{cr}, given by

$$\alpha_{min} > \alpha_{cr} \tag{4.23}$$

as presented in Section 2.2.4.

4.3.6 General procedure multiscale LEM-FEM coupling for large-scale structures

The proposed multiscale framework allows the solver to deal with different models in an adaptive manner by the concurrent coupling. The flowchart of the multiscale approach is shown in Figure 4.9. In the study of the heterogeneous material, a homogeneous bulk is considered with the equivalent elastic stiffness matrices for the coarse domains. The equivalent elastic stiffness matrices are retrieved from the numerical homogenization method at each domain. The criterion is adopted to indicate the linear/nonlinear character of the material in each domain. When nonlinearities occur in a certain domain, a zoom-in event takes place and the macroscopic continuous approach by FEM is replaced by the mesoscopic discrete approach by LEM. The nonlinear analysis is only performed on subdomains represented by the LEM approach. When a LEM subdomain is completely cracked, a zoom-out event carries out and the cracked LEM subdomain is replaced by two new FEs obtained from a decomposition of the corresponding FEM subdomain. The continuity of displacements among FEM and LEM subdomains (Equations (4.7) and (4.8)) is assured by the so-called "master/slave" approach (Belytschko et al., 2000). The FEM subdomain is the master whereas the LEM is the slave. Equations (4.7) and (4.8) can be written in the general form as

$$\mathfrak{u}_S = \left[\mathbf{J}\right] \mathfrak{u}_M \tag{4.24}$$

in which vector $\mathfrak{u}_S$ collects the displacements (translations and rotations) of the slave node and $\mathfrak{u}_M$ collects the displacements of the master node; $\left[\mathbf{J}\right]$ is the combined matrix of shape function matrix and rotation matrix for LEM-FEM connection.

The internal forces $\mathbb{P}_M$ at the master nodes, which include the effect of slave nodes, can be calculated from the principal of virtual work by imposing the condition that

$$\mathfrak{u}_M^T \mathbb{P}_M = \mathfrak{u}_M^T \hat{\mathbb{P}}_M + \mathfrak{u}_S^T \hat{\mathbb{P}}_S \tag{4.25}$$

where $\hat{\mathbb{P}}_M$ and $\hat{\mathbb{P}}_S$ are the internal forces of the master and slave nodes, respectively, considered unconstrained.

By substituting (4.24) into (4.25), one obtains

$$\mathbb{P}_M = \hat{\mathbb{P}}_M + \left[\mathbf{J}\right]^T \hat{\mathbb{P}}_S \tag{4.26}$$

Since the proposed multiscale approach is based on the domain decomposition of FETI-DP method, it allows to deal with the large scale structures by parallel computations. The parallel computing can be designed as *One Subdomain per Processor* approach. This approach has been particularly typical of implementations on Distributed Memory (DM) architecture. However, this kind of implementations requires an increasing number of processors when dealing with an increasing number of subdomains for large scale structures. Alternatively, the parallel implementations can be affected on the Distributed Shared Memory (DSM) architecture where the simulation can be realized with the number of subdomains independent of the number of processors, see e.g. (Lesoinne and Pierson, 1998).

4.4 Implementation into SOFA architecture

The purpose of this work is to implement the LEM approach into the open-source software SOFA and then develop the coupling algorithm with FEM approach for multiscale simulations of

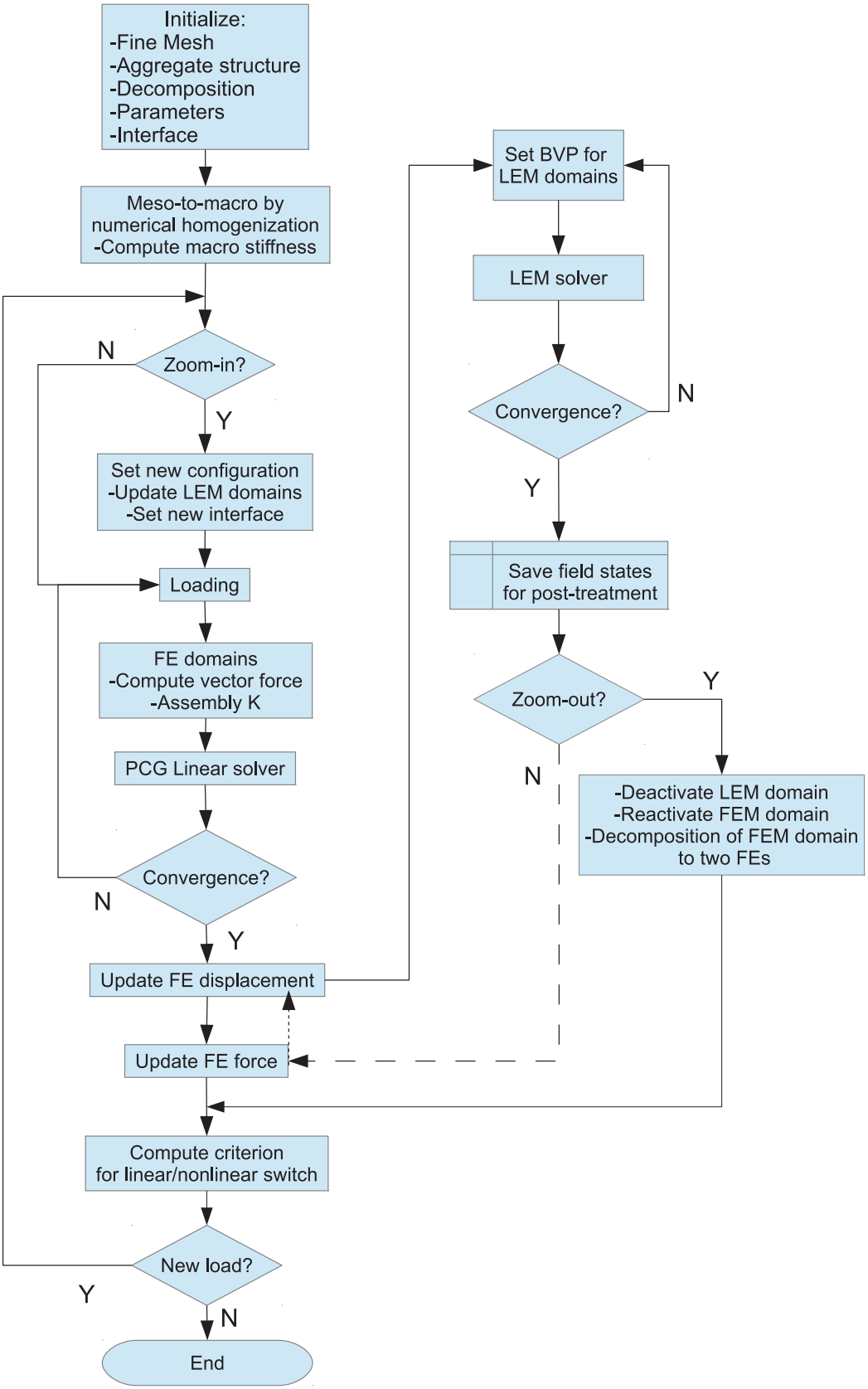

Figure 4.9 – Flowchart of the proposed multiscale approach by LEM-FEM coupling.

failure of large structures. One of the reasons why SOFA framework is used in the thesis is that it is based on the open-source philosophy which allows one's ability to freely improve/modify/reuse the existing code-base and implement a new model as a plugin.

4.4.1 What is SOFA?

SOFA (Simulation Open Framework Architecture) is an open-source C++ library primarily targeted at real-time simulation, with an emphasis on medical simulation. It is mostly intended for the research community to help develop newer algorithms, but can also be used as an efficient prototyping tool (`http://www.sofa-framework.org/home`).

SOFA is currently developed by 3 INRIA teams: Shacra, Evasion and Asclepios but the project also benefited from the help of the CIMIT Sim Group, ETH Zurich and CSIRO.

4.4.2 Philosophy of SOFA

In SOFA, a complex object of a problem of physics can be simulated by decomposing it into components. Each component describes one feature of the model, such as state vectors (displacement, acceleration), force vectors, constraints, integration schemes, and solving processes. The components are designed independently and organized as a hierarchical data structure similar to a scene graphs used in graphic libraries.

One of the innovative concepts of SOFA architecture is the multi-model representation. The simulated object can be decomposed into multiple partial models if needed. Typically, a physical object in SOFA can be described using three partial models: a mechanical model with constitutive law, a collision model with contact geometry, and a visual model with detailed geometry and rendering parameters. Each model can be designed independently of the others. These models are synchronized during run-time using a generic mechanism called *mapping* to propagate force and displacement vectors. The interesting thing is that a combination between mechanical models is possible through the same mechanism *mapping*, e.g. coupling of FEM model and LEM model.

Because of the flexibility in the notion of components and the use of scene-graph to organize and process the simulation, the simulation can be computed on the GPU instead of CPU to exploit the computational power of modern hardware architecture by simply replacing the solver and the state vectors (by editing an XML file), all the rest remains unchanged.

4.4.3 Why SOFA?

SOFA is designed within a highly modular efficient framework. It allows to focus on our own domain of expertise, while re-using other advanced contributions such as computationally efficient algorithms, multi-threading, or the capability for computations on the modern hardware architecture such as the GPU, etc. So it is considered as a high-performance C++ library.

Moreover, the code is open-source and the license is LGPL. The new model is built upon SOFA using the plug-in system. The new plug-in can have an other license than LGPL. Consequently, there is a considerable freedom to use SOFA to help the development and the sharing of new algorithms and models.

That are the reasons why SOFA is used. The lattice model has been implemented as a plug-in. Several constraint algorithms have been developed in addition to adapt the simulation of boundary conditions in mechanical engineering test. With the re-using of FEM model from the SOFA's contribution, the coupling with lattice model has been developed.

4.4.4 Implementations

For the LEM-FEM coupling, the beam lattice model is first implemented into SOFA library. Then two different strategies for coupling lattice elements with finite elements are implemented. The

3D beam lattice model is successfully implemented into SOFA where some numerical applications have been shown in Section 2.5. Here we will show a simple simulation using the lattice model with elastic parameters and compare the output with analytical results in order to demonstrate the capability of the implemented lattice model, refer to Section 4.4.4.1. The two implemented strategies for coupling the beam lattice model with finite elements will be shown by two simple examples presented in Sections 4.4.4.2 and 4.4.4.3.

4.4.4.1 Beam lattice model

The implemented beam lattice model is used here to model a cantilever beam subjected to a force P in y-direction and/or a bending moment M in xy-plane, see Figure 4.10. The beam has a length $l = 1$ m, a circular cross-section with the area $A = 2000$ mm^2, and the Young's modulus $E = 35$ GPa.

The cantilever beam is discretized by 10 lattice elements whose length is 0.1 m. Each element is assigned a cross-sectional A_b which equals to 2000 mm^2. Two elastic parameters of the beam lattice model are $E_b = 35$ GPa and $\lambda = \frac{4\pi I_b}{A_b^2} = 1$ with I_b the second moment of area being equal to the second moment of area of the cantilever beam I.

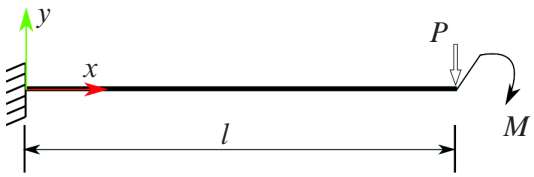

Figure 4.10 – Cantilever beam.

Figure 4.11a shows the deformed configuration of the cantilever beam subjected to a force $P = -10$ kN in y-direction. Each discretized node is attached to a local coordinate system in order to show the nodal rotations. The deformed configuration of the cantilever beam subjected to a bending moment $M = -10$ kNm in xy-plane (z-direction) is shown in Figure 4.11b.

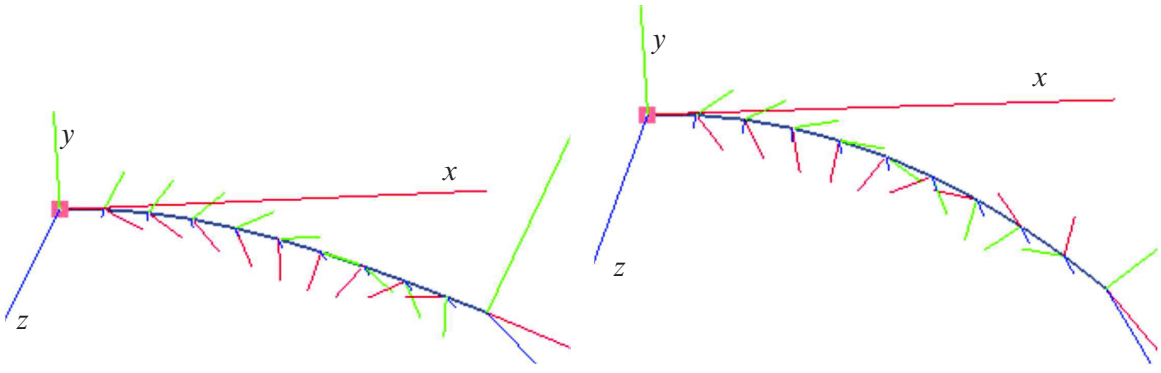

(a) (b)

Figure 4.11 – Deformed configuration of the cantilever beam subjected a force $P = -10$ kN in y-direction (a) or a bending moment $M = -10$ kNm in z-direction (b).

The analytical deflections of the cantilever beam subjected to a force P and a bending moment M are given by, respectively

$$\Delta y = \frac{-Px^2}{6EI}(3l - x) \tag{4.27}$$

and

$$\Delta y = \frac{-Mx^2}{2EI} \tag{4.28}$$

The numerical deflection of each node is shown in Figure 4.12 by means of an arrow whose magnitude is equal to the value of the deflection. The nodal deflections are compared with analytical deflections which are also plotted in Figure 4.12. It is shown that the numerical deflections are exactly the same as the analytical ones. This means that the implemented lattice model works correctly.

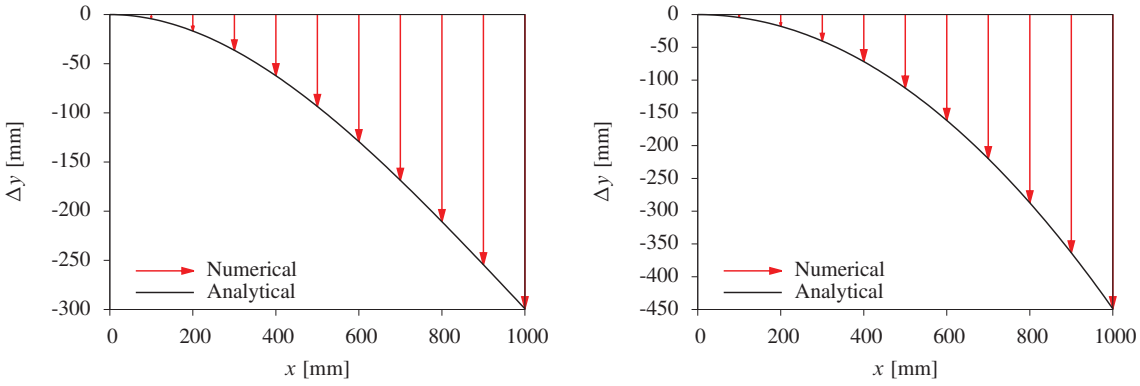

Figure 4.12 – Deflection of the cantilever beam subjected a force $P = -10$ kN in y-direction (a) or a bending moment $M = -10$ kNm in z-direction (b).

4.4.4.2 Elementary coupling

A simple example for the coupling between finite elements and lattice elements is performed in order to show the principle of SOFA and how the two types of elements are tied during the simulation. The work to be done concerns the coupling of an object described by two hexahedral eight-node FEs and a beam represented by two lattice elements, as shown in Figure 4.13 in which four nodes of one FE are fixed in all directions whereas the beam is vertically loaded by imposing the displacement at an end. The whole system simulates a cantilever beam.

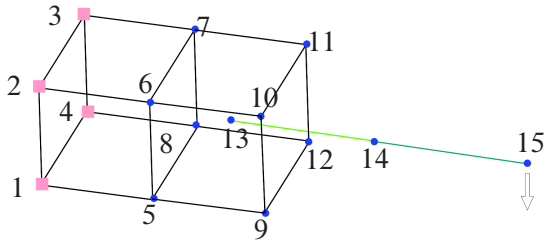

Figure 4.13 – Schematic representation of coupling between a hexahedral eight-node FE and a beam represented by two lattice elements.

In SOFA, the simulated objects are described as components. Figure 4.14a shows the two main components of the simulated cantilever beam. The **Node** "FEM" is used to store all components related to the hexahedral FEs and the **Node** "LEM" stores those related to the lattice elements. The **RegularGridTopology** describes the shape of the FEs and all the degrees of freedom of the FEs are stored in the component **MechanicalObject**. By the same way, all the degrees of freedom of the lattice model are stored in another **MechanicalObject** in the LEM **Node**. In order to find the static equilibrium of the system, the solver **StaticSolver** is added in the **Node** "Root" which is the parent of the FEM and LEM **Nodes**. It is worth noting that the hierarchy is important. The solver is added in a higher level compared to the LEM and FEM **Nodes** which means that it is used to solve the equilibrium of the whole system. The **StaticSolver** uses an auxiliary component, the **CGLinearSolver**, to solve the equations of equilibrium of the system.

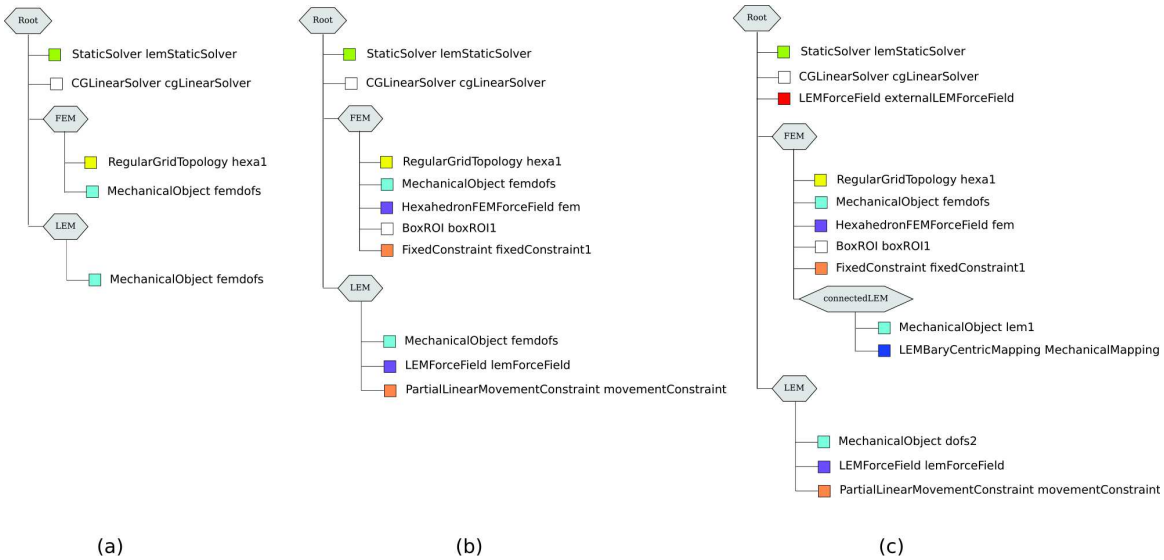

Figure 4.14 – Step by step to build the scene graph of the coupling.

So far, only the DOFs of the FEM and LEM are added in the model. The concept of forces and stiffnesses are handled by components called **ForceField** in SOFA. As shown in Figure 4.14b, the **HexahedronFEMForceField** component is used to describe the behavior of the hexahedral FEs while the **LEMForceField** describes the behavior of the lattice elements. Moreover, within the FEM **Node**, the component **BoxROI** is added to captured all the indices of the nodes to be fixed. Then the component **FixedConstraint** is used to set to zero the displacements of all the DOFs of the captured nodes provided by **BoxROI**. Similarly, the component **PartialLinearMovementConstraint** is added within the LEM **Node** to impose the vertically prescribed displacement to simulate the load applied to the lattice node at the beam end.

Next, for the valid model, the coupling between the two types of elements FEM and LEM has to be accomplished. The strategy of coupling is described as follows. The lattice node inside the FE, the node 13 in Figure 4.13, is classified as another LEM object. It is stored in the **Node** "connectedLEM" which is considered as the slave of the FEM **Node**, see Figure 4.14c. The DOFs of that node is described using another **MechanicalObject** component. In order to tie that node to the FE, we implemented into SOFA a component called the **LEMBarycentricMapping** which is used to map the displacement field of the FE to the displacement of that node while the force at that node is transferred back to the FE nodes. Finally, we should describe the link between the FE with an embedded LEM node 13 stored in the FEM **Node** and the lattice element 14-15 stored in the LEM **Node** by the "external" lattice element 13-14. This is performed by adding the component **LEMForceField** in the Root **Node**. Note that, by this coupling strategy, the implemented component **LEMForceField** is derived from a **PairInteractionForceField** component such that it can describe an "interaction" between two **MechanicalObject**s. With several "default" components such as the **VisualStyle**, the **InteractiveCamera**, etc., the complete scene graph of the coupling is shown in Figure 4.15.

The elastic parameters of the two FEs are Young's modulus $E = 25$ GPa and Poisson's ratio $\nu = 0.2$. The beam lattice elements are assigned the values of Young's modulus and cross-sectional area being $E_b = 35$ GPa, $A_b = 0.1$ m^2, respectively.

The initial and deformed configurations of the model provided by SOFA simulation is shown in Figure 4.16. The simulation shows that the coupling strategy works well. However, a drawback of this coupling strategy is that one has to distinguish the lattice nodes inside and outside a FE, called embedded LEM nodes and free LEM nodes described by two different **MechanicalObject**s, and from that two types of lattice elements are built. The first type of lattice elements is those connecting the embedded LEM nodes with the free LEM nodes and the other consists of those

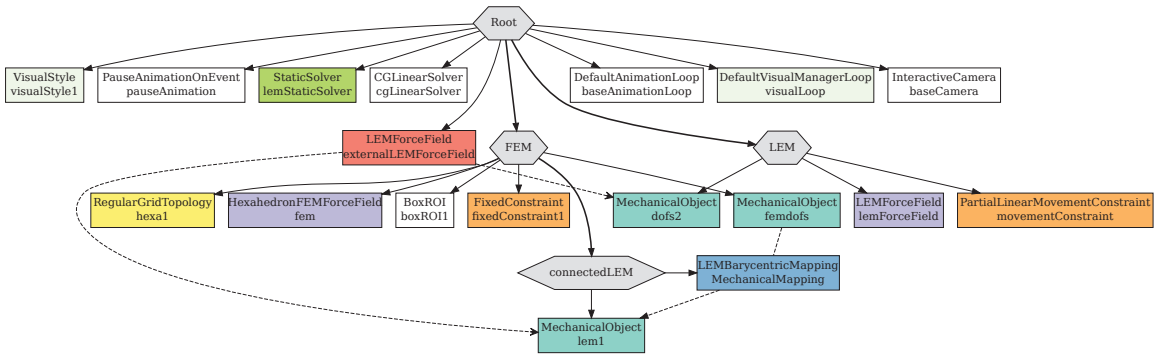

Figure 4.15 – Scene graph of the coupling.

connecting the free LEM nodes. Therefore, in the case that the lattice elements are generated from a fine mesh using a component topology, the connectivities have to be changed to adapt to two different **MechanicalObject**s. And this makes complicated the coupling procedure. Nevertheless, this coupling procedure can be easily done in the case that two type of lattice elements are generated from two meshes with *compatible* connectivities. But how to produce these two meshes? Rather than that, another coupling strategy is proposed to adapt the fact that the lattice elements are generated from only one mesh.

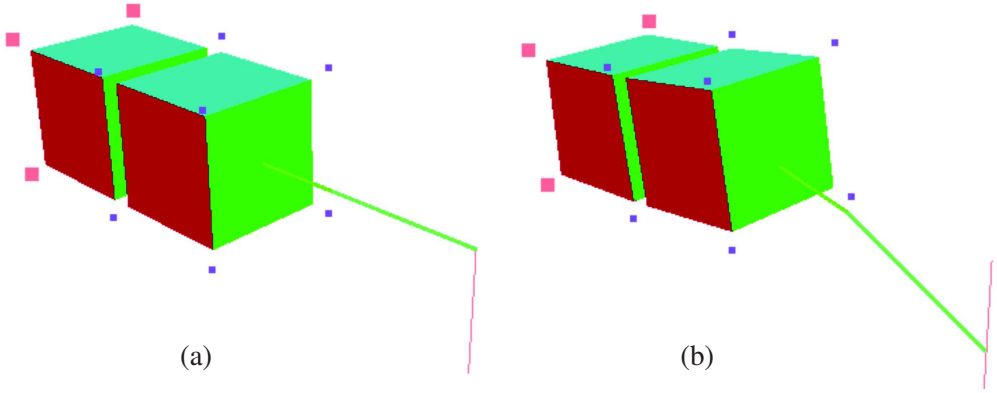

Figure 4.16 – A hybrid model constituted by two hexahedral FEs and two lattice elements in series: the initial configuration (a) and the deformed one (b). Note that in SOFA a hexahedral FE is represented by a colored box whose size is smaller than the size of the FE, this is not at all related to the deformation of the element.

4.4.4.3 Alternative coupling strategy

The work to be done concerns the coupling of a hexahedral FE and a cell of the same size represented by the lattice model. The system represents the structure under uniaxial tension in which four FE nodes in the bottom are fixed why the LEM nodes of the top boundary are vertically imposed by the prescribed displacement, as schematically shown in Figure 4.17.

The scene graph of the coupling is shown in Figure 4.18, in which the **Node** "FEM-LEM system" consists of two main **Node**s "FEM" and "Free LEM". Similarly, the DOFs in each **Node** are stored in the component **MechanicalObject**s. Two different components **BoxROI** are added in each **Node** to capture the nodes whose DOFs are fixed and the DOFs to be imposed by the prescribed displacement. The behavior of the FE is described by using the component **HexahedronFEMForceField**.

The key issue of the coupling strategy, different from the previous strategy, is that the third **Node** "LEM" is added, which is the child of *both* the "FEM" and the "Free LEM" **Node**s. This results

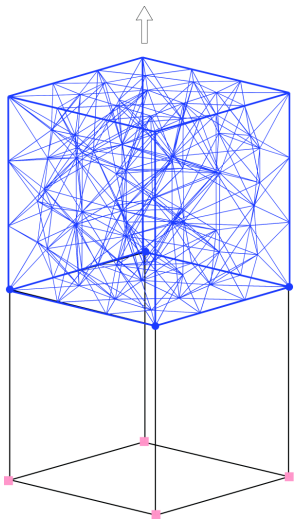

Figure 4.17 – Schematic representation of coupling between a hexahedral FE and a lattice cell of the same size under uniaxial tension.

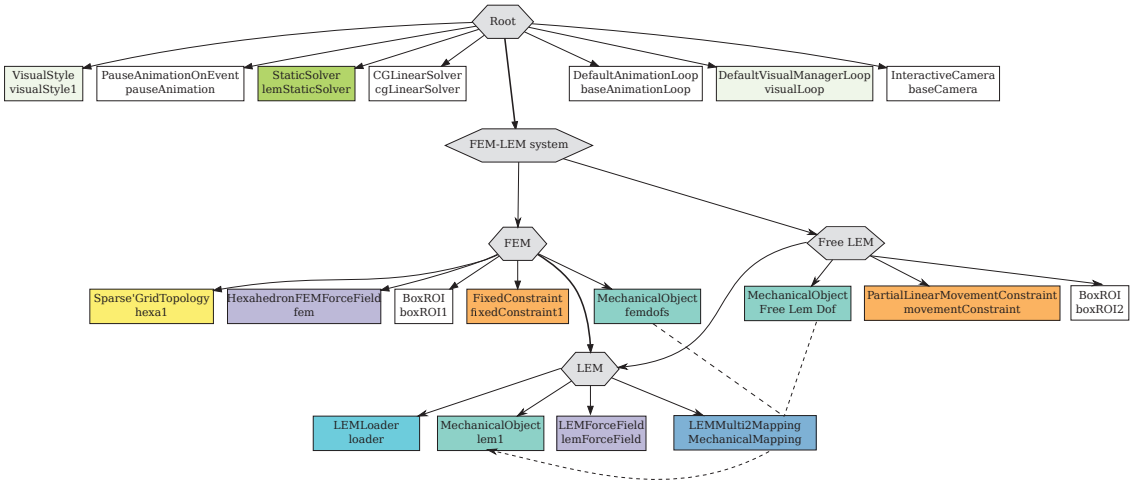

Figure 4.18 – Scene graph of the coupling.

in the so-called **MultiNode**. The **MultiNode** "LEM" consists of a component, the **LEMLoader**, that loads the topology of the lattice cell from an input mesh. Again, the DOFs of the lattice cell is stored in the **MechanicalObject** and the behavior of the lattice model is described by the component **LEMForceField**. The coupling is done via the implemented component **LEMMulti2Mapping** in which the displacement of all the LEM DOFs attached to the nodes found on the surface of the FE are mapped to the displacement field of the FE whereas the displacement of all the remaining LEM DOFs are mapped to the displacement of the DOFs in "Free LEM" **Node**. Of course, the forces are mapped in the inverse order. By this way, it is not necessary to split the lattice elements into two categories as done in the previous strategy. Therefore, the connectivities of the lattice elements are directly taken from those of the lattice mesh.

It should be noted that the in-plane lattice elements found on the interface plane between the FE and the lattice cell are removed from the lattice description. In fact, it is necessary to avoid the double of stiffness on the coupling interface since if it is not the case, the stiffnesses of the FE and the lattice elements are both taken into consideration on the interface.

The coupling model in SOFA is shown in Figure 4.19.

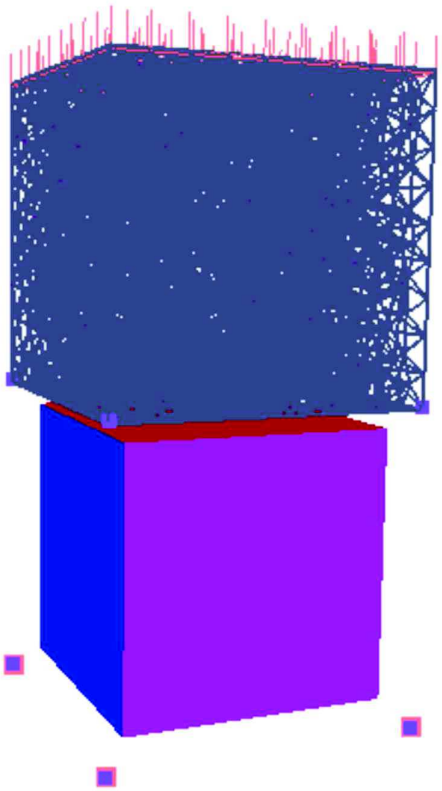

Figure 4.19 – The coupling configuration between a hexahedral FE and a LEM cell of the same size in SOFA. Note again that in SOFA the hexahedral FE is represented by a colored box whose size is smaller than the size of the FE.

4.4.5 On the complete implementation of the LEM-FEM coupling procedure

The above implementations have been done for the LEM-FEM coupling. However, they are restricted to the elementary level, i.e. it exists only two **MechanicalObject**s in which one describes the FEM and the other accounts for the LEM. The implementation for the *full* multiscale procedure with the zoom-in, zoom-out techniques, presented previously, has not, however, been performed. Therewith, the parallel characteristic of the algorithm has not been exploited either. This simply due to the fact that the exploitation of the multiple parallel resources such as parallel computa-

tion on GPUs requires a significant programming effort. Furthermore, since the concept of SOFA is strongly modular, sometimes the flexibility of the implementation of the coupling algorithm is limited.

Moreover, using a developing software for a general purpose, not all features related to mechanical simulations had been introduced. In addition to the LEM approach, we have developed during the thesis, three new components implemented in SOFA. The **PartialLinearMovementConstraint** and the **PartialFixedConstraint** are used to give ability to impose a prescribed displacement and fix the displacement, respectively, only within a given direction. The component **PauseAnimationOnEvent** serves to pause the animation of a simulation when, e.g., the complete failure of the lattice model attains. It all accounts for the time consuming of the implementation.

4.5 Conclusions

The study of the equivalence of the stiffness matrix between a lattice cell and a finite element of the same size has been performed. It is observed that with the appropriate parameters, a lattice cell can represent a material with given macroscopic properties such as Young's modulus and Poisson's ratio like a FE does. However in terms of the stiffness, the study shows that the stiffness matrix of the lattice cell is not exactly equivalent to that of the FE for a reasonable space discretization. An interesting observation is also provided from the study is that the beam lattice model reproduces a "closer" stiffness matrix to the stiffness matrix of the FE than the normal-shear spring lattice model.

It all leads to the proposed algorithm for coupling between the beam lattice approach and the finite element approach, in which the structure is initially modeled by FE approach but the stiffness matrix of a FE is not constructed by integration over the volume/area of that FE but it is computed by means of a *homogenization process* over a lattice cell of same size.

The following conclusions can be drawn on the proposed coupling algorithm between the lattice model and the finite element approach:

- The LEM-FEM coupling algorithm is proposed within an adaptive manner. This means that the LEM approach is not present in the zone in which the FPZ is known to occur in advance, but as the FPZ evolves, a FE is replaced by a lattice cell of same size for the nonlinear analysis of the material behavior.

- The coupling algorithm is provided for parallel computations.

- The proposed algorithm is a strong coupling. This means that the continuity of the displacement field on the coupling interface is assured by the master/slave algorithm. The translational and rotational displacements of the lattice nodes on the interface coupling are restrained to the displacement field and the rotational vector of the skew-symmetric tensor which derived from the displacement field of the FE, respectively. The stress field at the interface coupling of the lattice cell is transfered to the neighboring FEs. It does not exist a homogenized nonlinear behavior of the lattice approach that is introduced in a integration point of a FE like many works proposed by other authors which are weak couplings.

However, the implementation of the proposed coupling procedure in SOFA framework is still restricted to the elementary coupling. It requires future works in order to implement the complete algorithm into SOFA.

Conclusions and perspectives

Conclusions and discussions

By presenting the mechanical behavior of concrete-like materials at the beginning of this report, we highlighted that the behavior of such materials exhibit a complex fracture mechanism under extreme loading conditions. Indeed, the fracture mechanism is characterized by microcracking occurring before the peak load is reached. Nearly from the peak, localization of damage occurs in the fracture process zone with finite size, the microcracks continue to develop and coalesce for the formation of macrocrack(s). The macrocrack gradually grows which causes the gradual drop in load carrying capacity, until it gets through the structure and separates the latter into two parts. This complex fracture mechanism is clearly related to the disordered microstructure of the materials. An overview of the existing numerical models for modeling the behavior of such materials was stated in Chapter 1. We showed that continuum-based models which generally neglect the heterogeneity of the materials are not suitable for characterizing entirely the complex fracture process from initiation, propagation and coalescence of microcracks to the formation of macrocrack(s). Furthermore, these models do not always reflect all physical effects observed in experiments through their internal variables, e.g., grain decohesion, microcracking and crack bridging observed in concrete. In addition, to remedy the problem related to mesh sensitivity when dealing with softening materials, an internal length has to be introduced as done in nonlocal models, used as a localization limiter, to prevent the spurious localization of damage under mesh refinement. However, as stated, the assessment of the internal length from the heterogeneity of the material is still a difficult question, which is an obscure issue in using nonlocal models.

We highlighted that lattice models are very good candidates to model the fracture mechanism of concrete-like materials. Using the lattice models at the mesoscale, it is no need to introduce any internal length parameter together with many advantages of the lattice model stated previously in the report. Instead, the mesotructure of the material can be introduced explicitly. However, using the lattice models at the mesoscale, especially for large scale three-dimensional structures, requires tremendous computational efforts due to a vast number of degrees of freedom. Therefore, a multiscale approach performed by coupling between discrete approach at the mesoscale dealt by a lattice approach and continuous approach at the macroscale treated by the finite element method is essential.

The objective of Chapter 2 is to present the lattice model that was used in the thesis. The model is extremely simple since it only makes use of a linear elastic analysis. The material is represented as a network of lattice elements. Local constitutive law of elements is elastic brittle. By performing some test cases, we demonstrated that, when accounting for material heterogeneities by generating an aggregate structure, a global ductility behavior can be obtained. Moreover, by performing 3D tensile tests it was shown that fracture is a three-dimensional phenomenon, which leads to the fact that the attention should be paid when drawing conclusions from the results of two-dimensional simulations since the global behavior of 2D simulations is more brittle than that of 3D ones.

Two types of lattice elements are implemented in the SOFA framework: normal-shear spring elements and beam elements. The normal-shear spring lattice model is originally part of our self-writing code using C++ programing language. The normal-shear spring elements can transfer the

normal and shear forces. The beam elements can transfer in addition bending moment and torque. The difference between simulation results when using the normal-shear spring and beam lattice models are negligible on mode-I of failure. Therefore, in order to gain in computational time, almost all simulations in the thesis were performed using the normal-shear spring lattice model because we only focused on mode-I failure of the material. The beam lattice model is used for the coupling with finite elements for simulations of real structures subjected to mixed mode failure in general purposes. To better estimate the geometrical heterogeneity due to the random mesh, and thus reduce the mesh bias on crack propagation which is an inherent feature of lattice models, a new tessellation is adopted to assign the cross section areas to lattice elements, refer to Section 2.2.3.2.

From the numerical tool, we performed two types of numerical tensile tests: localized damage tests and distributed damage tests on specimens made of brittle elastic model material with varying aggregate (inclusion) structure, boundary conditions and specimen size. The fracture process zone size and the material characteristic length were measured from these tests in order to study the influence of different parameters that characterize the mesotructure of the material and of the stress gradient and material rotation (resulting from different boundary conditions and specimen size) on their values. The assessment of the fraction process size ℓ_{FPZ} is achieved via localized damage tests while the material characteristic length ℓ_{c} is measured via both localized and distributed damage tests. The results were presented in Chapter 3. The study pointed out the influences of: the interfacial transition zones (ITZs), the fine aggregate particles (matrix heterogeneity), the applied stress gradient and material rotation, the aggregate size with fixed volume fraction, the aggregate volume fraction with fixed size, the aggregate size dispersion and the ligament size of the specimen on the fracture process zone size. The study of the material characteristic length was only concerned with the size of aggregates placed at fixed positions on the one hand, and placed so that their volume fraction is nearly the same on the other hand. The main observations and conclusions can be discussed as follows:

- When the ITZ is considered in-between the aggregate and matrix phases (the material is modeled as three-phase material instead of two-phase one when the ITZ is not taken into consideration), not only the value but also the variation of the FPZ size with respect to the aggregate size is higher than that of the case of two-phase material. So, for better simulating and predicting fracture in concrete(-like) material, interfacial transition zones have to be taken into consideration in numerical models.

- When a random field of the local strengths are introduced to the matrix elements to mimic the effect of fine aggregate particles (since the latter was not explicitly introduced like the coarse aggregates to reduce computational time), we showed that, again, not only the value but also the variation of the FPZ size with respect to the aggregate size is higher than that of the case in which no random field of strengths is introduced. This leads to the conclusion that, in addition to the coarse aggregates, the fine aggregates need to be introduced in numerical models in order to better simulate and predict fracture in concrete(-like) material. We suggest that the fine aggregates should be explicitly introduced like the coarse aggregates if possible since a limitation of the method of mimicking the effect of the fine aggregates by introducing a random field of strengths to the matrix phase is that, if too large values of the standard deviations of the local strengths of the matrix phase are introduced, the physical meaning of the mesostructure can be lost because of the fact that the matrix elements can have the generated values of strengths which are smaller than the corresponding values of ITZ elements.

- Since the numerical simulations required for assessment of the FPZ size take less time than those for assessment of the characteristic length (only one-type of localized damage tests needed vs. both types of localized and distributed damage tests needed), many studies were performed concerning the FPZ size. However, by the studies performed on the influence of aggregate size with fixed positions and of the aggregate size with fixed volume fraction, we demonstrated that the characteristic length of the material and the FPZ size have the same

order of magnitude. Also, the variations of the material characteristic length and of the FPZ size with respect to the aggregate size have the same tendency (increase with an increase of aggregate size). Moreover, the standard deviations of the material characteristic length, obtained from difference positions of aggregates, behave in the same way as that of the FPZ size. This leads to the logical conclusion that a certain equivalence exists between the FPZ size and the material characteristic length. For this reason, the conclusions drawn in Section 3.4 for the FPZ size can be extrapolated for the characteristic length of the material.

- It appears that not basically the size, but other parameters that characterize the aggregate structure of the material such as the volume fraction, the size dispersion, the fabric, the connectivity, the spacial distribution, and the aggregate spacing, strongly affects the size of the FPZ, and thus the characteristic length of the material. Furthermore, the measured value of the FPZ size is also dependent on the local stress level and/or on the stress gradient which may be related to the specimen geometry or the boundary conditions for instance. Therefore, it is difficult to avoid the ascertainment that the FPZ size is *not* an intrinsic property of the material as usually believed. Likely, characterizing the heterogeneity of the material by only single scalar value called the material characteristic length seems *debatable*. However, it was checked that the FPZ size, thus the (conventional) characteristic length, remains in the same order when the tested system is the same (mesostructure, global geometry and dimensions, loading conditions...).

- The assessment of the characteristic length of the material is essential for using its value as the internal length in nonlocal models. However, just like the FPZ size, it is difficult to avoid structural effects in the measurement of the characteristic length (at least for the current method used in the study). Moreover, the fact that determining the internal length for nonlocal models based only on the maximum aggregate size, as usually reported in the literature, does not deserve to be accepted, according to the author's opinion.

- Despite the fact that, in our studies the characteristic length and the FPZ size were not measured upon the course of the fracture process, given the development of cracking process from our simulations, there is no doubt that the FPZ size, as well as the characteristic length, evolves during the fracture process, as observed experimentally in the literature by acoustic emission analyses, for example.

- The fact that dissociating the internal length of the classical nonlocal model into two parts: the geometric and the structural parts, as in the nonlocal model proposed by Giry et al. (2011), to take into account the evolution of the FPZ size over time and the structural effect on the FPZ size, seems interesting. However, for an apparent use of this nonlocal model, the geometric part of the internal length should be identified. But, so far the method for assessment of the geometric part of the internal length has not been uncovered. We hopefully suggest that, for example, the geometric part of the internal length can be measured from a tensile test performed on a very large-scale specimen so that the structural effect can be imperceptible from the internal length viewpoint. Or, possibly, the geometric part can be determined from two tensile tests from which the structural part of the internal length could be revoked.

- It should be noted that, since many simulations are needed in our studies, so to have a reasonable computational time, our studies were performed only on 2D specimens and only five realizations of aggregate positions are generated for each considered case of the mesostructure. Therefore, if 3D simulations and more realizations of aggregate positions can be carried out (for future works), the conclusions drawn in Chapter 3 can be more or less robust. This is simply because the fracture process is a three-dimensional phenomenon, as shown in Section 2.5.4.

- It is however worth stressing that we only did focus on the geometric influence of the mesotructure of the material on the FPZ size and on the material characteristic length. The mechanical properties, especially, the changes of ratios of the different stiffnesses and strengths of the material phases have been set aside. This should be planed for future works.

Until the geometric part of the internal length is reliably determined for using as an internal variable of nonlocal models, we suggest using the lattice model with an explicit description of the mesostructure of the material for better simulating and predicting fracture in concrete(-like) material. However, as stated, simulations of a complete large-scale structure using the lattice model at the mesoscale requires tremendous computation and storage efforts due to a vast number of degrees of freedom. In Chapter 4, we presented the original algorithm for coupling the beam lattice model with finite elements within a multiscale framework to reduce the computational effort. By analyzing the equivalence of the stiffness matrix between a lattice cell and a finite element of the same size, we demonstrated that a lattice cell can represent a material with given macroscopic properties such as Young's modulus and Poisson's ratio like a FE does. However in terms of stiffness, it was seen that the stiffness matrix of the lattice cell is not exactly equivalent to that of the FE. We also showed the beam lattice model reproduces a more accurate stiffness matrix compared to the stiffness matrix of the FE of same size than the normal-shear spring lattice model. Therefore, we decided to couple the beam lattice model with finite elements. Let us summarize the coupling strategy as follows. First, a structure is modeled only with elastic finite elements. However the stiffness matrix of a FE is not constructed by integration over the volume/area of that FE but it is computed by means of a *homogenization process* over a lattice cell of same size. As soon as somewhere in the structure, a certain (to be defined) maximum strain level is reached, the finite element represented that part is substituted by a beam lattice cell of same size. Subsequently, fracturing takes place in that lattice cell by performing elastic analysis on the lattice cell. The global nonlinear behavior of the structure can be obtained. The continuity of the displacement field on the coupling interface is assured by the master/slave algorithm. The translational and rotational displacements of the lattice nodes on the interface coupling are restrained to the displacement field and the rotational vector of the skew-symmetric tensor which derived from the displacement field of the FE, respectively. The stress field at the interface coupling of the lattice cell is transfered to the neighboring FEs. If in the meantime, the strain state of another finite element reaches the maximum strain, this element is replaced by a lattice cell of same size. The continuity of the displacement between two adjacent lattice cells is also assured. When a lattice cell is completely cracked, it is removed again and two half finite elements are replaced by the zoom-out technique.

Note that the coupling is strong. Nonlinearities of structures come from the lattice approach. It does not exist a homogenized nonlinear behavior of the lattice approach that is introduced in a integration point of a FE like many works proposed by other authors, which are weak couplings. Moreover, the coupling algorithm is provided for parallel computations.

For the numerical implementation of the algorithm into SOFA framework, our works have been accomplished for elementary coupling, i.e., only two objects (one represented by finite elements and other represented by lattice cells) are coupled. Two strategies of coupling were implemented into SOFA, as presented in Chapter 4. The *full* coupling algorithm with zoom-in, zoom-out techniques, criteria that allow the zoom-in and zoom-out events occur, and parallel computation scheme have not been implemented yet. Future works on such implementation are required.

Perspectives

Before going into more complex applications on modeling of large-scale structures made of concrete-like materials, using whether nonlocal models or a multiscale approach via LEM-FEM coupling, different works to do, in our view, in order to better simulate and predict fracture process in such materials, are:

- Studying the influence of the mesostructure on the FPZ size and the characteristic length of the material by 3D simulations using the lattice model. From that, one should identify/extract the "geometric" part from the characteristic length of the material for using its value as the internal length in nonlocal models.
- Analyzing the effect of the mechanical properties, especially the ratios of the different stiffnesses and strengths of the material phases, on the resulting FPZ size and material characteristic length.
- Implementing a softening constitutive law for the matrix phase (e.g. a bilinear law with a softening branch) while the behavior of the aggregate and ITZ phases can be assumed linear elastic, in order to get closer to a global behavior of concrete in terms of ductility. From that, studying the influence of softening parameter(s) on the FPZ size and on the characteristic length of the material.
- Comparing with experimental tests in order to validate the identified geometric part of the characteristic length.
- Implementing the full LEM-FEM coupling algorithm with zoom-in, zoom-out techniques in order to deal with large-scale structures.
- Further, if the tool based on LEM-FEM coupling is available, studying the statistical size effect performed by multiscale 3D simulations in order to provide insight into the origin and nature of size effect of quasi-brittle materials observed in experiments.

Appendices

Appendix A

Continuum-based models

A.1 Discontinuous models

As the name implies, in discontinuous models, the displacement field exhibits a sharp jump due to an apparition of a crack that could be modeled by a numerical tool.

For quasi-brittle materials, the fracture behavior is greatly influenced by the Fracture Process Zone (FPZ) with a finite size in front of a crack tip. FPZ is defined as the zone in which damage occurs and causes the softening behavior of the material. The linear elastic fracture mechanics (LEFM) fails to describe the behavior of quasi-brittle materials because it cannot account for the PFZ and assumes that the stress concentration only occurs at a point (the crack tip) leading to a brittle failure. In other words, the LEFM is only applicable when the FPZ size is small compared to crack size and specimen size (Bažant and Planas, 1998). Based on the work of Barenblatt (1959) who assumed that a small zone near the crack ends where cohesive forces act on the faces of the crack, Hillerborg et al. (1976) proposed a *cohesive crack model* for concrete. As shown in Figure A.1a, the model includes a softening process zone through a fictitious (cohesive) crack ahead of the initial (pre-existing) crack such that there is no stress concentration at the initial crack tip. On the faces of the fictitious crack, cohesive forces act as closing forces that vary from 0 at the initial crack tip to the value of the tensile strength of the material f_t at the tip of the fictitious crack. In other words, the model includes a

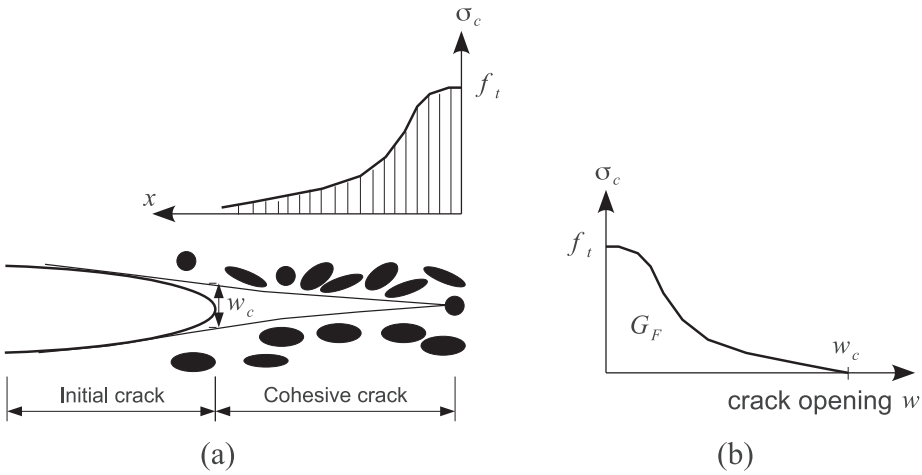

Figure A.1 – Cohesive crack model of Hillerborg et al. (1976) (a) and cohesive law (b).

cohesive law (also called tension-separation law) that relates the crack opening w to the cohesive stress σ_c, see Figure A.1b

$$\sigma_c = g(w, \boldsymbol{\beta}) \tag{A.1}$$

where $\boldsymbol{\beta}$ represents some internal variables characterizing cracking phenomenon. It is noted that,

in the cohesive crack model, the energy produced by the applied load is assumed to be completely balanced by the cohesive stress. Hillerborg et al. (1976) introduced the fracture energy G_F that is defined as the area under the cohesive law's curve

$$G_F = \int_0^{w_c} \sigma_c(w)\,\mathrm{d}w \tag{A.2}$$

where w_c is the critical crack opening. Together with tensile strength f_t, G_F is also considered as a material property. They are determined by experimental tests, see e.g., (Hillerborg, 1985) or (Shah and Carpinteri, 1991).

From a numerical viewpoint, various shapes of the cohesive laws have been used to approximate the fracture energy G_F including linear (Hillerborg et al., 1976), bilinear (Roesler et al., 2007), trilinear (Liaw et al., 1990), exponential (Gopalaratnam and Shah, 1985) or power (Foote et al., 1986) curves. Reviews can be found in Murthy et al. (2009) or in Zhao et al. (2010). It should be noted that, in comparison with a cohesive law, a separate criterion for crack growth is needed when using cohesive crack models because the former does not predict a damage initiation or propagation at all.

When using cohesive crack models in the FEM framework, two constitutive relations are needed to be implemented to describe the behavior of a solid, namely, the standard cohesive equation (1.8c) for the bulk material and the cohesive law (A.1) for the material in the cohesive zone. One of the challenges in using cohesive crack models is how to deal with displacement discontinuities. Various techniques have been used in the literature such as inserting *interface elements* (Carpinteri, 1989; Ortiz and Pandolfi, 1999; Tijssens et al., 2000), using elements with *embedded discontinuities* (Oliver, 1996; Wells and Sluys, 2000; Linder and Armero, 2007) or employing adaptive remeshing techniques (Bouchard et al., 2000, 2003). However, inserting interface elements into inter-elements prior to simulations requires that the crack path is known *a priori*. Remeshing techniques are required when the crack path is not known in advance. This is expensive in term of the computational time. Embedding discontinuities into an element level provides a way to propagate intraelement cracks and has an advantage that the method can be directly implemented in the existing FEM code. Nevertheless, some disadvantages of these techniques were pointed out in Jirásek (2000) such as the problem of reflecting the kinematics of a completely open crack or the problem of loss of well-posedness of the boundary value problem (de Borst et al., 1993).

Nowadays, the extended finite element method (XFEM) (Moës et al., 1999) that exploits the partition of unity (PU) of finite element shape functions (Melenk and Babuška, 1996) and allows local enrichments on the element level by defining additional unknowns and an enrichment function is widely used to model displacement discontinuities. Modelings of cohesive cracks using XFEM are found in Wells and Sluys (2001), Moës and Belytschko (2002), and Cox (2009). However, implementing XFEM in the existing FEM code is not straightforward and requires an important effort of programing. Computer implementations of XFEM are presented in Sukumar and Prévost (2003), Bordas et al. (2007), Giner et al. (2009), and Shi et al. (2010). An overview of XFEM and its applications can be found in Fries and Belytschko (2010).

A.2 Continuous models

The approach using continuous models considers that the displacement filed is continuous and the cracking description consists of introducing a softening behavior between stress and strain in a continuous medium.

A.2.1 Smeared crack models

Instead of directly modeling a crack by a geometric discontinuity, Rashid (1968) introduced a *smeared crack model* based on the concept of replacing a crack by a continuous medium with altered physical properties. This means that when the major principal tensile stress exceeds the tensile

strength of the material, the isotropic stress-strain relation is replaced by an orthotropic law with n, s-axes the axes of orthotropy (see Figure A.2) expressed in plane stress condition as (Rashid, 1968)

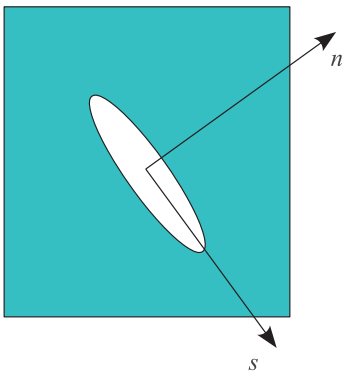

Figure A.2 – Orthotropy axes aligned with the crack.

$$\boldsymbol{\sigma}_{ns} = \mathbf{D}^{s}_{ns}\boldsymbol{\varepsilon}_{ns} \tag{A.3}$$

with

$$\boldsymbol{\sigma}_{ns} = \begin{Bmatrix} \sigma_{nn} \\ \sigma_{ss} \\ \sigma_{ns} \end{Bmatrix}, \ \mathbf{D}^{s}_{ns} = \begin{bmatrix} 0 & 0 & 0 \\ 0 & E & 0 \\ 0 & 0 & 0 \end{bmatrix}, \ \boldsymbol{\varepsilon}_{ns} = \begin{Bmatrix} \varepsilon_{nn} \\ \varepsilon_{ss} \\ \varepsilon_{ns} \end{Bmatrix} \tag{A.4}$$

where n is the direction normal to the crack and s is the direction tangential to the crack. This concept has an advantage that it is simple to implement in a FEM code because one can avoid the problems coming from changes of mesh topology. However, the concept of Rashid (1968) where the normal and shear stiffnesses were set to zero upon crack initiation results in premature convergence difficulties, unrealistic crack patterns and brittle failures. Many enhancements have been developed to reproduce the experimental observed characteristic behavior of concrete. Cope et al. (1980) introduced the so-called *shear retention factor* β to reduce the numerical difficulties and improve the physical reality of crack patterns. Moreover, concrete is not a perfectly brittle material in the Griffith sense but shows some residual load-carrying capacity after reaching the peak load observed in displacement control experiments. In the similar way of using the shear retention factor, a *normal reduction factor* μ was inserted in the secant orthotropic stiffness matrix. Finally, the secant stiffness matrix is defined as

$$\mathbf{D}^{s}_{ns} = \begin{bmatrix} \mu E & 0 & 0 \\ 0 & E & 0 \\ 0 & 0 & \beta G \end{bmatrix}. \tag{A.5}$$

The local relation (A.3) is transformed into those in the global x, y-coordinate system via the standard transformation matrix $\mathbf{T}$ as

$$\boldsymbol{\sigma}_{xy} = \mathbf{T}^{T}(\phi)\mathbf{D}^{s}_{ns}\mathbf{T}(\phi)\boldsymbol{\varepsilon}_{xy} \tag{A.6}$$

with $\boldsymbol{\sigma}_{ns} = \mathbf{T}(\phi)\boldsymbol{\sigma}_{xy}$ and $\boldsymbol{\varepsilon}_{ns} = \mathbf{T}(\phi)\boldsymbol{\varepsilon}_{xy}$; ϕ is the angle from x-axis to the n-axis. If ϕ is fixed upon crack initiation, the approach is known as *fixed smeared crack model* whereas if ϕ changes continuously to keep the direction of the crack orthogonal to the direction of the major principal stress, the *rotating smeared crack model* is obtained (Rashid, 1968).

The smeared crack models discussed above are based on total strain concepts leading to the situation where cracking and other nonlinear phenomena such as creep, shrinkage, thermal effects are not combined properly. The *non-orthogonal crack model* was proposed by de Borst and Nauta (1985) and de Borst (1987) that based on the decomposition of the total strain into two parts –

one corresponds to the deformation of the uncracked material, and the other is the contribution of cracking. This reads

$$\boldsymbol{\varepsilon} = \boldsymbol{\varepsilon}^e + \boldsymbol{\varepsilon}^c \tag{A.7}$$

in which the crack strain $\boldsymbol{\varepsilon}^c$ can be decomposed further so that

$$\boldsymbol{\varepsilon}^c = \boldsymbol{\varepsilon}_1^c + \boldsymbol{\varepsilon}_2^c + \dots \tag{A.8}$$

which allows to multiple cracks develop such that $\boldsymbol{\varepsilon}_1^c$ owing to the primary crack, $\boldsymbol{\varepsilon}_2^c$ owing to the secondary crack and so on. It is noted that each crack is fixed upon its initiation and this results in the so-called *multiple fixed smeared crack model*. A general classification of smeared crack models is presented in Weihe et al. (1998).

A.2.2 Crack band model

The above smeared crack models, when implemented in a FEM code, suffer from the mesh sensitivity i.e., the crack propagation is dependent on the mesh refinement (Crisfield, 1982). To remedy this problem, the concept of fracture energy of Hillerborg et al. (1976) has been proposed and considered as a material property. Adapting this concept of energy release upon crack propagation, Bažant and Oh (1983) introduced the *crack band model* (CBM) in which the fracture energy introduced by Hillerborg is smeared out over the width w_b of the area in which the crack localizes (the FPZ), see Figure A.3. For simplicity, consider a uniaxial situation. The constitutive law in the crack band is

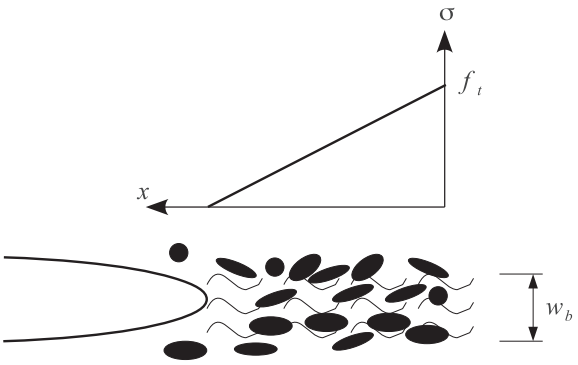

Figure A.3 – Schematic representation of the CBM of Bažant and Oh (1983).

described in the general form

$$\sigma = f(\varepsilon) \tag{A.9}$$

in which the total strain is decomposed into an elastic part and a fracture (inelastic) part as

$$\varepsilon = \varepsilon_e + \varepsilon_f \tag{A.10}$$

The fracture strain in turn can be derived from the traction-separation law of a discrete cohesive crack where the cracking opening w is smeared over a band width w_b

$$\varepsilon_f = \frac{w}{w_b} = \frac{g^{-1}(\sigma_c)}{w_b} \tag{A.11}$$

in which g^{-1} is the inverse function of the traction-separation law (A.1). Combining (A.10) and (A.11) gives an inverse stress-strain relation in the crack band as (see Figure A.4)

$$\varepsilon = \varepsilon_e + \varepsilon_f = \frac{\sigma}{E} + \frac{g^{-1}(\sigma_c)}{w_b} \tag{A.12}$$

We refer to Bažant and Oh (1983) for more details.

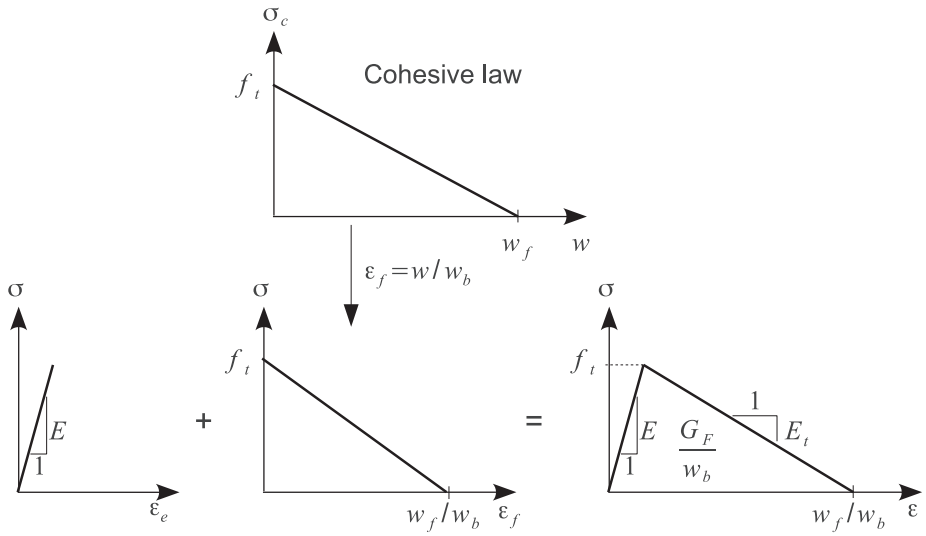

Figure A.4 – Constitutive diagram of the CBM derived from a traction-separation law.

The energy dissipates upon crack propagation is given by

$$G_F = \frac{1}{2}\left(\frac{1}{E} + \frac{1}{E_t}\right) f_t^2 w_b \tag{A.13}$$

where E_t stands for the tangent softening modulus of the material. When the CBM is implemented in a FEM code, it exhibits the mesh sensitivity as shown in Bažant and Cedolin (1983): the dissipated energy decreases with a decrease in size of the finite elements with an observation that the localization of deformation occurs only in a single finite element. This causes crack localization in a band of width zero in the extreme case of elements with vanishing size, thus yielding a null dissipated energy ($\lim_{w_b \to 0} G_F = 0$). This spurious mesh sensitivity is only solved by adjusting the dependence of the tangent softening modulus on the finite element size h as

$$E_t = \left(\frac{2G_F}{f_t^2 h} - \frac{1}{E}\right)^{-1}. \tag{A.14}$$

The reader is referred to Bažant and Oh (1983) for further discussions.

So far, the above models have been used for simple applications under simple boundary conditions. For applications in three dimensions under complex boundary conditions, they are not suitable because, for example, the CBM does not take into consideration the third dimension (the deep) of the FPZ. The progressive deterioration of the material can be described by a more formal treatment that considers the softening behavior of the material coming from the degradation of the material stiffness. This kind of treatment is referred to *damage models*.

A.2.3 Anisotropic damage models

The above isotropic damage models are based on the assumption that the material stiffness degradation is isotropic, i.e., stiffnesses corresponding to different directions decrease proportionally, independently of the direction of the loading. However, in most situations, specially in compression and shear problems or in analysis of reinforced concrete problems, damage is not isotropic but has preferential directions. To take into account the anisotropy induced by damage, Dragon et al. (1994) and Halm and Dragon (1996) proposed an *anisotropic damage model* by mesocrack growth of brittle materials and applied for simulation of the behavior of Fontainebleau sandstone. Later, many developments have been taken place accounting for induced anisotropy, dilatancy, etc., of quasi-brittle materials that one can cite here the work of Desmorat et al. (2007) who proposed an anisotropic

damage model for concrete. In this model, anisotropic damage is represented by a tensorial thermodynamics variable $\mathbf{D}$ (Chaboche, 1978; Chow and Wang, 1987; Lemaitre et al., 2000), a second order tensor, so that the strain tensor $\boldsymbol{\varepsilon}$ is related to the effective stress tensor $\tilde{\boldsymbol{\sigma}}$ by

$$\boldsymbol{\varepsilon} = \frac{1+\nu}{E}\tilde{\boldsymbol{\sigma}} - \frac{\nu}{E}\operatorname{tr}\tilde{\boldsymbol{\sigma}}\mathbf{1} \tag{A.15}$$

where the symmetric effective stress tensor is defined as

$$\tilde{\boldsymbol{\sigma}} = (\mathbf{H}\boldsymbol{\sigma}^{D}\mathbf{H})^{D} + \frac{1}{3}\left(\frac{\langle \operatorname{tr}\boldsymbol{\sigma}\rangle}{1-\operatorname{tr}\mathbf{D}} - \langle -\operatorname{tr}\boldsymbol{\sigma}\rangle\right)\mathbf{1} \tag{A.16}$$

with $(\cdot)^{D} = (\cdot) - \frac{1}{3}\operatorname{tr}(\cdot)\mathbf{1}$ the deviatoric part of $\cdot$, $\mathbf{1}$ the identity tensor, $\mathbf{H} = (\mathbf{1}-\mathbf{D})^{-1/2}$ the effective damage tensor. This effective stress-strain relation is again complemented by a damage loading function f described by Equation (1.43) in which the scalar history variable κ reads

$$\kappa = \kappa(\operatorname{tr}\mathbf{D}) = a\tan\left[\frac{\operatorname{tr}\mathbf{D}}{aA} + \arctan\left(\frac{\kappa_0}{a}\right)\right] \tag{A.17}$$

with κ_0 the damage threshold, a and A two damage parameters determine the damage evolution such that

$$\dot{\mathbf{D}} = A\left[1+\left(\frac{\tilde{\varepsilon}}{a}\right)^{2}\right]^{-1}\frac{\langle\boldsymbol{\varepsilon}\rangle_{+}^{2}}{\tilde{\varepsilon}^{2}}\dot{\tilde{\varepsilon}} \tag{A.18}$$

where $\langle\boldsymbol{\varepsilon}\rangle_{+}$ denotes the positive part (in terms of principal components) of the strain tensor. It is noted that a single set of damage parameters A and a is sufficient and valid for both tensile or compressive loading. The reader is referred to Fichant et al. (1999), Dragon et al. (2000), Lemaitre et al. (2000), and de Borst (2002) and references therein for more details on anisotropic damage models. Though anisotropic damage models can better describe the behavior of concrete compared to isotropic damage models since they induce damage anisotropy that is responsible for the dissymmetry tension/compression. However, this type of models is still complex, not easy to implement and the computational efficiency has not yet been proven for structural applications (of course, compared to isotropic damage models).

When the above damage models are implemented in the FEM code, they suffer, however, from the spurious mesh sensitivity in the postpeak regime, which yields nonobjective results with regard to the choice of the mesh, see (Murakami and Liu, 1996). This nonphysical response is, mathematically, caused by localization instabilities due to loss of ellipticity of the partial differential governing equations and - more importantly - singularity of damage rate at the crack tip (Peerlings et al., 2002). It is noted that the mesh sensitivity is not unique for damage models, but also occurs in softening plasticity and other continuous representations of material degeneration that based on the local formulation, see e.g., (Pietruszczak and Mróz, 1981; Bažant et al., 1984). In the context of damage models, to overcome the mesh sensitivity problems, *nonlocal continuum* approach has been proposed.

Annexe B

Résumé étendu de la thèse en français

Introduction

Contexte et objectif

La motivation principale est de développer un modèle numérique qui n'introduit pas de longueur interne dans la loi de comportement du matériau et on peut affranchir ce paramètre en introduisant explicitement des agrégats dans la description géométrique. En outre, grâce à ce modèle, une étude de l'influence de la microstructure du matériau sur ses comportements à la fois pré-pic et régimes de post-pic peut être considérée. Ensuite, une longueur interne nécessaire pour les modèles nonlocaux est tentée d'être extrait à partir de la microstructure du matériau ou du moins une meilleure compréhension des éléments clés susceptibles d'influer sur la longueur interne peut être fournie à partir de cette étude.

Nous nous intéressons en particulier dans les modèles de lattice qui sont devenus des outils pertinents pour l'étude de la rupture des matériaux hétérogènes. En fait, l'approche de lattice est très appropriée pour des simulations de processus de rupture. D'abord, parce que le champ de déplacement discontinu est bien capturé grâce à la caractère discrète intrinsèque de ces modèles. Deuxièmement, en utilisant l'approche de lattice avec l'introduction de l'hétérogénéité du matériau en générant les constituants du matériau, la propagation des fissures et l'ouverture des fissures sont produits explicitement, qui sont un outil direct dans les analyses de la durabilité des structures en béton au lieu de les estimer à partir d'une approche continue. En outre, l'approche de lattice fournit un aperçu direct de l'origine et de la nature du comportement non linéaire du matériau et peut également refléter les effets physiques observés dans des expériences telles que la décohésion du grain, microfissures et le pontage des fissures observées dans le béton. Cependant, des simulations avec le modèle du lattice à la méso-échelle exigent les résolutions fines du maillage discrétisé. Pour les structures à grande échelle, ils conduisent donc à un grand nombre de degrés de liberté, en particulier pour les analyses en trois dimensions. Par conséquent, l'analyse de grandes structures seulement par des modèles de lattice à la méso-échelle n'est pas possible. Ainsi, il semble qu'une combinaison appropriée de l'approche discrète à la méso-échelle représentée par l'approche de lattice et l'approche continue à l'échelle macroscopique traitée par la méthode des éléments finis (MEF), qui se traduit par une approche multi-échelle, est essentielle.

L'objectif de la recherche présentée dans cette thèse est de développer un outil numérique basée sur les modèles de lattice qui permet de simuler le processus de rupture des matériaux hétérogènes quasi-fragiles. Basé sur cet outil, une étude de l'origine mésoscopique de la taille de la process zone (FPZ) et la longueur caractéristique du matériau est effectuée dans le but de trouver une corrélation entre la mésostructure du matériau et la longueur interne utilisée dans les modèles nonlocaux ou simplement pour préciser le rôle de la mesotructure sur la taille de la FPZ. En raison de la nature localisée du processus de rupture dans le régime adoucissant, la taille de l'échantillon et des conditions aux limites doivent avoir un effet significatif sur le processus de rupture. Leur influence peut

être analysée utilisant cet outil numérique. Et à long terme, tel outil numérique doit être capable de modéliser la rupture des grandes structures en matériaux quasi-fragiles en génie civil via une approche numérique multi-échelle.

Cadre et plan de la thèse

La recherche présentée dans cette thèse concerne la modélisation des matériaux quasi-fragiles en insistant sur le béton, soumis à des sollicitations mécaniques. L'étude est limitée aux problèmes de rupture sous mode I survenant aux petites déformations dans des conditions de chargement quasi-statique. La mécanique des milieux continus est supposée tenir à l'échelle macroscopique s'il y a plus d'une échelle de longueur impliqués dans le modèle. Quand il y a une seule échelle impliqué dans le modèle, le modèle de lattice discret est utilisé à l'échelle mésoscopique pour mieux capturer les mécanismes de rupture à l'échelle matérielle, et la mécanique des milieux continus n'est plus supposée tenir. Le terme « multi-échelle » doit être compris comme plusieurs (plus d'un) échelles de longueur qui sont inclues dans le même système.

Le manuscrit se compose de quatre chapitres. Chapitre 1 décrit brièvement ce que l'on sait actuellement sur le comportement, en particulier lié à la fissuration des matériaux quasi-fragiles en insistant sur le béton. Une vue d'ensemble de l'état de l'art des modèles numériques traitant de ces matériaux est donnée. Les pathologies de chaque modèle sont signalées, qui conduisent aux objectifs de la thèse.

Chapitre 2 présente le modèle de lattice qui est utilisé pour simuler la rupture des matériaux quasi-fragiles comme le béton. La formulation et l'implantation du modèle seront présentées. La procédure d'identification des paramètres du modèle est ensuite examinée avant de valider le modèle par quelques essais.

Dans Chapitre 3, l'influence de la microstructure du matériau sur la longueur caractéristique du matériau et de la taille de la FPZ est analysée en utilisant le modèle de lattice avec une description géométrique explicite des agrégats. L'étude de l'influence de la taille de l'échantillon et des conditions aux limites qui résultent en différent gradient de contrainte sur la taille de la FPZ est aussi précisée. Ces études fournissent des recommandations/avertissements lors de l'extraction d'une longueur interne nécessaire pour les modèles d'endommagement nonlocaux à partir de la microstructure du matériau.

Pour simuler la rupture des structures à grande taille en génie civil, Chapitre 4 présente une procédure de couplage entre le modèle de lattice et les éléments finis dans une approche multi-échelle avec des calculs en parallèle.

Enfin, la thèse se termine en résumant les principaux enjeux du travail présentés dans ce rapport puis elle affichera des recommandations et des perspectives pour la recherche au futur.

Chapitre 1
Fissuration des matériaux quasi-fragiles : l'état de l'art

Aujourd'hui, les matériaux quasi-fragiles tels que la céramique, les roches ou en particulier le béton sont largement utilisés dans l'industrie ou dans le génie civil. La fissuration du béton et son mécanisme jouent un rôle très important dans le comportement et la durabilité des structures en béton. La modélisation est un outil indispensable pour la conception des structures en béton, car il fournit une prédiction du comportement des structures. Toutefois, la précision de la prédiction dépend surtout de la fiabilité des modèles décrivant les comportement des matériaux. Par conséquent, les modèles de matériaux doivent être dérivés à partir d'une mesure expérimentale du comportement du matériau.

1.1 Comportement mécanique des matériaux quasi-fragiles hétérogènes

Matériaux quasi-fragiles, tels que le béton, présentent un mécanisme de fracture complexe impliquant des microfissures et macrofissures sous des charges extrêmes. Ce mécanisme de fracture complexe est clairement lié à leur microstructure hétérogène. Le béton présente une structure hétérogène du matériau à un certain niveau d'observation. Variant de millimètres à nanomètres, sa structure contient des différents constituants aléatoires, dans lesquels chaque constituant peut être considéré comme un nouveau matériau composite lorsqu'il est vu à l'échelle de longueur inférieure (voir Figure B.1).

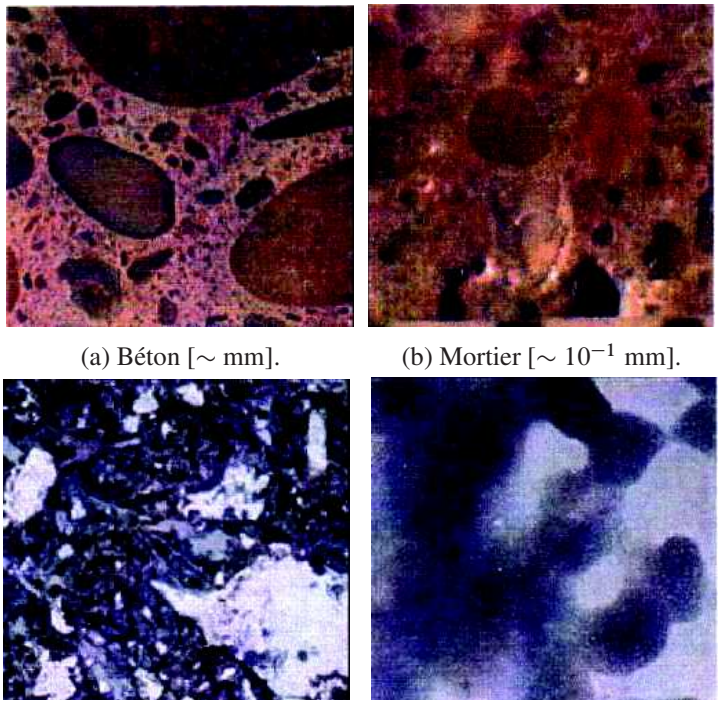

(a) Béton [$\sim$ mm]. (b) Mortier [$\sim 10^{-1}$ mm].

(c) Pâte de ciment [$\sim \mu$m]. (d) Gel C-S-H [$\sim$ nm].

FIGURE B.1 – La structure du béton à différentes échelles de longueur. Basé sur (Garboczi and Bentz, 1995).

Pour le béton ordinaire, le gravier, la pierre concassée et le sable sont des agrégats primaires utilisés. Cela dépend de chaque type de béton, mais en général, les agrégats représentent 60-80% du volume de béton. Ils peuvent être divisés en deux catégories distinctes, fin et grossier. Les fins constituent la plupart des particules passant à travers un tamis de $4,75$ mm. Les plus gros occupent environ 40-50% du volume du béton. Graviers constituent la majorité des agrégats grossiers utilisés dans le béton tandis que la pierre concassée constitue l'essentiel du reste (Portland Cement Association, 2013). La forme des particules d'agrégats dépend du type d'agrégats. En général, les graviers ont une forme arrondie alors que les pierres concassées ont une forme angulaire (Wang et al., 1999).

En pratique, pour étudier l'influence des constituants sur les propriétés macroscopiques et également d'avoir un aperçu sur l'origine et la nature du comportement non linéaire, le béton est souvent considéré à l'échelle mésoscopique (échelle millimétrique) où trois composants principales sont séparés : (i) gros granulats, (ii) homogène matrice de mortier avec des fins granulats qui y sont dissous, et (iii) la zone de transition interfaciale (ITZ) entre eux . Les pores au sein de la matrice est généralement ignorés à cette échelle de longueur. La ITZ est d'environ 20-100 μm d'épaisseur (Liao et al., 2004). La résistance expérimentale de l'ITZ est d'environ 33% to 67% de la résistance à la traction de la matrice (Hsu and Slate, 1963). Cette dernière est à son tour d'environ 30% to 50% de la résistance à la traction des agrégats (Alexander et al., 1968; Husem, 2003). En outre, pour le béton de poids normal, les agrégats sont environ deux fois à trois fois plus rigide que la matrice de mortier. Ces ratios ont été utilisés pour la modélisation de comportements du béton à l'échelle mésoscopique, voir, e.g., Schlangen and Garboczi (1997), Sagar and Prasad (2009), and Grassl et al. (2012).

Le comportement mécanique du béton, sous une charge mécanique extérieure, se caractérise d'abord par un stade quasi-élastique, ce qui signifie que le matériau revient à sa configuration d'origine si déchargé. Puis, au fur et à mesure que les charges augmentent, les microfissures apparaissent avant le pic de contrainte est atteinte. Les microfissures fusionnent également pour former la (les) macrofissure(s). Cette macrofissure va croître et se propager jusqu'à la rupture complète. Parallèlement à la croissance de fissures, le béton montre une diminution progressive de leur capacité portante lorsqu'il est déformé au-delà d'une certaine limite, voir Figure B.2. Par conséquent, le béton est appelé matériau « adoucissant ». Le comportement adoucissant du béton est observée à la fois sous compression et traction (Bažant, 1976; van Mier, 1984; Torrenti et al., 1993; Markeset and Hillerborg, 1995; Jansen and Shah, 1997). La taille des spécimens et les conditions aux limites

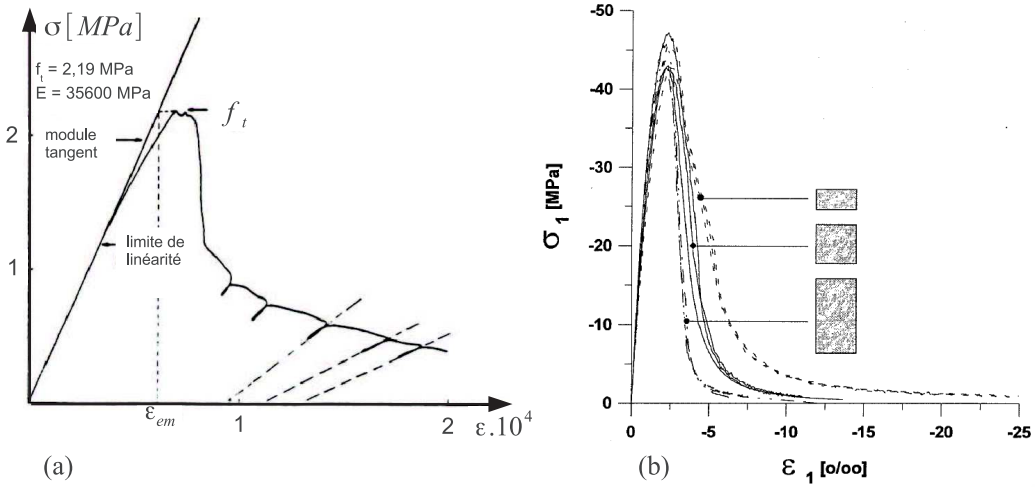

FIGURE B.2 – Comportement du béton sous sollicitations axiales : traction (a) (Terrien, 1980) et compression (b) (Geel and Eindhoven, 1998).

ont des effets importants sur le comportement adoucissant du béton. Figure B.2b montre que, pour différentes tailles des échantillons, avant le pic, le comportement contrainte-déformation presque identiques sont obtenus alors que dans le régime adoucissant, les échantillons de tailles différentes se traduisent par différentes courbes adoucissantes. Plus de discussions sur les dépendances de la taille et des conditions aux limites peuvent être trouvées, e.g., dans Hordijk (1991) and van Mier et al. (1996).

Dans des conditions de chargement uniaxial, la localisation de la déformation se produit à partir du pic. Sous tension, la déformation se localise dans une bande étroite de taille finie, qui est appelé la localisation de mode I. En compression multiaxiale (à faible confinement i.e. en dessous de la transition fragile- ductile), la localisation se manifeste le long de bandes de cisaillement, ce qui est

appelée la localisation de mode II. En outre, en compression uniaxiale, une bande de cisaillement peut être trouvée si l'échantillon est très courte (van Mier, 1984; Desrues and Viggiani, 2004). En dehors de la zone de localisation, le matériau présente un déchargement élastique. La macrofissure se développe dans la zone de localisation et croît progressivement à travers l'échantillon, ce qui provoque la chute progressive de la capacité portante, jusqu'à ce que la séparation complète. Autrement, la macrofissure ne se développe pas de façon continue d'un côté à l'autre de l'échantillon, elle peut être formée à partir des mécanismes de pontage et de branchement. Ou à l'inverse, la macrofissure peut se développer à partir d'un côté, et à un moment il pourrait alors se bifurquer et puis se coalescer pour atteindre l'autre côté de l'échantillon.

La rupture des structures en matériaux quasi-fragiles présente un effet d'échelle, i.e. la résistance nominale et énergie nominale de rupture de ces structures dépendent fortement de leur taille. L'analyse de l'effet d'échelle est d'intérêt parce que souvent le comportement des structures réelles est estimé à partir des essais de structures de taille petite au laboratoire.

Diverses théories ont été développées et proposées pour expliquer l'effet d'échelle. Weibull (1939) est la première personne, qui a tenté d'expliquer l'effet d'échelle sur la résistance du matériau basée sur la théorie statistique. En fait, il a suggéré que plus la structure est large plus la probabilité de rencontrer dans son volume un élément matériel avec une faible résistance qui peut conduire à une rupture complète. Cette approche, la théorie de Weibull, est également connue comme la théorie du maillon faible.

Compte tenu de la redistribution de contrainte et la restitution de l'énergie en raison de la croissance des micro- et macro-fissures, Bažant (1984) a proposé une loi de l'effet d'échelle (SEL), à savoir, la loi de l'effet d'échelle énergétique déterministe. Une autre explication pour les effets d'échelle basée sur la géométrie fractale des les surfaces de rupture (à l'état final) a été proposée par Carpinteri and Ferro (1994) and Carpinteri et al. (1995). Ils ont supposé une multifractalité pour la microstructure endommagée du matériau et ont proposé la loi d'échelle multifractale (MFSL). La Figure B.3 montre les trois précédentes théories des effets d'échelle avec la gamme de la majorité des données expérimentales (jusqu'à présent !). Le domaine expérimental est petit par rapport aux structures à échelle réelle. D'autre part, ces théories sont toutes phénoménologiques. Soit la géométrie structurale, rôle du développement des microfissures soit la rugosité de la fissure ne peut pas être prise en considération par ces approches. Il a été largement reconnu que l'effet d'échelle semble dépendre non seulement de la microstructure du matériau, e.g., la forme ou la densité des agrégats, mais aussi sur des conditions aux limites i.e. les effets structuraux. Par conséquent, il semble que la modélisation numérique est intéressante lorsqu'on traite des structures à grande échelle dans les deux cas : (i) soit modéliser directement des structures à grande échelle pour obtenir la résistance nominale avec des lois de comportement représentant l'effet d'échelle, soit (ii) modéliser seulement des structures à petite échelle, mais les résultats numériques doivent reproduire des effets d'échelle fiables pour l'extrapolation à des structures à grande échelle.

1.2 Modélisation des comportements macroscopiques des matériaux quasi-fragiles

Pour modéliser la rupture des matériaux quasi-fragiles, la méthode des éléments fins (MEF) est un outil qui est généralement utilisé. La MEF décrit le matériau comme un milieu continu et la non-linéarité est implantée à l'aide des comportements adoucissants mesurés.

1.2.1 Modèles d'endommagement isotropes

Sous l'hypothèse que le coefficient de Poisson reste constant tout au long de l'évolution de l'endommagement, un matériau adoucissant peut être décrite par un modèle d'endommagement isotrope qui spécifie la relation contrainte-déformation en (Lemaître, 1996)

$$\boldsymbol{\sigma} = (1 - d)\mathbf{C} : \boldsymbol{\varepsilon} \tag{B.1}$$

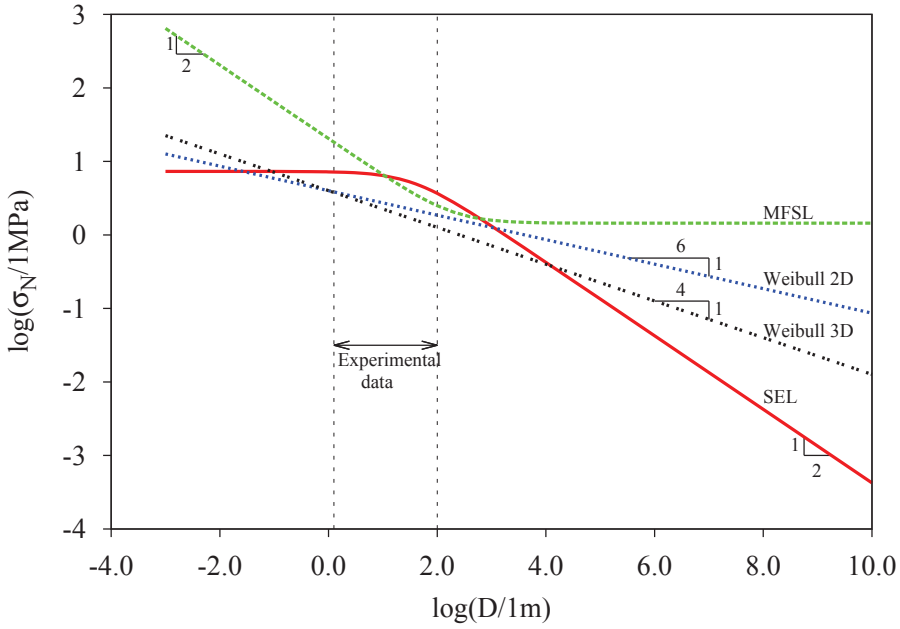

FIGURE B.3 – Représentation des lois de l'effet d'échelle.

avec d la variable scalaire d'endommagement et $\mathbf{C}$ le tenseur de rigidité élastique du quatrième ordre. La variable d'endommagement se développe à partir de 0 (matériau intact) à 1 (matériau complètement endommagé) selon une loi d'évolution de l'endommagement telle que

$$d = d(\kappa) \tag{B.2}$$

dans lequel κ est la variable d'historique qui représente la plus grande déformation jamais atteinte lors de l'histoire de chargement. La variable d'histoire κ est définie par une surface de charge f

$$f(\tilde{\varepsilon}, \kappa) = \tilde{\varepsilon} - \kappa \tag{B.3}$$

avec $\tilde{\varepsilon}$ la fonction scalaire du tenseur de déformation $\boldsymbol{\varepsilon}$. La surface de charge f définit une surface élastique, i.e., l'ensemble des états pour lesquels les endommagements n'évoluent pas. L'endommagement n'augmente que lorsque le seuil actuel de déformation (la plus grande déformation actuelle) κ est dépassée, i.e., l'endommagement ne change pas au cours d'une étape de déchargement ou un stade de chargement élastique. Cela se traduit mathématiquement par la condition de Kuhn-Tucker :

$$f \leq 0, \quad \dot{\kappa} \geq 0, \quad \dot{\kappa} f = 0 \tag{B.4}$$

Différents modèles d'endommagement se distinguent en spécifiant différentes lois d'évolution d'endommagement (B.2) et différente définition de la déformation équivalente $\tilde{\varepsilon}$. Mazars (1984) a proposé la définition

$$\tilde{\varepsilon} = \sqrt{\sum_{i=1}^{3} (\langle \varepsilon_i \rangle_+)^2} \tag{B.5}$$

avec ε_i les déformations principales et les crochets de McCauley $\langle x \rangle_+$ désigne la partie positive d'un scalaire x, ce qui signifie $\langle x \rangle_+ = \max(x, 0)$.

Il y a aussi autres formulations de la déformation équivalente et de la loi d'évolution de l'endommagement, voir de Vree et al. (1995) and Peerlings et al. (1998). Cependant, tous ces modèles d'endommagement isotropes, lorsqu'ils sont implémentés dans un code de MEF, souffrent de la sensibilité de maille i.e., la propagation de la fissure est dépendante de la finesse du maillage. Pour y remédier, la théorie de continuum nonlocal est appliquée aux modèles d'endommagement.

1.2.2 Modèles d'endommagement nonlocaux

Il existe principalement deux formulations nonlocales du modèle d'endommagement, i.e., *nonlocal intégral* et *nonlocal en gradient*.

Modèle nonlocal intégral La valeur locale $\tilde{\varepsilon}$ dans la fonction de chargement (B.3) est remplacée par sa définition nonlocale correspondante comme

$$\bar{\varepsilon}(\mathbf{x}) = \frac{1}{V_r(\mathbf{x})} \int_\Omega \psi(\mathbf{x}, \boldsymbol{\xi}) \tilde{\varepsilon}(\boldsymbol{\xi}) \, \mathrm{d}\boldsymbol{\xi} \quad \text{with} \quad V_r(\mathbf{x}) = \int_\Omega \psi(\mathbf{x}, \boldsymbol{\xi}) \, \mathrm{d}\boldsymbol{\xi} \tag{B.6}$$

où $\psi(\mathbf{x}, \boldsymbol{\xi})$ est une fonction de poids nonlocale qui dépend de la distance entre la « source » $\boldsymbol{\xi}$ et le « récepteur » $\mathbf{x}$, $r = \|\mathbf{x} - \boldsymbol{\xi}\|$. La variable d'histoire κ est alors la plus grande valeur précédemment atteinte de la déformation équivalente nonlocale.

Plusieurs formes ont été proposées pour la fonction de pondération. Il est souvent considéré comme la fonction de distribution gaussienne

$$\psi(\mathbf{x}, \boldsymbol{\xi}) = \exp\left(-\frac{4r^2}{\ell_c^2}\right) \tag{B.7}$$

avec ℓ_c une longueur interne du modèle qui reflète la caractéristique de non-localité du modèle.

Basé sur le travail de Pijaudier-Cabot and Dufour (2010) montrant que la non-localité correspond à une redistribution de contrainte due à la présence de défauts, Giry et al. (2011) a proposé un modèle d'endommagement nonlocal dans lequel l'interaction nonlocale, i.e. la longueur interne, évolue dans le temps en fonction de l'état de contrainte des points matériels voisins. La fonction de poids proposée par Giry et al. (2011) a la même forme que (B.7) mais la longueur interne ℓ_c a été proposée comme

$$\ell_c = \ell_{c0} \cdot \rho(\mathbf{x}, \boldsymbol{\sigma}_{prin}(\boldsymbol{\xi})) \tag{B.8}$$

où ℓ_{c0} est la longueur intrinsèque qui peut être corrélée avec la taille des agrégats, ρ représente l'évolution de la longueur interne au cours du processus d'endommagement et dépend de l'état de contrainte principale du point situé à $\boldsymbol{\xi}$.

Modèle nonlocal en gradient Il existe deux formulations de la régularisation en gradient le modèle *explicite* et celui *implicite*. Les modèles d'endommagement en gradient ont été proposés par Peerlings et al. (1996, 1998). La déformation équivalente nonlocale est définie sous la formulation explicite comme

$$\bar{\varepsilon} = \tilde{\varepsilon} + l^2 \nabla^2 \tilde{\varepsilon} \tag{B.9}$$

où l est un paramètre du matériau avec la dimension de la longueur. Avec la formulation implicite, la déformation équivalente nonlocale est définie comme

$$\bar{\varepsilon} - l^2 \nabla^2 \bar{\varepsilon} = \tilde{\varepsilon} \tag{B.10}$$

En résumé, le point commun des modèles nonlocaux est l'introduction d'une longueur interne. La question doit être posée est que comment déterminer le lien entre la longueur caractéristique du matériau (e.g., la taille des agrégats) et la longueur interne du modèle nonlocal.

1.2.3 Valeur de la longueur interne

Physiquement, la longueur interne est liée à la taille effective de la FPZ dont l'évolution dépend (au moins) des détails de microstructure du matériau et du mécanisme de rupture spécifique qui se développe pour un type donné de chargement (Jirásek et al., 2007; Giry et al., 2011).

La longueur interne ne peut pas être mesurée directement mais peut être indirectement déduite de résultats expérimentaux. Par exemple, la longueur interne peut être déterminée par analyse inverse

sur la base de calculs des essais de l'effet d'échelle (Bellégo et al., 2003) ou par comparaison de l'énergie dissipée dans les deux types d'essais de traction : (i) ceux menant à des endommagements localisés et (ii) ceux où l'endommagement reste distribué (Bažant and Pijaudier-Cabot, 1989). Cependant, la première procédure nécessite un nombre important de calculs et est toujours basé sur une technique d'essai-erreur manuelle et est réalisée pour une gamme de taille limitée des échantillons alors que la dernière procédure présente la sensibilité aux conditions aux limites où la condition que la déformation reste homogène tout au long de l'échantillon est difficile (voire impossible) à assurer. En outre, de telles procédures ne sont basées que sur une hétérogénéité caractéristique du matériau et conduisent à des observations que la longueur interne est proportionnelle à la taille caractéristique D_0 dans la courbe de l'effet d'échelle ou de la taille maximale des agrégats $d_{\max}$. Ainsi, elles peuvent difficilement être considérées comme une règle générale.

Une autre technique pour déterminer la longueur interne qui est basée sur des expériences avec l'analyse par émission acoustique (Maji and Shah, 1988). Haidar et al. (2005) a montré que la FPZ s'élargit au cours des processus de dégradation. Cela a conduit à l'idée que la longueur interne ne dépend pas seulement des aspects géométriques du matériau, mais aussi de la déformation/contrainte.

Toutes ces raisons expliquent le fait que le calage de la longueur interne des modèles nonlocaux est toujours une question difficile car elle semble dépendre non seulement de l'hétérogénéité du matériau, mais aussi des conditions aux limites et de contrainte et de déformation dans la FPZ.

Jusqu'à présent, aucune relation explicite entre la longueur interne et la longueur caractéristique du matériau a été élaborée pour les modèles nonlocaux. Cela motive à développer un modèle numérique qui n'introduit pas de longueur interne et peut affranchir ce paramètre en introduisant explicitement des agrégats dans la description géométrique. De plus, grâce à ce modèle, une étude de l'influence de la microstructure du matériau sur ses comportements aux deux régimes de prépic et postpic peut être réalisée. Nous tirons alors une longueur interne nécessaire pour le continuum nonlocal (type intégral ou gradient) à partir de la microstructure du matériau. Le modèle parlant appartient à la classe des modèles discrets qui sont présentés par la suite.

1.3 Approches discrètes

Pour la modélisation des comportements des matériaux quasi-fragiles, il existe au moins trois types de méthodes numériques discrètes que l'on peut citer ici : (i) la méthode des éléments discrets, (ii) la dynamique moléculaire, and (iii) le modèle de lattice.

La méthode des éléments discrets (MED) a été initiée par Cundall and Strack (1979). Le concept de MED, c'est que le milieu est divisé en un assemblage d'éléments géométriques rigides ou déformables tels que des disques, des ellipses, des polygones (en deux dimensions) ou des sphères, des ellipsoïdes, des polyèdres (en trois dimensions), etc. Chaque élément a un mouvement qui est régi par les principes fondamentaux de la dynamique, issus de la deuxième loi de Newton et par les lois d'interaction intergranulaires. Ayant le même concept que MED mais la dynamique moléculaire (DM) a des atomes et des molécules comme les éléments de base. Les méthodes de MED et DM sont relativement faciles à comprendre parce qu'elles sont basées sur la solution numérique de la deuxième loi de Newton. Elles ont été largement appliquées avec succès. Toutefois, les simulations longues de DM et MED sont mathématiquement mal conditionnés, générant des erreurs cumulées dans les calculs numériques. Les MED et DM sont les plus appropriées pour les matériaux granulaires non cohérents comme le sable.

Les modèles de lattice pour les matériaux hétérogènes dérivent de la méthode des éléments en treillis (Lattice element method–LEM) qui est basé sur la discrétisation de treillis du milieu (Radjai et al., 2010). Tout comme MED, pour les problèmes dans lesquels les discontinuités sont dominants, les modèles de lattice sont considérés comme un outil approprié, car ils fournissent une représentation discrète de l'hétérogénéité matérielle et de la rupture. Cependant, les modèles de lattice, par rapport à MED, sont appropriés pour la modélisation de la fracture de matériaux granulaires *cohésives* tels que le béton et ont un avantage majeur en termes de calculs numériques.

Dans cette thèse, nous nous concentrons principalement sur le mode I de rupture du matériau soumis à des charges mécaniques monotones. Un modèle de lattice, dans lequel les ressorts normales et de cisaillement sont introduits, est entièrement développé en trois dimensions pour des applications à la fois en deux et trois dimensions. Le modèle comprend également une estimation plus réaliste des sections transversales assignées aux éléments de lattice pour mieux refléter la mésostructure aléatoire du matériau.

1.4 Approches multi-échelles

La modélisation multi-échelle des matériaux hétérogènes est effectuée soit dans le cadre de « méthodes d'homogénéisation » ou dans le cadre de « méthodes concurrentes ». Dans le premier, les modèles incluent plusieurs échelles de longueur qui sont complètement séparées et dans le second, les échelles restent couplées.

L'hypothèse principale des techniques d'homogénéisation est l'existence du volume élémentaire représentatif (VER). Cependant, lorsqu'il s'agit de la localisation des déformations et des phénomènes de rupture dans les matériaux adoucissants, un VER pour le régime adoucissant ne peut pas être trouvé puisque le matériau perd homogénéité statistique sur la localisation des déformations (Gitman et al., 2008; Bažant, 2010).

Plusieurs stratégies ont été proposées pour remédier ces problèmes tels que l'homogénéisation du second ordre (Kouznetsova et al., 2002; Kaczmarczyk et al., 2008), l'approche de volume couplé (Gitman et al., 2008), la méthode de discontinuités d'agrégation multi-échelles (Belytschko and Song, 2010). Toutefois, le principal inconvénient de toutes ces techniques est qu'elles fournissent une représentation simplifiée de rupture i.e., les fissures, la localisation des déformations, etc., à l'échelle macroscopique.

Les techniques multi-échelles concurrentes sont caractérisées par la résolution *simultanée* des échelles macroscopique et méso/microscopique. Cela signifie que les échelles sont couplées dans le même cadre et donc, l'équilibre global et la compatibilité de déplacement doivent être assurés sur l'ensemble de la structure, voir e.g. Garikipati (2002), Larsson and Runesson (2008), and Mergheim (2009).

Chapitre 2
Modèle de lattice pour la rupture du béton

Le modèle de lattice est une méthode numérique basée sur une discrétisation d'un milieu continu par des éléments à une dimension (1D) qui permet de transférer des charges, voir Figure B.4a. Les lois de comportement des éléments 1D sont des relations élastiques linéaires dans les directions normale et tangentielle définies par chaque élément. Si le système subit de très petites perturbations autour de son état initial, les positions des nœuds sont supposées fixes et des variables inconnues sont les déplacements des nœuds $\vec{u}$. La direction axiale $\vec{n}_0^{ij}$ et la direction transversale $\vec{t}_0^{ij}$ associées à chaque élément ij restent ainsi fixées. Les variations de longueur entre le nœud i et j sont définies par $\delta_n^{ij} = (\vec{u}_i - \vec{u}_j) \cdot \vec{n}_0^{ij}$ et $\delta_t^{ij} = (\vec{u}_i - \vec{u}_j) \cdot \vec{t}_0^{ij}$ pour les directions normales et tangentielles, respectivement. Les forces sont liées à ces variations de longueur par $f_n^{ij} = K_n^{ij}\,\delta_n^{ij}$ et $f_t^{ij} = K_t^{ij}\,\delta_t^{ij}$, où K_n^{ij} et K_t^{ij} sont les raideurs normales et de cisaillement de l'élément, respectivement.

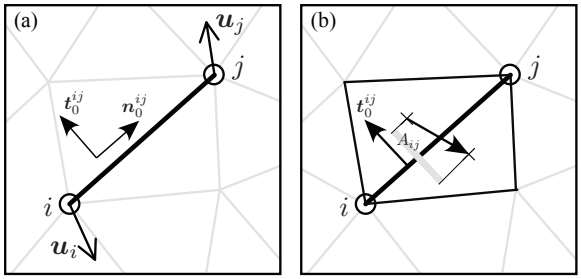

FIGURE B.4 – Elément 1D avec son système de coordonnées local (a) et sa largeur effective A^{ij} (b).

L'approche consiste à trouver l'ensemble des déplacements des nœuds $[\vec{u}]$ – dont certains sont imposés – qui minimisent l'énergie élastique totale du système :

$$\mathcal{U}_e([\vec{u}]) = \frac{1}{2} \sum_{ij} \left\{ K_n^{ij} (\delta_n^{ij})^2 + K_t^{ij} (\delta_t^{ij})^2 \right\} \tag{B.11}$$

Pour faire cette minimisation, la méthode du gradient conjugué est utilisée avec la définition suivante du gradient :

$$\frac{\partial \mathcal{U}_e}{\partial u_i^\alpha} = -\vec{e}_\alpha \cdot \sum_{j,\ i \in ij} \left\{ K_n^{ij}\,\delta_n^{ij}\,\vec{n}_0^{ij} + K_t^{ij}\,\delta_t^{ij}\,\vec{t}_0^{ij} \right\} \tag{B.12}$$

où $\vec{e}_\alpha$ représente les deux directions du système de coordonnées global.

L'endommagement du système de lattice est pris en compte en enlevant chaque élément qui casse selon un critère $\psi(f_n^{ij},\ f_t^{ij}) \geq 0$. Parce que le béton es très faible en résistance à la traction par rapport à sa résistance au cisaillement, la surface de Mohr-Coulomb avec une coupure de la résistance à la traction (Bolander Jr. and Saito, 1998) peut être adoptée. Cependant, nous avons choisi d'utiliser une autre surface qui a l'avantage d'être plus générique alors qu'elle est exprimée dans une seule fonction :

$$\psi(f_n^{ij},\ f_t^{ij}) = \frac{f_n^{ij}}{A^{ij}\sigma_n^0} + \left(\frac{f_t^{ij}}{A^{ij}\sigma_t^0} \right)^n - 1 \tag{B.13}$$

où σ_n^0 et σ_t^0 sont les seuils de contraintes normale et tangentielle, respectivement ; n est un paramètre positif qui modifie la surface de charge à partir d'une forme linéaire ($n = 1$) – correspondant au critère de Mohr-Coulomb classique – en une forme non-linéaire ($n > 1$).

Les hétérogénéités du matériau sont introduites par une structure des inclusions. La dernière peut être générée par le processus « take-and-place » (Wang et al., 1999; Häfner et al., 2006). Après la

génération de la structure d'inclusions, les différentes phases de matériau sont définies et différentes propriétés mécaniques locales sont affectées à des éléments tombant dans chaque phase. A l'échelle mésoscopique, trois phases peuvent être distinguées : l'inclusion, la matrice et la zone de transition d'interface (ITZ), voir Figure B.5. Si les deux extrémités de l'élément sont situées dans la même phase, cet élément est attribué les mêmes propriétés mécaniques de la phase correspondante (inclusion ou matrice), sinon il est considéré comme l'élément d'interface ou d'inclusion en fonction du emplacement de son point médian. Si son point médian se trouve dans le grain, l'élément est classé comme élément d'inclusion, ou bien il sera classé comme élément ITZ. La raison de cette définition de l'élément ITZ, c'est que la fraction résultante d'inclusions (le rapport entre le nombre d'éléments d'inclusion et le nombre total d'éléments) est plus proche de la fraction désirée des inclusions en matériau que celles développées par d'autres auteurs (Schlangen and van Mier, 1992a; Lilliu and van Mier, 2003; Sagar and Prasad, 2009). Dans leurs modèles, tous les éléments qui relient deux zones différentes de structures de grains sont considérés comme des éléments ITZ.

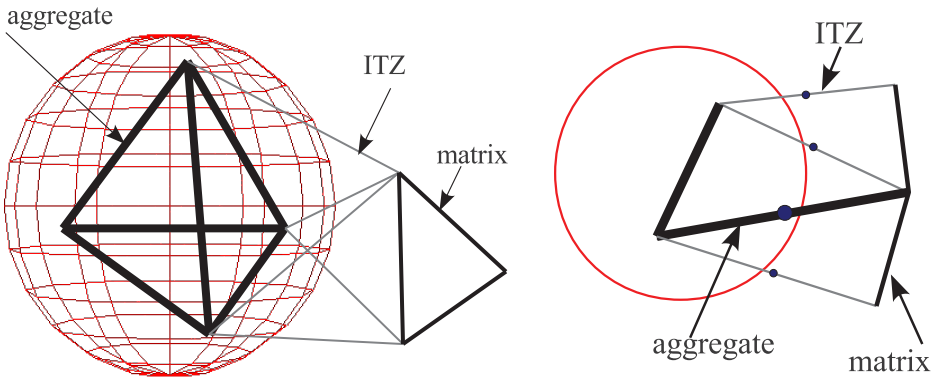

FIGURE B.5 – Distinction entre l'inclusion, la matrice et la phase ITZ selon l'emplacement d'un élément de lattice dans la particule (a) ; Définition de l'élément de l'inclusion ou élément d'ITZ en fonction de la localisation du point médian de l'élément (b).

Chapitre 3
Étude de l'origine de la longueur caractéristique et la taille de la FPZ

Pour étudier le rôle joué par des plus grosses inclusions dans la longueur interne, plusieurs simulations ont été effectuées. Dans la modélisation de la mésostructure du matériau, les inclusions sont prises en compte, qui sont noyées dans la matrice séparées par des zones de transition d'interface (ITZ). Les inclusions, la matrice et les ITZs sont supposées être linéaires élastiques fragiles. Les inclusions sont également supposées être plus rigides et plus résistantes que la matrice, alors que les ITZs sont supposées être moins rigides et ayant une résistance inférieure à celle de la matrice. Dans les simulations suivantes, la rigidité et la résistance des inclusions est de 10 fois plus grandes que celles de la matrice. À son tour, la rigidité et la résistance de la matrice est de 2 fois plus grandes que celles de ITZs. Les paramètres élastiques et de résistance de la matrice sont donnés dans le tableau B.1, et ils sont maintenus fixes pour toutes les simulations.

TABLE B.1 – Paramètres élastiques et de résistance utilisés pour la phase de matrice. Module de Young et le coefficient de Poisson au niveau macroscopique sont également indiqués.

Phase φ	$\bar{K}_n$ (GPa)	$\bar{K}_t$ (GPa)	σ_n^0 (MPa)	σ_t^0 (MPa)	E (GPa)	ν (–)
Matrix	16.50	5.10	6.07	18.21	13.20	0.20

Deux types de la structure des inclusions sont étudiées : monodispersité et polydispersité. Dans le premier cas, la façon que les inclusions sont structurées est limitée à deux caractéristiques : le diamètre de grain d et leur fraction volumique P_a. Dans l'espace des paramètres $P_\mathrm{a} - d$, voir Figure B.6, trois chemins de variation sont envisagés :

(*I*) varier d tandis que les positions des inclusions restent les mêmes, P_a varie donc à peu près comme d^2,

(*II*) varier d tandis que P_a est maintenue à 40%[1],

(*III*) varier P_a pour un diamètre donné de l'inclusion $d = 8$ mm.

Dans le cas de polydispersité, quatre types de la structure d'inclusions sont générés dans lesquels la taille minimum de l'inclusion $d_\mathrm{min} = 3.15$ mm et la taille maximum de l'inclusion d_max est variée en prenant les valeurs de 6.3, 8, 10 and 12.5 mm tout en conservant la fraction volumique de « référence » des inclusions constante à 40%. Ce chemin de variation est noté le chemin (*IV*), voir Figure B.7.

Différentes caractéristiques de la mésostructure telles que la présence ou non de la zone d'interface ITZ, l'effet des plus petites inclusions, la taille et la fraction volumique des inclusions qui peuvent influencer sur la taille de la FPZ sont analysées. En outre, les influences des paramètres structuraux comme la taille, la forme des échantillons, la manière que les charges sont appliquées (via des barres métalliques ou tirer directement sur les échantillons) et la taille du ligament sont aussi étudiées.

Le résultat montre que lorsque la ITZ est prise en compte, la taille des inclusions joue un effet plus fort sur la variation de la taille de la FPZ que le cas dans lequel la ITZ n'est pas prise en considération. Lorsque les agrégats fins sont pris en compte dans le modèle, un effet plus important de la taille des agrégats grossiers sur la taille et la variation de la FPZ est obtenu. Ce résultat peut nous conduire à penser, par extrapolation, que si le matériau est modélisé avec la mésostructure plus complexe, l'effet des agrégats grossiers à la taille de la FPZ pourrait être encore plus grand.

[1]Notez cependant que la fraction de surface des inclusions n'est pas exactement maintenue constante à 40% lors du changement de la taille de l'inclusion. Ceci est dû au fait que plus la taille de l'inclusion, plus le nombre de particules sont nécessaires, ce qui entraîne un plus grand nombre d'éléments de ITZ et conduisant donc à un plus petit nombre d'éléments d'inclusion.

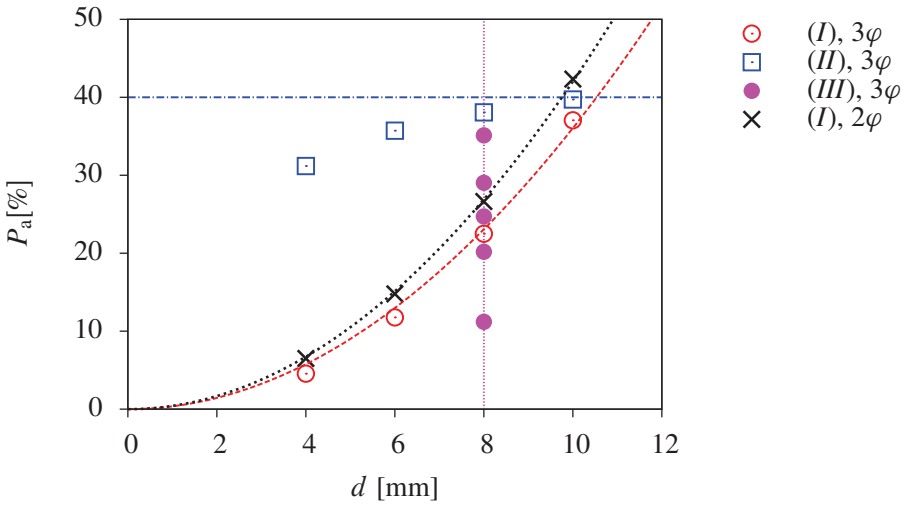

FIGURE B.6 – Trois chemins de variation (*I*), (*II*) and (*III*) pour le matériau de trois phases (3φ) et le chemin de variation (*I*) pour le matériau deux phases (2φ) dans l'espace de paramètres (P_a – d) dans le cas de distribution monodisperse de la structure des inclusions.

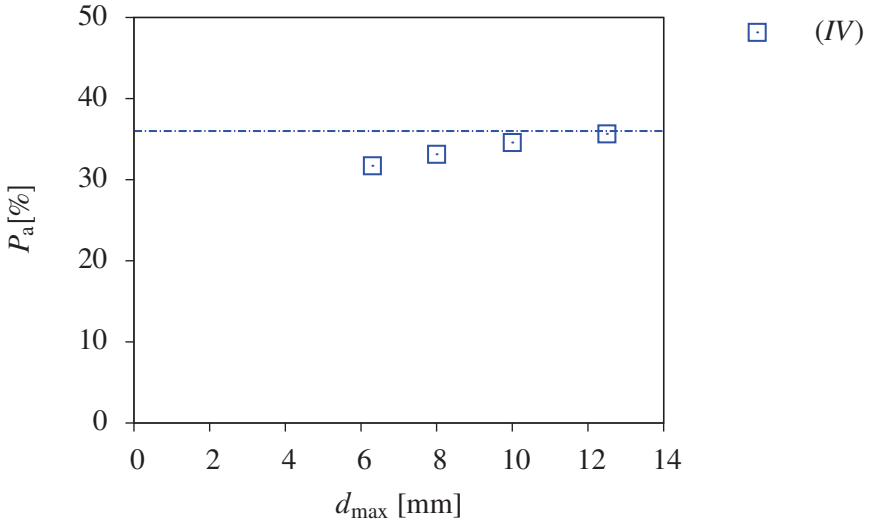

FIGURE B.7 – Le chemin de variation (*IV*) dans l'espace de paramètres (P_a – d_{max}).

Les analyses sur les influences de la taille et de la forme des échantillons montre que la relation entre la taille de la FPZ et la taille des inclusions est également influencée par la taille de l'échantillon ou en général des conditions aux limites qui résultent en différents champs de gradient de contrainte et de rotation du matériau. L'effet des conditions aux limites sur la taille de la FPZ pourrait s'expliquer par le fait que l'intensité du gradient de contrainte et la non-uniformité de la déformation pour les échantillons sont plus ou moins importantes. En fait, quand il existe un gradient de contrainte intense qui consiste dans les échantillons, la position de rupture est fortement imposée qui amène la FPZ en étant plus étroite que dans le cas d'un faible gradient de contrainte. Et lorsque la non-uniformité de la déformation est importante à travers la section transversale des échantillons, elle se traduit par une rotation relative de la partie supérieure et la partie inférieure des échantillons séparées par la macrofissure et donc cela provoque le changement de la direction principale de la charge qui permet probablement la FPZ d'évoluer dans une zone plus large.

Après l'étude des essais de traction sur une éprouvette de taille fixe en un matériau de modèle élastique fragile avec des inclusions variées selon les chemin de variation (*I*) et (*II*), les résultats mettent en évidence que la taille de la FPZ ℓ_{FPZ} est liée aux caractéristiques de la structure des inclusions, y compris leur taille, leur répartition/position, leur fraction volumique ainsi que la distance entre les inclusions. Selon la situation, l'une des caractéristiques prévaut. Quoi qu'il en soit, la répartition spatiale des inclusions impacts toujours ℓ_{FPZ}, et cela est exposé *via* l'écart-type non-nul des tailles de la FPZ. Si la distance entre les inclusions est maintenue constante en maintenant la fraction volumique de référence des inclusions inchangée tout en modifiant la taille des inclusions, la valeur moyenne de ℓ_{FPZ} semble être indépendante de la taille des inclusions. Lorsque la fraction volumique/la distance entre les inclusions change due à la variation de la taille des inclusions tout en gardant la même position pour les différentes tailles des inclusions, la valeur moyenne de ℓ_{FPZ}, prise par la moyenne des tailles de la FPZ obtenues par des distributions aléatoires des inclusions de la même taille, augmente avec l'augmentation de la taille des inclusions.

L'étude de l'influence de la taille du ligament sur la taille de la FPZ est effectuée. On voit que, pour la taille de ligament en dessous d'une moitié de la largeur de l'éprouvette, la pente de la variation de la FPZ en fonction de la taille des inclusions est négligeable, ce qui signifie que la taille des inclusions ne semble avoir aucune influence sur la valeur moyenne de ℓ_{FPZ}. Entre ces limites, la pente de variation évolue progressivement, ce qui indique à la fois la structure d'inclusions et la dimension de l'échantillon elle-même peuvent jouer un rôle sur la taille de la FPZ. Tout peut suggérer que la FPZ n'est pas complètement développée dans les échantillons avec le ligament « trop petit ».

L'étude de l'influence de la mésostructure sur la longueur caractéristique du matériau est également effectuée. L'observation principale est que la longueur caractéristique et la largeur de la FPZ ont le même ordre de grandeur et la même tendance par rapport à la taille des inclusions.

À partir de toutes ces études, les conclusions suivantes peuvent être tirées :

- Il apparaît que non essentiellement la taille, mais les autres paramètres caractérisant la structure des inclusions du matériau telle que la fraction volumique, la dispersion de taille, le tissu, la connectivité, et les propriétés d'interface… affectent fortement la taille de la FPZ, et ainsi la longueur caractéristique du matériau.

- La valeur mesurée de la taille de la FPZ dépend également du champ de la contrainte locale et/ou du gradient de contrainte qui peut être lié à la géométrie de l'éprouvette ou des conditions aux limites, par exemple. Par conséquent, il est difficile d'éviter la conclusion que la taille de la FPZ n'est pas une propriété intrinsèque du matériau comme on le croit généralement. Cependant, il semble vrai que la taille de la FPZ reste dans le même ordre de grandeur quand le système testé est le même (la mésostructure, la géométrie, les dimensions, et les conditions de chargement…).

- L'évaluation de la longueur caractéristique du matériau est essentielle pour l'utilisation de la valeur comme étant la longueur interne dans les modèles nonlocaux. Cependant, tout comme

la taille de la FPZ, il est difficile d'éviter des effets de structure de la méthode de mesure de la longueur caractéristique.

Chapitre 4
Couplage multi-échelle

Ce chapitre traite du couplage entre l'approche continue et l'approche discontinue pour la simulation de rupture des matériaux quasi-fragiles. Les méthodes numériques utilisées pour les modèles continue et discret sont la méthode des éléments finis (MEF) et la méthode des éléments de lattice (LEM), respectivement. Cela est tout à fait pertinent sachant qu'il est inutile de modéliser par des éléments de lattice, coûteux en terme de résolution numérique, l'ensemble d'une structure alors que les zones endommagées sont généralement localisées, et leur position peut-être connue.

Puisque une cellule de lattice ne produit pas la même matrice de rigidité en tant qu'un élément fini (EF) de la même taille, même si ils peuvent représenter macroscopiquement un matériau ayant les mêmes paramètres élastiques telles que le module d'Young et le coefficient de Poisson. Par conséquent, nous proposons un algorithme dans lequel la structure est aussi initialement modélisée par la MEF, mais la matrice de rigidité d'un EF n'est pas construite par intégration sur le volume/ la surface de cet EF, mais elle est calculée au moyen d'une *procédure d'homogénéisation* sur une cellule LEM de la même taille. Les EFs où le comportement reste inférieure à un seuil, le matériau est supposé de se comporter de manière élastique et les matrices de rigidité initiales sont conservées. Le EF, lorsque le seuil est dépassé, est remplacé par une cellule LEM sur laquelle une mise à jour de la matrice de rigidité est effectuée au moyen d'une analyse nonlinéaire de la cellule LEM lorsque les noeuds de frontière de la cellule LEM sont retenus par le champ de contrainte au niveau des bords des éléments finis voisins. Ensuite, le champ de contraintes aux bords de la cellule LEM est transféré aux éléments finis voisins. Quand une cellule LEM est complètement fissurée, un événement de zoom arrière est effectué et la cellule LEM fissurée est remplacée par deux nouveaux EF obtenus à partir d'une décomposition du EF correspondant. La continuité des déplacements entre les cellules LEM et MEF est assurée par la méthode « maître/esclave » (Belytschko et al., 2000).

La méthode multi-échelle proposée permet le solveur de traiter avec différents modèles d'une manière adaptative par le couplage simultané. Elle est basée sur la méthode de la décomposition de domaine FETI-DP (Farhat et al., 2000, 2001), elle permet alors de traiter les structures à grande échelle par des calculs parallèles.

Dans ce travail, tout d'abord l'approche LEM est implantée dans le logiciel open-source SOFA. Puis, l'algorithme de couplage avec l'approche MEF est proposé et implanté. Une des raisons pour lesquelles SOFA est utilisé dans la thèse est qu'il est basé sur la philosophie open-source qui nous permet à améliorer/modifier/réutiliser librement la base de code existante et mettre en œuvre un nouveau modèle comme un plugin.

Les conclusions suivantes peuvent être tirées à partir de l'algorithme de couplage proposé entre le modèle de lattice et l'approche par éléments finis :

- L'algorithme de couplage LEM-MEF est proposé dans une manière adaptative. Cela signifie que l'approche LEM n'est pas présente dans la zone dans laquelle la FPZ est connue à l'avance, mais que la FPZ évolue, un EF est remplacé par une cellule de lattice de même taille pour l'analyse non linéaire du comportement du matériau.

- L'algorithme de couplage est prévu pour des calculs parallèles.

- L'algorithme proposé est un couplage fort. Cela signifie que la continuité du champ de déplacement de l'interface de couplage est assuré par l'algorithme « maître/esclave ». Les déplacements de translation et de rotation des noeuds du lattice sur l'interface de couplage sont retenus par le champ de déplacement et le vecteur de rotation du tenseur antisymétrique qui dérive du déplacement du EF, respectivement. Le champ de contrainte au niveau du couplage de l'interface de la cellule de lattice est transféré aux EFs voisins. Il n'existe pas un comportement nonlinéaire homogénéisé de l'approche de lattice qui est introduit dans un point d'intégration du EF comme des travaux proposés par d'autres auteurs qui sont des faibles couplages.

Cependant, la mise en œuvre de la procédure de couplage proposée dans SOFA est encore limitée au couplage élémentaire. Il nécessite des travaux futurs afin d'implanter l'algorithme complet dans SOFA.

Conclusions et perspectives

Dans la thèse, nous avons souligné que les modèles de lattice sont de très bons candidats pour modéliser le mécanisme de rupture des matériaux quasi-fragiles comme le béton. En utilisant les modèles de lattice à l'échelle mésoscopique, il n'est pas nécessaire d'introduire une longueur interne et ils ont de nombreux avantages indiqués précédemment dans le rapport. La mesotructure du matériau peut être introduite de manière explicite. Cependant, en utilisant les modèles de lattice à l'échelle mésoscopique, en particulier pour les structures 3D à grande échelle, il exige des efforts énormes de calcul en raison d'un grand nombre de degrés de liberté. Par conséquent, une approche multi-échelle réalisée par un couplage entre approche discrète à l'échelle mésoscopique traitée par une approche de lattice et l'approche continue à l'échelle macroscopique traitée par la méthode des éléments finis est essentielle.

Le modèle de lattice est très simple, car il ne fait que l'utilisation d'une analyse élastique linéaire. Le matériau est représenté comme un réseau d'éléments de lattice. La loi de comportement locale des éléments est élastique fragile.

Deux types d'éléments de lattice sont implantés dans SOFA : des éléments de ressort normal et de cisaillement, et des éléments de poutre. Le modèle de ressort normal et de cisaillement est à l'origine partie de notre code d'auto-écrit en utilisant le langage C++.

À partir de l'outil numérique, nous avons réalisé deux types d'essais de traction numériques : tests de l'endommagement localisé et tests de l'endommagement réparti sur des spécimens en matériau modèle élastique fragile avec des variations de la structure des agrégats (inclusions), des conditions aux limites et la taille des échantillons. La taille de la Fracture Process Zone et la longueur caractéristique du matériau ont été mesurées à partir de ces tests en vue d'étudier l'influence des différents paramètres caractérisant la mesotructure du matériau et du gradient de contrainte et la rotation matérielle (par suite des différentes conditions aux limites et tailles du spécimen) sur leurs valeurs. L'évaluation de la taille de la FPZ ℓ_{FPZ} est obtenue via des tests de l'endommagement localisé tandis que la longueur caractéristique ℓ_{c} est mesurée via les deux tests de l'endommagement localisé et réparti. Les résultats ont été présentés dans Chapitre 3.

Jusqu'à ce que la partie géométrique de la longueur interne est déterminée de manière fiable pour l'utiliser comme une variable interne dans les modèles nonlocaux, nous vous conseillons d'utiliser le modèle de lattice avec une description explicite de la mésostructure du matériau pour mieux simuler et prédire la fracture dans les matériaux quasi-fragiles. Toutefois, comme indiqué, les simulations de l'ensemble d'une structure à grande échelle en utilisant le modèle de lattice à l'échelle mésoscopique nécessite des efforts énormes de calcul et de stockage en raison d'un grand nombre de degrés de liberté. Dans Chapitre 4, nous avons présenté l'algorithme original pour coupler le modèle du lattice de poutre avec des éléments finis dans un cadre multi-échelle afin de réduire l'effort de calcul. Il est le couplage bord à bord et est prévu pour des calculs en parallèle.

Pour la mise en œuvre numérique de l'algorithme proposé dans SOFA, nous avons réalisé le couplage élémentaire. Le couplage *complet* avec les techniques zoom avant, zoom arrière, les critères qui permettent le zoom avant et zoom arrière se produisent, et schéma de calcul parallèle n'ont pas encore été mis en œuvre. Les travaux futurs sur cette implantation sont nécessaires.

Il s'agit d'une première étape pour étudier l'influence des propriétés d'inclusion sur la longueur caractéristique. Plusieurs conclusions qualitatives intéressantes sur le matériau modèle numérique ont déjà été signalés. Pour les travaux futurs, nous prévoyons d'étudier l'effet des propriétés mécaniques, en particulier les rapports des différentes rigidités et des différentes résistances des phases du matériau, sur la taille de la FPZ résultant et la longueur caractéristique du matériau. Les développements futurs viseront également à développer le modèle numérique d'être plus représentatif des matériaux quasi-fragiles, en particulier en béton.

References

[1] Ahrens, J., Geveci, B., and Law, C. “Paraview: An end-user tool for large data visualization”. In: *The Visualization Handbook* 717 (2005), p. 731 (cit. on p. 67).

[2] Aifantis, E. C. “On the microstructural origin of certain inelastic models”. In: *J. Eng. Mater. Technology* 106.4 (1984), pp. 326–330 (cit. on p. 28).

[3] Alexander, K. M., Gilbert, D. J., and Wardlaw, J. “Aggregate-cement bond, cement paste strength and the strength of concrete”. eng. In: *Proceedings of International Conference on The Structure of Concrete*. London, UK: Cement & Concrete Association, 1968, pp. 59–81 (cit. on pp. 8, 172).

[4] Allard, J., Cotin, S., Faure, F., Bensoussan, P.-J., Poyer, F., Duriez, C., Delingette, H., Grisoni, L., et al. “Sofa-an open source framework for medical simulation”. In: *Medicine Meets Virtual Reality, MMVR 15*. 2007 (cit. on p. 67).

[5] Arslan, A., Ince, R., and Karihaloo, B. “Improved lattice model for concrete fracture”. In: *Journal of Engineering Mechanics* 128.1 (2002), pp. 57–65 (cit. on pp. 31, 46, 54).

[6] Arslan, A., Schlangen, E., and Van Mier, J. “Effect of model fracture law and porosity on tensile softening of concrete”. In: *Fracture mechanics of concrete structures (FraMCoS-2). AEDIFICATIO Publishers, Freiburg* (1995), pp. 45–54 (cit. on p. 72).

[7] Aubertin, P., Réthoré, J., and de Borst, R. “A coupled molecular dynamics and extended finite element method for dynamic crack propagation”. In: *International Journal for Numerical Methods in Engineering* 81.1 (2010), pp. 72–88 (cit. on p. 36).

[8] Azevedo, N. M. and Lemos, J. “Hybrid discrete element/finite element method for fracture analysis”. In: *Computer Methods in Applied Mechanics and Engineering* 195.33-36 (2006), pp. 4579–4593 (cit. on pp. 36, 37).

[9] Babuška, I. and Melenk, J. M. “The partition of unity method”. In: *International Journal for Numerical Methods in Engineering* 40.4 (1997), pp. 727–758 (cit. on p. 36).

[10] Bagi, K. “Stress and strain in granular assemblies”. In: *Mechanics of materials* 22.3 (1996), pp. 165–177 (cit. on pp. 69, 70).

[11] Barenblatt, G. I. “The formation of equilibrium cracks during brittle fracture: general ideas and hypothesis, axially symmetric cracks”. In: *Appl. Math. Mech.* 23 (1959), pp. 622–636 (cit. on p. 163).

[12] Bathurst, R. J. and Rothenburg, L. “Observations on stress-force-fabric relationships in idealized granular materials”. In: *Mechanics of Materials* 9.1 (1990), pp. 65–80 (cit. on p. 69).

[13] Bažant, Z. P. “Instability ductility and size effect in strain - softening concrete”. In: *Journal of the Engineering Mechanics Division* 102.2 (1976), pp. 331–344 (cit. on pp. 8, 172).

[14] Bažant, Z. P. “Can Multiscale-Multiphysics Methods Predict Softening Damage and Structural Failure?” In: *International Journal for Multiscale Computational Engineering* 8.1 (2010), pp. 61–67 (cit. on pp. 34, 177).

[15] Bažant, Z. and Oh, B. “Crack band theory for fracture of concrete”. English. In: *Matériaux et Construction* 16 (3 1983), pp. 155–177 (cit. on pp. 88, 166, 167).

[16] Bažant, Z. “Scaling of quasibrittle fracture: asymptotic analysis”. English. In: *International Journal of Fracture* 83 (1 1997), pp. 19–40 (cit. on p. 17).

[17] Bažant, Z. “Scaling of structural strength”. In: *Computational Mechanics* 32.1 (2003), pp. 140–140 (cit. on p. 40).

[18] Bažant, Z. “Size Effect in Blunt Fracture: Concrete, Rock, Metal”. In: *Journal of Engineering Mechanics* 110.4 (1984), pp. 518–535 (cit. on pp. 16, 17, 173).

[19] Bažant, Z., Belytschko, T., and Chang, T. “Continuum theory for strain-softening”. In: *Journal of Engineering Mechanics* 110.12 (1984), pp. 1666–1692 (cit. on p. 168).

[20] Bažant, Z. and Cedolin, L. “Finite element modeling of crack band propagation”. In: *Journal of Structural Engineering* 109.1 (1983), pp. 69–92 (cit. on p. 167).

[21] Bažant, Z. and Jirásek, M. “Nonlocal Integral Formulations of Plasticity and Damage: Survey of Progress”. In: *Journal of Engineering Mechanics* 128.11 (2002), p. 1119 (cit. on p. 27).

[22] Bažant, Z. and Kazemi, M. T. “Size dependence of concrete fracture energy determined by RILEM work-of-fracture method”. English. In: *International Journal of Fracture* 51 (2 1991), pp. 121–138 (cit. on p. 11).

[23] Bažant, Z. and Lin, F. “Nonlocal smeared cracking model for concrete fracture”. In: *Journal of Structural Engineering* 114.11 (1988), pp. 2493–2510 (cit. on p. 27).

[24] Bažant, Z. and Ožbolt, J. “Nonlocal microplane model for fracture, damage, and size effect in structures”. In: *Journal of Engineering Mechanics* 116.11 (1990), pp. 2485–2505 (cit. on p. 27).

[25] Bažant, Z. and Pijaudier-Cabot, G. “Measurement of Characteristic Length of Nonlocal Continuum”. In: *Journal of Engineering Mechanics* 115.4 (1989), pp. 755–767 (cit. on pp. 11, 29, 88, 90, 176).

[26] Bažant, Z. and Planas, J. *Fracture and Size Effect: In Concrete and Other Quasibrittle Materials*. New Directions in Civil Engineering. CRC Press, 1998 (cit. on pp. 10, 130, 163).

[27] Bažant, Z., Tabbara, M., Kazemi, M., and Pijaudier-Cabot, G. “Random particle model for fracture of aggregate or fiber composites”. In: *Journal of Engineering Mechanics* 116.8 (1990), pp. 1686–1705 (cit. on pp. 31, 41).

[28] Bažant, Z., Xi, Y., and Reid, S. “Statistical Size Effect in Quasi-Brittle Structures: I. Is Weibull Theory Applicable?” In: *Journal of Engineering Mechanics* 117.11 (1991), pp. 2609–2622 (cit. on p. 16).

[29] Bellégo, C. L., Dubé, J. F., Pijaudier-Cabot, G., and Gérard, B. “Calibration of nonlocal damage model from size effect tests”. In: *European Journal of Mechanics - A/Solids* 22.1 (2003), pp. 33–46 (cit. on pp. 29, 176).

[30] Belytschko, T. and Black, T. “Elastic crack growth in finite elements with minimal remeshing”. In: *International Journal for Numerical Methods in Engineering* 45.5 (1999), pp. 601–620 (cit. on pp. 35, 36).

[31] Belytschko, T., Liu, W., and Moran, B. *Nonlinear finite elements for continua and structures*. Wiley, 2000 (cit. on pp. 20, 144, 184).

[32] Belytschko, T., Loehnert, S., and Song, J.-H. “Multiscale aggregating discontinuities: A method for circumventing loss of material stability”. In: *International Journal for Numerical Methods in Engineering* 73.6 (2008), pp. 869–894 (cit. on p. 35).

[33] Belytschko, T. and Song, J.-H. “Coarse-graining of multiscale crack propagation”. In: *International Journal for Numerical Methods in Engineering* 81.5 (2010), pp. 537–563 (cit. on pp. 35, 177).

[34] Bensoussan, A., Lions, J.-L., and Papanicolaou, G. *Asymptotic analysis for periodic structures*. Vol. 374. American Mathematical Soc., 2011 (cit. on p. 33).

[35] Bésuelle, P., Desrues, J., and Raynaud, S. "Experimental characterisation of the localisation phenomenon inside a Vosges sandstone in a triaxial cell". In: *International Journal of Rock Mechanics and Mining Sciences* 37.8 (2000), pp. 1223–1237 (cit. on p. 10).

[36] Bolander Jr, J., Hong, G., and Yoshitake, K. "Structural Concrete Analysis Using Rigid-Body-Spring Networks". In: *Computer-Aided Civil and Infrastructure Engineering* 15.2 (2000), pp. 120–133 (cit. on p. 31).

[37] Bolander Jr., J. and Saito, S. "Fracture analyses using spring networks with random geometry". In: *Engineering Fracture Mechanics* 61.5-6 (1998), pp. 569–591 (cit. on pp. 31, 41, 54, 178).

[38] Bordas, S., Nguyen, P. V., Dunant, C., Guidoum, A., and Nguyen-Dang, H. "An extended finite element library". In: *International Journal for Numerical Methods in Engineering* 71.6 (2007), pp. 703–732 (cit. on p. 164).

[39] Bouchard, P., Bay, F., and Chastel, Y. "Numerical modelling of crack propagation: automatic remeshing and comparison of different criteria". In: *Computer Methods in Applied Mechanics and Engineering* 192.35-36 (2003), pp. 3887–3908 (cit. on p. 164).

[40] Bouchard, P., Bay, F., Chastel, Y., and Tovena, I. "Crack propagation modelling using an advanced remeshing technique". In: *Computer Methods in Applied Mechanics and Engineering* 189.3 (2000), pp. 723–742 (cit. on p. 164).

[41] Burt, N. and Dougill, J. "Progressive failure in a model heterogeneous medium". In: *Journal Of The Engineering Mechanics Division-Asce* 103.3 (1977), 365–376 (cit. on p. 31).

[42] Cambou, B., Dubujet, P., Emeriault, F., and Sidoroff, F. "Homogenization for granular materials". In: *European journal of mechanics. A. Solids* 14.2 (1995), pp. 255–276 (cit. on p. 33).

[43] Carpinteri, A. "Post-peak and post-bifurcation analysis of cohesive crack propagation". In: *Engineering Fracture Mechanics* 32.2 (1989), pp. 265–278 (cit. on p. 164).

[44] Carpinteri, A., Chiaia, B., and Ferro, G. "Size effects on nominal tensile strength of concrete structures: multifractality of material ligaments and dimensional transition from order to disorder". English. In: *Materials and Structures* 28 (6 1995), pp. 311–317 (cit. on pp. 17, 173).

[45] Carpinteri, A. and Ferro, G. "Size effects on tensile fracture properties: a unified explanation based on disorder and fractality of concrete microstructure". English. In: *Materials and Structures* 27 (10 1994), pp. 563–571 (cit. on pp. 17, 173).

[46] Castañeda, P. P. "The effective mechanical properties of nonlinear isotropic composites". In: *Journal of the Mechanics and Physics of Solids* 39.1 (1991), pp. 45–71 (cit. on p. 33).

[47] Chaboche, J. "Description thermodynamique et phénoménologique de la viscoplasticité cyclique avec endommagement". PhD thesis. Paris: Université Paris 6, 1978 (cit. on p. 168).

[48] Chang, C. and Ma, L. "Modeling of discrete granulates as micropolar continua". In: *Journal of Engineering Mechanics* 116.12 (1990), pp. 2703–2721 (cit. on p. 41).

[49] Chang, C., Wang, T., Sluys, L., and Van Mier, J. "Fracture modeling using a microstructural mechanics approach—-II. Finite element analysis". In: *Engineering Fracture Mechanics* 69.17 (2002), pp. 1959–1976 (cit. on p. 41).

[50] Chang, C., Wang, T., Sluys, L., and van Mier, J. "Fracture modeling using a micro-structural mechanics approach–I. Theory and formulation". In: *Engineering Fracture Mechanics* 69.17 (2002), pp. 1941–1958 (cit. on pp. 32, 41, 76).

[51] Cheung, K. S. and Yip, S. “Brittle-ductile transition in intrinsic fracture behavior of crystals”. In: *Physical review letters* 65.22 (1990), pp. 2804–2807 (cit. on p. 30).

[52] Chiaia, B., van Mier, J., and Vervuurt, A. “Crack Growth Mechanisms in Four Different Concretes: Microscopic Observations and Fractal Analysis”. In: *Cement and Concrete Research* 28.1 (1998), pp. 103–114 (cit. on pp. 11, 12).

[53] Chiaia, B., Vervuurt, A., and van Mier, J. “Lattice model evaluation of progressive failure in disordered particle composites”. In: *Engineering Fracture Mechanics* 57.2-3 (1997), pp. 301–318 (cit. on p. 40).

[54] Chow, C. and Wang, J. “An anisotropic theory of elasticity for continuum damage mechanics”. English. In: *International Journal of Fracture* 33.1 (1987), pp. 3–16 (cit. on p. 168).

[55] Christman, T., Needleman, A., and Suresh, S. “An experimental and numerical study of deformation in metal-ceramic composites”. In: *Acta Metallurgica* 37.11 (1989), pp. 3029–3050 (cit. on p. 33).

[56] Cifuentes, H., Alcalde, M., and Medina, F. “Measuring the Size-Independent Fracture Energy of Concrete”. In: *Strain* 49.1 (2013), pp. 54–59 (cit. on p. 11).

[57] Comi, C. “A non-local model with tension and compression damage mechanisms”. In: *European Journal of Mechanics - A/Solids* 20.1 (2001), pp. 1–22 (cit. on p. 27).

[58] Cope, R., Rao, P., Clark, L., and Norris, P. “Modelling of reinforced concrete behaviour for finite element analysis of bridge slabs”. In: *Numerical methods for nonlinear problems*. Ed. by Taylor, C., Hinton, E., and Owen, D. Swansea: Pineridge Press, 1980, pp. 457–470 (cit. on p. 165).

[59] Cox, J. V. “An extended finite element method with analytical enrichment for cohesive crack modeling”. In: *International Journal for Numerical Methods in Engineering* 78.1 (2009), pp. 48–83 (cit. on p. 164).

[60] Crisfield, M. “Local instabilities in the non-linear analysis of reinforced-concrete beams and slabs”. In: *Proceedings Of The Institution Of Civil Engineers Part 2-Research And Theory* 73.MAR (1982), 135–145 (cit. on p. 166).

[61] Cundall, P. A. and Strack, O. D. L. “A discrete numerical model for granular assemblies.” In: *Geotechnique* 29.1 (1979), pp. 47–65 (cit. on pp. 30, 176).

[62] Curtin, W. A. and Miller, R. E. “Atomistic/continuum coupling in computational materials science”. In: *Modelling and Simulation in Materials Science and Engineering* 11.3 (2003), R33 (cit. on p. 36).

[63] Cusatis, G., Bažant, Z. P., and Cedolin, L. “Confinement-shear lattice model for concrete damage in tension and compression: I. Theory”. In: *Journal of Engineering Mechanics* 129.12 (2003), pp. 1439–1448 (cit. on p. 31).

[64] Cusatis, G., Bažant, Z., and Cedolin, L. “Confinement-shear lattice CSL model for fracture propagation in concrete”. In: *Computer Methods in Applied Mechanics and Engineering* 195.52 (2006). Computational Modelling of Concrete, pp. 7154–7171 (cit. on p. 49).

[65] D’Addetta, G. A., Kun, F., and Ramm, E. “On the application of a discrete model to the fracture process of cohesive granular materials”. In: *Granular Matter* 4 (2 2002). 10.1007/s10035-002-0103-9, pp. 77–90 (cit. on pp. 31, 54).

[66] de Borst, R. “Fracture in quasi-brittle materials: a review of continuum damage-based approaches”. In: *Engineering Fracture Mechanics* 69.2 (2002), pp. 95–112 (cit. on p. 168).

[67] de Borst, R. “Smeared cracking, plasticity, creep, and thermal loading-A unified approach”. In: *Comput. Methods Appl. Mech. Eng.* 62.1 (May 1987), pp. 89–110 (cit. on p. 165).

[68] de Borst, R. and Mühlhaus, H.-B. "Gradient-dependent plasticity: Formulation and algorithmic aspects". In: *International Journal for Numerical Methods in Engineering* 35.3 (1992), pp. 521–539 (cit. on p. 28).

[69] de Borst, R. and Nauta, P. "Non-orthogonal cracks in a smeared finite element model". In: *Engineering Computations* 2.1 (1985), pp. 35–46 (cit. on p. 165).

[70] de Borst, R., Sluys, L., Muhlhaus, H.-B., and Pamin, J. "Fundamental issues in finite element analyses of localization of deformation". In: *Engineering Computations: Int J for Computer-Aided Engineering* 10.2 (1993), pp. 99–121 (cit. on p. 164).

[71] de Vree, J., Brekelmans, W., and van Gils, M. "Comparison of nonlocal approaches in continuum damage mechanics". In: *Computers & Structures* 55.4 (1995), pp. 581–588 (cit. on pp. 25, 174).

[72] Delaplace, A. *Modélisation discrète appliquée au comportment des matériaux et des structures*. Mémoire d'Habilitation à Diriger des Recherches. Cachan, 2008 (cit. on p. 55).

[73] Delaplace, A. "Fine description of fracture by using discrete particle model". In: *Proceedings of ICF*. 2005 (cit. on p. 31).

[74] Delaplace, A. and Desmorat, R. "Discrete 3D model as complimentary numerical testing for anisotropic damage". In: *International Journal of Fracture* 148.2 (2007), pp. 115–128 (cit. on pp. 55, 73).

[75] Dempsey, J., Adamson, R., and Mulmule, S. "Scale effects on the in-situ tensile strength and fracture of ice. Part II: First-year sea ice at Resolute, N.W.T." English. In: *International Journal of Fracture* 95 (1-4 1999), pp. 347–366 (cit. on pp. 15, 16).

[76] Dempsey, J., Defranco, S., Adamson, R., and Mulmule, S. "Scale effects on the in-situ tensile strength and fracture of ice Part I: Large grained freshwater ice at Spray Lakes Reservoir, Alberta". English. In: *International Journal of Fracture* 95 (1-4 1999), pp. 325–345 (cit. on p. 15).

[77] Desmorat, R., Gatuingt, F., and Ragueneau, F. "Nonlocal anisotropic damage model and related computational aspects for quasi-brittle materials". In: *Engineering Fracture Mechanics* 74.10 (2007), pp. 1539–1560 (cit. on pp. 27, 167).

[78] Desrues, J. and Viggiani, G. "Strain localization in sand: an overview of the experimental results obtained in Grenoble using stereophotogrammetry". In: *International Journal for Numerical and Analytical Methods in Geomechanics* 28.4 (2004), pp. 279–321 (cit. on pp. 9, 10, 173).

[79] Dewar, J. *Computer Modelling of Concrete Mixtures*. Taylor & Francis, 1999 (cit. on p. 62).

[80] Dhia, H. B. and Rateau, G. "The Arlequin method as a flexible engineering design tool". In: *International Journal for Numerical Methods in Engineering* 62.11 (2005), pp. 1442–1462 (cit. on p. 36).

[81] Donzé, F. V., Richefeu, V., and Magnier, S.-A. "Advances in discrete element method applied to soil, rock and concrete mechanics". In: *State of the art of geotechnical engineering. Electronic Journal of Geotechnical Engineering* 44 (2009) (cit. on p. 31).

[82] Dragon, A., Cormery, F., Désoyer, T., and Halm, D. "Localized failure analysis using damage models". In: *Localization and bifurcation theory for solids and rocks*. Ed. by Chambon, R., Desrues, J., and Vardoulakis, I. Rotterdam: A.A. Balkema, 1994, pp. 127–140 (cit. on p. 167).

[83] Dragon, A., Halm, D., and Désoyer, T. "Anisotropic damage in quasi-brittle solids: modelling, computational issues and applications". In: *Computer Methods in Applied Mechanics and Engineering* 183.3-4 (2000), pp. 331–352 (cit. on p. 168).

[84] Dufour, F., Legrain, G., Pijaudier-Cabot, G., and Huerta, A. “Estimation of crack opening from a two-dimensional continuum-based finite element computation”. In: *International Journal for Numerical and Analytical Methods in Geomechanics* 36.16 (2012), pp. 1813–1830 (cit. on p. 130).

[85] Eckardt, S., Häfner, S., and Könke, C. “Simulation of the fracture behaviour of concrete using continuum damage models at the mesoscale”. In: *European Congress on Computational Methods in Applied Sciences and Engineering, ECCOMAS 2004*. Ed. by Neittaanmäki, P., Rossi, T., Majava, K., Pironneau, O., Owen, R., and Mikkola, M. Jyväskylä, 2004 (cit. on p. 30).

[86] Emeriault, F., Cambou, B., and Mahboubi, A. “Homogenization for granular materials: non reversible behaviour”. In: *Mechanics of Cohesive-frictional Materials* 1.2 (1996), pp. 199–218 (cit. on p. 34).

[87] Eringen, A. “Linear theory of micropolar elasticity”. In: *Journal of Mathematics and Mechanics* 15 (1996), pp. 909–931 (cit. on p. 41).

[88] Fakhimi, A. “A hybrid discrete-finite element model for numerical simulation of geomaterials”. In: *Computers and Geotechnics* 36.3 (2009), pp. 386–395 (cit. on p. 36).

[89] Farhat, C., Lesoinne, M., and Pierson, K. “A scalable dual-primal domain decomposition method”. In: *Numerical Linear Algebra with Applications* 7.7-8 (2000), pp. 687–714 (cit. on pp. 134, 135, 184).

[90] Farhat, C., Lesoinne, M., Tallec, P. L., Pierson, K., and Rixen, D. “FETI-DP: a dual-primal unified FETI method?part I: A faster alternative to the two-level FETI method”. In: *International Journal for Numerical Methods in Engineering* 50 (7 2001), pp. 1523–1544 (cit. on pp. 134, 135, 184).

[91] Farhat, C. and Mandel, J. “The two-level FETI method for static and dynamic plate problems Part I: An optimal iterative solver for biharmonic systems”. In: *Computer Methods in Applied Mechanics and Engineering* 155.1-2 (1998), pp. 129–151 (cit. on p. 135).

[92] Farhat, C. and Roux, F.-X. “A method of finite element tearing and interconnecting and its parallel solution algorithm”. In: *International Journal for Numerical Methods in Engineering* 32.6 (1991), pp. 1205–1227 (cit. on p. 135).

[93] Farkas, D., Van Swygenhoven, H., and Derlet, P. “Intergranular fracture in nanocrystalline metals”. In: *Physical review B. Condensed matter and materials physics* 66.6 (2002), pp. 060101–1 (cit. on p. 30).

[94] Faure, F., Allard, J., Cotin, S., Neumann, P., Bensoussan, P.-J., Duriez, C., Delingette, H., Grisoni, L., et al. “SOFA: A modular yet efficient simulation framework”. In: *Surgetica 2007: Computer-Aided Medical Interventions: tools and applications*. 2007 (cit. on p. 67).

[95] Feyel, F. “A multilevel finite element method (FE^2) to describe the response of highly nonlinear structures using generalized continua”. In: *Computer Methods in applied Mechanics and engineering* 192.28 (2003), pp. 3233–3244 (cit. on p. 34).

[96] Feyel, F. “Multiscale FE^2 elastoviscoplastic analysis of composite structures”. In: *Computational Materials Science* 16.1-4 (1999), pp. 344–354 (cit. on p. 34).

[97] Fichant, S., La Borderie, C., and Pijaudier-Cabot, G. “Isotropic and anisotropic descriptions of damage in concrete structures”. In: *Mechanics of Cohesive-frictional Materials* 4.4 (1999), pp. 339–359 (cit. on p. 168).

[98] Fish, J., Yu, Q., and Shek, K. “Computational damage mechanics for composite materials based on mathematical homogenization”. In: *International journal for numerical methods in engineering* 45.11 (1999), pp. 1657–1679 (cit. on p. 33).

[99] Fisher, R. A. and Tippett, L. H. “Limiting forms of the frequency distribution of the largest or smallest member of a sample”. In: *Proceedings of the Cambridge Philosophical Society* 24 (1928), p. 180 (cit. on p. 15).

[100] Fokwa, D. “Matériaux hétérogènes: analyse expérimentale et modélisation numérique par une approche hiérarchique”. PhD thesis. 1992 (cit. on p. 90).

[101] Foote, R. M., Mai, Y.-W., and Cotterell, B. “Crack growth resistance curves in strain-softening materials”. In: *Journal of the Mechanics and Physics of Solids* 34.6 (1986), pp. 593–607 (cit. on p. 164).

[102] Frangin, E., Marin, P., and Daudeville, L. “Coupled finite/discrete elements method to analyze localized impact on reinforced concrete structure”. In: *Computational modelling of concrete structures*. Ed. by Meschke, G and DeBorst, R and Mang, H and Bicanic, N. EURO-C Conference 2006, Mayrhofen, AUSTRIA, MAR 27-30, 2006. 2006, 89–96 (cit. on p. 36).

[103] Fries, T.-P. and Belytschko, T. “The extended/generalized finite element method: An overview of the method and its applications”. In: *International Journal for Numerical Methods in Engineering* 84.3 (2010), pp. 253–304 (cit. on p. 164).

[104] Fuller, W. B. and Thompson, S. E. “The laws of proportioning concrete”. In: *Transactions of the American Society of Civil Engineers* LVII.2 (1906), pp. 67–143 (cit. on p. 62).

[105] Garboczi, E. and Bentz, D. *Multi-scale Picture of Concrete and Its Transport Properties: Introduction for Non-cement Researchers*. National Institute of Standards and Technology, 1995 (cit. on pp. 7, 171).

[106] Garikipati, K. “A variational multiscale method to embed micromechanical surface laws in the macromechanical continuum formulation”. In: *Cmes-Computer Modeling In Engineering & Sciences* 3.2 (2002), 175–184 (cit. on pp. 36, 177).

[107] Gaweska Hager, I. “Comportement à haute température des bétons à haute performance–évolution des principales propriétés mécaniques”. PhD thesis. Paris, France: Ecole Nationale Des Ponts et Chaussées, 2004 (cit. on p. 62).

[108] Geel, E. van and Eindhoven, T. U. *Concrete Behaviour in Multiaxial Compression: Experimental Research*. Techn. Univ., 1998 (cit. on pp. 8, 172).

[109] Geers, M., Kouznetsova, V., and Brekelmans, W. “Multi-scale computational homogenization: Trends and challenges”. In: *Journal of Computational and Applied Mathematics* 234.7 (2010). Fourth International Conference on Advanced Computational Methods in ENgineering (ACOMEN 2008), pp. 2175–2182 (cit. on p. 34).

[110] Geuzaine, C. and Remacle, J.-F. “Gmsh: A 3-D finite element mesh generator with built-in pre-and post-processing facilities”. In: *International Journal for Numerical Methods in Engineering* 79.11 (2009), pp. 1309–1331 (cit. on p. 67).

[111] Giner, E., Sukumar, N., Tarancon, J. E., and Fuenmayor, F. J. “An Abaqus implementation of the extended finite element method”. English. In: *ENGINEERING FRACTURE MECHANICS* 76.3 (Feb. 2009), 347–368 (cit. on p. 164).

[112] Giry, C., Dufour, F., and Mazars, J. “Stress-based nonlocal damage model”. In: *International Journal of Solids and Structures* 48.25-26 (2011), pp. 3431–3443 (cit. on pp. 27, 29, 88, 157, 175).

[113] Gitman, I., Askes, H., and Sluys, L. “Coupled-volume multi-scale modelling of quasi-brittle material”. In: *European Journal of Mechanics - A/Solids* 27.3 (2008), pp. 302–327 (cit. on pp. 34, 177).

[114] Gitman, I., Askes, H., and Aifantis, E. “Gradient Elasticity with Internal Length and Internal Inertia Based on the Homogenisation of a Representative Volume Element”. In: *Journal of the Mechanical Behavior of Materials* 18.1 (2007), pp. 1–16 (cit. on p. 34).

[115] Gitman, I., Askes, H., and Aifantis, E. “The Representative Volume Size in Static and Dynamic Micro-Macro Transitions”. In: *International Journal of Fracture* 135.1-4 (2005), pp. L3–L9 (cit. on p. 34).

[116] Gopalaratnam, V. and Shah, S. “Softening response of plain concrete in direct tension”. English. In: *Journal Of The American Concrete Institute* 82.3 (1985), 310–323 (cit. on pp. 10, 164).

[117] Grassl, P., Grégoire, D., Solano, L. R., and Pijaudier-Cabot, G. “Meso-scale modelling of the size effect on the fracture process zone of concrete”. In: *International Journal of Solids and Structures* 49.13 (2012), pp. 1818–1827 (cit. on pp. 8, 172).

[118] Grassl, P. and Jirásek, M. “Meso-scale approach to modelling the fracture process zone of concrete subjected to uniaxial tension”. In: *International Journal of Solids and Structures* 47.7 (2010), pp. 957–968 (cit. on pp. 67, 76).

[119] Griffith, A. A. “The Phenomena of Rupture and Flow in Solids”. In: *Philosophical Transactions of the Royal Society of London. Series A, Containing Papers of a Mathematical or Physical Character* 221.582-593 (1921), pp. 163–198 (cit. on p. 15).

[120] Guo, X. and Gilbert, R. “The effect of specimen size on the fracture energy and softening function of concrete”. English. In: *Materials and Structures* 33 (5 2000), pp. 309–316 (cit. on p. 11).

[121] Häfner, S., Eckardt, S., Luther, T., and Könke, C. “Mesoscale modeling of concrete: Geometry and numerics”. In: *Computers & structures* 84.7 (2006), pp. 450–461 (cit. on pp. 61, 178).

[122] Haidar, K., Pijaudier-Cabot, G., Dube, J., and Loukili, A. “Correlation between the internal length, the fracture process zone and size effect in model materials”. In: *Materials And Structures* 38.276 (Mar. 2005), 201–210 (cit. on pp. 27, 29, 176).

[123] Halm, D. and Dragon, A. “A model of anisotropic damage by mesocrack growth; unilateral effect”. In: *International Journal of Damage Mechanics* 5.4 (1996), pp. 384–402 (cit. on p. 167).

[124] Hasnaoui, A., Van Swygenhoven, H., and Derlet, P. “Dimples on nanocrystalline fracture surfaces as evidence for shear plane formation”. In: *Science* 300.5625 (2003), pp. 1550–1552 (cit. on p. 30).

[125] Herrmann, H., Hansen, A., and Roux, S. “Fracture of disordered, elastic lattices in two dimensions”. In: *Phys. Rev. B* 39 (1 Jan. 1989), pp. 637–648 (cit. on pp. 31, 54).

[126] Hill, R. “The elastic behaviour of a crystalline aggregate”. In: *Proceedings of the Physical Society. Section A* 65.5 (1952), p. 349 (cit. on p. 33).

[127] Hill, R. “Continuum micro-mechanics of elastoplastic polycrystals”. In: *Journal of the Mechanics and Physics of Solids* 13.2 (1965), pp. 89–101 (cit. on p. 33).

[128] Hillerborg, A. “The theoretical basis of a method to determine the fracture energy G_F of concrete”. English. In: *Materials and Structures* 18 (4 1985), pp. 291–296 (cit. on p. 164).

[129] Hillerborg, A., Modéer, M., and Petersson, P.-E. “Analysis of crack formation and crack growth in concrete by means of fracture mechanics and finite elements”. In: *Cement and Concrete Research* 6.6 (1976), pp. 773–781 (cit. on pp. 163, 164, 166).

[130] Hordijk, D. “Local approach to fatigue of concrete”. PhD thesis. The Netherlands: Delft University of Technology, 1991 (cit. on pp. 9, 172).

[131] Hrennikoff, A. “Solution of problems of elasticity by the framework method”. In: *Applied Mechanics* A8.1 (1941), pp. 169–175 (cit. on p. 31).

[132] Hsu, T. T. C. and Slate, F. O. “Tensile bond strength between aggregate and cement paste or mortar”. In: *Journal of the American Concrete Institute* 60.4 (1963), pp. 465–486 (cit. on pp. 8, 78, 172).

[133] Hughes, T. J., Feijóo, G. R., Mazzei, L., and Quincy, J.-B. “The variational multiscale method-a paradigm for computational mechanics”. In: *Computer Methods in Applied Mechanics and Engineering* 166.1-2 (1998). Advances in Stabilized Methods in Computational Mechanics, pp. 3–24 (cit. on p. 36).

[134] Hughes, T. *The finite element method: linear static and dynamic finite element analysis*. Dover Civil and Mechanical Engineering Series. Dover Publications, 2000 (cit. on p. 20).

[135] Husem, M. “The effects of bond strengths between lightweight and ordinary aggregate-mortar, aggregate-cement paste on the mechanical properties of concrete”. In: *Materials Science and Engineering: A* 363.1–2 (2003), pp. 152–158 (cit. on pp. 8, 172).

[136] Ieşan, D. “On the linear theory of micropolar elasticity”. In: *International Journal of Engineering Science* 7.12 (1969), pp. 1213–1220 (cit. on p. 41).

[137] Issa, M. A., Issa, M. A., Islam, M., and Chudnovsky, A. “Fractal dimension–a measure of fracture roughness and toughness of concrete”. In: *Engineering Fracture Mechanics* 70.1 (2003), pp. 125–137 (cit. on p. 14).

[138] Jansen, D. and Shah, S. “Effect of Length on Compressive Strain Softening of Concrete”. In: *Journal of Engineering Mechanics* 123.1 (1997), pp. 25–35 (cit. on pp. 8, 11, 172).

[139] Jirasek, M. and Bažant, Z. *Inelastic Analysis of Structures*. John Wiley & Sons, 2002 (cit. on p. 130).

[140] Jirásek, M., Kondo, D., and Viggiani, C. *Damage and fracture in geomaterials (Revue européenne de génie civil)*. Vol. 11. 7-8. Hermes Science Publications, 2007 (cit. on pp. 29, 175).

[141] Jirásek, M. “Comparative study on finite elements with embedded discontinuities”. In: *Computer Methods in Applied Mechanics and Engineering* 188.1-3 (2000), pp. 307–330 (cit. on p. 164).

[142] Jirásek, M. and Bazant, Z. P. “Particle model for quasibrittle fracture and application to sea ice”. In: *Journal of engineering mechanics* 121.9 (1995), pp. 1016–1025 (cit. on p. 46).

[143] Kaczmarczyk, Ł., Pearce, C. J., and Bićanić, N. “Scale transition and enforcement of RVE boundary conditions in second-order computational homogenization”. In: *International Journal for Numerical Methods in Engineering* 74.3 (2008), pp. 506–522 (cit. on pp. 34, 177).

[144] Karihaloo, B., Shao, P., and Xiao, Q. “Lattice modelling of the failure of particle composites”. In: *Engineering Fracture Mechanics* 70.17 (2003), pp. 2385–2406 (cit. on p. 41).

[145] Kawai, T. “New discrete models and their application to seismic response analysis of structures”. In: *Nuclear Engineering and Design* 48.1 (1978), pp. 207–229 (cit. on p. 31).

[146] Kikuchi, A., Kawai, T., and Suzuki, N. “The rigid bodies-spring models and their applications to three-dimensional crack problems”. In: *Computers & structures* 44.1 (1992), pp. 469–480 (cit. on p. 31).

[147] Kouznetsova, V., Geers, M. G. D., and Brekelmans, W. A. M. “Multi-scale constitutive modelling of heterogeneous materials with a gradient-enhanced computational homogenization scheme”. In: *International Journal for Numerical Methods in Engineering* 54.8 (2002), pp. 1235–1260 (cit. on pp. 34, 177).

[148] Larsson, F. and Runesson, K. “Adaptive Bridging of Scales in Continuum Modeling Based on Error Control”. In: *International Journal for Multiscale Computational Engineering* 6.4 (2008), 371–392 (cit. on pp. 36, 177).

[149] Lemaître, J. *A course on damage mechanics*. Springer, 1996 (cit. on pp. 23, 173).

[150] Lemaitre, J., Desmorat, R., and Sauzay, M. "Anisotropic damage law of evolution". In: *European Journal of Mechanics - A/Solids* 19.2 (2000), pp. 187–208 (cit. on p. 168).

[151] Lesoinne, M. and Pierson, K. "An efficient FETI implementation on distributed shared memory machines with independent numbers of subdomains and processors". In: *Contemporary Mathematics* 218 (1998), pp. 318–324 (cit. on p. 144).

[152] Liao, K.-Y., Chang, P.-K., Peng, Y.-N., and Yang, C.-C. "A study on characteristics of interfacial transition zone in concrete". In: *Cement and Concrete Research* 34.6 (2004), pp. 977–989 (cit. on pp. 8, 172).

[153] Liaw, B., Jeang, F., Du, J., Hawkins, N., and Kobayashi, A. "Improved Nonlinear Model for Concrete Fracture". In: *Journal of Engineering Mechanics* 116.2 (1990), pp. 429–445 (cit. on p. 164).

[154] Lilliu, G. and van Mier, J. "3D lattice type fracture model for concrete". In: *Engineering Fracture Mechanics* 70.7-8 (2003), pp. 927–941 (cit. on pp. 40, 66, 179).

[155] Lilliu, G. *3D analysis of fracture processes in concrete*. Delft: Eburon Academic Publishers, 2007 (cit. on p. 40).

[156] Linder, C. and Armero, F. "Finite elements with embedded strong discontinuities for the modeling of failure in solids". In: *International Journal for Numerical Methods in Engineering* 72.12 (2007), pp. 1391–1433 (cit. on p. 164).

[157] Lloberas-Valls, O., Rixen, D., Simone, A., and Sluys, L. "Multiscale domain decomposition analysis of quasi-brittle heterogeneous materials". In: *International Journal for Numerical Methods in Engineering* 89.11 (2012), pp. 1337–1366 (cit. on pp. 36, 143).

[158] Lloberas-Valls, O., Rixen, D., Simone, A., and Sluys, L. "On micro-to-macro connections in domain decomposition multiscale methods". In: *Computer Methods in Applied Mechanics and Engineering* 225-228 (2012), pp. 177–196 (cit. on p. 36).

[159] Loehnert, S. and Belytschko, T. "A multiscale projection method for macro/microcrack simulations". In: *International Journal for Numerical Methods in Engineering* 71.12 (2007), pp. 1466–1482 (cit. on p. 35).

[160] Maji, A. and Shah, S. "Process zone and acoustic-emission measurements in concrete". In: *Experimental Mechanics* 28.1 (Mar. 1988), 27–33 (cit. on pp. 29, 176).

[161] Man, H.-K. and van Mier, J. "Size effect on strength and fracture energy for numerical concrete with realistic aggregate shapes". In: *International Journal of Fracture* 154 (1 2008). 10.1007/s10704-008-9270-y, pp. 61–72 (cit. on p. 61).

[162] Mariotte, E. *Traité du mouvement des eaux et autres corps fluides*. E. Michallet, 1686 (cit. on p. 15).

[163] Markeset, G. and Hillerborg, A. "Softening of concrete in compression - Localization and size effects". In: *Cement and Concrete Research* 25.4 (1995), pp. 702–708 (cit. on pp. 8, 172).

[164] Markovič, M., Saje, M., Planinc, I., and Bratina, S. "On strain softening in finite element analysis of RC planar frames subjected to fire". In: *Engineering Structures* 45 (2012), pp. 349–361 (cit. on p. 11).

[165] Maturana, P., Planas, J., and Elices, M. "Evolution of fracture behaviour of saturated concrete in the low temperature range". In: *Engineering Fracture Mechanics* 35.4-5 (1990), pp. 827–834 (cit. on p. 11).

[166] Mazars, J. *Application de la mécanique de l'endommagement au comportement non linéaire et à la rupture du béton de structure*. Laboratoire de mécanique et technologie, 1984 (cit. on pp. 24, 174).

[167] Mazars, J. and Pijaudier-Cabot, G. "Continuum Damage Theory—Application to Concrete". In: *Journal of Engineering Mechanics* 115.2 (1989), pp. 345–365 (cit. on pp. 24, 25).

[168] Meakin, P., Li, G., Sander, L., Louis, E., and Guinea, F. "A simple two-dimensional model for crack-propagation". In: *Journal Of Physics A-Mathematical And General* 22.9 (May 1989), 1393–1403 (cit. on p. 41).

[169] Melenk, J. M. and Babuška, I. "The partition of unity finite element method: Basic theory and applications". In: *Computer Methods in Applied Mechanics and Engineering* 139 (1 1996), pp. 289–314 (cit. on p. 164).

[170] Mergheim, J. "A variational multiscale method to model crack propagation at finite strains". In: *International Journal for Numerical Methods in Engineering* 80.3 (2009), pp. 269–289 (cit. on pp. 36, 177).

[171] Miehe, C. and Koch, A. "Computational micro-to-macro transitions of discretized microstructures undergoing small strains". English. In: *Archive of Applied Mechanics* 72 (4-5 2002), pp. 300–317 (cit. on pp. 34, 140).

[172] Miehe, C., Schotte, J., and Lambrecht, M. "Homogenization of inelastic solid materials at finite strains based on incremental minimization principles. Application to the texture analysis of polycrystals". In: *Journal of the Mechanics and Physics of Solids* 50.10 (2002), pp. 2123–2167 (cit. on p. 33).

[173] Mihashi, H. and Nomura, N. "Correlation between characteristics of fracture process zone and tension-softening properties of concrete". In: *Nuclear engineering and design* 165.3 (1996), pp. 359–376 (cit. on p. 112).

[174] Moës, N. and Belytschko, T. "Extended finite element method for cohesive crack growth". In: *Engineering Fracture Mechanics* 69.7 (2002), pp. 813–833 (cit. on p. 164).

[175] Moës, N., Dolbow, J., and Belytschko, T. "A finite element method for crack growth without remeshing". In: *International Journal for Numerical Methods in Engineering* 46.1 (1999), pp. 131–150 (cit. on pp. 36, 164).

[176] Murakami, S. and Liu, Y. "Local approach of fracture based on continuum damage mechanics and the related problems". In: *Materials Science Research International* 2.3 (Sept. 1996), 131–142 (cit. on p. 168).

[177] Murthy, A., Palani, G., and Iyer, N. "State-of-the-art review on fracture analysis of concrete structural components". English. In: *Sadhana* 34 (2 2009), pp. 345–367 (cit. on p. 164).

[178] Musielak, M. "Etude numérique et expérimentale des transferts de Composés Organiques Volatils du sol à l'air ambiant, en passant au travers du béton". PhD thesis. Toulouse, France: Institut National Polytechnique de Toulouse - INPT, 2012 (cit. on p. 13).

[179] Nakashima, H. and Oida, A. "Algorithm and implementation of soil-tire contact analysis code based on dynamic FE-DE method". In: *Journal of Terramechanics* 41.2-3 (2004). 14th International Conference of the ISTVS, pp. 127–137 (cit. on p. 36).

[180] Nguyen, D., Lawrence, C., La Borderie, C., Matallah, M., and Nahas, G. "A mesoscopic model for a better understanding of the transition from diffuse damage to localized damage". In: *European Journal of Environmental and Civil Engineering* 14.6-7 (2010), pp. 751–776 (cit. on p. 30).

[181] Nguyen, G. D. "A damage model with evolving nonlocal interactions". In: *International Journal of Solids and Structures* 48.10 (2011), pp. 1544–1559 (cit. on p. 27).

[182] Nguyen, V. P., Lloberas-Valls, O., Stroeven, M., and Sluys, L. "Homogenization-based multiscale crack modelling: From micro-diffusive damage to macro-cracks". In: *Computer Methods in Applied Mechanics and Engineering* 200.9-12 (2011), pp. 1220–1236 (cit. on p. 35).

[183] Nicot, F., Hadda, N., Bourrier, F., Sibille, L., and Darve, F. “Failure mechanisms in granular media: a discrete element analysis”. In: *Granular Matter* 13.3 (2011), pp. 255–260 (cit. on p. 30).

[184] Oliver, J. “Modelling strong discontinuities in solid mechanics via strain softening constitutive equations. Part 2: Numerical simulation”. In: *International Journal for Numerical Methods in Engineering* 39.21 (1996), pp. 3601–3623 (cit. on p. 164).

[185] Oliver, J., Huespe, A. E., Pulido, M. D. G., and Samaniego, E. “On the strong discontinuity approach in finite deformation settings”. In: *International Journal for Numerical Methods in Engineering* 56.7 (2003), pp. 1051–1082 (cit. on p. 36).

[186] Onate, E. and Rojek, J. “Combination of discrete element and finite element methods for dynamic analysis of geomechanics problems”. In: *Computer methods in applied mechanics and engineering* 193.27 (2004), pp. 3087–3128 (cit. on pp. 36, 37).

[187] Ortiz, M. and Pandolfi, A. “Finite-deformation irreversible cohesive elements for three-dimensional crack-propagation analysis”. In: *International Journal for Numerical Methods in Engineering* 44.9 (1999), pp. 1267–1282 (cit. on p. 164).

[188] Ostoja-Starzewski, M. “Lattice models in micromechanics”. In: *Applied Mechanics Reviews* 55.1 (2002), pp. 35–59 (cit. on p. 32).

[189] Otsuka, K. and Date, H. “Fracture process zone in concrete tension specimen”. In: *Engineering Fracture Mechanics* 65.2 (2000), pp. 111–131 (cit. on pp. 88, 112).

[190] Paul, B. *Prediction of elastic constants of multi-phase materials*. Tech. rep. DTIC Document, 1959 (cit. on p. 33).

[191] Peerlings, R. H. J., de Borst, R., Brekelmans, W. A. M., and Geers, M. G. D. “Gradient-enhanced damage modelling of concrete fracture”. In: *Mechanics of Cohesive-frictional Materials* 3.4 (1998), pp. 323–342 (cit. on pp. 26, 28, 174, 175).

[192] Peerlings, R. H. J., de Borst, R., Brekelmans, W. A. M., and Vree, J. H. P. de. “Gradient enhanced damage for quasi-brittle materials”. In: *International Journal for Numerical Methods in Engineering* 39.19 (1996), pp. 3391–3403 (cit. on pp. 28, 175).

[193] Peerlings, R., de Borst, R., Brekelmans, W., and Geers, M. “Localisation issues in local and nonlocal continuum approaches to fracture”. In: *European Journal of Mechanics - A/Solids* 21.2 (2002), pp. 175–189 (cit. on p. 168).

[194] Peerlings, R., Geers, M., de Borst, R., and Brekelmans, W. “A critical comparison of nonlocal and gradient-enhanced softening continua”. In: *International Journal of Solids and Structures* 38.44-45 (2001), pp. 7723–7746 (cit. on p. 28).

[195] Petryna, Y. and Krätzig, W. “Computational framework for long-term reliability analysis of RC structures”. In: *Computer Methods in Applied Mechanics and Engineering* 194.12-16 (2005). Special Issue on Computational Methods in Stochastic Mechanics and Reliability Analysis, pp. 1619–1639 (cit. on p. 10).

[196] Pietruszczak, S. and Mróz, Z. “Finite element analysis of deformation of strain-softening materials”. In: *International Journal for Numerical Methods in Engineering* 17.3 (1981), pp. 327–334 (cit. on p. 168).

[197] Pijaudier-Cabot, G. and Bažant, Z. “Nonlocal Damage Theory”. In: *Journal of Engineering Mechanics* 113.10 (1987), pp. 1512–1533 (cit. on pp. 26, 88, 142).

[198] Pijaudier-Cabot, G., Dufour, F., and Choinska, M. “Permeability due to the Increase of Damage in Concrete: From Diffuse to Localized Damage Distributions”. In: *Journal of Engineering Mechanics* 135.9 (2009), pp. 1022–1028 (cit. on p. 130).

[199] Pijaudier-Cabot, G., Mazars, J., and Pulikowski, J. "Steel-Concrete Bond Analysis with Nonlocal Continuous Damage". In: *Journal of Structural Engineering* 117.3 (1991), pp. 862–882 (cit. on p. 25).

[200] Pijaudier-Cabot, G. and Dufour, F. "Non local damage model: Boundary and evolving boundary effects". In: *European Journal of Environmental and Civil Engineering* 14.6-7 (2010), pp. 729–749 (cit. on pp. 27, 175).

[201] Pijaudier-Cabot, G., Haidar, K., and Dubé, J.-F. "Non-local damage model with evolving internal length". In: *International Journal for Numerical and Analytical Methods in Geomechanics* 28.7-8 (2004), pp. 633–652 (cit. on p. 27).

[202] Pompe, W., Herrmann, H., and Roux, S. "Statistical models for the fracture of disordered media. North-Holland, 1990, 353 p., ISBN 0444 88551x (hardbound) US 92.25, 0444885501($paperback$)US 41.00". In: *Crystal Research and Technology* 26.8 (1991), pp. 1076–1076 (cit. on p. 54).

[203] Portland Cement Association. *Cement and concrete basics: Aggregate*. `http://www.cement.org/basics/concretebasics_aggregate.asp`. [Online; accessed 12-April-2013]. 2013 (cit. on pp. 7, 171).

[204] Potyondy, D., Cundall, P., and Lee, C. "Modelling rock using bonded assemblies of circular particles". In: *2nd North American Rock Mechanics symposium*. 1996 (cit. on p. 31).

[205] Prado, E. and van Mier, J. "Effect of particle structure on mode I fracture process in concrete". In: *Engineering fracture mechanics* 70.14 (2003), pp. 1793–1807 (cit. on pp. 10, 80).

[206] Press, W. H., Teukolsky, S. A., Vetterling, W. T., and Flannery, B. P. *Numerical Recipes 3rd Edition: The Art of Scientific Computing*. 3rd ed. New York, NY, USA: Cambridge University Press, 2007 (cit. on pp. 22, 55, 60).

[207] Quarteroni, A. and Valli, A. *Domain Decomposition Methods for Partial Differential Equations*. Numerical Mathematics and Scientific Computation. Clarendon Press, 1999 (cit. on p. 36).

[208] Radjaï, F. and Dubois, F. *Discrete-element modeling of granular materials*. ISTE, 2011 (cit. on p. 31).

[209] Radjai, F., Vincent, T., Vincent, R., Voivret, C., Delenne, J.-Y., Azéma, E., El Youssoufi, M. S., et al. "Force transmission in cohesive granular media". In: *Mathematical Modeling and Physical Instances of granular Flows* (2010), pp. 240–260 (cit. on pp. 31, 176).

[210] Rashid, Y. "Ultimate strength analysis of prestressed concrete pressure vessels". In: *Nuclear Engineering and Design* 7.4 (1968), pp. 334–344 (cit. on pp. 164, 165).

[211] RILEM, T. "Determination of the fracture energy of mortar and concrete by means of three-point bend tests on notched beams". English. In: *Materials and Structures* 18 (6 1985), pp. 484–484 (cit. on p. 11).

[212] Roesler, J., Paulino, G. H., Park, K., and Gaedicke, C. "Concrete fracture prediction using bilinear softening". In: *Cement and Concrete Composites* 29.4 (2007), pp. 300–312 (cit. on p. 164).

[213] Rojek, J. and Oñate, E. "Multiscale analysis using a coupled discrete/finite element model". In: *Interaction and Multiscale Mechanics* 1.1 (2007), pp. 1–31 (cit. on p. 36).

[214] Rousseau, J., Frangin, E., Marin, P., and Daudeville, L. "Multidomain finite and discrete elements method for impact analysis of a concrete structure". In: *Engineering Structures* 31.11 (2009), pp. 2735–2743 (cit. on pp. 36, 37).

[215] Saether, E., Yamakov, V., and Glaessgen, E. H. “An embedded statistical method for coupling molecular dynamics and finite element analyses”. In: *International Journal for Numerical Methods in Engineering* 78.11 (2009), pp. 1292–1319 (cit. on p. 36).

[216] Sagar, R. V. and Prasad, B. K. R. “Modelling heterogeneity of concrete using 2D lattice network for concrete fracture and comparison with AE study”. In: *Sadhana-Academy Proceedings In Engineering Sciences* 34.6 (Dec. 2009), 865–886 (cit. on pp. 8, 66, 172, 179).

[217] Schlangen, E. “Experimental and numerical analysis of fracture processes in concrete”. PhD thesis. Delft, Netherlands: Delft University of Technology, 1993 (cit. on p. 31).

[218] Schlangen, E. and Garboczi, E. “Fracture simulations of concrete using lattice models: Computational aspects”. In: *Engineering Fracture Mechanics* 57.2-3 (1997), pp. 319–332 (cit. on pp. 8, 41, 54, 172).

[219] Schlangen, E. and Garboczi, E. “New method for simulating fracture using an elastically uniform random geometry lattice”. In: *International Journal of Engineering Science* 34.10 (1996), pp. 1131–1144 (cit. on pp. 32, 46, 60).

[220] Schlangen, E. and van Mier, J. “Experimental and numerical analysis of micromechanisms of fracture of cement-based composites”. In: *Cement and Concrete Composites* 14.2 (1992b), pp. 105–118 (cit. on pp. 31, 40).

[221] Schlangen, E. and van Mier, J. “Simple lattice model for numerical-simulation of fracture of concrete materials and structures”. In: *Materials And Structures* 25.153 (Nov. 1992a), 534–542 (cit. on pp. 31, 40, 66, 179).

[222] Scholtès, L., Chareyre, B., Nicot, F., and Darve, F. “Micromechanics of granular materials with capillary effects”. In: *International journal of engineering science* 47.1 (2009), pp. 64–75 (cit. on p. 30).

[223] Scholtès, L. and Donzé, F.-V. “A DEM model for soft and hard rocks: Role of grain interlocking on strength”. In: *Journal of the Mechanics and Physics of Solids* (2012) (cit. on p. 30).

[224] Scholtès, L. and Donzé, F.-V. “Modelling progressive failure in fractured rock masses using a 3D discrete element method”. In: *International Journal of Rock Mechanics and Mining Sciences* 52 (2012), pp. 18–30 (cit. on p. 30).

[225] Schrader, K. and Koenke, C. “Hybrid computing models for large-scale heterogeneous 3d microstructures”. In: *international Journal For Multiscale Computational Engineering* 9.4, SI (2011), 365–377 (cit. on p. 36).

[226] Şener, S. “Size Effect Tests of High Strength Concrete”. In: *Journal of Materials in Civil Engineering* 9.1 (1997), pp. 46–48 (cit. on p. 15).

[227] Sfer, D., Carol, I., Gettu, R., and Etse, G. “Study of the Behavior of Concrete under Triaxial Compression”. In: *Journal of Engineering Mechanics* 128.2 (2002), pp. 156–163 (cit. on pp. 9, 12).

[228] Shah, S. and Carpinteri, A. *Fracture Mechanics Test Methods For Concrete*. RILEM Reports. Taylor & Francis, 1991 (cit. on p. 164).

[229] Shi, J., Chopp, D., Lua, J., Sukumar, N., and Belytschko, T. “Abaqus implementation of extended finite element method using a level set representation for three-dimensional fatigue crack growth and life predictions”. In: *ENGINEERING FRACTURE MECHANICS* 77.14 (Sept. 2010), 2840–2863 (cit. on p. 164).

[230] Shioya, T., Iguro, M., Nojiri, Y., Akiyama, H., and Okada, T. “Shear Strength of Large Reinforced Concrete Beams”. English. In: *ACI, Special Publication* 118 (1990), pp. 259–280 (cit. on p. 15).

[231] Shiu, W., Donze, F. V., and Daudeville, L. "Discrete element modelling of missile impacts on a reinforced concrete target". In: *International Journal of Computer Applications in Technology* 34.1 (2009), pp. 33–41 (cit. on p. 30).

[232] Simo, J., Oliver, J., and Armero, F. "An analysis of strong discontinuities induced by strain-softening in rate-independent inelastic solids". English. In: *Computational Mechanics* 12 (5 1993), pp. 277–296 (cit. on p. 36).

[233] Skarżyński, Ł., Syroka, E., and Tejchman, J. "Measurements and calculations of the width of the fracture process zones on the surface of notched concrete beams". In: *Strain* 47.s1 (2011), e319–e332 (cit. on p. 112).

[234] Sluis, O. van der, Schreurs, P., Brekelmans, W., and Meijer, H. "Overall behaviour of heterogeneous elastoviscoplastic materials: effect of microstructural modelling". In: *Mechanics of Materials* 32.8 (2000), pp. 449–462 (cit. on p. 33).

[235] Sluys, L. "Wave propagation, localisation and dispersion in softening solids". PhD thesis. Technische Univ., Delft (Netherlands)., Jan. 1992 (cit. on p. 10).

[236] Smit, R., Brekelmans, W., and Meijer, H. "Prediction of the large-strain mechanical response of heterogeneous polymer systems: local and global deformation behaviour of a representative volume element of voided polycarbonate". In: *Journal of the Mechanics and Physics of Solids* 47.2 (1999), pp. 201–221 (cit. on p. 34).

[237] Smit, R., Brekelmans, W., and Meijer, H. "Prediction of the mechanical behavior of nonlinear heterogeneous systems by multi-level finite element modeling". In: *Computer Methods in Applied Mechanics and Engineering* 155.1 (1998), pp. 181–192 (cit. on p. 34).

[238] Song, J.-H., Areias, P. M. A., and Belytschko, T. "A method for dynamic crack and shear band propagation with phantom nodes". In: *International Journal for Numerical Methods in Engineering* 67.6 (2006), pp. 868–893 (cit. on p. 36).

[239] Squillacote, A. H. *The ParaView guide: a parallel visualization application*. Kitware, 2007 (cit. on p. 67).

[240] Sukumar, N. and Prévost, J.-H. "Modeling quasi-static crack growth with the extended finite element method Part I: Computer implementation". In: *International Journal of Solids and Structures* 40.26 (2003), pp. 7513–7537 (cit. on p. 164).

[241] Talbot, D. and Willis, J. "Variational principles for inhomogeneous non-linear media". In: *IMA Journal of Applied Mathematics* 35.1 (1985), pp. 39–54 (cit. on p. 33).

[242] Tallec, P., Roeck, Y., and Vidrascu, M. "Domain decomposition methods for large linearly elliptic three-dimensional problems". In: *Journal of Computational and Applied Mathematics* 34.1 (1991), pp. 93–117 (cit. on p. 36).

[243] Taylor, H. *Cement Chemistry, Second Edition*. Thomas Telford, 1997 (cit. on p. 6).

[244] Temizer, I. and Zohdi, T. "A numerical method for homogenization in non-linear elasticity". English. In: *Computational Mechanics* 40 (2 2007), pp. 281–298 (cit. on p. 33).

[245] Terrien, M. "Émission acoustique et comportement mecanique post-critique d'un béton sollicité en traction". In: *Bulletin de liaison Ponts et Chaussées* 105 (1980), pp. 65–72 (cit. on pp. 8, 172).

[246] Tijssens, M. G., Sluys, L., and Giessen, E. van der. "Numerical simulation of quasi-brittle fracture using damaging cohesive surfaces". In: *European Journal of Mechanics - A/Solids* 19.5 (2000), pp. 761–779 (cit. on p. 164).

[247] Torrenti, J., Benaija, E., and Boulay, C. "Influence of Boundary Conditions on Strain Softening in Concrete Compression Test". In: *Journal of Engineering Mechanics* 119.12 (1993), pp. 2369–2384 (cit. on pp. 8, 9, 172).

[248] Tran, V., Donzé, F.-V., and Marin, P. "A discrete element model of concrete under high triaxial loading". In: *Cement and Concrete Composites* 33.9 (2011), pp. 936–948 (cit. on p. 30).

[249] van Mier, J. "Framework for a generalized four-stage fracture model of cement-based materials". In: *Engineering Fracture Mechanics* 75.18 (2008), pp. 5072–5086 (cit. on pp. 9, 10, 80).

[250] van Mier, J. "Multiaxial strain-softening of concrete". English. In: *Materials and Structures* 19 (3 1986), pp. 179–190 (cit. on p. 8).

[251] van Mier, J. "Similarities between Fracture Processes in Concrete, Rock and Ceramics: Recorders Report to Session 5 'Experimental Methods to Assess Damage'". English. In: *Toughening Mechanisms in Quasi-Brittle Materials*. Ed. by Shah, S. Vol. 195. NATO ASI Series. Springer Netherlands, 1991, pp. 329–335 (cit. on p. 10).

[252] van Mier, J. *Strain-softening of Concrete Under Multiaxial Loading Conditions*. 1984 (cit. on pp. 8–10, 172, 173).

[253] van Mier, J. and Man, H.-K. "Some Notes on Microcracking, Softening, Localization, and Size Effects". In: *International Journal of Damage Mechanics* 18.3 (2009), pp. 283–309 (cit. on pp. 10, 12).

[254] van Mier, J., Schlangen, E., and Vervuurt, A. "Tensile cracking in concrete and sandstone: Part 2—Effect of boundary rotations". English. In: *Materials and Structures* 29 (2 1996), pp. 87–96 (cit. on pp. 9, 172).

[255] van Mier, J., van Vliet, M., and Wang, T. K. "Fracture mechanisms in particle composites: statistical aspects in lattice type analysis". In: *Mechanics of Materials* 34.11 (2002), pp. 705–724 (cit. on p. 67).

[256] van Mier, J. and Vervuurt, A. "Lattice model for analysing steel-concrete interface behaviour". In: *Mechanics of Geomaterial Interfaces*. Ed. by Selvadurai, A. and Boulon, M. Vol. 42. Studies in Applied Mechanics. Elsevier, 1995, pp. 201–225 (cit. on p. 31).

[257] van Mier, J. and Vervuurt, A. "Numerical analysis of interface fracture in concrete using a lattice-type fracture model". In: *International Journal of Damage Mechanics* 6.4 (1997), pp. 408–432 (cit. on p. 40).

[258] van Vliet, M. R. and van Mier, J. G. "Experimental investigation of size effect in concrete and sandstone under uniaxial tension". In: *Engineering Fracture Mechanics* 65.2 (2000), pp. 165–188 (cit. on p. 15).

[259] Vasseur, L., Matthys, S., Taerwe, L., and Van Hemelrijck, D. "Measuring of crack bridging of CFRP strengthened concrete by digital image correlation". eng. In: *Non-Destructive Testing in Civil Engineering, 7th International symposium, CD Proceedings*. Ed. by Abraham, O. and Dé robert, X. Nantes, France: Laboratoire Central des Ponts et Chaussé es, 2009, pp. 1009–1014 (cit. on pp. 12, 13).

[260] Vervuurt, A. H. J. M. "Interface fracture in concrete". PhD thesis. Delft University of Technology, 1997 (cit. on p. 72).

[261] Villard, P., Chevalier, B., Hello, B. L., and Combe, G. "Coupling between finite and discrete element methods for the modelling of earth structures reinforced by geosynthetic". In: *Computers and Geotechnics* 36.5 (2009), pp. 709–717 (cit. on p. 36).

[262] Vonk, R., Rutten, H., van Mier, J., and Fijneman, H. "Micromechanical simulation of concrete softening". In: *Proceedings of the international RILEM/ESIS conference fracture processes in concrete, rock and ceramics. E. & FN, London*. 1991 (cit. on p. 30).

[263] Voyiadjis, G. Z. and Kattan, P. I. "Damage of fiber-reinforced composite materials with micromechanical characterization". In: *International journal of solids and structures* 30.20 (1993), pp. 2757–2778 (cit. on p. 33).

[264] Wang, Z., Kwan, A., and Chan, H. "Mesoscopic study of concrete I: generation of random aggregate structure and finite element mesh". In: *Computers & Structures* 70.5 (1999), pp. 533–544 (cit. on pp. 7, 61, 65, 171, 178).

[265] Weibull, W. *A statistical theory of the strength of materials*. Ingeniörsvetenskapsakademiens handlingar. Generalstabens litografiska anstalts förlag, 1939 (cit. on pp. 16, 173).

[266] Weihe, S., Kröplin, B., and Borst, R. de. "Classification of smeared crack models based on material and structural properties". In: *International Journal of Solids and Structures* 35.12 (1998), pp. 1289–1308 (cit. on p. 166).

[267] Wellmann, C. and Wriggers, P. "A two-scale model of granular materials". In: *Computer Methods in Applied Mechanics and Engineering* 205-208 (2012), pp. 46–58 (cit. on pp. 36, 38).

[268] Wells, G. N. and Sluys, L. J. "A new method for modelling cohesive cracks using finite elements". In: *International Journal for Numerical Methods in Engineering* 50.12 (2001), pp. 2667–2682 (cit. on p. 164).

[269] Wells, G. and Sluys, L. "Three-dimensional embedded discontinuity model for brittle fracture". In: *International Journal of Solids and Structures* 38.5 (2000), pp. 897–913 (cit. on p. 164).

[270] Wittmann, F. *Fracture mechanics of concrete*. Developments in civil engineering. Elsevier, 1983 (cit. on pp. 17, 18).

[271] Wriggers, P. and Moftah, S. "Mesoscale models for concrete: Homogenisation and damage behaviour". In: *Finite elements in analysis and design* 42.7 (2006), pp. 623–636 (cit. on p. 30).

[272] Xiao, S. and Belytschko, T. "A bridging domain method for coupling continua with molecular dynamics". In: *Computer Methods In Applied Mechanics And Engineering* 193.17-20 (2004), 1645–1669 (cit. on p. 36).

[273] Yi, Y.-M., Park, S.-H., and Youn, S.-K. "Asymptotic homogenization of viscoelastic composites with periodic microstructures". In: *International Journal of Solids and Structures* 35.17 (1998), pp. 2039–2055 (cit. on p. 33).

[274] Young, T. and Kelland, P. *A course of lectures on natural philosophy and the mechanical arts*. A course of lectures on natural philosophy and the mechanical arts. 1845 (cit. on p. 15).

[275] Zech, B. and Wittmann, F. H. "A complex study on the reliability assessment of the containment of a PWR, Part II: Probabilistic approach to describe the behaviour of materials". In: *Nuclear Eng. Design* 48 (1978), pp. 575–584 (cit. on p. 16).

[276] Zhao, Z. F., Zhao, Z. G., Feng, X. J., and Li., M. "State-of-the-Art Review on Concrete Softening Curve". English. In: *Advanced Materials Research* 168 (2010), pp. 669–673 (cit. on p. 164).

[277] Zienkiewicz, O. and Taylor, R. *The Finite Element Method: Solid Mechanics*. The Finite Element Method v. 2. Butterworth-Heinemann Limited, 2000 (cit. on p. 20).

[278] Zienkiewicz, O., Taylor, R., and Zhu, J. *The Finite Element Method: Its Basis and Fundamentals: Its Basis and Fundamentals*. Elsevier Science, 2005 (cit. on pp. 20, 23).